MEASUREMENT OF THE NEUTRINO ASYMMETRY IN THE BETA DECAY OF LASER-COOLED, POLARIZED 37K

by

Dan G. Melconian
B.Sc., McMaster University, 1995
M.Sc., Simon Fraser University, 2000

A thesis submitted in partial fulfillment
of the requirements for the degree of
DOCTOR OF PHILOSOPHY
in the
Department of Physics

Simon Fraser
University

SIMON FRASER UNIVERSITY
Fall 2005

TRIUMF

APPROVAL

Name:	Dan G. Melconian
Degree:	Doctor of Philosophy
Title of thesis:	**Measurement of the Neutrino Asymmetry in the Beta Decay of Laser-cooled, Polarized 37K**
Examining Committee:	Dr. Dugan O'Neil – Chair Assistant Professor
	Dr. K. Peter Jackson – Senior Supervisor Senior Research Scientist, TRIUMF
	Dr. John A. Behr Senior Research Scientist, TRIUMF
	Dr. Howard Trottier Professor
	Dr. Michel Vetterli Professor
	Dr. Paul Vetter – External Examiner Staff Scientist, BERKELEY
	Dr. Jeff McGuirk – Internal Examiner Assistant Professor
Date Approved:	November 29, 2005

Abstract

The TRINAT collaboration began investigating fundamental symmetries searching for scalar contributions to the predominantly $V-A$ structure of the weak interaction by measuring the $\beta-\nu$ correlation parameter using the pure Fermi decay of magneto-optically trapped ^{38m}K. This thesis describes the first physics measurement using *polarized*, laser-cooled ^{37}K, and represents the next generation of TRINAT experiments aimed at searching for right-handed currents predicted to restore parity at higher energy scales in some extensions to the Standard Model.

Using a detector geometry similar to that of the scalar search, we have learned to implement optical pumping techniques to achieve very high ($\gtrsim 96\%$) nuclear polarizations of our radioactive atom sample. Furthermore, we have pioneered techniques to measure this observable – independent of the β decay observables – *in situ* on all the nuclei that are decaying. By observing the emitted β^+ and recoiling ^{37}Ar in the back-to-back geometry, we have extracted a measurement of the neutrino asymmetry parameter: $B_\nu = -0.755 \pm \underset{\text{(stat)}}{0.020} \pm \underset{\text{(syst)}}{0.013}$, in agreement with the Standard Model prediction of $-0.7692(15)$.

This 3% measurement of the B_ν represents the first β decay physics measurement using a polarized, laser-cooled source. This is not yet competitive with other limits on right-handed current parameters; however, we have identified our dominant systematics and have learned how to minimize them so that the next time the experiment is performed, we expect to be able to reduce our uncertainty to the 0.5% level. Additionally, we have outlined how we may make use of a correlation unique to our setup to further enhance our sensitivity. We expect that future experiments will be able

to have a significant impact in either finding new physics or helping to constrain the variety of models considered as viable extensions to the Standard Model.

Keywords: neutrino asymmetry, β decay, magneto-optic trap, right-handed currents, optical pumping.

To my parents, Melcon and Zdenka, my brother, Leon, and sister, Sonja, for all their love, support and encouragement.

And I think to myself,
What a wonderful world.

Louis Armstrong
recorded in 1968
written by G. D. Weiss and B. Thiele

Acknowledgements

It has been a great pleasure and wonderful experience working with the TRINAT collaboration and interacting with the many good people at TRIUMF. I would like to thank SFU and everyone at TRIUMF for providing me with a strong physics education and preparing me for post-graduate life.

I am extremely indebted to K. Peter Jackson and John Behr for always being available to talk, for introducing me to the world of experimental nuclear physics and for all their help over the years. Other TRINAT collaborators have all had an impact over the years, including Alexandre Gorelov, Mike Trinczek, Matthew Pearson, Sihong Gu, Ofer Aviv, Pierre Dubé, Danny Ashery, Erika Prime and W. Parker Alford.

Thanks to the many other people at TRIUMF who took an interest in my work and/or generally made life more interesting: Fred Sarazin, Jens Dilling, Mike Lamey, Dario Gigliotti, John D'Auria and Jean-Michel Poutissou. I was fortunate to have a chance to work with Gordon Ball, Greg Hackman and the rest of the 8π collaboration and thank them for the experience. I am indebted to the staff at TRIUMF who have helped with the experiments, particularly Pierre-Andre Amaudruz for the DAQ, and of course Marik Dombsky and Pierre Bricault for providing us with the ^{37}K beam. Candida Mazza has gone way beyond her job description as graduate secretary at SFU in making sure I stayed on top of administrative details (at least the *important* ones!). And I cannot forget Otto Häusser who first took me in and introduced me to TRINAT.

I would also like to thank all of my committee members for their interest and particularly to Peter Jackson, John Behr and Paul Vetter for their detailed critiques

of this thesis.

Finally, I could not have done any of this without the unconditional love and support of my family, for which I am eternally grateful.

Table of Contents

List of Tables

List of Figures

CHAPTER 1

Introduction

Nature is a beautiful, complicated beast. The questions one can ask are endless: How did our universe come to be? What are the building blocks of matter and the forces? How does the human body work, and what is consciousness?

One cannot possibly hope to understand all of Nature, but some of us can be blessed to catch a glimpse of part of it and to see the beauty of a small corner of this fantastic universe. What a wonderful world indeed!

This thesis will outline the research done at TRIUMF, Canada's national subatomic physics laboratory, to explore one area of the physical sciences. Using novel atom-trapping techniques on radioactive ^{37}K, we can probe the details of the weak interaction, and in particular are able to search for right-handed currents in what we know is a predominantly left-handed $(V-A)$ form of the weak interaction.

1.1 β Decay

Nuclear β decay has proven to be an invaluable tool in our study of nuclear and particle physics since the discovery of radioactive decay at the turn of the century. The first experiments following the discovery of β decay appeared to observers as having only two decay products: the daughter atom and a charge-conserving 'β ray,' which was soon realized to be either an electron (β^-) or a positron (β^+). The simple kinematics of such a two-body decay would require that the β energy spectrum be a peak corresponding to the energy released in the transition, as in α decay. The fact that the emitted β ray was observed to have a continuous energy spectrum prompted Pauli in

1931 to propose that β decay is a *3-body* process, the extra product being a light (or even massless), neutral particle that interacts very weakly with matter and so escapes detection. Only three years later, but over twenty years before it was ever *proven* to exist*, Fermi called this elusive particle a *neutrino* when he incorporated it in his theory of β decay. Fermi's model provides us with a simple, intuitive understanding of β decay that, even to this day, remains essentially unchanged.

1.1.1 The Fermi Model

A nucleus that undergoes β decay converts one of its neutrons into a proton, or vice-versa, so that its nuclear charge, Z, changes by ± 1 but the total number of nucleons, A, remains constant. The basic processes underlying these decays at the nucleon level are:

$$\begin{aligned} n &\longrightarrow p + e^- + \overline{\nu}_e \qquad \beta^- \text{ decay} \\ p &\longrightarrow n + e^+ + \nu_e \qquad \beta^+ \text{ decay} \\ p + e^- &\longrightarrow n + \nu_e \qquad \text{orbital electron capture } (\epsilon) \end{aligned}$$

When Fermi first proposed his theory [2], little else was known at the time except that the force inducing the decay was weak compared to the strong force binding the protons and neutrons together to form the nucleus. This allowed Fermi to use first order perturbation theory (his 'Golden Rule') to calculate the transition rate for any suitably weak potential V_{int}:

$$\Gamma = \frac{1}{\tau} = 2\pi |\mathcal{M}_{fi}|^2 \rho(E_f) \tag{1.1}$$

where $\mathcal{M}_{fi} = \int \psi_f^* \, V_{\text{int}} \, \psi_i \, d^3x$ is the matrix element of the perturbing interaction and $\rho(E_f)$ is the density of states available to a final state of energy E_f. The mathematical form of V_{int} for weak interactions is not predicted by Fermi's theory, but there are only five combinations of the γ-matrices that are Lorentz covariant; these interaction types are given in Table 1.1.

*Cowan and Reines reported direct observation at the Savannah River Reactor in 1956-7 [1].

Type	Operator	Parity
Scalar	1	+
Pseudo-scalar	γ_5	−
Vector	γ_μ	−
Axial vector	$\gamma_\mu\gamma_5$	+
Tensor	$\gamma_\mu\gamma_\nu - \gamma_\nu\gamma_\mu$	N/A

TABLE 1.1: Possible forms for an interaction consistent with Lorentz invariance.

Inspired by electromagnetism, Fermi hypothesized that the form of the interaction was vector (see Fig. 1.1). The strength of the electromagnetic interaction is scaled by α, so by analogy Fermi defined what we now call the "universal Fermi coupling constant," G_F, to characterize the strength of the interaction. The currently accepted value of $G_F = 1.16639(1) \times 10^{-5}$ GeV^{-2} [3] is derived from the measured lifetime of the muon. In relation to the other forces, this (overall, effective) coupling is the weakest, hence the force that causes β decay is known as the "weak" interaction.

Using this contact vector model, Fermi derived an expression for the differential decay rate in β decay:

$$\frac{d^5W_{\text{Fermi}}}{dE_e d\Omega_e d\Omega_{\nu_e}} = \frac{G_F^2}{(2\pi)^5} p_e E_e (E_\circ - E_e)^2 F(E_e, Z', R) |\mathcal{M}_{fi}|^2 \tag{1.2}$$

where $E_\circ$ is the maximum energy transferred to the leptons and the 'Fermi function', $F(E_e, Z', R)$, accounts for Coulomb interactions between the emitted β and electric

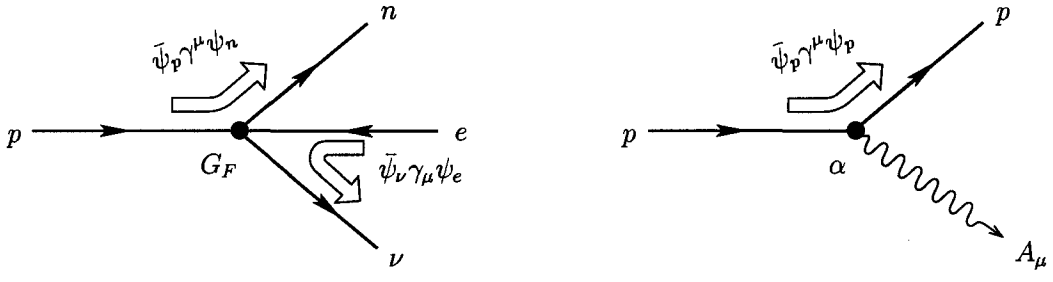

FIGURE 1.1: Fermi's contact model of β^+ decay (left) and analogy with electromagnetism (right). The hadron and lepton currents of β decay was presumed to be analogous to a proton interacting with an electromagnetic field, but with the strength of the coupling G_F instead of α.

field of daughter nucleus. Fermi derived an analytic expression for this function when he first proposed his theory [2]:

$$F(E_e, Z', R) = 4(2p_eR)^{2(s-1)}e^{\pi\eta}\frac{|\Gamma(s+i\eta)|^2}{|\Gamma(1+2s)|^2}, \tag{1.3}$$

where $\eta = \mp E_e/p_e$ for $\beta^{\pm}$ decay, $s^2 = 1 - \alpha^2 Z'^2$ (Z' refers to the daughter nucleus), R is the nuclear radius, and $\alpha = e^2/4\pi$ is the fine structure constant. The shape of the decay rate is generally dominated by the density of states available to the leptons, given by the $p_eE_e(E_\circ - E_e)^2$ term.

1.1.2 Beyond the Fermi Model

In 1957, Lee and Yang [4] made a survey of the experimental evidence regarding parity conservation. They found that though parity conservation had been proven for electromagnetic and strong interactions, there was no proof that this was true of weak interactions. This inspired C. S. Wu [5, 6] and co-workers to specifically look for parity violation in the β decay of polarized ^{60}Co: a tensor interaction (which incidentally was favoured at the time based on experiments of ^{6}He and ^{19}Ne decays) compared to an axial-vector interaction could be discerned based on the angular distribution of the decay. They looked at the correlation of the emitted β's momentum with the initial nuclear spin. In the mirror-world (*i.e.* under a parity transformation), the spin – being an axial vector – will not change sign whereas the β momentum – being a polar vector – will; thus if a β asymmetry was seen, it would necessarily violated parity conservation. Two other experiments were performed at the same time by Garwin *et al.* [7] on the decay of the μ^+, and by Friedman *et al.* [8] on the π^+ decay; all three of these experiments were *not* consistent with parity conservation. This was surprising at the time because all other forces obeyed parity conservation, and so most people expected the same to be true of the weak interaction. The fact that the weak interaction was found to differentiate between left- and right-handedness proved that Fermi's proposed vector form for the interaction was incomplete. The data of these three early experiments, as well as all other experiments which followed, were in fact consistent with an interaction that was *maximally* parity violating! They found that the form

for the weak interaction had equal contributions of vector and axial-vector currents; this showed that via the weak interaction, Nature does indeed differentiate between the physical (left-handed) and mirror-image (right-handed) worlds, and rejects the latter which gives rise to parity non-conservation.

With further theoretical and experimental developments, the electromagnetic and weak interactions were unified by Glashow, Weinberg and Salam in the late sixties. This was a triumphant accomplishment for which the three rightfully shared the Nobel Prize in 1979. We now know that the weak interaction is mediated by three massive vector bosons which naturally arise as a consequence of electroweak unification: the $W^{\pm}$ mediate weak charged currents and the Z° propagates weak neutral currents. The fact that the $W^{\pm}$ have a mass $M_W = 80.425(33)$ GeV means that this force is extremely short-ranged, on the order of $1/M_W \approx 0.003$ fm; it is for this reasons that Fermi's assumption of a four fermion contact interaction is valid to a very good approximation. Electroweak unification has allowed us to understand Fermi's coupling constant in terms of the weak coupling constant, g_w, and the W propagator mass: $G_F/\sqrt{2} = g_w^2/8M_W^2$. This also explains why the weak force is so 'weak': $g_w \approx 0.65$ is actually over two times *stronger* than the electromagnetic, $g_e = \sqrt{4\pi\alpha} \approx 0.30$, but the *effective* coupling is weaker due to the large mass of the W mediating the interaction.

With many questions regarding the nature of the weak interaction answered, but many questions still remaining, we now wonder "what other aspects of the weak interaction will β decay reveal to us ...?"

1.2 Introduction to TRINAT

The experiment performed in the fall of 2002 has many similarities to previous TRINAT experiments involving ^{38m}K described in references [9, 10, 11, 12, 13]: they use a magneto-optical trap (MOT) to provide a cold, clean, backing-free source of radioactive atoms, and observe both the β and recoiling ion (in this case ^{37}Ar) daughter products using very similar detection systems. Indeed, the scintillator-DSSSD β-telescope, electrostatic field and microchannel plate (MCP) detector of the ^{38m}K experiments were exactly the same. The double-MOT system, used to accept radioactive ions

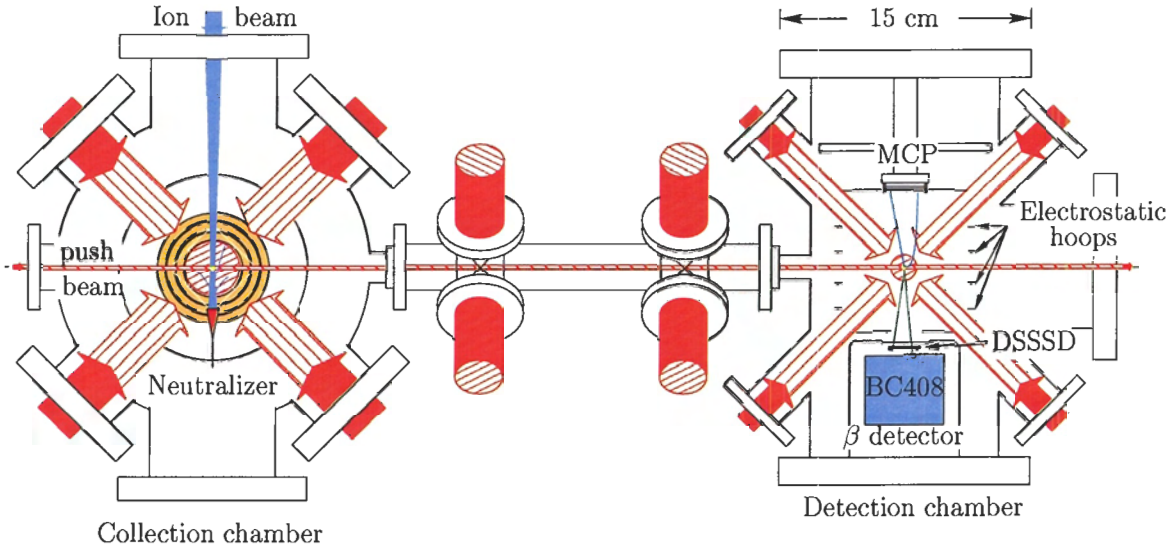

FIGURE 1.2: Schematic diagram of TRINAT's double–MOT system. The ion beam from ISAC is deposited and neutralized in a Zr foil and then trapped in the first 'collection' trap. The cold, trapped atoms are then transferred to the 2nd trap where the decay is observed using a micro-channel plate (recoils) and the β-telescope (positrons).

from ISAC and transfer them to a clean detection chamber, is shown in Fig. 1.2; concentrating on the 2nd (detection) MOT, we see a β-telescope in the back-to-back geometry with a MCP detector. The β-telescope consists of a double-sided Si-strip (DSSSD) detector to measure the β's position and ΔE, and a large plastic scintillator to measure the total energy of the β.

Additions to the ^{38m}K detection system include two phoswich (plastic ΔE + CaF_2(Eu) E) detectors as well as a D_1 optical pumping laser beam used to polarize the atom cloud. By reflecting this beam off of thin mirrors in front of the phoswiches, the polarization axis is aligned with the detection axis of these β detectors; this was done so as to optimize the asymmetry in the β count rates of these detectors whether the polarization is aligned or anti-aligned with the detector. This was meant to allow a precise measurement of the β asymmetry parameter but as we will see, backgrounds from atoms implanting on the mirrors introduced a large systematic which made such a measurement impossible.

The back-to-back geometry of the β-telescope and recoil detector will be shown to

provide a clean measurement of the neutrino asymmetry parameter. From conservation of momentum, one can see how the recoil momentum along the polarization axis is directly given by the neutrino's momentum when the β is emitted perpendicular to the polarization axis. Thus the clean $\beta-$Ar coincidences provide a good measurement of the neutrino's asymmetry, which we use to search for right-handed currents.

CHAPTER 2

Theoretical Background

2.1 Nuclear β-Decay

The Fermi model outlined in the Introduction provided us with a simple, intuitive understanding of β decay which successfully describes most aspects of β decay. However, experiments have shown that the Fermi model does not provide a complete description. As an inherently weak process, nuclear β decay is sensitive to the details of the weak interaction and probes energies on the scale of the mass of the propagator, namely $M_W = 80$ GeV. In this section, we describe in greater detail our current understanding of β decay.

2.1.1 A Generalized Interaction

In 1957, Jackson, Treimann and Wyld derived the β decay rate without any assumptions about symmetries such as charge-conjugation (C), parity (P) or time reversal invariance (T) [14]. They began with a Hamiltonian which includes all forms of the weak interaction listed in Table 1.1:

$$\begin{aligned} H_{\text{int}} = & (\overline{\psi}_p \psi_n)(C_S \overline{\psi}_e \psi_\nu + C'_S \overline{\psi}_e \gamma_5 \psi_\nu) \\ & + (\overline{\psi}_p \gamma_\mu \psi_n)(C_V \overline{\psi}_e \gamma^\mu \psi_\nu + C'_V \overline{\psi}_e \gamma^\mu \gamma_5 \psi_\nu) \\ & + (\overline{\psi}_p \sigma_{\lambda\mu} \psi_n)(C_T \overline{\psi}_e \sigma^{\lambda\mu} \psi_\nu + C'_T \overline{\psi}_e \sigma^{\lambda\mu} \gamma_5 \psi_\nu) \\ & + (\overline{\psi}_p \gamma_\mu \gamma_5 \psi_n)(C_A \overline{\psi}_e \gamma^\mu \gamma_5 \psi_\nu + C'_A \overline{\psi}_e \gamma^\mu \psi_\nu) \\ & + (\overline{\psi}_p \gamma_5 \psi_n)(C_P \overline{\psi}_e \gamma_5 \psi_\nu + C'_P \overline{\psi}_e \psi_\nu) \quad + \quad \text{h.c.} \end{aligned} \tag{2.1}$$

The coupling constants C_i and C_i', which characterize the relative strengths of the five possible currents (S, P, V, A and T), are in general complex and not equal in magnitude. The so-called Standard Model, guided by experimental results, sets $C_S = C_S' = C_T = C_T' = C_P = C_P' = 0$ and $C_V = C_V' = -C_A = -C_A' = 1$. This is the well-known $V - A$ structure of the weak interaction. The vector component changes sign under a parity transformation while the axial vector does not, and so parity is not conserved by the weak force; the fact that the relative sign is negative means that this interaction is left-handed. In fact, this parity violation is thought to be *maximally* violated because no evidence of the mirror image, or a $(V + A)$ right-handed current, has been observed to date.

In going from the (u, d) quark to (p, n) nucleon level, the hadron currents must be modified to account for the fact that the nucleon wavefunctions are not structureless Dirac spinors (like the quarks and leptons). One includes this correction by defining form factors for the hadronic currents. For Fermi (vector) transitions we write the nuclear matrix element as*:

$$\bar{\psi}_p \gamma_\mu \psi_n = \langle p|\bar{u}\gamma_\mu d|n\rangle = g_V(q^2) M_F, \tag{2.2}$$

where for the low-energy limit applicable to β decay, the momentum transfer $q \approx 0$. The conserved vector current (CVC) hypothesis [15] states that, due to its intimate connection with electromagnetism, the vector current in β decay is protected from the strong interaction and so predicts $g_V \equiv g_V(0) = 1$. Spin and isospin then define the Fermi matrix element and the selection rules for vector decays:

$$M_F = \sqrt{T(T+1) - T_3(T_3 \pm 1)}, \qquad \Delta I = 0,\ \Delta T = 0. \tag{2.3}$$

We define a form factor for Gamow-Teller (axial-vector) transitions in a fashion similar to the Fermi case:

$$\bar{\psi}_p \gamma_\mu \gamma_5 \psi_n = \langle p|\bar{u}\gamma_\mu \gamma_5 d|n\rangle \rightarrow g_A M_{GT}. \tag{2.4}$$

*Convention is to use g_i instead of C_i to differentiate between the hadron and lepton currents, but we take $C_i = g_i$ throughout.

The axial vector current *is* renormalized by the strong interaction, at least somewhat. The partially conserved axial current (PCAC) hypothesis [16, 17] predicts $g_A \approx -1.31$ in agreement with the value deduced from free neutron decay ($g_A^{\text{neutron}} \approx -1.27$); however this coupling gets quenched in the nuclear medium of complex nuclei such that $g_A \approx -1$. Another complication of Gamow-Teller decays is that their matrix element can only be reliably calculated in neutron decay, where its value is $M_{GT} = \sqrt{3}$; in other cases, it must be experimentally measured. The axial current transfers angular momentum to the spin of the leptons and furthermore the T_3 component of the isospin in the parent and daughter nuclei can change; so the selection rules* for GT decays are $\Delta I = 0, \pm 1$ and $\Delta T = 0, \pm 1$.

In addition to the vector and axial-vector form factors above, there will generally be induced scalar, tensor and pseudo-scalar terms as well, which one characterizes in a similar fashion by defining additional form factors: g_S, g_T and g_P. These induced terms will be addressed shortly when we discuss recoil-order effects in the β decay rate.

The nuclear β decay rate

Evaluation of Eq. (2.1) in terms of all possible observables is presented in [14]. The decay rate for an atom with an initial nuclear polarization, $\boldsymbol{I}$, in terms of the β and ν momenta is given by:

$$\frac{d^5W}{dE_e d\Omega_e d\Omega_{\nu_e}} = \frac{G_F^2}{(2\pi)^5}|V_{ud}|^2 p_e E_e (E_\circ - E_e)^2 \; F(E_e, Z', R) \, \frac{d^4W(\boldsymbol{p}_e, \boldsymbol{p}_\nu, \boldsymbol{I})}{d\Omega_e d\Omega_{\nu_e}} \tag{2.5}$$

*However for the particular case of $0^+ \rightarrow 0^+$ decays, the transition must be pure Fermi since no angular momentum is transferred and thus cannot have a Gamow-Teller component.

where the angular distribution is given by:

$$\frac{d^4W(\boldsymbol{p}_e,\boldsymbol{p}_\nu,\boldsymbol{I})}{d\Omega_e d\Omega_{\nu_e}} = \xi\left\{1 + a_{\beta\nu}\frac{\boldsymbol{p_e}\cdot\boldsymbol{p}_{\nu_e}}{E_e E_{\nu_e}} + b_{\text{Fierz}}\frac{m_e}{E_e} + \frac{\langle \boldsymbol{I}\rangle}{I}\cdot\left[A_\beta\frac{\boldsymbol{p}_e}{E_e} + B_\nu\frac{\boldsymbol{p}_\nu}{E_\nu} + D\frac{\boldsymbol{p}_e\times\boldsymbol{p}_\nu}{E_e E_\nu}\right] + c_{\text{align}}\left[\frac{\boldsymbol{p}_e\cdot\boldsymbol{p}_\nu}{3E_eE_\nu} - \frac{(\boldsymbol{p}_e\cdot\hat{i})(\boldsymbol{p}_\nu\cdot\hat{i})}{E_eE_\nu}\right]\left[\frac{I(I+1)-3\langle(\boldsymbol{I}\cdot\hat{i})^2\rangle}{I(2I-1)}\right]\right\}. \quad (2.6)$$

The terms in front of the angular distribution in Eq. (2.5) are seen to be identical to the Fermi model, aside from the inclusion of another constant: $|V_{ud}|^2$, the up-down element of the Cabibbo-Kobayashi-Maskawa quark mixing matrix. The angular distribution of the decay, Eq. (2.6), accounts for: spin-independent correlations (1st line); lepton correlations with the initial nuclear polarization (2nd line); and correlations with the alignment of the nucleus (3rd line). Expressions for the angular correlation parameters, ξ, $a_{\beta\nu}$, b_{Fierz}, A_β, B_ν,, D and c_{align} are presented in [18], and include corrections for the Coulomb final state interaction between the β and daughter nucleus. These expressions are also reproduced in Appendix D. Inner and outer radiative corrections are not included at this time because they are known generate small corrections (on the order of 0.2%, which is the effect when including radiative corrections the the $0^+ \rightarrow 0^+$ decay of ^{38m}K), however once our experiment reaches this level of precision, we will include their effects [19].

The correlation parameters depend not only on the type of transition (Fermi, Gamow-Teller or mixed F/GT) and energy of the leptons, but also on the nature of the weak interaction. For example, according to Eq. (D.5), if the scalar and tensor couplings are actually identically zero (as assumed in the Standard Model), then the Fierz interference parameter, b_{Fierz}, must also be identically zero; if one were to one day observe, in contradiction to this prediction, a finite value for b_{Fierz} in say a pure Fermi decay, then it would prove that a small scalar current is present in addition to the predominantly $(V-A)$ structure of the weak interaction. In this way, precise measurements of the angular distribution parameters in nuclear β decay can be used to further our understanding of the fundamental symmetries of the weak interaction.

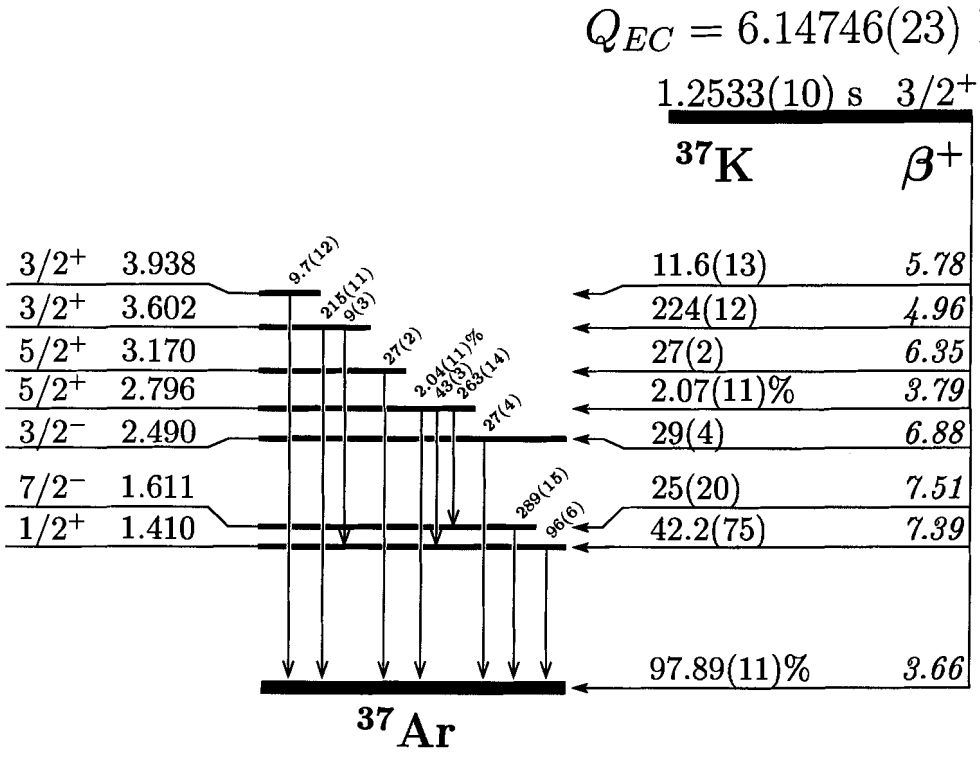

FIGURE 2.1: The β decay of ^{37}K. Values for the absolute β and γ intensities per ^{37}K decay are in ppm unless otherwise indicated.

2.1.2 β Decay of ^{37}K

The β^+ decay of ^{37}K [20] is depicted in Fig. 2.1. The decay is predominantly an $I^\pi = \frac{3}{2}^+ \rightarrow \frac{3}{2}^+$ transition to the ground state of ^{37}Ar and as such is a mixed Fermi/Gamow-Teller decay. The magnitude of the Fermi component is $|M_F|^2 = 1$ since the ground state transition is between isobaric analog states. The Gamow-Teller component was inferred from the ft value to be $|g_A M_{GT}|^2 = 0.338(8)$ in [20]; however, a more precise measurement of the half-life [21] gave $t_{1/2} = 1.2533(10)$ s and improved the ft measurement leading to a Gamow-Teller matrix element $|g_A M_{GT}|^2 = 0.3311(18)$. The magnitude of the ratio of Gamow-Teller to Fermi matrix elements is therefore found to be $|\lambda| \equiv |g_A M_{GT}/g_V M_F| = 0.5754(16)$.

With the magnitude of λ measured, we now only need its sign to be able to calculate values of A_β, B_ν and D within the Standard Model framework (other correlations

TABLE 2.1: Standard Model predictions for the correlation parameters for the decay of polarized ^{37}K. The Standard Model is based on a $(V-A)$ structure (only) and respects the symmetries of CP and time-reversal invariance (so that $C_i = C_i' \in \Re e$, $i = V, A$). With these assumptions, the predictions are based solely on the measured value of $\lambda = +0.5754(16)$ [21].

Correlation	SM prediction
$\beta - \nu$ correlation:	$a_{\beta\nu} = 0.6683(14)$
Fierz interference parameter:	$b_{\rm Fierz} \equiv 0$
β asymmetry:	$A_\beta = -0.5702(6)$
ν asymmetry:	$B_\nu = -0.7692(15)$
Alignment parameter:	$c_{\rm align} \equiv A_\beta - B_\nu = 0.1990(8)$
Time-violating D coefficient:	$D \equiv 0$

are independent of the relative sign). We expect that a shell model calculation will unambiguously provide the sign of λ [22] since the magnitude of the Gamow-Teller strength is not small; from a calculation presented in 1978, such a calculation predicted [23] $M_{GT} = -0.523$. Note that Ref. [21] also quotes a negative sign for the combination $g_A M_{GT}/g_V M_F$. However, in neither case do they explicitly state the sign convention of g_A for β^+ versus β^- decays; the overall phase is arbitrary, but the axial current is defined differently for the two cases. In going from $\beta^\pm$ to $\beta^\mp$, one takes the Hermitian conjugate of Eq. (2.1) which does not modify the vector current, but does introduce a sign change in the axial current. Some people favour putting this sign change in the coupling constant directly (so $g_A = \pm 1$ for $\beta^\pm$ decay), while others (like Jackson, Treiman and Wyld) have chosen to reflect the sign change in their expressions for observables, and keep g_A *constant*. In order to obtain the same Standard Model predictions for the correlation parameters as Ref. [21] (see Table 2.1) using the expressions in Appendix D, we must chose $\lambda = +0.5754(16)$ indicating that Refs. [21] and [23] have opted to place the sign change in the coupling constant g_A.

The only other branch appreciably populated in the β decay of ^{37}K is the 2.8 MeV level with a 2% branching ratio. As a $\frac{3}{2}^+ \rightarrow \frac{5}{2}^+$ transition, it must be purely Gamow-Teller. De-excitation from this level proceeds directly to the ground state 98.5% of

the time, producing a γ with $E_\gamma = 2.967$ MeV. The next strongest β branch is to the 3.6 MeV level, however its branching ratio is comparatively negligible at less than a part per thousand. This (and all other allowed) transitions must also be purely Gamow-Teller because the ground state is the isobaric analogue state and takes all of the Fermi strength. A Fermi component could arise from isospin mixing, but this is ignored in light of the very weak branching ratio. All other branches are below 50 ppm and so are completely negligible.

Recoil Order Effects

An assumption that is frequently made when deriving the decay rate for β decay is that of an infinitely heavy nucleus; the expressions simplify greatly if one ignores the recoil of the daughter nucleus. Very precise β decay experiments should include these calculable recoil order corrections when analyzing their observables. For the pure Fermi decays, calculation of the decay rate to recoil order is relatively simple, with the result simply renormalizing the total decay rate by $1+(3E_e - A_\circ - 3p_e \cos\theta_{e\nu})/M$, which is at most a 0.1% correction in ^{38m}K. For Gamow-Teller and mixed decays when the nuclei have $I > 0$, the situation quickly becomes more complicated. Much of what follows is based on the thorough review of this subject given by B. R. Holstein in [24].

To first order in q/M and q^2R^2 where q is the momentum transfer and R is the nuclear radius, there are in general 10 structure functions which account for nuclear-dependent corrections arising from the strong force. For isobaric analog decays, CVC allows one to relate electromagnetic and weak form factors. Weak magnetism, which is b in Holstein's notation [24], can be related to the nuclear magnetic moments via:

$$b = AM_F\sqrt{\frac{I+1}{I}}\left(\frac{\mu-\mu'}{T_3-T_3'}\right), \tag{2.7}$$

where A is the mass number, μ is the nuclear magnetic moment in units of the nuclear magneton, μ_N, and T_3 is the isospin (primes denote the daughter state). Similarly,

TABLE 2.2: Magnetic dipole and electric quadrupole moments of ^{37}Ar and ^{37}K used to calculate recoil-order corrections.

Isotope	μ	reference	Q	reference
^{37}Ar	$+1.146(1)\ \mu_N$	[29]	$+7.6(9)$ fm^2	[33]
^{37}K	$+0.20321(6)\ \mu_N$	[25]	$+10(4)$ fm^2	[26]

the induced electric quadrupole, g, can be related to the nuclear quadrupole moment:

$$g = -M_F \sqrt{\frac{(I+1)(2I+3)}{I(2I-1)}} \frac{2M^2}{3\hbar^2 c^2}(Q - Q'), \tag{2.8}$$

where $M = \frac{1}{2}(M_i + M_f)$ is the average mass of the daughter and parent nucleus, and Q is the quadrupole moment in units of fm^2. For ^{37}K, these moments have been measured to be $\mu_{\rm K} = +0.20321(6)\ \mu_N$ [25] and $Q_{\rm K} = 10(4)$ fm^2 [26]. In ^{37}Ar, an older measurement found $\mu_{\rm Ar} = +0.95(20)\ \mu_N$ [27] which is consistent with a more recent and much more precise value quoted originally in the Bulletin of the American Physical Society [28]: $\mu_{\rm Ar} = +1.145(5)\ \mu_N$; a final analysis brought this preliminary result to $\mu_{\rm Ar} = +1.146(1)\ \mu_N$ [29]. Though never published in a refereed journal, the measurement is accepted by the community as it has been adopted by a number of reviewers [30, 31, 32], and so we will also use this value in what follows. The quadrupole moment of ^{37}Ar is $Q_{\rm Ar} = +7.6(9)$ fm^2 [33].

Using these values for the magnetic and quadrupole moments (see Table 2.2), we find $b = -45.03(4)$ and $g = (-1.1 \pm 0.5) \times 10^5$ for weak magnetism and the induced electric quadrupole moment in ^{37}K. As we will see, the uncertainty in g (dominated by the quadrupole measurement in ^{37}K) does not have a large effect on the β asymmetry, however TRINAT would be able to improve this measurement if it were to become important.

To estimate the effect of recoil-order corrections, we evaluate $F_1(E)/F_0(E)$ from Eq. (52) of Ref. [24]*, which corresponds to the β asymmetry parameter. This calcu-

*Note that we discovered errors in Holstein's simplified expressions for some of the spin-dependent functions given in Eq. (B8) of [24]; for $I + I' \geq 2$, one should evaluate the Racah coefficients directly when using $\lambda_{u,v}$, $\epsilon_{u,v}$, $\sigma_{u,v}$ and $\phi_{u,v}$ (though this last one is never actually used ...).

lation does not include the alignment terms which will effect the normalization of the asymmetry (i.e. we don't include the F_2 or F_3 terms which will sum in the denominator of a β asymmetry measurement). In the absence of second-class currents, which violate G parity*, all other form factors are either zero for isobaric analog transitions or do not contribute to F_0 or F_1. The one exception is the induced pseudoscalar, h, which has a negligible contribution to the β asymmetry parameter. The results are plotted as a function of β energy in Fig. 2.2, where we also show the effect of uncertainties in the predicted value of A_β as well as the evaluations of weak magnetism and the induced electric quadrupole moment. One can see that including recoil-order effects enhances the asymmetry slightly, especially at higher β energy. As expected, the overall effect is small at $\lesssim 0.0015$, even when including current uncertainties in the form factors. This can be compared to the ± 0.0006 uncertainty in the SM prediction of A_β due to the present uncertainty in λ; recoil-order effects will only become important once our experiment reaches this level of sensitivity and an improved ft measurement better constrains the value of λ. Note that based on this calculation, we can expect the neutrino asymmetry and other correlations to have contributions of similar magnitude.

The effect of an induced tensor (denoted by d in Holstein's notation) is also shown where we have assumed its value is equal to the weak magnetism. There is no electromagnetic relationship to deduce the magnitude of the induced tensor, however Holstein points out in Ref. [34] that if the first- and second-class axial currents had comparable strengths, then d would be comparable to b. It is interesting to note that the effect of the induced tensor is considerably larger than weak magnetism and the induced electric quadrupole moment. If a precision measurement of the correlation parameters could be made as a function of β energy (and special care would need to be taken to understand the β detector's response function and energy calibration), the induced tensor — if it exists and is large — would have a clear signature which would point to the existence of second-class currents not in the Standard Model.

*A G parity transformation interchanges particles with their anti-particles and rotates the system in isospin space about the T_2 axis.

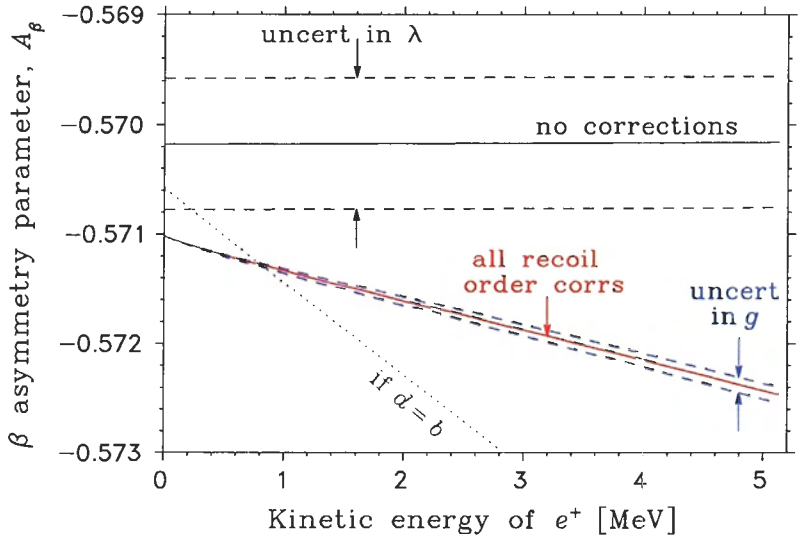

FIGURE 2.2: Recoil-order effects on the β asymmetry parameter in the decay of ^{37}K. As labeled on the plot, we compare the calculated value without recoil-order corrections to the calculation which includes weak magnetism and the induced electric quadrupole moment. The dashed lines show the effect of the uncertainty in λ and g (the uncertainty in b is negligible); the dotted line shows the effect of an induced tensor (a second-class current) with the same magnitude as weak magnetism.

2.2 Physics Beyond the Standard Model

Many extensions to the Standard Model [35, 36, 37, 38] restore parity at higher energy scales, and explain the observed left-handedness of Nature as a symmetry breaking apparent at low energies. Much like with electroweak unification, at some higher energy scale where the weak and fine structure constants are equal, parity becomes a good symmetry again. A right-handed boson may simply be very massive and so its influence, at β decay energies of typically tens of MeV, is suppressed by the $1/M^2$ propagator term of the decay rate. Depending on the mass, and what its coupling is, these massive bosons may have small but finite observable effects on the decay.

2.2.1 Right-Handed Currents

In the Standard Model, maximal parity violation in the weak sector is incorporated by the fact that the weak interaction only acts on left-handed fermions. In most grand

unified theories, however, Nature is taken to be left-right symmetric, with parity violation only manifest at low energies due to a spontaneous symmetry breaking at some higher energy scale. Unlike the Standard Model in which parity is maximally violated, the weak interaction may have small components of right-handed currents arising as a suppressed or relic component of the initial symmetry. Models incorporating left-right symmetry [35] necessarily extend the $SU(2)_L \otimes U(1)$ Standard Model electroweak gauge group to include a right-handed component. The simplest extensions do nothing more than add a right sector akin to the $SU(2)_L$ sector, *i.e.* $SU(2)_R \otimes SU(2)_L \otimes U(1)$. Such a gauge group necessitates the addition of (at least) three new gauge bosons, the $W_R^{\pm}$ and Z'. The Z', along with the Standard Model Z° boson, mediates weak neutral currents. The $W_R^{\pm}$, associated with the $SU(2)_R$ group, is the right-handed counterpart of the Standard Model $W_L^{\pm}$ boson arising from the $SU(2)_L$ group. The two gauge group eigenstates mix so that the observed bosons are the mass eigenstates $W_{1,2}$ of mass $M_{1,2}$:

$$\begin{aligned} W_L &= W_1 \cos\zeta - W_2 \sin\zeta \\ W_R &= \left(W_1 \sin\zeta + W_2 \cos\zeta\right) e^{-i\omega} \end{aligned} \tag{2.9}$$

Here ζ is a mixing angle and ω is a phase which is only non-zero if the combined symmetry CP is violated. The mixing of these states is necessarily small since no evidence of a right-handed current has been observed, so that $W_L \approx W_1$, $M_L \approx M_1$, $W_R \approx W_2$ and $M_R \approx M_2$.

In general extensions to the Standard Model that restore parity at high energies, the left and right sectors are completely independent. The parameters of the right sector in these models are free to take on arbitrary values, not necessarily the same as those in the left sector. This means that the parameter space allows: the bosons to have different masses, $M_1 \neq M_2$; for the coupling constants have different values, $g_L \neq g_R$; for the left and right sector's Cabibbo-Kobayashi-Maskawa matrices to have different elements, $V_{ij}^L \neq V_{ij}^R$; and for a new family of neutrinos, $\nu^{(L)} \neq \nu^{(R)}$. The *simplest* extensions to the Standard Model which restore parity are known as *manifest left-right symmetric* models [39]; these models assume that the Lagrangian is explicitly

parity conserving (so $g_L = g_R$ and $V_{ij}^L = V_{ij}^R \, \epsilon \, \Re e$) and neutrinos are Dirac neutrinos*. In the manifest L-R symmetric model, then, the couplings and transformations of the two currents are identical, and parity violation occurs only from the mass difference of the bosons. Since the weak interaction is predominantly left-handed (at least), this implies that $M_2 \gg M_1 \approx 80$ GeV.

Effect on β Decay Observables

In the manifest left-right symmetric model, as mentioned above, there are only two new parameters added to the model: the mass of the W_2 and the mixing angle ζ. Holstein and Treiman [40] defined an effective Lagrangian in terms of two parameters that depend on these right-handed current parameters according to:

$$x = \frac{\delta(1+\tan\zeta) - \tan\zeta(1-\tan\zeta)}{\delta\,\tan\zeta(1+\tan\zeta) + \tan\zeta(1-\tan\zeta)} \xrightarrow[\zeta\ll 1]{\delta\ll 1} \delta - \zeta \tag{2.10}$$

$$\text{and} \qquad y = \frac{\tan\zeta(1+\tan\zeta) + \delta(1-\tan\zeta)}{\delta\,\tan\zeta(1-\tan\zeta) + \ (1+\tan\zeta)} \xrightarrow[\zeta\ll 1]{\delta\ll 1} \delta + \zeta \tag{2.11}$$

where $\delta \equiv M_1^2/M_2^2$ goes to zero as $M_2 \to \infty$. In the limit that the weak interaction is purely $(V-A)$, x and y go linearly to zero.

This parameterization is fine for the manifest left-right symmetric models, but does not tell us how to allow for different couplings, CKM matrices, etc. We therefore turn to a paper by Herczeg [41] where he defines a completely general Lagrangian for semileptonic processes, and which emphasizes the chiral nature of the weak interaction:

$$\begin{aligned} H = {} & a_{LL}\bar{l}\gamma_\mu(1-\gamma_5)\nu_l^{(L)}\,\overline{u}\gamma^\mu(1-\gamma_5)d \\ & + a_{LR}\bar{l}\gamma_\mu(1-\gamma_5)\nu_l^{(L)}\overline{u}\gamma^\mu(1+\gamma_5)d \\ & + a_{RL}\bar{l}\gamma_\mu(1+\gamma_5)\nu_l^{(R)}\overline{u}\gamma^\mu(1-\gamma_5)d \\ & + a_{RR}\bar{l}\gamma_\mu(1+\gamma_5)\nu_l^{(R)}\overline{u}\gamma^\mu(1+\gamma_5)d + \text{h.c.}. \end{aligned} \tag{2.12}$$

Here $l = e, \mu$ and the left- and right-handed neutrinos have separate mixing matrices, U and V, so that $\nu_l^{(L)} = \sum_j U_{lj}\nu_j$ and $\nu_l^{(R)} = \sum_j V_{l,j}\nu_j$. The coefficients in Eq. (2.12)

*Meaning $\bar{\nu}^{(L,R)} \neq \nu^{(L,R)}$ as compared to Majorana neutrinos where $\bar{\nu}^{(L,R)} = \nu^{(L,R)}$

are given by:

$$a_{LL} = V_{ud}^{L}\left(\frac{g_L^2}{8M_1^2}\cos^2\zeta + \frac{g_L^2}{8M_2^2}\sin^2\zeta\right) \tag{2.13a}$$

$$a_{LR} = V_{ud}^{R}\left(-\frac{g_L g_R}{8M_1^2} + \frac{g_L g_R}{8M_2^2}\right)\cos\zeta\sin\zeta\, e^{i(\alpha+\omega)} \tag{2.13b}$$

$$a_{RL} = V_{ud}^{L}\left(-\frac{g_L g_R}{8M_1^2} + \frac{g_L g_R}{8M_2^2}\right)\cos\zeta\sin\zeta\, e^{i(\alpha-\omega)} \tag{2.13c}$$

$$a_{RR} = V_{ud}^{R}\left(\frac{g_R^2}{8M_1^2}\sin^2\zeta + \frac{g_R^2}{8M_2^2}\cos^2\zeta\right). \tag{2.13d}$$

The new CP violating phase, α, comes from mixing in the right-handed neutrino sector. For simplicity, we neglect CP violation and take $a_{LR} = a_{RL}\ \epsilon\ \Re e$. In terms of the x and y variables defined above:

$$x = \frac{a_{RR} + a_{RL}}{a_{LL} + a_{LR}} \tag{2.14}$$

$$\text{and} \quad y = \frac{a_{RR} - a_{RL}}{a_{LL} - a_{LR}}. \tag{2.15}$$

With this parameterization, we can now easily incorporate dependences in generalized models where $g_R \neq g_L$, $V_{ud}^{R} \neq V_{ud}^{L}$, etc., with Herczeg's expressions for the a_{ij}.

There are many β decay observables that are sensitive to right-handed currents, but the ones relevant to this thesis are the β and neutrino asymmetries, A_β and B_ν. We are therefore interested in deducing the effects of right-handed currents on these parameters in order to estimate our sensitivity to the model parameters. The Lagrangian and parameterization of Holstein and Treiman was adopted by Naviliat-Cuncic et al* which we turn to because they derived a general expression for the β asymmetry parameter in the left-right symmetric model. Neglecting recoil order corrections, assuming CVC, and a $(V \pm A)$ interaction that respects T invariance, they found that for any allowed transition [42]:

$$A_\beta = \frac{\mp\lambda_{I'I}(1-y^2)\lambda^2 \ - \ 2\,\delta_{I'I}\lambda\sqrt{\frac{I}{I+1}}(1-xy)}{(1+x^2) \ + \ \lambda^2(1+y^2)}, \tag{2.16}$$

*Note that there is a typo in Eq.(3a) of [42]; both x and y are missing a δ in the denominator. The expressions above, Eq. (2.11), are correct.

where $\lambda_{I'I}$ is given in Appendix D, $\delta_{I'I}$ is the Kronecker delta-function and the lower sign corresponds to β^+ decay. Note that if there are no right-handed currents, the above reduces to Eq. (D.7) given the quoted assumptions. As Holstein and Treiman explicitly state in [40], one does not know the value of $g_A M_{GT}$ (except in the case of the neutron) and so one must compare the observed ft value to that of the $0^+ \rightarrow 0^+$ decays. This is because the value of λ deduced from the observed ft value will itself be affected by right-handed currents if they exist; hence one would not measure the "bare" value of λ. Instead, one would observe λ' which is related to the quantity of interest by:

$$\lambda' = \lambda \frac{1+y^2}{1+x^2}. \tag{2.17}$$

This can be seen to be the correct renormalization by inspecting a re-arrangement of the expression for the ratio of ft values given in [42]:

$$\frac{ft^{0^+\rightarrow 0^+}}{ft} = \frac{1}{2}\left[1 + \lambda^2 \frac{(1+y^2)}{(1+x^2)}\right]. \tag{2.18}$$

In the absence of right-handed currents, this ratio goes to $(1+\lambda^2)/2$; similarly, if we replace λ by λ' in the presence of right-handed currents, the expression reduces to $(1+\lambda')/2$. Hence the λs in Eq. (2.16) above should be replaced by λ'. Doing so and simplifying, we find:

$$A_\beta = \lambda_{I'I} \frac{\mp(1-y^2)\lambda^2}{(1+y^2)(1+\lambda^2)} - 2\,\delta_{I'I} \frac{\lambda\sqrt{\frac{I}{I+1}\frac{1+x^2}{1+y^2}}(1-xy)}{(1+\lambda^2)}. \tag{2.19}$$

Inspection of Eq. (D.8) and comparison to Eq. (D.7) allows us to write a similar term for B_ν since the two differ only in a sign for purely vector/axial-vector interactions:

$$B_\nu = \lambda_{I'I} \frac{\pm(1-y^2)\lambda^2}{(1+y^2)(1+\lambda^2)} - 2\,\delta_{I'I} \frac{\lambda\sqrt{\frac{I}{I+1}\frac{1+x^2}{1+y^2}}(1-xy)}{(1+\lambda^2)}. \tag{2.20}$$

Note that with the above renormalization of λ, the expressions for $a_{\beta\nu}$ and c_{align} (see Eqs. (D.4) and (D.6)) are not modified; this is what we expect because, with these

parameters quadratic in C_V, C_A, it is difficult to see why they would be sensitive to right-handed currents.

The above expressions for the β and ν asymmetries tell us how sensitive we are to right-handed currents. If our measurements differ from the Standard Model predictions, we can use these expressions to extract values of the model parameters; in the absence of a signal, they tell us how sensitive we are and what limits we can place on the possible existence of a $(V + A)$ interaction.

2.2.2 Other precision experiments using traps

Other groups are interested in harnessing the favourable conditions provided by modern trapping techniques (cold, compact, backing-free source of radioactive atoms). In addition to the two described below, there are programs at: Argonne National Lab (^{6}He); Francium studies at JILA (Colorado), INFN Legnaro (Italy) and Stony Brook/TRIUMF; and a program to search for time-violation and EDMs at KVI in Groningen. A number of programs using ion traps are also planning precision β decay experiments to test fundamental symmetries, including the TITAN collaboration at TRIUMF, the WITCH group at Leuven/ISOLDE, the CPT at Argonne National Lab, and the LPC trap in Caen (among others).

^{21}Na decay

At Lawrence Berkeley National Lab, a group is trapping ^{21}Na and have possible evidence of scalar currents with the atoms unpolarized [43]. If they were to pursue a polarized program, this mirror decay would make them sensitive to right-handed currents.

^{82}Rb polarized decay

A collaboration working out of Los Alamos National Lab is pursuing a time-orbiting potential (TOP) magnetic trap for ^{82}Rb [44]. A magneto-optical trap loads the TOP trap and, using optical pumping techniques, efficiently prepares atoms in the stretched $5S_{1/2}|F = 3/2\ m_F = 3/2\rangle$ ground state. The TOP trap provides a rotating, highly

polarized 'beacon' of radioactive atoms confined in a trap. A β detector views this trap and counts the positrons emitted as the polarization of the cloud rotates. In their first proof-of-principle experiment [45], they describe their technique and show a large asymmetry; however large uncorrelated backgrounds made a precision experiment impossible. The group is working to reduce systematics and we await the results using the TOP trap.

2.2.3 Present Limits on Right-Handed Currents

Here we present existing constraints on right-handed current parameters within the context of the manifest left-right symmetric model, *i.e.* M_2 and ζ. Summaries of the different model-independent limits are shown throughout the rest of this section in Figs. 2.3– 2.5. These are 90% C.L. exclusion plots of the two right-handed current parameters. The Standard Model has the $M_2 \rightarrow \infty$ and $\zeta = 0$; the different contours indicate the parameter space experiments have excluded to date.

High-energy searches

The CDF [46] and D0 [47] collaborations have searched for a W_R boson by colliding p with $\bar{p}$ at high (1.8 TeV) centre-of-mass energies. They are not sensitive to the mixing angle, ζ, but if the mass of the W_R is within their thresholds, they can produce it directly and look for its subsequent decay to lighter particles. Their analysis scheme is generally to generate a number of missing mass spectra for candidate events and for each mass bin, look for an excess of events above background that would indicate a W_R had been produced. Although no positive signal has ever been observed, they have been able to use their results to place relatively high limits on the mass, M_2. The D0 collaboration, using the $e\nu_R$ decay channel, limits boson masses above 200 and below 650 (720) GeV at the 95% CL for $M_\nu < M_2/2$ ($M_\nu \ll M_2$). The CDF collaboration excludes a W_R boson at the 95% CL limit between masses of 225 and 566 (536) GeV assuming the right-handed neutrino mass that is heavier (or much lighter) than M_2 using the $t\bar{b}$ decay channel. This channel has the advantage that the decay mode can still occur regardless of the mass of the ν_R; however it is a difficult

measurement and so has lower limits.

The limits from the D0 ($W \rightarrow e\,\nu_R$) and CDF ($W \rightarrow q\bar{q}$) experiments are horizontal lines in the 2D exclusion plot; this is because they are doing a mass search and are not sensitive to the mixing angle.

These limits require that the decay products used to search for the W_R are able to be produced kinematically, and so if, for example, the mass of the ν_R were larger than the W_R, the D0 experiment would not be able to observe it. Additional caveats include the model-dependence needed to extract the expected signals if the boson was produced (more so for the $e\nu_R$). However, the limits imposed by high-energy searches is formidable and represent a stringent limit on the W_R mass.

$\nu - N$ scattering

The differential cross section of ν_μ- and $\overline{\nu}_\mu$-induced reactions are sensitive to right-handed quark currents which couple to the usual left-handed lepton current. As originally pointed out by Bég [39], left-right symmetric models can be probed by comparing the ratio of $\overline{\nu}$ to ν deep inelastic scattering on nucleons at large $y = E_{\text{had}}/E_\nu$. This ratio for high and low Bjorken-x thresholds is sensitive to [48]:

$$\eta^2 = \tan^2\zeta(1-\delta)^2 \tag{2.21}$$

Using the neutrino beam at Fermilab's Tevatron, the CCFR collaboration was able to place a limit of $\eta^2 < 0.0015$ at the 90% C.L. [49]. This corresponds to limits on the mixing angle of $|\zeta| \leq 0.04$. This limit is shown in Fig. 2.3. As we will soon see, these limits on ζ are not as stringent as limits from the $0^+ \rightarrow 0^+$ decays, however the $\nu - N$ scattering limits do not assume the right-handed neutrino is relatively light as in β decay and muon experiments, and so provides a very useful bound for models where $\nu^{(R)}$ have masses $m_{\nu^{(R)}} \gtrsim 10$ MeV.

Muon decay

The Michel parameters [50], ρ, δ, η and ξ completely describe the differential decay spectrum of a muon decaying with an initial polarization P_μ. These parameters are

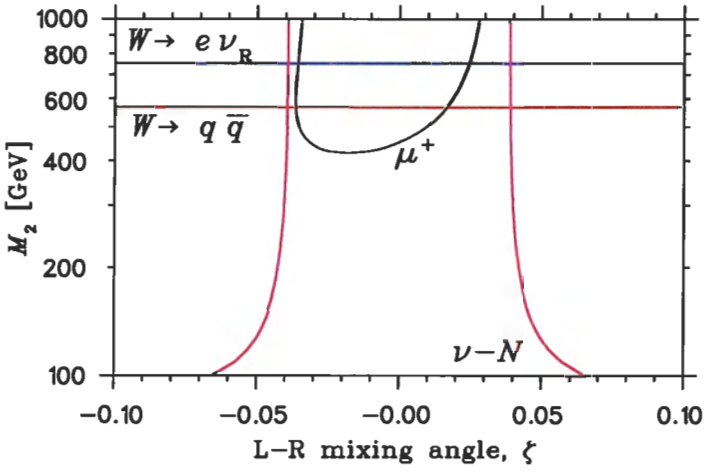

FIGURE 2.3: 90% C.L. limits in the manifest L-R symmetric model from particle physics experiments. In the Standard Model, the mixing angle is $\zeta = 0$ and the mass $M_2 \to \infty$. The $p\bar{p}$ collider experiments limit the mass to $\gtrsim 600$ GeV while the $\nu - N$ scattering constrains $|\zeta| \leq 0.04$. The muon decay limits are sensitive to both parameters.

bilinear combinations of the coupling constants in Eq. (2.1) so are sensitive to right-handed currents. A recent measurement of ρ and δ by the $\mathcal{TWIST}$ collaboration at TRIUMF have improved the limits on a possible $(V + A)$ interaction [51, 52]. In this experiment, highly polarized muons are implanted in the centre of a large spectrometer made up of 44 drift and 12 multiwire proportional chamber planes. The detector is mounted within a 2 T magnetic field so that the positrons emitted in the decay spiral through many of these chambers and their helical tracks can be used to deduce the e^+ energy and direction with high precision.

The limits obtained [53] from the recent $\mathcal{TWIST}$ result are shown in Fig. 2.3. In the analysis of both ρ and δ, the three dominant systematics were the spectrometer alignment, the chamber response and the ability to model positron interactions using GEANT. The next phase of the experiment involves measuring ξP_μ which is expected to increase their sensitivity to ρ and δ by a factor of five.

$0^+ \longrightarrow 0^+$ decays

The superallowed Fermi decays have been the source of an intense research program for many years owing to the simple theoretical interpretation of results coming from

precision studies of their β decay. A recent survey by Hardy and Towner [54] summarizes the results to date. In addition to being the best way to determine V_{ud}, to testing CVC, and to being sensitive to scalar currents, the $0^+ \rightarrow 0^+$ decays are also sensitive to the right-handed current mixing angle, ζ. Much like the high-energy searches are insensitive to the mixing angle, superallowed β decays are essentially independent of the mass of the W_R; also like the collider experiments, the limits that the pure Fermi decays can place on ζ are very stringent.

According to CVC, the ft value of the pure Fermi decays are predicted to be a constant once small nuclear (δ_C) and radiative (δ_R, Δ_R^V) corrections are applied:

$$\mathcal{F}t \equiv ft(1+\delta_R)(1-\delta_C) = \frac{K}{2G_V^2(1+\Delta_R^V)}, \tag{2.22}$$

There is remarkable consistency with the CVC prediction, with $\mathcal{F}t$ being found to be constant at the 0.05% level.

The measurement $|V_{ud}| = 0.9738(4)$ [54] combined with the Particle Data Group's recommended values [3] of $|V_{us}| = 0.2200(26)$ and* $|V_{ub}| = 0.00367(47)$ provides a unitarity test of the CKM matrix which disagrees with the Standard Model by 2.4σ:

$$|V_{ud}|^2 + |V_{us}|^2 + |V_{ub}|^2 = 0.9966(14). \tag{2.23}$$

Two recent measurements [55, 56] of $|V_{us}|$ are inconsistent with earlier ones; if one takes the average of just these two, $|V_{us}| = 0.2259(18)$ and unitarity is restored.

In terms of right-handed currents, an unseen propagator that mixes with the normal W_L will steal strength away from the measured $\mathcal{F}t$ values and would therefore violate the unitarity condition described above. By *assuming* unitarity and using the uncertainty to constrain right-handed currents, the $0^+ \rightarrow 0^+$ decays are able to place very stringent limits on the mixing angle. Specifically, with a CKM matrix that is presumed to be unitary, the test for right-handed currents becomes:

$$|V_{ud}|^2(1-2\zeta) + |V_{us}|^2 + |V_{ub}|^2 = 1 \tag{2.24}$$

*Note that V_{ub} has a negligible contribution to the unitarity test; its value is well below the uncertainties from V_{ud} and V_{us}.

These limits are shown as a tight band at $-0.0015 \leq \zeta \leq 0.0037$. For the plot, we were conservative and took the value of V_{us} to be half-way between the PDG recommended value and the average of the two latest measurements, and we increased the uncertainties so both values were encompassed.

β polarization asymmetry measurements

The β and ν asymmetries are not the only ones sensitive to right-handed currents in nuclear β decay. Excellent limits have been realized by looking at the polarization of the emitted positron in the polarized decay of ^{107}In [57] and more recently using similar techniques in ^{12}N [58]. In the latter, the ^{12}N were produced by bombarding a carbon target with polarized protons. The recoiling 76% polarized ^{12}N were then stopped in nearby aluminum foils which held their polarization better than carbon in a 3.8 kG field. The energy of the emitted positrons was measured using a spectrometer and their polarization observed using time-resolved spectroscopy of positronium annihilation in a strong field (see, for example, references [59, 60]). The longitudinal polarization of the β are measured and compared when they are emitted parallel, P^+, and anti-parallel, P^-, to the initial nuclear polarization. The sensitivity to right-handed currents is given by [61]:

$$\frac{P^-}{P^+} = R_\circ \left[1 - \frac{8\beta^2 \mathcal{A}_{\rm obs}}{\beta^4 - \mathcal{A}_{\rm obs}^2} \Delta\right], \tag{2.25}$$

where

$$\Delta \equiv \frac{y^2}{(1-y^2)^2} \tag{2.26}$$

is a measure of the deviation from the Standard Model prediction and $R_\circ$ is the ratio expected in the absence of right-handed currents. Note that one can get a large enhancement factor if the positron's velocity is about equal in magnitude to the observed asymmetry, *i.e.* if $\beta \approx \mathcal{A}_{\rm obs}$. In the case of ^{37}K, the Standard Model prediction is $\mathcal{A} = -0.57$, which can lead to an $\approx 7\times$ enhancement factor.

The average of all ^{12}N and ^{107}In experiments finds Δ consistent with zero [58]:

$$\Delta = -0.0004 \pm 0.0026 \tag{2.27}$$

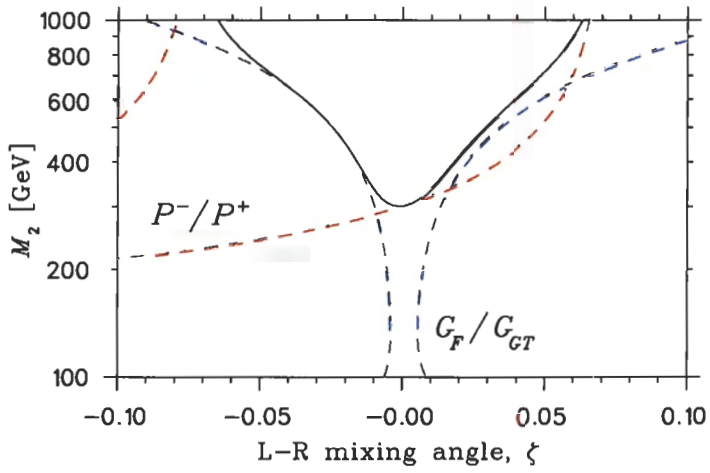

FIGURE 2.4: 90% C.L. limits in the manifest L-R symmetric model from experiments using β polarization techniques. The solid line represents the combined limit from both P^-/P^+ and G_F/G_{GT} techniques.

which results in the limits shown Fig. 2.4.

Another β polarization measurement looks at the ratio of two measurements, one a pure Fermi and one pure Gamow-Teller. The dependence on right-handed current parameters is [62]:

$$\frac{G_F}{G_{GT}} = \frac{1 - 2|a_{RL} + a_{RR}|^2}{1 - 2|a_{RL} - a_{RR}|^2} \tag{2.28}$$

where G_F and G_{GT} are given in [18]. Such an experiment is described in [63] where they compared the decays of ^{14}O (pure F) to ^{10}C (pure GT) and found $G_F/G_{GT} = 0.9996(37)$. Similar results were seen in an earlier experiment using ^{26m}Al and ^{30}P [64], which when combined yield a limit of [63] $G_F/G_{GT} = 1.0010(27)$. For modest masses M_2, this observable is particularly sensitive to the mixing angle as seen in Fig. 2.4.

Neutron decay

H. Abele has made a relatively recent survey of all neutron decay measurements [65] which can be used, among other things, to place limits on right-handed currents. A recent measure of the neutron lifetime [66] is in serious disagreement (6.5σ!) with the world average of previous measurements, and it is unclear where the discrepancy lies.

If the lifetime really were to be 7 s shorter than previously measured, the results given by Abele would need to be updated to reflect the change. However, until this issue is resolved, the average of all neutron decay experiments as summarized in [65] reflects the current status. To be conservative, we took the lifetime to be a weighted average of all measurements — including Serebrov's — and increased the uncertainty to 2.4 s so that it spans both the PDG and Serebrov's results.

To properly calculate the limits these (and the following) experiments place on right-handed currents, we must remember that g_A is essentially a free parameter; neutron decay determines it most precisely, but g_A itself is affected by right-handed currents. The method for generating the exclusion contours was to start by defining a grid in the ζ vs. M_2 plane. For each point on that grid, we varied λ over a wide range to find the minimum χ^2 value of the combination of all three observables: $t_{1/2} = 881.4 \pm 2.4$ s (through comparing the ft to the $0^+ \rightarrow 0^+$ value of $\mathcal{F}t$), $A_\beta = -0.1174 \pm 0.0011$ and $B_\nu = 0.9824 \pm 0.0040$. The resulting 90% C. L. limit is shown in Fig. 2.5. The limits are comparable to those obtained from the β polarization in Fig. 2.4. It should be noted that there are a number of experiments working to improve the measured values of $t_{1/2}$ and A_β, especially with the large fluxes available once the Spallation Neutron Source (SNS) at Oak Ridge National Laboratory becomes operational next year.

^{19}Ne decay

The β^+ decay of ^{19}Ne is in many ways similar to neutron decay because it is an $I = 1/2 \rightarrow 1/2$ transition of mirror nuclei. It too has $M_F = 1$ and M_{GT} will be close to $\sqrt{3}$, but since it is a decay in a complex nucleus, it gets quenched and the exact value is not as theoretically clean as for the simpler neutron case. We can therefore fix g_A to be the value derived from neutron decay, but we must again vary $\lambda \equiv g_A M_{GT}/g_V M_F$ like a free parameter and generate the contour limits from the simultaneous, combined observations of $ft = 1725.1 \pm 4.4$ s, $A_\beta = -0.0390 \pm 0.0020$ and $B_\nu = -0.90 \pm 0.13$ [67]. The authors admit that this B_ν measurement is very coarse and rather than a Standard Model test, it served as a good check that the

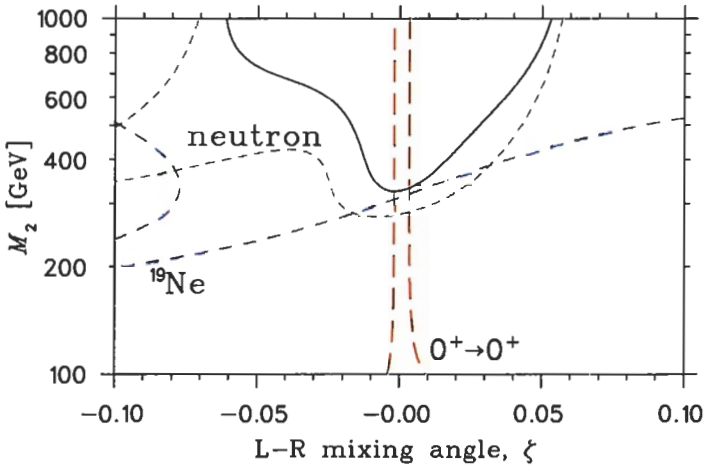

FIGURE 2.5: 90% C.L. limits in the manifest L-R symmetric model from all nuclear β decay experiments. The solid line represents the combined limits of the neutron, ^{19}Ne and $0^+ \rightarrow 0^+$ decays, combined with the G_F/G_{GT} and P^-/P^+ limits from Fig. 2.4.

system was working properly. The results, shown in Fig. 2.5, are dominated by the A_β measurement. One can see how particularly sensitive A_β is in ^{19}Ne: because the magnitude of A_β is small, a 5% relative (but 0.2% absolute) measurement of the β asymmetry already results in limits of $M_2 > 300$ GeV at the 90% C.L.

Other model-dependent limits

There are measurements from other experiments which can be used, with some model-dependent assumptions, to infer additional (generally very stringent) constraints on right-handed weak currents. We will not go into details here except to make the reader aware of them. A good summary, which does go into detail, can be found in Ref. [68].

The general properties of the Higg's structure of the weak interaction in left-right symmetric models requires that $|\zeta| \leq \delta$ [68].

The observation of supernova 1987A has many interesting consequences, one of which is to limit the existence of a right-handed current. If a $\nu^{(R)}$ were copiously produced, it would take energy away from the core and would change the observed time-structure and neutrino yield. The limits are dependent on (admittedly reasonable) assumptions which yield $M_2 \lesssim 540$ GeV or $M_2 > 22$ TeV [69]. This paper also

considers the effect of light ($\lesssim 1$ MeV) right-handed neutrinos on big-bang nucleosynthesis. If produced in the early universe, such neutrinos would change the rate of expansion of the universe, thereby affecting the ratio of primordial neutrons to protons. This then would have observable effects on the abundance of primordial ^{4}He. To agree with observations, one finds $M_2 \gtrsim 1$ TeV.

If the neutrino is a Majorana particle, neutrinoless double-β decay ($\beta\beta_{0\nu}$) can place severe limits: $M_2 \gtrsim 1.2$ TeV. Of course if the ν is a Dirac particle, however, these limits do not hold.

Finally we allude to the limits imposed by the $K_L \rightarrow K_S$ mass difference. Though M_2 limits are often quoted in the TeV-range, Langacker and Sankar [68] argue that in non-manifest models and with reasonable restrictions on fine-tuning of the parameters, these limits should be relaxed to $M_2 > 300$ GeV.

2.2.4 Beyond the manifest model

The limits from all modern experiments sensitive to right-handed currents has been presented and summarized within the framework of the manifest left-right symmetric model in Figs. 2.3 and 2.5. The different types of experiments all have vastly different systematics which is an enjoyable situation because it helps to ensure that if a signal is seen in one, the consistency of all the other experiments will help clarify if the new physics is real, or just an unknown systematic. In this way, the different experiments are complementary to each other and it is important that these varied techniques continue to strive to increase their sensitivity and continue to search for physics outside the Standard Model.

If one goes to more general models which are not manifestly symmetric, then one sees the added importance of the different classes of experiments. Table 2.3 lists the sensitivity of the high-energy, muon and nuclear β decay experiments to parameters in the non-manifest models: the right-handed coupling constant, g_R; the right-handed up-down CKM matrix element, V_{ud}^R; as well as the W_R boson mass. Here one can see that the μ and β decay experiments are able to constrain the parameter space where $g_R > g_L$ better than the high energy searches owing to the fourth-power dependence

TABLE 2.3: Dependence of various types of experiments on right-handed currents in non-manifest symmetric models. The different experiments discussed have different dependences when considering models more general than the manifest left-right symmetric. For the collider experiments, $F(M_L/M_R)$ represents a non-analytic function of the ratio of the masses.

Type of experiment	Non-manifest dependence
high-energy:	$(g_R/g_L)^2 \ (V_{ud}^R/V_{ud}^L) \ F(M_L/M_R)$
β decay:	$(g_R/g_L)^4 \ (V_{ud}^R/V_{ud}^L)^2 \ (M_L/M_R)^4$
μ decay:	$(g_R/g_L)^4 \left[1 + (V_{ud}^R/V_{ud}^L)^2\right] (M_L/M_R)^4$

on the couplings versus the quadratic in the collider experiments. Inspired by Fig. 11 (and 12) in Ref. [58], we generated an exclusion plot of the coupling strengths (V_{ud}^R element) versus the heavy boson mass in Figure 2.6. In these non-manifest exclusion plots, we assume that the mixing angle is zero, and that the right-handed neutrino is lighter than the W_R. In the top panel we show the current limits from the D0 collaboration (taken from Fig. 11 of [58]) and compare them to the limits we calculate from the world average of nuclear β decay. In this case, we have set $V_{ud}^R = V_{ud}^L$. In the manifest model, when $g_R = g_L$, the high-energy limits are stronger; however if $g_R \gtrsim 3g_L$, then the β decay limits better constrain the parameter space.

The sensitivity to M_2 for small V_{ud}^R is different for β decay and the collider searches. As seen in the bottom panel of Fig. 2.6 we once again find the two complementing each other by limiting different parts of the parameter space; for $M_2 < M_1$, the collider searches do not limit right-handed currents if V_{ud}^R is significantly smaller than V_{ud}^L.

If one day real right-handed currents are observed, the physics community would need to work hard to define characteristics of the right sector. It is clear that the different sensitivities of the varied types of experiments would all be needed to could help understand the source of right-handed currents, and may make it possible to deduce the values of the different parameters.

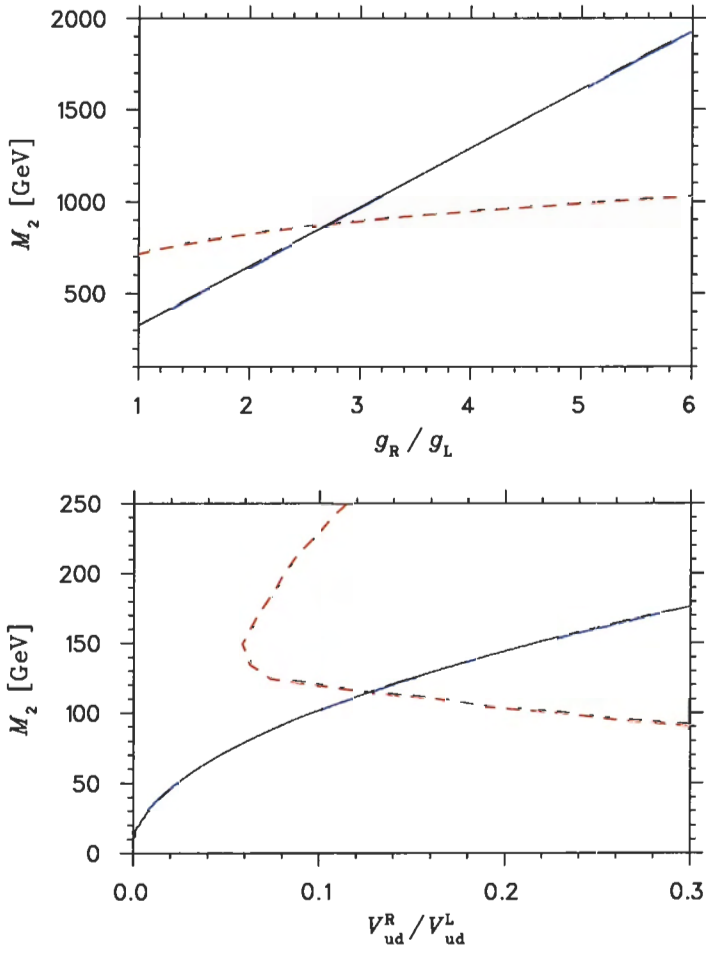

FIGURE 2.6: Comparison of β decay (solid contour) and $p\bar{p}$ limits (dashed contour, taken from Ref. [58]) in non-manifest left-right symmetric models. The exclusion plots show the limits one gets with $\zeta = 0$ but $g_R \neq g_L$ (top) or $V^R_{ud} \neq V^L_{ud}$ (bottom). Note that unlike the previous exclusion plots versus ζ, the scale of M_2 is linear instead of logarithmic.

CHAPTER 3

Atom Interactions

The following chapter provides a description of the physics relevant for the manipulation of the ^{37}K atoms. Using lasers and magnetic fields, we are able to cool and confine the atoms to provide a well-localized source. We then optically pump these atoms to achieve high polarizations. A laser which photoionizes atoms from the $4P$ excited state is utilized as a very clean monitor of the degree to which the sample is optically pumped, providing us with a quantitative estimate of both the atomic and nuclear polarization of the atoms that are decaying.

Alkali atoms are well-suited for neutral atom traps and optical pumping processes are efficient because of their relatively simple electronic configurations. One can ignore the inert gas closed shell (argon, in the case of potassium) and treat the system as a single valence electron orbiting within the screened field of the nucleus.

In this chapter, we describe the energy level structure of an alkali atom (§3.2), including the effects of a weak magnetic field, and the interaction with a circularly-polarized laser field. The theory outlined here forms the basis for understanding magneto-optical traps as well as the optical pumping process used to achieve high (atomic *and* nuclear) polarizations (both of which are described in §3.3). To begin, however, a general outline of the "big picture" is given.

3.1 General Considerations

In order to ensure the reader is aware of why we are exploring these aspects of atomic physics, we briefly summarize how we prepare the sample of ^{37}K in our online experiment.

We begin with a magneto-optic trap (MOT), which is discussed in many papers [70, 71] and even textbooks [72]. The 1997 Nobel Prize in Physics was awarded to S. Chu, W. D. Phillips and C. Cohen-Tannoudji for their "development of methods to cool and trap atoms with laser light." Basically, a MOT uses the fact that with each absorption from a laser beam, a neutral atom absorbs momentum, and then decays back to the ground state either by stimulated emission or by spontaneous emission. In the latter case, the emission is isotropic and so the atom will, on average, feel a force in the direction of the laser beam. Clearly, for any appreciable force to be realized, a great number of photons must be absorbed since $h\nu \ll \frac{1}{2}Mv^2$. This is where the alkali atoms' valence electron makes them ideal candidates for traps. In the alkali atom involving a nucleus of spin I ($I = 3/2$ for ^{37}K), the hyperfine interaction splits the lowest $nS_{1/2}$ ($L = 0, J = 1/2$) atomic state into two states with total angular momentum $\boldsymbol{F} = \boldsymbol{I} + \boldsymbol{J}$ ($F = I - 1/2$ or $F = I + 1/2$; see Fig. 3.1). The magneto-optic trap involves a laser tuned in frequency to stimulate a specific hyperfine transition between two of the $nS_{1/2}$ and $nP_{3/2}$ multiplets: $nS_{1/2}$ ($F = I + 1/2$) $\rightarrow$ $nP_{3/2}$ ($F' = I + 3/2$). Since an electric dipole ($E1$) decay of this final state will populate only the original initial state, this sequence is referred to as a *cycling* transition*. With a lifetime for spontaneous decay less than 30 ns, the atoms are able to absorb and emit thousands of photons per second; after repeated absorptions from a coherent laser beam, the small optical force of each absorption is summed and in total these optical forces can play a significant role on relatively short timescales.

If now one considers the energy level structure of an atom in a weak quadrupole magnetic field, one can show that the Doppler shift combined with the Zeeman effect creates a weak potential trap at the zero of the field in which atoms may be collected (see §3.3.1). These traps can accumulate billions of atoms in a localized position,

*In ^{37}K, the $4S_{1/2}$ ($F = 2$) $\rightarrow$ $4P_{3/2}$ ($F' = 3$) states.

suspended by a weak potential and cooled to extremely low (~mK) temperatures. In the case of ^{37}K, we trap using the $S_{1/2}, F = 2 \rightarrow P_{3/2}, F' = 3$ (D_2) line and have a repump laser tuned to the $S_{1/2}, F = 1 \rightarrow P_{3/2}, F' = 2$ transition to pump atoms that leak to the $F = 1$ state. The repump laser is essential to pump atoms back into the cycling transition; without it, atoms would collect in the $F = 1$ level of the ground state and not be trapped.

Once we have a trap of ^{37}K, we wish to polarize the atomic sample for our Standard Model tests using β decay. The alkali's electronic structure is again well-suited for highly efficient optical pumping. The idea behind optical pumping is that one is able to prepare atoms in certain magnetic sublevel states by manipulating them with polarized laser light. A weak magnetic field is used to lift the Zeeman degeneracy of the hyperfine levels. With each absorption of a photon with positive circular polarization, the projection of the angular momentum per atom (on the optical pumping axis) is increased by one unit of $\hbar$. With repeated absorptions from the polarized laser beam, a very large fraction of the atoms accumulate into the highest (lowest) M_F sublevel, which is to say they become highly polarized (see §3.3.2).

When optical pumping, we apply a weak holding field of 2 G to define the magnetic field direction and lift the Zeeman degeneracy of the sublevels. We then excite the $4S_{1/2} \rightarrow 4P_{1/2}$ (D_1) transition with a 770 nm titanium:sapphire ring laser beam and collect the atoms into the extremal $|F = 2\ M_F = \pm 2\rangle$ states. These are known as 'stretched' states because they correspond to full alignment of the atomic *and* nuclear spins. In this way, one not only achieves high atomic polarizations, one also gets high nuclear polarizations due to the hyperfine coupling of the spins. Once in the stretched state, the atom can no longer absorb D_1 light because there is no $M_F = \pm 3$ state in the $P_{1/2}$ manifold for it to get excited to. Thus we do not expect to see fluorescence from a sample of highly polarized atoms.

The optical pumping process is properly described by the optical Bloch equations, which describe the evolution of an atom subject to a radiation field within the framework of the density matrix formalism. An approach that is equivalent in the limit that coherences may be neglected are the rate equations, which are in general easier to deal with because all the parameters are real. With a model for the evolution of

the atom, we can fit the fluorescence spectrum during the optical pumping process and, in a slightly model-dependent manner, can extract a good estimate of the sub-level populations. Once these are estimated, one can calculate the average nuclear polarization and alignment, *independent* of the nuclear observables.

All of the above requires an understanding of a Hamiltonian of the form:

$$\mathcal{H}(t) = \mathcal{H}_\circ + \mathcal{H}_{\rm hf} + \mathcal{H}_{\boldsymbol{B}}(t) + \mathcal{H}_{\boldsymbol{E}}(t), \tag{3.1}$$

where $\mathcal{H}_\circ$ is the basic Hamiltonian including the fine structure of an alkali atom; $\mathcal{H}_{\rm hf}$ is the hyperfine interaction that couples an atom's nuclear and atomic spins; $\mathcal{H}_{\boldsymbol{B}}(t)$ results from an externally applied (possibly time-varying) magnetic field; and $\mathcal{H}_{\boldsymbol{E}}(t)$ is the interaction term of a radiation field coupling to the induced dipole moment of the atom.

3.2 Energy Level Structure of an Alkali Atom

This section begins with the fine structure of an atom and is followed by the hyperfine interaction. Magnetic fields are then included so that we will have described each of $\mathcal{H}_\circ$, $\mathcal{H}_{\rm hf}$ and $\mathcal{H}_{\boldsymbol{B}}$. The optical pumping process, described by $\mathcal{H}_E$, will be discussed in the following section.

3.2.1 Fine structure

In the absence of external interactions and neglecting spin, the basic energy level structure of an alkali atom will be determined simply by the spatial wavefunction of the valence electron in the field of the nucleus. This gives rise to the principle quantum numbers and the zeroth-order energy levels: there will be an $L = 0$ (S) ground state, as well as excited states for $L = 1, 2, \ldots$ (P, D, $\ldots$) where L represents the total orbital angular momentum of the valence electron.

Including the $S = 1/2$ spin of the electron, its total angular momentum becomes $\boldsymbol{J} = \boldsymbol{L} + \boldsymbol{S}$. The orbital and spin momenta are coupled by the spin-orbit interaction and give rise to the fine structure of the atom. The energy levels are shifted depending

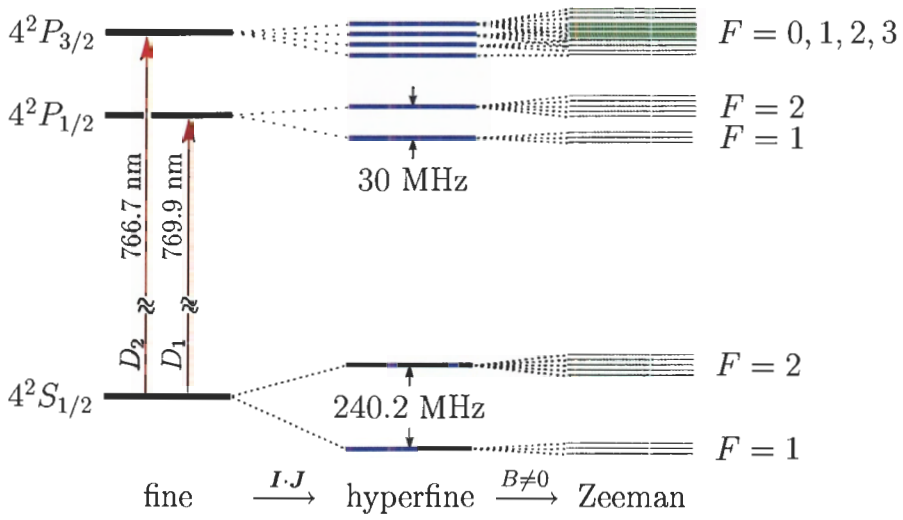

FIGURE 3.1: Fine, hyperfine and Zeeman structure of ^{37}K (not to scale). Experimentally, we optically pump on the D_1 line and trap using the D_2 cycling transition. In the absence of an external magnetic field, the Zeeman sublevels within each hyperfine manifold are degenerate.

on how the spin is aligned with L. For a given L, the total angular momentum can take on values $|L-\frac{1}{2}| \leq J \leq |L+\frac{1}{2}|$; for $L = 0$, there is only one $J = 1/2$ state and no splitting occurs. The electronic states of an alkali can be specified using the notation $n^{(2S+1)}L_J$ where n is the principle quantum number. For ^{37}K, the ground state is $4^2S_{1/2}$, and the first excited states are $4^2P_{1/2}, 4^2P_{3/2}$ as depicted in Fig. 3.1. Also shown are the hyperfine and Zeeman substructures, which are discussed in following sections.

The L, S coupling is very strong, giving rise to the large energy difference between the $P_{1/2}$ and $P_{3/2}$ states: $E_{P_{3/2}} - E_{P_{1/2}} = 0.0067$ eV$=$ 1.6 THz. This means that J remains a good quantum number as long as the energy scale of other interactions is small in comparison, and the effects can be treated perturbatively and independently for each fine state.

TABLE 3.1: The (I, J)-basis states and their ordering used to define the F, M_F coupled basis. The convention used to label the states are $|M_I\ M_J\rangle$.

$M_F = -2$	$M_F = -1$	$M_F = 0$	$M_F = 1$	$M_F = 2$
$\left\|\frac{-3}{2}\ \frac{-1}{2}\right\rangle_{k=1}$	$\left\|\frac{-1}{2}\ \frac{-1}{2}\right\rangle_{k=2}$	$\left\|\frac{1}{2}\ \frac{-1}{2}\right\rangle_{k=3}$	$\left\|\frac{3}{2}\ \frac{-1}{2}\right\rangle_{k=4}$	
	$\left\|\frac{-3}{2}\ \frac{1}{2}\right\rangle_{k=5}$	$\left\|\frac{-1}{2}\ \frac{1}{2}\right\rangle_{k=6}$	$\left\|\frac{1}{2}\ \frac{1}{2}\right\rangle_{k=7}$	$\left\|\frac{3}{2}\ \frac{1}{2}\right\rangle_{k=8}$

3.2.2 Hyperfine structure

The dominant correction to the fine structure is from the interaction of $\boldsymbol{J}$ with the nuclear spin, $\boldsymbol{I}$. The two become strongly coupled and the eigenstates of the atomic Hamiltonian are defined by the quantum number $\boldsymbol{F} = \boldsymbol{I} + \boldsymbol{J}$. Any $|I\ J\ F\ M_F\rangle$ wavefunction can be expressed in terms of $|I\ J\ M_I\ M_J\rangle$ basis states via:

$$|I\ J\ F\ M_F\rangle = \sum_{M_I, M_J} |I\ J\ M_I\ M_J\rangle\, \langle I\ J\ M_I\ M_J | I\ J\ F\ M_F\rangle \tag{3.2}$$

where $\langle I\ J\ M_I\ M_J | I\ J\ F\ M_F\rangle$ are the well-known Clebsch-Gordon coefficients we are interested in solving for. Of course we could simply look them up in this case, but once magnetic fields are considered (see the next section), tables no longer suffice and we must find a general method for determining them. Therefore, like in subsequent sections, we outline how we deduce the values of the Clebsch-Gordon coefficients by solving for the eigenvectors of the Hamiltonian matrix using numerical techniques [73].

In the case of an atom with angular momenta $I = 3/2$ and $J = 1/2$ (e.g. $S_{1/2}$ or $P_{1/2}$ in ^{37}K), we will have $k = (2I + 1)(2J + 1) = 8$ basis states. These states and their ordering are given in Table 3.1, where we have suppressed the I and J labels* and describe the states simply by $|M_I\ M_J\rangle_k$, with k representing the ordering that defines the basis of our Hamiltonian matrix.

In no magnetic field and for an atom with $J = 1/2$ and hence no electric quadrupole

*In what follows, we are working only with D_1 transitions for optical pumping, and so are only concerned with the $S_{1/2}$ and $P_{1/2}$ states, which both have $J = 1/2$. Hence the I, J labeling is redundant.

moment, the Hamiltonian for the interaction of $\boldsymbol{I}$ with $\boldsymbol{J}$ is [74]:

$$\mathcal{H}_{\text{hf}} = A_J \boldsymbol{I} \cdot \boldsymbol{J} \tag{3.3}$$

which causes the energy levels of the fine structure to be split, depending on the relative orientation of I with respect to J. For the $S_{1/2}$ state in ^{37}K, the hyperfine structure constant has been measured [75] to be $A_{S_{1/2}} = 120.1$ MHz, which defines the magnitude of this splitting. $A_{P_{1/2}}$ has not been measured, but we can estimate the value by scaling the measured value in ^{39}K (also from ref. [75]) based on the ratio of their nuclear g-factors [76], and find $A_{P_{1/2}} \approx 15$ MHz.

In order to generate our $\mathcal{H}_{\text{hf}}$ matrix, we express Eq. (3.3) in terms of the nuclear and atomic angular momentum operators, $I_z, I_\pm$ and $J_z, J_\pm$ respectively:

$$\mathcal{H}_{\text{hf}} = A_J \Big[I_z J_z + \frac{1}{2}\big(I_+ J_- + I_- J_+\big) \Big] \tag{3.4}$$

Physically, I_z and J_z pick out the component of spin aligned with the quantization axis — which we take to be $\hat{z}$ — while the ladder operators change the M_I and M_J of the states by ± 1. Mathematically,

$$\begin{aligned} I_z|M_I\ M_J\rangle &= M_I|M_I\ M_J\rangle \\ I_\pm|M_I\ M_J\rangle &= \sqrt{I(I+1) - M_I(M_I \pm 1)}|M_I \pm 1\ M_J\rangle, \end{aligned} \tag{3.5}$$

and similarly for the J operators. These eigenvalue equations define the (I, J)-selection rules for these interactions, which are summarized in Table 3.2.

With the above expressions, we can evaluate each of the elements of the 8×8 matrix in Eq. (3.4). Diagonal matrix elements in the hyperfine Hamiltonian arise from the $I_z J_z$ term which only couples identical states. The $I_\pm J_\mp$ terms, which overall result in $\Delta M_F = 0$ (but no $F = 0 \to 0$), add off-diagonal elements.

We are interested in finding the eigenvectors and eigenvalues of the resulting Hamiltonian, which one can do by hand for the above case; however, to accommodate additional perturbations (see the following sections), a program was written [73] which diagonalizes any real matrix, returning the eigenenergies and their corresponding eigenvectors. Thus we will have numerically calculated the coefficients of the

TABLE 3.2: Selection rules for the angular momentum operators in the (I, J)-basis.

Operator	Selection rules			
	ΔJ	ΔM_J	ΔI	ΔM_I
J_z	0	0	0	0
$J_\pm$	0	± 1	0	0
I_z	0	0	0	0
$I_\pm$	0	0	0	± 1

expansion:

$$|F\ M_F\rangle = \sum_k a_k |M_I\ M_J\rangle_k. \tag{3.6}$$

As expected, the coefficients, a_k, are equal to the values of the Clebsh-Gordon coefficients one looks up in tables. Indeed, diagonalizing the Hamiltonian and evaluating the Clebsch-Gordon coefficients are equivalent means of deducing the expansion of the F states in the (I, J)-basis.

The result, as mentioned earlier, is a splitting of the fine structure into two $F = I \pm J$ manifolds, the size of which is given in terms of the hyperfine structure constant:

$$E_{\rm hf} = \frac{1}{2} A_J \big[F(F+1) - I(I+1) - J(J+1)\big] \tag{3.7}$$

The $F = 2$ level will be shifted up by a factor $+\frac{3}{4}A_J$ and will consist of five degenerate $M_F = -2, -1, \ldots, 2$ sublevels. The $F = 1$ level, with only three $M_F = 0, \pm 1$ sublevels, gets shifted by $-\frac{5}{4}A_J$; note that the center-of-gravity of the manifold remains the same.

As an explicit example, both the numerical calculation outlined above and the Clebsh-Gordon coefficients give for the $|F\ M_F = 1\rangle$ states:

$$\begin{aligned} |2\ 1\rangle &= \tfrac{\sqrt{3}}{2}\big|\tfrac{1}{2}\ \tfrac{1}{2}\big\rangle + \tfrac{1}{2}\big|\tfrac{3}{2}\ \tfrac{-1}{2}\big\rangle \\ |1\ 1\rangle &= \tfrac{1}{2}\big|\tfrac{1}{2}\ \tfrac{1}{2}\big\rangle - \tfrac{\sqrt{3}}{2}\big|\tfrac{3}{2}\ \tfrac{-1}{2}\big\rangle \end{aligned} \tag{3.8}$$

i.e. with the basis states defined by Table. 3.1, we have $a_4 = 0.5$ and $a_7 = 0.866$ for the $F = 2, M_F = 1$ coupled state, with all other coefficients equal to zero.

Finally, we note that the F-selection rules akin to those of Eqs. (3.5) (and Table 3.2) will naturally arise when evaluating the observables in the (I, J)-basis; one can easily show, that $F_z|F\ M_F\rangle = (I_z + J_z)\sum_k a_k|M_I\ M_J\rangle_k = M_F|F\ M_F\rangle$ and similarly that $F_\pm|F\ M_F\rangle = \sqrt{F(F+1) - M_F(M_F \pm 1)}|F\ M_F \pm 1\rangle$.

3.2.3 Magnetic Field Effects

An external (possibly time-varying) magnetic field will couple to the magnetic dipole moment, $\boldsymbol{\mu}$, of the atom giving:

$$\mathcal{H}_B(t) = -\boldsymbol{\mu} \cdot \boldsymbol{B}_{\text{ext}}(t). \tag{3.9}$$

In what follows, we will be working in the weak field limit, where $B_{\text{ext}} \ll A_J/|\boldsymbol{\mu}|$. In this limit, the nuclear and atomic spins are still strongly coupled compared to the perturbative interaction with the applied field, and so the $|F\ M_F\rangle$ basis remains (at least approximately) valid.

The magnetic dipole of an alkali atom

The orbital motion of the valence electron induces a moment that goes like $\boldsymbol{\mu}_L = -g_L\mu_B\boldsymbol{L}$ where $g_L = 1$ is the orbital g-factor and $\mu_B = e\hbar/2m_e \approx 1.4$ MHz/Gauss is the Bohr magneton. The field also couples to the spin of this electron, adding a $\boldsymbol{\mu}_S = -g_S\mu_B\boldsymbol{S}$ term where this time the g-factor is 2.0023. In total, the magnetic dipole moment arising from the valence electron is:

$$\boldsymbol{\mu} = -\mu_B(g_L\boldsymbol{L} + g_S\boldsymbol{S}) \tag{3.10}$$

which, because J is a good quantum number in low fields, we can write as:

$$\boldsymbol{\mu} = -g_J\mu_B\boldsymbol{J} \tag{3.11}$$

where we have defined the Landé g-factor as:

$$g_J = g_L\frac{J(J+1) + L(L+1) - S(S+1)}{2J(J+1)} + g_S\frac{J(J+1) + S(S+1) - L(L+1)}{2J(J+1)} \tag{3.12}$$

Note that the atom interacts with the B-field via L and S, but since this coupling is weak compared to the spin-orbit coupling, the J-selection rules apply. Also, though S and J are always equal to $1/2$ for the $S_{1/2}$ and $P_{1/2}$ states, L will differ by 1 and so the ground and excited states of an atom will have different g_J factors.

Similarly, the nuclear magnetic moment will also couple to the field according to:

$$\boldsymbol{\mu} = +g_I \mu_N \boldsymbol{I} \tag{3.13}$$

where the g-factor has been measured to be $g_I = 0.2029$ for ^{37}K [25]. This coupling will be much weaker than the electron's (Eq. (3.11)), however, because the nuclear magneton, $\mu_N = e\hbar/2m_N$, is much smaller than μ_B, specifically by the ratio of the electron to nucleon mass: $m_e/m_N \approx 1/1846$. For this reason, one generally neglects the nuclear coupling; for completeness and since we are working in the (I, J) basis anyway, we will continue to include it. Note that the convention in defining g_I is of opposite sign to g_J; for simplicity, we absorb the the sign and the μ_N/μ_B factor into g_I, and define $g_I' = -g_I \mu_N/\mu_B$, which can then be treated on the same footing as g_J.

The coupling of the magnetic field to the total magnetic dipole moment of the atom from Eq. (3.9) gives:

$$\mathcal{H}_{\boldsymbol{B}} = -g_F \mu_B \boldsymbol{F} \cdot \boldsymbol{B}_{\text{ext}}, \tag{3.14}$$

where again $\boldsymbol{F} = \boldsymbol{I} + \boldsymbol{J}$ and the effective g-factor is:

$$g_F = g_J \frac{F(F+1) + J(J+1) - I(I+1)}{2F(F+1)} + g_I' \frac{F(F+1) + I(I+1) - J(J+1)}{2F(F+1)}. \tag{3.15}$$

The hyperfine interaction has already split the fine structure of the $S_{1/2}$ and $P_{1/2}$ states into two separate $F = I \pm 1/2$ levels, so the effective g-factor for the $F = I + 1/2$ level will be of opposite sign and approximately* equal in magnitude to the $F = I - 1/2$ level.

*In the limit that the small g_I' (nuclear interaction) term may be neglected.

As we did with the hyperfine interaction, we will again use the angular momentum operators to numerically construct the Hamiltonian, this time including a weak, applied magnetic field. Here we only consider static fields aligned with the quantization axis; Appendix C considers the effects of a small component of B perpendicular to $\hat{z}$.

Fields aligned with $\hat{z}$

We begin with the simplest case where the applied field, $\boldsymbol{B}_{\text{ext}}$, is static and aligned with the quantization axis

$$\boldsymbol{B}_{\text{ext}} = B_{\circ}\hat{z}, \tag{3.16}$$

so that $\mathcal{H}_{\boldsymbol{B}}$ reduces to:

$$\mathcal{H}_{\boldsymbol{B}} = -\boldsymbol{\mu} \cdot \boldsymbol{B} = g_F \mu_B B_{\circ} F_z. \tag{3.17}$$

The field exerts a torque on components of $(\boldsymbol{I}, \boldsymbol{J})$ that are perpendicular to its direction; as depicted in Fig. 3.2, one may classically imagine that this torque causes $\boldsymbol{\mu}$ (or equivalently, $\boldsymbol{F}$) to rotate around the field direction at a rate equal to the Larmor frequency:

$$\Omega_L = g_F \mu_B |\boldsymbol{B}_{\text{ext}}|/\hbar. \tag{3.18}$$

For the $S_{1/2}$ ground state in ^{37}K, the precession rate in a typical field of 2 G is ± 220 kHz, where the upper sign refers to the $F = 2$ level for which g_F is positive.

As can be seen by Eq. (3.17), a field aligned with the quantization axis introduces diagonal matrix elements via the F_z operator; unlike the hyperfine interaction, these expectation values depend on the M_F of the state and so lifts the degeneracy of the Zeeman sublevels. For the weak fields we are considering, the dependence on B_{ext} is linear and the $(2F + 1)$ sublevels are shifted by:

$$E_{\text{Zeeman}} \approx g_F \mu_B B_{\text{ext}} M_F, \tag{3.19}$$

as shown schematically earlier in Fig. 3.1.

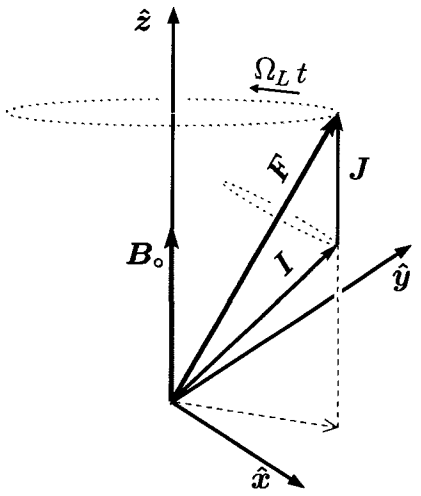

FIGURE 3.2: Vector model of an atom's spin precessing around the axis of an applied magnetic field. The field is assumed to be weak enough that $\boldsymbol{I}$ and $\boldsymbol{J}$ are still strongly coupled by the hyperfine interaction.

In terms of the nuclear and atomic angular momentum operators, the Hamiltonian for a constant field aligned with the quantization axis, Eq. (3.17), becomes:

$$\mathcal{H}_{\boldsymbol{B}} = \mu_B B_o \left(g_J J_z + g_I' I_z\right). \tag{3.20}$$

It is this equation which we use to calculate the matrix elements for field components parallel with the quantization axis. Diagonalization of the matrix yields eigenvectors, let us call them $|Q\ M_Q\rangle$, which, for fields that are small compared to the hyperfine splitting*, are a slight mixture of zero-field F eigenvectors that share the same M_F. As before, we express the eigenvectors in terms of coefficients of the (I, J)-basis:

$$|Q\ M_Q\rangle = \sum_k \tilde{a}_k |M_I\ M_J\rangle_k, \tag{3.21}$$

where this time the coefficients are labeled $\tilde{a}_k$ to point out that they depend on the magnitude of the B-field. For $B = 0$, $\tilde{a}_k \to a_k$ and $Q \to F$. In a typical field of 2 G, the coefficients change from their zero-field values by $\lesssim 2\%$ for the $S_{1/2}$ state, and by as much as 5% for the $P_{1/2}$ state. Specifically, compared to the example given in the case

*In large enough fields, I and J couple independently and more strongly to the field, so that F is no longer the preferred basis.

of the hyperfine interaction (Eq. (3.8)), the coefficients for the $S_{1/2}, |F = 2\ M_F = 1\rangle$ state in a 2 G field become $\tilde{a}_4 = 0.4913$ and $\tilde{a}_7 = 0.8710$, while the same for the $P_{1/2}$ state are $\tilde{a}_4 = 0.5247$ and $\tilde{a}_7 = 0.8513$. These represent very small mixings because physical observables go like the square of these amplitudes: in a 2 G field, $|Q{=}2\ M_Q{=}1\rangle$ has only 0.01% (0.07%) of $|F{=}1\ M_F{=}1\rangle$ mixed in for the $S_{1/2}$ ($P_{1/2}$) state. Note that parallel fields do not mix components of different M_F, and so all other coefficients remain zero. Thus we can say, to a very good approximation, that in a field of a couple of Gauss, the $|Q\ M_Q\rangle$ eigenvectors are the same as $|F\ M_F\rangle$.

The eigenvalues, which are the energy shifts of the states in the presence of a field, are small compared to the hyperfine splitting. In the $S_{1/2}$ state, the shifts are $\lesssim 1\%$ of the ground state splitting; even in the $P_{1/2}$ state, where A_J is about $10\times$ smaller, the differences are $\lesssim 3\%$. This is expected because we are working in the weak field limit and the magnetic interactions are a perturbation to the dominant hyperfine structure.

3.3 Interactions with a radiation field

A radiation field of a laser beam interacts with an atom through its electric dipole transition moments. The transition is between orbital levels of the valence electron in the case of an alkali atom, and so couples to L. The photon carries one unit of angular momentum, so transitions caused by a radiation field will be between states where $L' = L \pm 1$. In the case of an alkali, this means that the field can excite atoms from the $S \rightarrow P$ state, or it can go in the reverse direction and (coherently) stimulate emission back down to the ground state.

Coherent monochromatic radiation, *i.e.* a laser beam, will only interact with an atom if the energy difference between these states, $\hbar\omega_\circ$, is equal to the photon's energy, $\hbar\omega_L$. In this way, one is able to excite very specific transitions and hence affect the atom's external *and* internal degrees of freedom with great precision.

In the following sections, we discuss both of these aspects. In the first, we outline how magneto-optic traps use lasers to create an external force on the atom which acts like a damped harmonic oscillator and confines them to a specific point in space. Following this is a description of how the internal degrees of freedom can be manipulated

using the process of optical pumping.

3.3.1 Magneto-Optical Traps

The salient feature of magneto-optic traps — indeed the reason they *work* as a trap at all — is that their force is dependent upon the atom's position as well its velocity; much like a spring, the positional force returns atoms back to a common centre while the velocity-dependent force adds a damping effect, as if the spring was submerged in a viscous liquid. A laser field generates the velocity-dependent force which cools the atoms in an optical molasses, while a polarized laser field and an applied magnetic field adds the positional dependence needed to actually confine them to a localized point in space.

Initially, if one considers how small the incident photon's momentum, $\hbar\boldsymbol{k}$, is compared to that of an atom at room temperature, a trap based on the light forces from a laser beam seems futile. For example, the $4S_{1/2} \rightarrow 4P_{3/2}$ (D_2) transition in ^{37}K has a wavelength of $\lambda = 766.7$ nm so that $p_{\text{phot}} \approx 1.5$ eV/c while the atom's thermal momentum is typically 45 keV/c. In addition, when the atom decays from the excited state via stimulated emission, this small momentum kick is nullified since the atom will recoil by $-\hbar\boldsymbol{k}$ if the photon is emitted coherently. Spontaneous emission, on the other hand, emits photons homogeneously into 4π so that, at least on average, there will be a net momentum transfer in the direction of the incident photon. As stated earlier, the atoms must absorb and spontaneously emit many photons if one hopes to affect their external degrees of freedom.

The transition from the $F = I + \frac{1}{2}$ ground state to the $F' = I + \frac{3}{2}$ excited state *cannot* decay back into the other $F = I - \frac{1}{2}$ ground state because that would require a change in the total angular momentum of the system by 2; the atom must return to the same $F = I + \frac{1}{2}$ ground state where it started. This cycling transition allows an atom to absorb many photons from the same laser, so even though the force with each absorption is relatively small, a great number of absorptions summed together *can* significantly affect the atom's motion. The cycling is not perfect due to off-resonant transitions and finite linewidths, and so atoms may be optically pumped into the

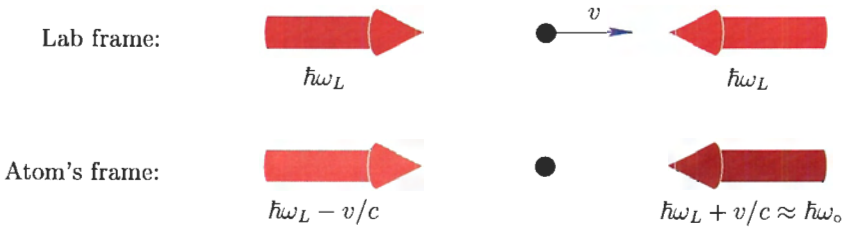

FIGURE 3.3: Principle of cooling neutral atoms by optical molasses. An atom moving against the red-detuned laser beam will be Doppler shifted closer into resonance and absorb momentum; with many repeated absorptions, the atom can be appreciably decelerated. This is not a trap, however, because there is no preferred position in space.

$F = I - \frac{1}{2}$ state where they will no longer be in resonance with the laser light. Atoms in this 'dark' state are not trapped, so a 'repumping' laser, tuned to the $F = I - \frac{1}{2} \rightarrow F' = I + \frac{1}{2}$ transition, is used to transfer atoms back into the cycling transition.

Doppler Cooling

Consider the effect on an alkali atom that is placed within a laser field generated by two identical, counter-propagating laser beams detuned Δ MHz below the atomic resonance, ω_o. Thermal atoms will have a Maxwellian velocity distribution in all directions and, due to the Doppler effect, will be affected by each beam differently. As depicted in Fig. 3.3, an atom moving collinear with one of the laser beams will see the light red-shifted *farther* below resonance by a factor v_{atom}/c while the counter-propagating beam will be blue-shifted *closer* to resonance. The atom will preferentially absorb photons from the laser beam that is against the atom's direction of motion and, with each absorption, the atom's momentum is reduced. It is in this way that the atoms are cooled and where the name for this process, *optical molasses*, is derived.

It can be shown [77] that the force in an optical molasses is proportional to the velocity if (*i*) the Doppler shift isn't too large and (*ii*) the laser intensity, I_L, is weak enough that the atom is far more likely to decay by spontaneous (rather than stimulated) emission. Letting $\omega_L = \omega_o - \Delta$ represent the frequency of the laser light,

the Doppler force is [72]:

$$\boldsymbol{F}_D(\boldsymbol{v}) \approx \frac{8\hbar k^2 \Delta \; I_L/I_{\text{sat}}}{\Gamma(1+\frac{4\Delta^2}{\Gamma^2}+\frac{I_L}{I_{\text{sat}}})^2}\,\boldsymbol{v} \tag{3.22}$$

where $\Gamma = 1/\tau$ is the transition linewidth and $I_{\text{sat}} = \frac{h\pi c\Gamma}{3\lambda^3}$ is the saturation intensity.

The transition linewidth ends up being this force's limiting factor; in a simple model [77], the coldest temperature attainable is $T_{\text{D}} = \hbar\Gamma/2k_{\text{B}}$ where k_{B} is Boltzmann's constant. In the case of the $P_{3/2}$ state in ^{37}K for which $\tau = 26.2$ ns, this 'Doppler limit' is 150 μK.

The Magneto-Optic Trap

We have shown how a magnetic field removes the M_F degeneracy of the hyperfine levels of an alkali atom by splitting the $|F\ M_F\rangle$ energy levels according to Eq. (3.19). If we apply a magnetic field that linearly changes sign at the origin, $\boldsymbol{B} = zB_o\hat{z}$, to atoms in an optical molasses, the Zeeman effect and circularly polarized trapping light will provide us with a position-dependent force: the energy level shifts (hence the transition frequency and scattering rate) will be proportional to the distance from $z = 0$ as well as to the Doppler shift from its velocity.

Figure 3.4 depicts the scenario for the one-dimensional case. Note that here we will consider the simplified case of an atom with no nuclear spin, and hence no complicating hyperfine structure (e.g. $^{38\text{m}}$K). In this case, the F quantum number from previous sections reduces simply to J. The finite nuclear spin of ^{37}K slightly complicates the structure, and, as mentioned earlier, requires a repump laser to talk to the lower $S_{1/2}$ state. However, the basic idea behind how the MOT works remains the same, and is simpler to understand without the extra levels induced by the hyperfine interaction.

Referring to the Figure, we see that an atom at $z > 0$ will have its $|J{=}\frac{1}{2}\ M_J{=}\frac{1}{2}\rangle \rightarrow |\frac{3}{2}\ \frac{-1}{2}\rangle$ transition shifted closer to the laser frequency. The two counter-propagating beams are distinguished by their polarizations; the $\Delta M_J = -1$ transition can only be driven by the σ^- beam, so the atom feels a net force acting towards the left. Similarly, atoms at $z < 0$ will preferentially absorb the σ^+ light through the $|\frac{1}{2}\ \frac{-1}{2}\rangle \rightarrow |\frac{3}{2}\ \frac{1}{2}\rangle$ transition and be pushed back towards centre. If the laser field does not have

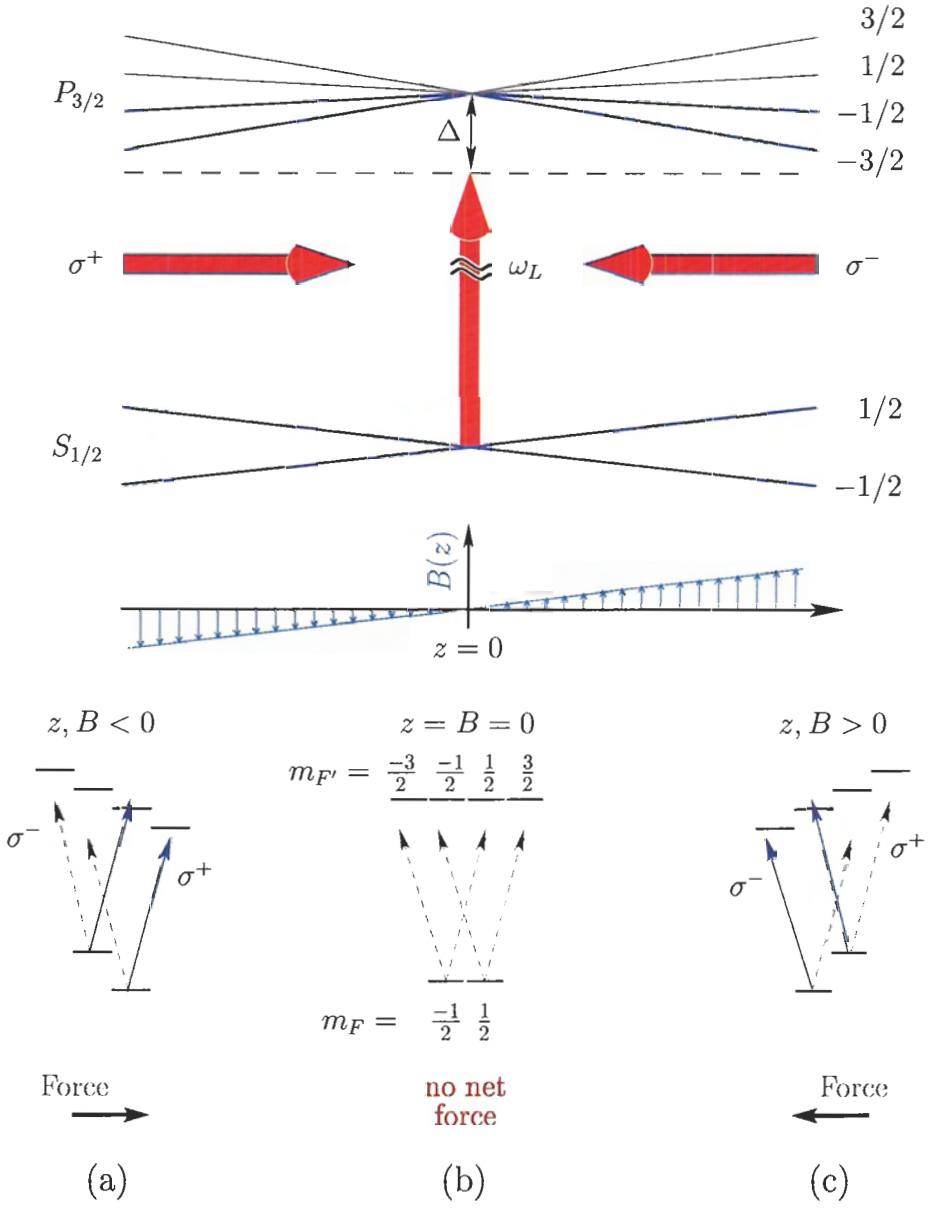

FIGURE 3.4: Atomic energy levels and Zeeman shifts of ^{38m}K in a one dimensional magneto-optic trap. The shift of the energy levels depends linearly on the magnetic field (for weak fields) giving a positional dependent force. The trapping arises because of preferential scattering off the laser that is shifted closer to resonance, depicted by the solid lines arising from σ^+ light in (a) and σ^- in (c); the force in either case pushes atoms towards $z = 0$. Both laser beams are equally off resonant at the trap centre (b) so neither is preferentially absorbed and the atom feels no net force.

perfect polarization, the atom can absorb photons from the wrong beam and will be heated rather than cooled. Thus, the quality of the circular polarization of the laser light is very important.

The magneto-optic force is a combination of the Doppler force with effects induced by the Zeeman shift. The trap centre is defined at $z = 0$ where the magnetic field changes sign. If we let $\xi = kv + \beta z$ where βz represents the Zeeman effect on the transition frequency, then the overall magneto-optic force is [71]:

$$F_{\mathrm{MOT}}(z,v) = \frac{\hbar k \Gamma}{2}\left[\frac{I_L/I_{\mathrm{sat}}}{1+\frac{I_L}{I_{\mathrm{sat}}}+\frac{4(\Delta-\xi)^2}{\Gamma^2}} - \frac{I_L/I_{\mathrm{sat}}}{1+\frac{I_L}{I_{\mathrm{sat}}}+\frac{4(\Delta+\xi)^2}{\Gamma^2}}\right] \tag{3.23}$$

It can be shown that [78], for small detunings, this force is proportional to ξ so that the trapped atoms behave like a simple, damped harmonic oscillator.

The generalization to three dimensions requires a magnetic field that is zero at the centre and which increases linearly with distance from there; this is generally accomplished using a quadrupole field generated by two coils in the anti-Helmholtz configuration. With six laser beams oriented along the axes as depicted in Figure 3.5, forces similar to those of the 1D case are present no matter which direction an atom within the trapping volume is traveling.

Typically, MOTs are not very deep and so considerable effort is needed to efficiently load them. The most popular method is known as the vapour-cell MOT [70] and it uses the fact that a MOT *can* capture the low-energy tail of the Maxwell-Boltzmann distribution of velocities. The cell which defines the trapping volume can be specially coated [79] so that atoms tend to bounce off the wall rather than (permanently) chemisorbing to it. When they bounce (physisorb), the atoms re-thermalize (repopulating the whole Maxwell-Boltzmann distribution) and are able to be trapped by the MOT again. The many repeated opportunities for capture allow this method of loading the MOT to have efficiencies on the order of several percent.

TRINAT's Double–MOT System

In order to reduce backgrounds from untrapped atoms as well as to iso*merically* differentiate between isotopes (e.g. for the scalar search to separate ^{38m}K from the ground

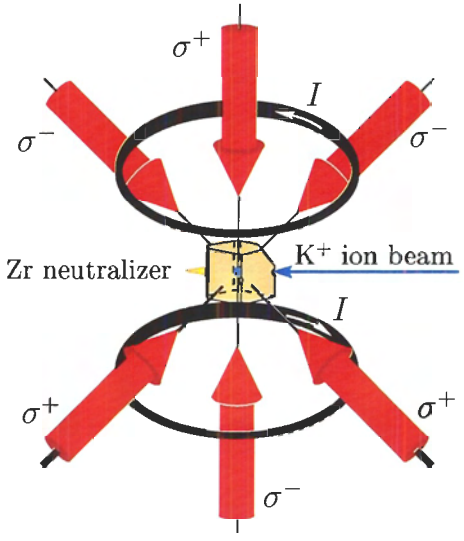

FIGURE 3.5: Schematic diagram of a vapour-cell MOT with an ion beam catcher and neutralizer. ISAC provides us with ^{37}K which is neutralized in the hot Zr cone, diffuse out into the vapour-cell MOT, and then trapped in the MOT. The quartz cube defines the trapping volume and is coated with SC-77 Dryfilm [79] so as to maximize the number of bounces off the walls and increase the trapping efficiency.

state), a double–MOT system is utilized (see Figure 1.2 on page 6). The first 'collection trap' [26] is a vapour-cell MOT that traps the potassium atoms once they diffuse out of a resistively heated neutralizer. The neutralizer is based on the Los Alamos scheme as described in [80]. A number of materials were tested at the TISOL facility [81], and Zr was found to release the largest fraction at the coolest temperatures. The laser linewidth is small enough that the fine structure of different atoms (even isomers of the same atom) are resolved, and only the species of interest are trapped. The cold, localized ^{37}K atoms at the centre of the collection trap are then pushed with a small (≈ 1 mm^2) pulsed laser beam to a second 'detection trap.' The push beam, aimed a few millimeters above the 2$^{\text{nd}}$ MOT so as not to interfere with any atoms already trapped there, generates a low-energy ($v_{\text{atom}} \approx 40$ m/s) atomic beam of ^{37}K that can be directly captured in the detection trap. The large separation of the two traps reduces the probability of a thermal ^{37}K randomly entering the detection chamber, and so provides a dramatically cleaner environment from which to observe the decay.

As the atoms are being transferred they expand radially, so the efficiency of the transfer will rapidly decrease as the inter-trap distance is increased. In order to be able to separate the collection and detection traps by 75 cm (enough to add approximately 15 cm of lead shielding) without a great loss of atoms, two 2D MOTs ('atomic funnels') have been employed to compress them back along the push beam axis. The detection trap typically catches 75% of the atoms pushed from the 1st trap. The efficiency of the system as a whole, including capture and transfer, is $\approx 5 \times 10^{-4}$ atoms trapped per ion incident into the neutralizer.

For a more thorough review of TRINAT's double–MOT system and the details regarding the transfer, the interested reader is referred to [82].

3.3.2 Optical Pumping

Outlined in this subsection is how we polarize our sample of atoms using a technique known as optical pumping. The idea of optical pumping was first proposed by Alfred Kastler [83] who realized that light could be used to manipulate an internal degree of freedom: the Zeeman sublevel populations, and hence the polarization and alignment of the atom.

Before we delve into the details of how to describe this dynamic process, let us outline the basic idea here. Consider an atom initially in one sublevel, say the $4S$ $|2\ 0\rangle$ state, as depicted in Fig. 3.6. If one shines in σ^+ polarized light onto the atom, tuned to the transition energy, the atom can absorb the photon. During this process, it also receives a momentum kick of $\hbar\boldsymbol{k}$ (affecting the external velocity), and must increase one M_F sublevel because the photon carries $+\hbar$ of angular momentum.

From the excited state, the atom can either decay back to the ground state by stimulated or spontaneous emission. If the laser intensity is very strong ($I_L \gg I_{\text{sat}}$), it has a high probability of inducing stimulated emission in which case the exact same energy, momentum and angular momentum are re-emitted and no net change is realized. When the spontaneous decay rate is much faster than the stimulated emission rate, angular momentum couplings and Clebsh-Gordon coefficients determine the decay branches to the different sublevels; in some cases, the atom returns to the

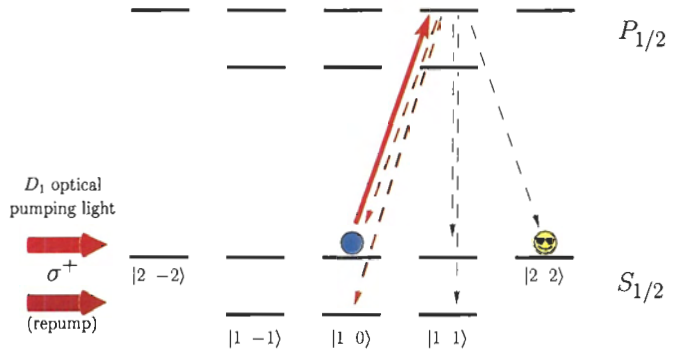

FIGURE 3.6: Simplified depiction of the principle of optical pumping.

same M_F level it came from (dashed red line in Fig. 3.6), but there is also a chance it de-excites to a higher M_F level (dashed green lines). As one can imagine, with repeated absorptions the atom's internal state will make a random walk towards the fully stretched $M_F = +2$ state. Once there, it is dark to the light because there is no excited state available with $M_F = 3$.

If we can achieve 100% population in the fully stretched state, our atomic sample will obviously have complete nuclear and atomic polarization. Assuming the atoms are initially distributed equally among the ground state sublevels, we would first observe an initial spike in the atomic fluorescence (aka the excited state populations) as most of the atoms would be excited by the D_1 light. The fluorescence would then decay away during the optical pumping process as the atoms get pumped and accumulate into the stretched state where they are dark to the pumping light. This is shown as the black line in Fig. 3.7 and as one can see, the fluorescence is entirely extinguished after $\approx$ 500 μs. Also shown are curves for which the optical pumping light is not perfectly circular, allowing atoms to get pumped out of the stretched state, resulting in imperfect polarizations and a baseline of fluorescence in the steady-state. Though requiring a model to interpret (see below, and in §4.7.2 we discuss systematic effects on the deduced polarization), the vanishing of the fluorescence can be used as a sensitive probe of the atomic sample's average nuclear polarization.

Let us consider the case where we apply σ^+ light and so are interested in optically pumping to the stretched $|2\ 2\rangle$ state. Let further assume that optical pumping

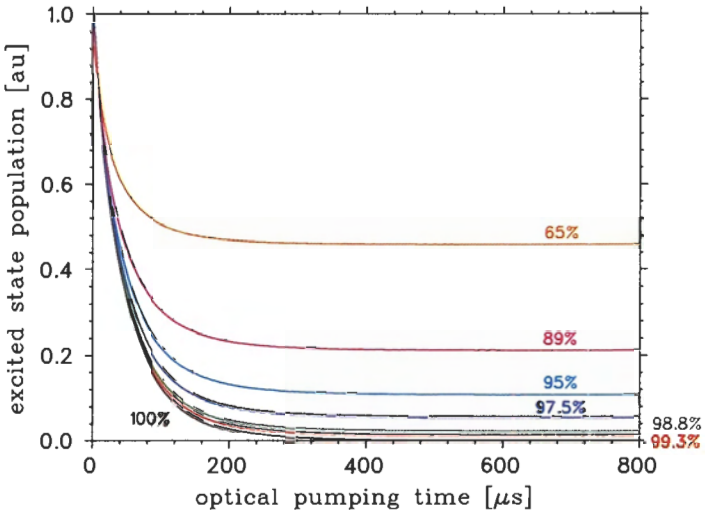

FIGURE 3.7: Vanishing of the fluorescence during the optical pumping process. The different curves correspond to different purities of the circular polarization of the optical pumping light. The labels represent the polarizations deduced from the sublevel populations at the end of the optical pumping process.

inefficiencies had a net result of leaving 10% of the atoms in the adjacent $|2\ 1\rangle$ state at asymptotically long times. In this case, there would be a baseline of fluorescence because the atoms *not* in the stretched-state *can* and will be excited by the σ^+ D_1 laser. In this toy model, the end result would be a distribution of sublevel populations of the form:

$$\begin{aligned} |\psi\rangle &= 0.949|2\ 2\rangle + 0.316|2\ 1\rangle \\ &= 0.949\left|\tfrac{3}{2}\ \tfrac{1}{2}\right\rangle + 0.274\left|\tfrac{1}{2}\ \tfrac{1}{2}\right\rangle + 0.158\left|\tfrac{3}{2}\ \tfrac{-1}{2}\right\rangle \end{aligned} \tag{3.24}$$

where for simplicity we have used the zero-field expansion. With wavefunctions in hand that are explicitly expressed in the (I, J)-basis, it is trivial to calculate the expectation values of the I_z operator. The first moment gives us the average value of M_I, *i.e* the component of $\boldsymbol{I}$ aligned with the axis of the laser beam. The polarization of the atom is the direction of this nuclear spin, and so is calculated according to:

$$P_{\text{nucl}} = \frac{\langle\psi|I_z|\psi\rangle}{|\boldsymbol{I}|}. \tag{3.25}$$

The second moment is related to the alignment of the nucleus, which is given by:

$$T = \frac{I(I+1) - 3\langle\psi|I_z^2|\psi\rangle}{I(2I-1)}. \tag{3.26}$$

Substituting the above expression for ψ, the polarization is found to remain relatively high at 95%. The fluorescence one would see from this same population leakage of 10% is a little over 7% of the initial spike. Thus, the fluorescence can be used as a very sensitive probe of the sublevel contamination; any observed fluorescence at long times immediately indicates the polarization is not perfect and some depolarizing mechanism persists in the steady-state.

To understand in greater detail how the observed steady-state fluorescence relates back to the sublevel populations, we need to develop a model of the optical pumping process. How the populations are distributed can have a significant effect on the deduced polarization. For example, if 10% of the population was in $|1\ 1\rangle$ instead of the $|2\ 1\rangle$ state as described above, then the fluorescence would rise to almost 20% and the nuclear polarization would be greater as well, at almost 98.5%! In order to estimate the polarization based on the fluorescence in a quantitative fashion, we developed a model which accounts for the dynamical optical pumping process and includes realistic depolarizing mechanisms.

The Optical Bloch and Rate Equations

The interaction of a radiation field with an atom is described in the interaction picture by the density matrix formalism leading to the optical Bloch equations (OBEs). As mentioned in §3.1, this approach is *not* used in this thesis; however, the OBEs are described in this section in order define the principles of optical pumping and to explicitly point out the approximations made in going to the rate equations.

The dynamics of the laser-atom system is contained in a time-dependent operator, commonly referred to as the *density operator*:

$$\rho = |\Psi\rangle\langle\Psi|. \tag{3.27}$$

Here the wavefunction of the system, $|\Psi\rangle$, is a linear combination of the n basis states,

$|\phi_i\rangle$, spanning the Hilbert space of an atom in a radiation field:

$$\Psi(\boldsymbol{r},t) = \sum_{k=1}^{n} c_k(t)\phi_k(\boldsymbol{r})\, e^{-i\omega_k t}. \tag{3.28}$$

The expectation value of the density operator,

$$\rho_{ij} = \langle\phi_i|\rho|\phi_j\rangle = \langle\phi_i|\Psi\rangle\langle\Psi|\phi_j\rangle = c_i c_j^* \tag{3.29}$$

will be an $n \times n$ matrix, whose diagonal elements are the real probabilities, $|c_i|^2$, for the atom to be in state i. The off-diagonal elements are in general non-zero and complex; they contain the quantum mechanical coherences between states $|\phi_i\rangle$ and $|\phi_j\rangle$.

We can understand the evolution of this density matrix using the analog of the Louiville equation from classical dynamics [72]:

$$\frac{\partial\rho}{\partial t} = \frac{1}{i\hbar}[\mathcal{H}(t),\rho], \tag{3.30}$$

where the Hamiltonian of the atom plus radiation field system is given by Eq. (3.1). All of the components of this Hamiltonian have previously been described, except for the laser-atom interaction term, $\mathcal{H}_{\boldsymbol{E}}(t)$. As one would expect, this is the coupling of the dipole moment of the atom to the electric field of the laser:

$$\mathcal{H}_{\boldsymbol{E}}(t) = -e\,\boldsymbol{d}\cdot\boldsymbol{\mathcal{E}}(\boldsymbol{r},t). \tag{3.31}$$

One normally adopts a semi-classical approach in which the atom is treated quantum-mechanically, and the laser beam is taken to be a classical plane wave traveling along $\hat{z}$ with wavelength $\lambda = 2\pi/\omega_L$. In this case, the electric field operator will be:

$$\boldsymbol{\mathcal{E}}(\boldsymbol{r},t) = E_{\circ}\cos(kz - \omega_L t)\,\hat{\epsilon}_q, \tag{3.32}$$

where $\hat{\epsilon}_q$ represent the polarization of the laser. For π polarization where the electric field of the laser is aligned with its direction of propagation, $\hat{\epsilon}_0 = \hat{z}$ and the photon carries no orbital angular momentum, so $q = 0$. In the case of circular polarization, the photon carries $q = \pm 1$ unit of angular momentum and the field polarization is

$\hat{\epsilon}_{\pm 1} = -(\pm\hat{x}+i\hat{y})/\sqrt{2}$. One then finds that the atom-photon interaction couples initial and final states according to:

$$\begin{aligned}\mathcal{H}_{fi}(t) &\equiv \langle f | \mathcal{H}_{\boldsymbol{E}}(t) | i \rangle \\ &= \hbar\Omega_{if}\cos(kz - \omega_L t).\end{aligned} \tag{3.33}$$

Here $\Omega_{if} = \Omega_{fi} \equiv -\mu_{f\to i}E_o/\hbar$ is known as the Rabi frequency, which is defined in terms of the electric dipole matrix element, or transition strength:

$$\mu_{i\to f} \equiv e\langle f | \boldsymbol{d}\cdot\hat{\boldsymbol{\epsilon}} | i \rangle. \tag{3.34}$$

Substituting Eq. (3.33) into Eq. (3.30) gives us the time-evolution of the density matrix.

$$i\hbar\frac{dc_j(t)}{dt} = \sum_{k=1}^{n} c_k(t)\mathcal{H}_{jk}(t)e^{i(\omega_j-\omega_k)t}. \tag{3.35}$$

Solving these coupled, complex differential equations for the density matrix elements gives rise to the OBEs.

Up until this stage, no approximations have been made, and Eqs. (3.35) are completely general. In order to write out explicit forms for the OBEs, one makes use of the fact that, for small laser detunings, $\Delta \equiv \omega_L - \omega_o$ is much smaller than the transition frequency, ω_o. Neglecting the very fast terms of order $1/\omega_L$ compared to $1/\Delta$ is called the *rotating wave approximation*; said another way, because the laser beam is resonant with the atomic transitions, the evolution of the density matrix is slaved to slowly oscillating terms.

The density matrix formalism accounts for quantum mechanical coherences between the sublevels, but in practice these are small and in fact are difficult to achieve. Based on earlier TRINAT work [84], we are able to ensure these quantum mechanical effects are very quickly damped compared to the evolution of the populations (by a slight detuning of the laser beam). Neglecting coherences, one can show that the OBEs reduce to the simpler *rate equations* (see, for example, Exercise 18 of [85]). The

result for a two-level atom with one ground state, $|g\rangle$, and one excited state, $|e\rangle$, is:

$$\frac{dN_g}{dt} = -W_{ge}\,N_g + W_{eg}\,N_e + \gamma_{\text{spon}}\,N_e \tag{3.36a}$$

$$\frac{dN_e}{dt} = \underbrace{+W_{ge}\,N_g}_{\text{absorption}} \underbrace{-W_{eg}\,N_e}_{\text{stimulated emission}} \underbrace{-\gamma_{\text{spon}}\,N_e}_{\text{spontaneous emission}}, \tag{3.36b}$$

where N_g, N_e are the populations* of ground and excited states, and W_{ge}, W_{eg} are the transition probabilities for absorption and stimulated emission.

The dominant relaxation process, spontaneous emission, has been phenomenologically included [86] which presently has the same form as stimulated emission; the difference is in the transition probability, which in the case of spontaneous emission is the natural width of the excited state, equal to the inverse of the radiative lifetime:

$$\gamma_{\text{spon}} = 1/\tau. \tag{3.37}$$

A full quantum-mechanical treatment of spontaneous emission has been shown to yield these terms, as discussed in §IV.E.1 of [85].

The transition probabilities for absorption and stimulated emission are equal and given by [87]:

$$W_{ij} = \frac{3\lambda^3\tau}{\pi hc} I_L \frac{|\mu_{ij}|^2}{8\tau^2} \int_{-\infty}^{\infty} g_{ij}(\nu)\rho_L(\nu)d\nu, \tag{3.38}$$

Assuming Lorentzian lineshapes for both the atomic transition $\big(g_{ij}(\nu)\big)$ and laser beam $\big(\rho_L(\nu)\big)$ with FWHMs of γ_{spon} and γ_L respectively, we find:

$$W_{ji} = W_{ij} = \frac{|\mu_{ij}|^2\gamma_{\text{spon}}}{2\tau\Gamma'}\left[\frac{I_L/I_{\text{sat}}}{1+4\left(\frac{\omega_L-\omega_{ij}}{\Gamma'/2\pi}\right)^2}\right] \tag{3.39}$$

where the total, effective linewidth is $\Gamma' = 2\pi(\gamma_{\text{spon}}+\gamma_L)$ and $I_{\text{sat}} = \pi hc/3\lambda^3\tau$ is again the saturation intensity.

*In relation to the OBEs, these are the diagonal elements of the density matrix, ρ_{gg}, ρ_{ee}.

Optical Pumping of an Alkali Atom

The generalization to a multi-level atom is straight-forward, however in that case one must factor in the recoupling of all angular momenta and the polarization of the optical pumping beam. From Eq. 3.21, we can expand the $|Q\ M_Q\rangle$ atomic eigenstates in terms of the $|I\ J\ M_I\ M_J\rangle$ basis, however the laser beam photon's couple only to $\boldsymbol{L}$, the orbital angular momentum of the atom; so we must further expand the J-basis eigenfunctions in terms of the (L, S)-basis, *i.e.*:

$$|\alpha\ L\ S\ J\ M_J\rangle = \sum_k C_k |\alpha\ L\ S\ M_L\ M_S\rangle \tag{3.40}$$

where α represents all other quantum numbers. The coupling of the two angular momenta, $\boldsymbol{L}$ and $\boldsymbol{S}$, give rise to Clebsh-Gordon coefficients, which can be expressed as:

$$C_k = (-1)^{-L+S-M_J}\sqrt{2J+1}\begin{pmatrix} L & S & J \\ M_L & M_S & -M_J \end{pmatrix} \tag{3.41}$$

The term in parentheses is known as the $3j$ symbol and is discussed in many textbooks (see, for example, §3 of [88]). The dipole transition matrix element in the J basis is then given by [72]:

$$\begin{aligned} \mu_{|J\,M_J\rangle\to|J'\,M'_J\rangle} &= \langle\alpha'\ L'\ S\ J'\ M'_J|\boldsymbol{d}\cdot\hat{\boldsymbol{\epsilon}}|\alpha\ L\ S\ J\ M_J\rangle \\ &= e(-1)^{L'+S-M'_J}\sqrt{(2J+1)(2J'+1)} \\ &\quad\times\begin{Bmatrix} L' & J' & S \\ J & L & 1 \end{Bmatrix}\begin{pmatrix} J & 1 & J' \\ M_J & q & -M'_J \end{pmatrix}\langle\alpha'\,L'\|d\|\alpha\,L\rangle \end{aligned} \tag{3.42}$$

where again $q = M_F - M'_F$ represents the angular momentum of the photon. The arrays of quantum numbers in curly bracket is known as the $6j$ symbol (discussed in §6 of [88]) which arises from the recoupling of three angular momenta (L, S and q in this case). This and the $3j$ symbol can both be easily evaluated using current computer libraries [89]. The reduced matrix element, $\langle\alpha'\,L'||\,d\,||\alpha\,L\rangle$, is independent of spin-selection rules, and arises from the radial part of the dipole matrix element.

It simply enters as an overall normalization and so only affects the magnitude of the coupling.

In evaluating the dipole matrix element of an alkali — including the atom's nuclear spin — the recoupling of all the Clebsh-Gordon coefficients leads to Eq. (4.33) of [72]:

$$\mu_{|F\,M_F\rangle\to|F'\,M_F'\rangle} = e(-1)^{1+L'+S+J+J'+I-M_F'}\,\langle\alpha'\;L'\|d\|\alpha\;L\rangle \times\sqrt{(2J+1)(2J'+1)(2F+1)(2F'+1)} \times\begin{Bmatrix} L' & J' & S \\ J & L & 1\end{Bmatrix}\begin{Bmatrix} J' & F' & I \\ F & J & 1\end{Bmatrix}\begin{pmatrix} F & 1 & F' \\ M_F & q & -M_F'\end{pmatrix}. \tag{3.43}$$

The transition strengths as calculated by Eq. (3.43) for ^{37}K are shown in Fig. 3.8 for both* π (top) and σ^+ circular (bottom) polarization of the light. The results for σ^- may be obtained from the σ^+ case by simply changing the sign of all the M_F sublevels. Note that Eq. (3.43) is only true in the absence of an external field. For weak fields, however, the transition strengths do not change much from the values shown in the Figure.

The rate equations as given in the previous section are only true for a two-level atom. We have just included angular momentum selection rules in the dipole matrix element, but we also must now consider the polarization of the laser beam (*i.e.* the dot product of $\boldsymbol{d}\cdot\hat{\boldsymbol{\epsilon}}$) and sum over all possible transitions. The resulting generalization of Eqs. 3.36, the rate equations for a multi-level atom, are [86]:

$$\frac{d}{dt}N_{|F'\,M_F'\rangle} = \sum_q\left[W_{|F\,M_F\rangle\to|F'\,M_F'\rangle}N_{|F\,M_F-q\rangle} - W_{|F'\,M_F'\rangle\to|F\,M_F-q\rangle}N_{|F'\,M_F'\rangle}\right] - \gamma_{\text{spon}}\sum_{k=M_F-1}^{M_F+1}|\mu_{|F'\,M_F'\rangle\to|F\,k\rangle}|^2 N_{|F'\,M_F'\rangle} \tag{3.44a}$$

*We only use circularly-polarized light to optically pump, however the π ($\Delta m_F = 0$) transition strengths are needed to calculate the relative branches for spontaneous emission.

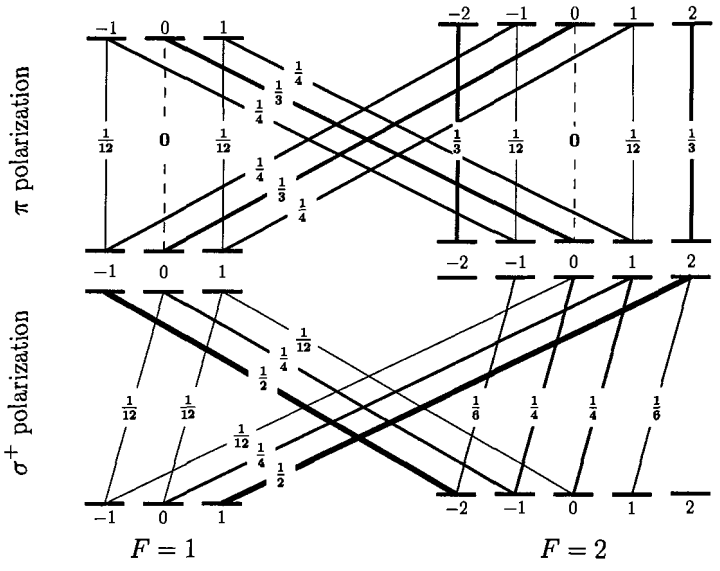

FIGURE 3.8: Transition strengths, $|\mu_{eg}|^2$, for the $4^2S_{1/2} \rightarrow 4^2P_{1/2}$ (D_1) line in ^{37}K.

for the excited state populations, and

$$\frac{d}{dt}N_{|F\,M_F\rangle} = \sum_q \Big[- W_{|F\,M_F\rangle\rightarrow|F'\,M'_F+q\rangle} N_{|F\,M_F\rangle} + W_{|F'\,M'_F\rangle\rightarrow|F\,M_F\rangle} N_{|F'\,M'_F+q\rangle} \Big]$$

$$+ \gamma_{\text{spon}} \sum_{k'=M'_F-1}^{M'_F+1} |\mu_{|F'\,k'\rangle\rightarrow|F\,M_F\rangle}|^2 N_{|F'\,k'\rangle} \tag{3.44b}$$

for the ground states. Note that the spontaneous emission terms are summed over *all* polarizations of the emitted light, regardless of the polarization of the laser beam. However, the sums over q in the absorption and stimulated emission terms are only over the polarization of the laser beam; e.g. for purely $\sigma^{\pm}$ polarization, the sums would collapse to only $q = \pm 1$.

Note that all of the above assumes the optical pumping magnetic field is perfectly aligned with the quantization axis defined by the laser beam. To include small deviations, we have phenomenologically incorporated perpendicular fields into our rate equation model of the optical pumping process as outlined in Appendix C. In order to *properly* include this effect, however, one must use the optical Bloch equations because the transverse components of $\boldsymbol{F}$ couple to the field; this is beyond the rate

equation model because unlike the $\hat{z}$ component of F, F_x and F_y are not eigenstates of the Hamiltonian of the system.

3.3.3 Photoionization of ^{37}K

We have developed a very powerful technique to image the cloud of atoms as part of the ^{38m}K program. We illuminate the cloud with a pulsed 355 nm laser, which carries more than the ionization energy, E_I, of a P-state valence electron of potassium (see Fig. 3.9). This electron is excited into a state in the continuum, becoming a free photoelectron with energy $\frac{1}{2}m_e v^2 = \hbar\omega - E_I$. The once neutral potassium atom suddenly becomes an ion which, in our geometry, gets swept by the electric field and strikes our microchannel plate recoil detector. The time difference between the laser pulse (start) and the MCP (stop) is a sharp peak in TOF*, the centroid of which will be related to the MCP–trap distance. This allows us to image the cloud — both centroid and width — of atoms in all three dimensions: two from the $\hat{x}$ and $\hat{y}$ positions of the event in the MCP, and the third from the TOF. Note in particular that:

1. because very few atoms are photoionized, this is a direct, *non-destructive* probe of the atoms that we are using for the β decay measurement;

2. this technique is extremely *clean* because we require a coincidence between the laser and the recoil detector, so there are very few backgrounds to contaminate the image of the trap (this "nuclear" measurement does not suffer from typical problems associated with an "atomic" measurement, such as scattered light and collection efficiencies of fluorescent light); and

3. it is extremely *sensitive* because, with essentially no backgrounds and only one photon to provide a photoionization event, we do not need many in order to reliably and completely image the cloud (unlike for example, fluorescence probes, which require many absorptions to obtain a finite signal).

*In practice, to avoid having the high-rate laser as an event trigger, we delay it by ≈ 1 μs so that the MCP starts the event, and the laser stops it.

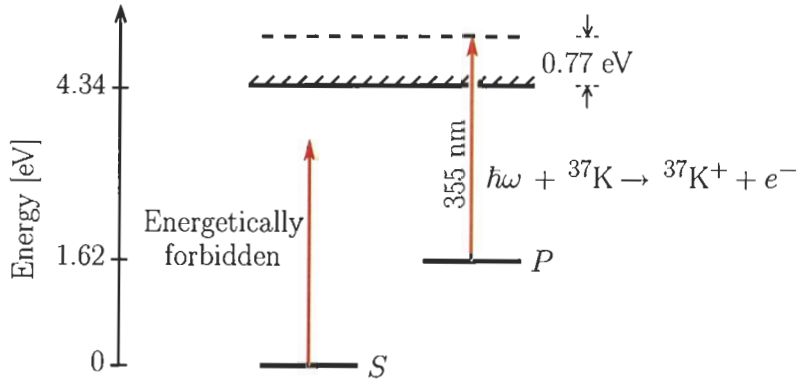

FIGURE 3.9: Photoionization of ^{37}K from the excited $4P$ states. A valence electron in the excited state can absorb a photon from a 355 nm laser and be promoted to a state in the ionization continuum, freeing the electron. There is not enough energy in this laser to photoionize atoms from the $4S$ ground state.

This photoinization technique has proven to be an absolutely critical part of the ^{37}K experiment, and indeed the polarized program as a whole. Not only do we need to have a detailed image of the cloud, but because it is a direct measure of the excited state population, we are able to have a non-destructive probe of the the cloud polarization *in situ* by measuring the excited state populations during the optical pumping process. As Fig. 3.9 shows, the 355 nm photons only carry enough energy to photoionize atoms from the $4P_{1/2}$ and $4P_{3/2}$ excited states, and is therefore directly related to the atomic fluorescence. The $4S_{1/2}$ ground state is blind to this light because the probability for two-photon photoionization is negligible (due to the low laser intensities used).

It is also important to note that the photoionizing laser does not perturb the polarization of the atomic cloud. Rayleigh scattering, which can destroy polarization, has a cross section on the order of only a barn, whereas non-resonant photoionization has a cross section of about one megabarns. Thus the 355 nm photons either ionizes an atom and removes it from the system, or it does nothing to one part in a million.

Using this technique, the excited state population is measured as a function of the optical pumping time, and curves such as those plotted in Fig. 3.7 can be generated and, as we will see in §4.7, can be fit to models of the pumping process to deduce the cloud polarization.

CHAPTER 4

Data Analysis and Characterization

4.1 Summary of the Fall 2002 Experiment

The experiment described in this thesis took place in the fall of 2002. The run was broken up into two distinct blocks: the first was from Sept. 8^{th} — 16^{th} and the second from Oct. 11^{th} — 20^{th}. There is considerable difference in how the atoms were polarized between the two: in the first, we used the trim coils* to generate the ≈ 2 G holding field applied while optically pumping the atoms. During the $3\frac{1}{2}$ week break between the two running periods, we constructed Helmholtz coils to generate a more uniform holding field; this also allowed us to quickly turn on and off the $\boldsymbol{B}$-field as well as to flip its sign. As we will see, the vanishing of the fluorescence for these data is improved, however we have indications that the optical pumping light was not fully overlapped with the cloud (see §4.6.3), and hence the bulk polarization of the whole cloud is unknown. For this reason, the final results quoted in this thesis are limited to the first block of runs, although analysis of the second block was performed in order to estimate how we may have improved the system for future considerations.

All compatible runs were taken together (same polarizing scheme, holding fields, trap/cloud positions, etc.), resulting in 10 different data sets. Table 4.1 summarizes these groups of runs. In all cases, the magnitude of the optical pumping holding field was nominally 2 G. For the first data sets, before field-switching was possible, the sign of the $\boldsymbol{B}$ field was always negative; the sign for the second block of runs is given

*These coils generate a uniform magnetic field in addition to the quadrupole trapping field, and are normally used to offset the Earth's field.

TABLE 4.1: Run summary of the polarized ^{37}K β^+ decay experiment and breakdown of the ten compatible data sets in terms of the total run time, number (total/polarized) of scintillator–DSSSD and scintillator–DSSSD–Ar$^{+1,2,3}$ coincident events.

Runs	Data set label	Run time [hrs]	β events (scin–DSSSD)	β–Ar events (scin–DSSSD–MCP)
905–919	1^a	9.99	881 621/ 169 630	30 962/ 6 228
949–975	1^b	25.73	1 512 927/ 341 434	57 984/ 11 395
		35.72	2 394 548/ 511 064	88 946/ 17 623
1118–1131	2^-	11.78	633 680/ 154 850	26 211/ 5 510
1132–1164	3^-	12.97	818 873/ 197 453	34 870/ 7 166
	3^+	20.90	1 304 220/ 313 568	55 492/ 11 307
1182–1189	4^-	11.20	1 060 532/ 249 627	109 123/ 9 177
	4^+	1.98	184 810/ 43 924	22 519/ 1 621
1196–1203	5^-	6.36	457 401/ 105 959	50 119/ 3 914
1212–1225	6^-	17.27	1 330 731/ 317 034	165 329/ 11 831
1226–1240	6^+	17.48	1 708 835/ 297 104	214 786/ 11 029
		99.94	7 499 082/1 679 519	678 449/ 61 555

by the label of the data set (e.g. the $3^{\pm}$ data sets used a field of ± 2 G). The total run time of each set is listed as well as the total number of accepted (and polarized, a subset defined by a timing cut in the MOT/OP cycle as discussed in §4.1.2) β singles and β–Ar coincidences to give an indication as to the relative weighting the data sets. The scintillator–DSSSD β-telescope is used here in defining β event because it is (a) cleaner than the phoswich detectors in singles, and (b) it is this β detector used in coincidence with the recoil detector to extract B_ν (and has much more statistics).

The 1^a and 1^b data sets were separated by a double-maintenance day; these data sets have slightly different trap positions and small development of the phoswich detectors resulted in different gains of these detectors. As mentioned above, all subsequent runs have an entirely different optical pumping holding field. In addition, during this break, we changed the cube of the vapour-cell MOT to enhance collection efficiency

of ^{37}K atoms from the first trap, and we moved the 2$^{\text{nd}}$ trap position ≈ -4 mm in $\hat{x}$ to offset the cloud centroid from the MCP's most inefficient area (see §4.4.2) as well as to have it better centred in chamber coordinates. The 2^- data set is not considered in what follows because during these runs we varied the 2$^{\text{nd}}$ trap position and made diagnostic tests. We first began changing the sign of the optical pumping field during the $3^{\pm}$ data sets on a run-by-run basis. The $4^{\pm}$ data sets are separated from the 3$^{\text{rd}}$ by tests we made to investigate the effect of a finite vacuum: for about a day, we intentionally worsened the vacuum in the 2$^{\text{nd}}$ chamber to see the effect on the observed asymmetries. The 5^- data set follows the 4$^{\text{th}}$ by another double-maintenance day, and at the end of these runs we scanned the frequency of the D_1 laser to improve the optical pumping process before finishing with the $6^{\pm}$ data sets.

4.1.1 Layout of the Detection Chamber

Before delving into details, we show diagrams of the 2$^{\text{nd}}$ chamber in Fig. 4.1 to indicate the general setup of the experiment. Fig. 4.1(a) is a schematic view of the $\hat{x}_{\text{chmbr}} - \hat{z}_{\text{chmbr}}$ plane as viewed from above ($+\hat{y}_{\text{chmbr}}$). The chamber coordinates are defined such that $\hat{x}_{\text{chmbr}}$ is the axis between the 1$^{\text{st}}$ and 2$^{\text{nd}}$ traps, $\hat{y}_{\text{chmbr}}$ points upwards, and $\hat{z}_{\text{chmbr}}$ points from the centre of the MCP to the β-telescope. The centre of this coordinate system is the centre of the chamber. As seen in Fig. 4.1(b), which shows the $\hat{z} = 0$ plane as viewed by the β-telescope, the coordinate system used throughout this thesis is rotated by 30° with respect to the chamber coordinates; in this system, the polarization axis — defined by the D_1 optical pumping light — lies along $\hat{x}$.

The recoil detector is a Z-stack of three 600 μm micro-channel plates [90] operated at saturation ($\approx$ 1 keV bias/plate) and read out by a resistive anode [91] with four separate readouts. The position is determined by the relative charge in the readouts to $\pm$0.25 mm. The MCP also provides a timing signal which is inherently extremely fast, typically hundreds of picoseconds, so that our time-of-flight measurements are in fact limited by the finite size of the atom cloud. The 2.4 cm diameter active area is defined by a collimator placed 0.25 mm in front of the MCP. The front plate of this detector is placed at $z = -6.25$ cm; the solid angle subtended by this detector

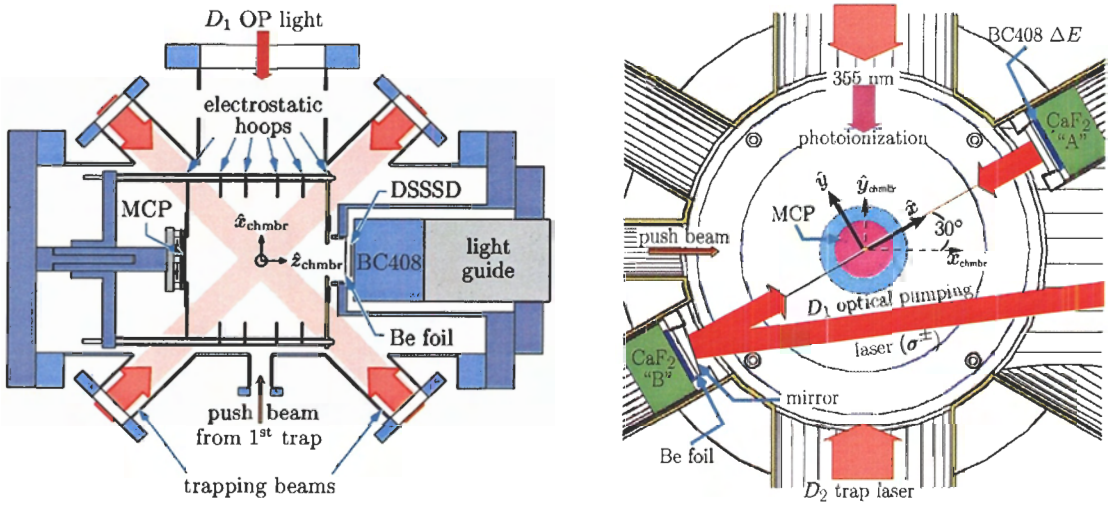

(a) horizontal cross-sectional view (b) vertical cross-sectional view

FIGURE 4.1: Geometry of the detection chamber showing the coordinate systems, nuclear detectors and laser beams. The atom cloud is nominally at chamber centre and polarized along $\pm\hat{x}$, which is rotated 30° with respect to the chamber coordinates.

is 0.14 sr, however the electrostatic hoops generate an electric field of ≈ -810 V/cm, which enhances the collection efficiency for charged recoils.

The β-telescope is a 2.4 cm × 2.4 cm × 491 μm double-sided Si-strip detector (DSSSD) backed by a BC408 plastic scintillator (6.5 cm diameter, 5.5 cm length). Valid β events are triggered by a coincidence between the E and ΔE detectors, where the energy in the $\hat{x}$ and $\hat{y}$ strips of the DSSSD must be equal to within 3σ of each strips' resolution of typically $\lesssim 20$ keV FWHM. The gain of the scintillator is stabilized using a temperature-controlled blue LED pulser. The energy resolution of the scintillator is described by a Gaussian width of $\sigma_{\text{scin}} = \sqrt{(1.80\text{ keV}) \times T_{\text{scin}}}$, where T_{scin} is the kinetic energy of β. The relative timing of the β-telescope with the MCP is 2.3 ns FWHM. This telescope, used throughout TRINAT's ^{38m}K program, has been characterized in great detail and found to agree very well with Monte Carlo simulations. The interested reader is referred to [10] (as well as [11, 12]) for more information and greater details on this detector.

The major difference in the nuclear detection system between the ^{38m}K and ^{37}K experiments is the addition of two plastic + CaF_2(Eu) phoswich β detectors (see

Fig. 4.1(b)). These detectors are not position sensitive like the β-telescope, and the fact that both the E (CaF_2(Eu)) and ΔE (plastic) scintillators are read out by the same photomultiplier tube means that they are inherently more susceptible to backgrounds. However, as we will see, the βs are prominent in a 2D plot of E vs. ΔE and so provide a good tag for β events. The thin BC408 plastic scintillator (1" diameter, 2 mm length; 8.77 cm from the chamber centre) is optically glued directly onto the 1.5" diameter, 2 cm long CaF_2(Eu); this in turn is glued to a light-guide which transports the scintillation light from both detectors to Electron Tubes 9112SB PMTs with a TB1107 transistorized base. The decay times of the plastic and CaF_2(Eu) are 2.1 ns and 0.96 μs respectively, so their signals are well separated by the inspection times of their respective ADCs: the fast plastic signal has a 32 ns gate to its charge-sensitive ADC, while the slow CaF_2(Eu) signal is shaped using a 0.5 μs time constant and has a long (~ 5 μs) gate given to its peak-sensing ADC.

As part of the can holding the phoswich detectors, we have placed a heavy metal collimator within which is situated a thin (0.015") Be foil to separate the chamber vacuum ($\sim 3\times10^{-10}$ Torr) from the phoswiches which are at atmospheric pressure. In front of these foils are 0.1 mm thick, 99.9% reflective dielectric mirrors which reflect the optical pumping light* brought in from $+\hat{x}_{\text{chmbr}}$ through a large viewport. As depicted in Fig. 4.1(b), the mirror in front of phoswich B is set at an angle of 11.5° with respect to the detector face so that the laser beam is directed towards and retroreflects off the mirror in front of phoswich A. The degree of circular polarization is preserved by initially reflecting the light off a mirror 11.5° in the other plane so that the phase shifts cancel [92]. In this way, the optical pumping axis — which defines the polarization axis — is along the detection axis defined by the two phoswich detectors; as mentioned earlier, this axis defines the 'polarized' coordinate system used throughout this thesis.

The pulsed 355 nm laser used to photoionize P state atoms is brought in from the $+\hat{y}_{\text{chmbr}}$ direction along with the vertical D_2 trapping beam. A mirror below the chamber retroreflects this beam in order to double the part-per-million number of atoms photoionized per pulse.

*Generated from a narrow 770 nm diode laser.

4.1.2 Polarized/Unpolarized Cycling

The magneto-optic trap destroys any polarization of the atoms because it indiscriminately excites atoms to all $P_{3/2}$ excited states, and so all M_F sublevels quickly become equally populated. Thus we must cycle between 'MOT on' — to collect, cool and trap atoms — and 'OP on,' when we polarize the atoms and make our asymmetry measurements. The timing for this cycling, as well as the transferring of atoms from the collection to detection traps, is shown in Fig. 4.2. The bottom panel shows that we transfer atoms every 700 ms, alternating between the σ^+ and σ^- polarization of the optical pumping light every 6^{th} transfer. In this way, we equally and homogeneously distribute in time the number of positive and negative cloud polarizations throughout a given run.

Zooming in on a 1 sec timescale, one can see that within each transfer we alternate between trapping and polarizing the cloud of atoms. One of these cycles lasts for 4 ms so that we have about 175 cycles/transfer. At the top of Fig. 4.2, we show a typical plot of the photoion event rate spectrum. During the MOT times, when the atoms are continually being excited to the P state, we have a large number of photoion events. As indicated in the figure, we initiate turning off the quadrupole magnetic trapping field about 400 μs before switching off the MOT laser beams to ensure the field is fully off before beginning the optical pumping part of the cycle (the small spike is due to electronic noise). The D_2 MOT beams are turned off by changing the frequency of an acousto-optic modulator which deflected the beams. Once the trapping light is extinguished, the photoion rate dies away because all the atoms quickly de-excite to the ground state where they cannot be photoionized by the 355 nm laser. Note that there are no events in the $\approx$ 100 μsec period between turning off the D_2 laser and the start of optical pumping with the D_1 light; this indicates that we do indeed fully extinguish the D_2 light and so they will not contaminate the optical pumping part of the cycle. At the start of the optical pumping process, we clearly discern the expected sharp rise in the photoion rate, or excited state population, as the atoms begin to get pumped into the stretched state. This curve dies away as the atoms accumulate in the $|M_F| = F$ sublevel, become highly polarized and dark to the optical pumping

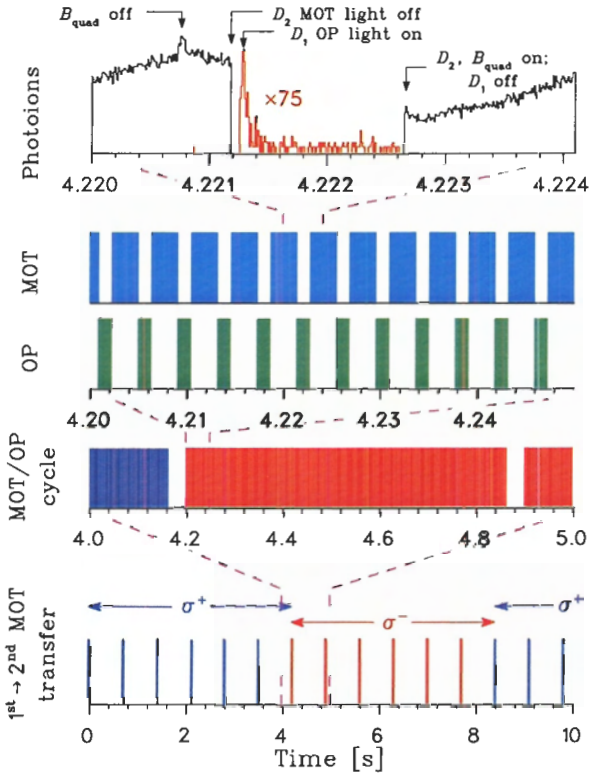

FIGURE 4.2: Timing diagram of the MOT/OP cycles (see text). Shown are the transfer times and OP laser polarization states. Above is a zoom in on one transfer time, above which a greater zoom in of the trapping and optically pumping times. The top panel shows the photon yield spectrum on the time scale of one trap/optical pumping cycle.

light (*cf.* Fig 3.7). The number of photoion events during the optical pumping times are much smaller than the MOT times because there are many fewer atoms in the excited state. After pumping for 1400 μs, we turn off the D_1 light and turn the MOT back on (both B_{quad} and the D_2 light) to recollect atoms before they expand too far and are lost; as one can see, the fluorescence rate immediately rises, though it takes a little while before the atoms are completely recollected and the fluorescence rate returns to its maximum value.

4.2 Monte Carlo Simulations

In order to include the theoretical decay rate given in Chapter 2 with detector responses, scattering effects, etc., we use Monte Carlo (MC) techniques to generate simulations of the experiment. We then compare our experimental results with these simulations to calibrate detectors and to extract physics results.

We have developed a detailed MC package, SMC, which uses CERN's GEANT detector description and simulation package [93] for tracking of βs and γs. SMC [94] is a ForTran77 code, described in detail in [10] but summarized below, that was initially used to analyze the data of the $0^+ \rightarrow 0^+$ decay of ^{38m}K in our searches for massive neutrinos [13, 12] and weak scalar currents [9, 11]. Additions to the code for the ^{37}K experiment include the addition of polarization and alignment of the optically pumped atoms to the decay generator, as well as including the new phoswich detectors.

The start of every event begins by defining the (x_o, y_o, z_o) position of the decay generated from a 3D Gaussian which is characterized separately for each data set. Referring ahead to §4.6, the Gaussian centroids and widths have a time-dependence over the optical pumping part of the cycle as the cold cloud ballistically expands, and it should be noted that this is included when generating the event's initial position.

The kernel of SMC then generates the β^+ decay of polarized ^{37}K shown in Fig. 2.1, including the two strongest branches to excited states. The decay rate, Eq. (2.5), is used in the generator where the values of the correlation parameters are input parameters. The Fermi function parameterized by Wilkenson [95] is used instead of Eq. 1.3 in order to include a finite mass (versus an infinitely massive) nucleus, the finite

spatial extent of wavefunction of the decaying nucleon and the finite electromagnetic size of the nucleus. Furthermore, we include the screening of the Coulomb field of the nucleus by the outer atomic electrons using the WKB approximation (see Eq. (6) of [96]). Radiative corrections from virtual (soft) and real (hard) bremsstrahlung photons are incorporated when modeling the $0^+ \rightarrow 0^+$ decay of ^{38m}K, but since we are not yet sensitive to this level of correction and the addition of spin complicates the 4-body calculation, we neglect these higher-order radiative corrections in ^{37}K; by doing so we reduce the problem to a simpler 3-body decay. We use the well-known acceptance–rejection technique (see, e.g., [97, 98, 3]) to randomly generate events according to Eq. (2.5): The kinematic variables of the decay (E_β, E_ν, $\theta_{\beta\hat{i}}$, $\theta_{\beta\nu}$ and the level in ^{37}Ar) are randomly generated and the decay rate calculated; this is then compared to another number, dW_{test}, generated randomly between zero and the maximum of the decay rate (calculated upon initialization). If the evaluated decay rate for a potential event is below dW_{test}, the event is accepted and tracking begun; otherwise it is rejected, and a new attempt is made with new kinematic variables. In general, these variables are generated homogeneously throughout their allowed ranges. For example, the β energy is taken to be between m_e and $E_\circ$; similarly, $\cos\theta_{\beta\nu}$ is evenly distributed between ± 1. In order to avoid lengthy tracking of βs which are extremely unlikely to fire a detector, the initial direction of positrons in the Lab frame is restricted as we will discuss shortly.

In generating events according to Eq. (2.5), the magnetic sublevel populations as deduced by our fits of the polarization to our atomic model (see §4.7.2) are included, again for each data set separately. The values of the correlation coefficients for the isobaric analogue state are generally taken to be the Standard Model predictions based on the measured value of $\lambda = +0.5754$ (see Table 4.2). Decay to excited states in ^{37}Ar is simulated, as well as the subsequent γ decay down to the ground state. Recoil-order effects have not been included yet because — like radiative corrections — they are known to be small (see §2.1.2) and we are not yet sensitive to them. However, as part of preparing for an isospin mixing experiment in ^{36}Ar, all of Holstein's [24] expressions have been encoded and used in SMC so that it will not be difficult to include full recoil-order corrections to our simulations.

TABLE 4.2: Values of the correlation coefficients input in SMC assuming the Standard Model. In all cases, independent of λ, the SM predicts $b = D = 0$ and $c = A_\beta - B_\nu$.

Energy level in ^{37}Ar [MeV]	I^π	β branching ratio	λ^{-1}	$a_{\beta\nu}$	A_β	B_ν
0	$3/2^+$	97.89%	0.5754^{-1}	0.6683	−0.5702	−0.7692
2.796	$5/2^+$	2.07%	0	−1/3	−3/5	3/5
3.601	$3/2^+$	0.0224%	0	−1/3	2/5	−2/5

Once an event is generated, we begin by tracking the recoiling ^{37}Ar through the uniform electric field generated by the electrostatic hoops. Due to the open geometry of our system and backing-free source of the atom cloud, GEANT is not needed to track the recoiling ^{37}Ar. We can calculate the trajectories of the recoils using simple parabolic paths of a particle in a uniform accelerating field, $\boldsymbol{a} = \frac{qU}{2M_{\mathrm{Ar}}}\hat{z}$:

$$\begin{aligned} x(t) &= x_\circ + v_{x_\circ} t \\ y(t) &= y_\circ + v_{y_\circ} t \\ z(t) &= z_\circ + v_{z_\circ} t + \frac{qU}{2M_{\mathrm{Ar}}} t^2 \end{aligned} \tag{4.1}$$

where $q = ne$ is the electric charge of the recoil (randomly generated according to the observed $n = 0, 1, 2, \ldots$ charge state ratios), U is the strength of the applied electric field (in units of V/cm), and $M_{\mathrm{Ar}} = 34.44$ GeV. The small initial velocity, $\boldsymbol{v}_\circ$, includes the momentum kick from the β decay as well as the (essentially negligible) thermal velocity of the atom. Once (and if) the recoil reaches the MCP at $z = -6.125$ cm, the time-of-flight (TOF), $\hat{x}$ and $\hat{y}$ positions are calculated; if the recoil is within the ⌀2.4 cm active area of the MCP defined by a collimator, then the MCP efficiencies are applied (see §4.4.2) to see if the event is registered by the detector. To ease comparison with the data, the $\approx$ 130 ns offset of our multihit TDC is added to the simulated TOF (actual values depend on which β detector is in coincidence).

For all simulations involving β−Ar coincidences, the tracking of the recoil is done first, and only if it struck the recoil detector are the other β and γ decay products

considered. This greatly increases the speed of our simulations because the recoil tracking is very simple, whereas the β and γ tracking are much more CPU expensive. This is because they are passed to GEANT where we have included our entire geometry (117 volumes); because these particles can scatter into large angles and the β^+ eventually annihilates into two 511 keV photons (annihilation-in-flight, though negligible, is included in our simulations), it is important to continue tracking them even if they do not go directly into a detector. For example, if a β goes directly into the DSSSD and then back-scatters out of the β-telescope's vacuum chamber, we continue tracking after this point because the annihilation radiation may leave energy in the telescope's plastic scintillator no matter where the positron eventually came to rest (and thus still satisfies the $E - \Delta E$ coincidence condition). However, the likelihood for these particles to scatter into a detector from a remote part of the geometry is still quite small overall. For this reason, the direction of βs at the start of an event is constrained to a cone of $\pm 18°$ centered on the detector of interest, e.g. the β-telescope or one of the phoswich detectors. This solid angle of initial β directions is mirrored in the opposite direction in order to account for backscattering; as part of the ^{38m}K analysis, this has been shown to be especially important for β-telescope–MCP coincidences. It has been confirmed, by analyzing simulations where events were generated into 4π, that events where the β was initially emitted outside this 18° cone have a negligible effect on the β singles spectra, and therefore an absolutely unnoticeable effect on $\beta-$Ar coincidences. The speed of the simulations using this restricted double-cone is increased by an order of magnitude compared to letting them decay into all angles (*i.e.* the ratio of the emitted solid angle to 4π).

During tracking in GEANT, the energy loss of the particles is tabulated and separately summed for all of the β detectors (phoswiches, DSSSD and scintillator). Once all primary and generated secondary particles are fully tracked, the final energy reading in all of the detectors are convoluted with their appropriate electronic noise. We do not convolute with a response function for the detectors because this is simulated by GEANT during tracking. The complicated analysis and position decoding of the 48 DSSSD strips is equivalent to that used in the data (see §4.2 of [10]), namely that one pixel fired with consistent energy readings in each $\hat{x}$ and $\hat{y}$ strip above thresh-

old. If more than one pixel fired, the event is vetoed because it was likely a β that back-scattered out of the plastic scintillator, and therefore did not deposit all of the energy in the telescope. Finally, if the observed energy deposited in a given detector passes the same threshold that is applied to the data (see the next section), then that detector is considered to have fired.

Once all particles have been tracked, the desired coincidences between detectors (e.g. scintillator–DSSSD or plastic–CaF_2(Eu) for β events, and coincidences with the MCP for β–Ar coincidences) are applied, and the appropriate histograms incremented.

At this time we would like to gratefully acknowledge the computing resources provided by WestGrid [99]. Their high-performance computing cluster was an invaluable tool for analysis of the experiment presented in this thesis. Without WestGrid it is hard to imagine how we could have made as thorough an analysis given the large number of CPU expensive Monte Carlo simulations needed.

4.3 β Detection

Our nuclear detector system consists of three β detectors: two plastic–CaF_2(Eu) phoswich and one DSSSD–plastic scintillator β-telescope. The β-telescope has been described and characterized in detail elsewhere [10] and so is not repeated in this thesis. As we will see in §5.1, the phoswich detectors — meant to measure the β asymmetry — were not able to provide a clean physics measurement, so they have not been characterized in as great a detail as the β-telescope.

Furthermore we note that with respect to the B_ν measurement, the E_β energy dependence is very weak and so we do not require extremely good characterizations. In this thesis, the β detectors are generally used only as tags for positrons, giving us their initial direction and a coincidence condition with the MCP.

4.3.1 The β-Telescope

The calibration of the β-telescope follows the methods described in Ref. [10]. Each of the 48 strips of the DSSSD was calibrated in detail for the ^{38m}K experiment, and this

same calibration was used in the present experiment. A new calibration was not found to be necessary because, once the gains were adjusted based on the pulser centroids, the efficiency for $\hat{x}$ and $\hat{y}$ strip energy agreement was found to be similar to earlier results; this would not be true if the gains were improperly matched.

The gain of the plastic scintillator, stabilized using a temperature-controlled blue LED pulser, was also found to be very close to previous calibrations. New calibrations were made by fitting the offset and gain of the calibration to a SMC simulation of the β decay of ^{37}K. Figure 4.3 shows a representative fit to the polarized β singles spectrum (points) for the 1^a data set. For details on how these fits were done, the reader is referred to Appendix B.1. On the left (right) is the result for $\sigma^+(\sigma^-)$ polarization, though since the detector is perpendicular to the polarization axis, the difference in the two spectrum shapes is negligible. The fitting function (solid line) included a small exponential background* (lighter dashed line) in addition to the simulation (darker dashed line). The two points which really determine the calibration are the Compton edge of the 511 keV annihilation radiation, and the 5.126 MeV end-point (magnified in the top-right inset). However, the gain and offset are highly correlated parameters, and one finds that one can get essentially equivalent calibrations for different fit values; e.g. if the offset is increased a little, a slightly decreased gain will give the same overall calibration. This is exemplified by the difference in the two calibrations (given above the plots) which must be equivalent since $\sigma^\pm$ are alternated on ≈ 4.2 ms timescales, and any minor polarization effects are accounted for by the MC. Indeed, if one compares the two calibrations (right plot of Fig. 4.3) one sees that the two are the same to within their uncertainties; of course the $\rho = 88\%$ correlations between the parameters must be included in estimating the calibration uncertainties. Finally we note that the incremental χ^2 of the fit is shown below the calibration fits as a solid line; the dashed line corresponding to $\chi^2/\nu = 1$ is also plotted to guide the eye. In both cases we obtain quite reasonable calibration fits.

*Presumably due to untrapped atoms, background γs and cosmic rays.

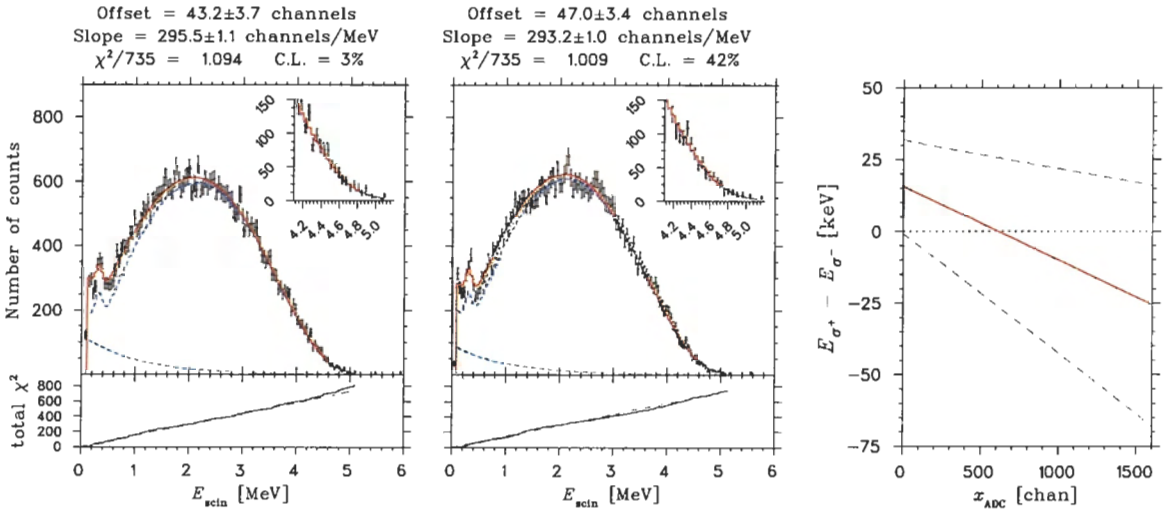

FIGURE 4.3: Sample calibration of the β-telescope using σ^+ (left) and σ^- (middle) polarized data from the 1^a data set. The points are the scintillator energy spectrum with a DSSSD coincidence, and the solid line is the fitting function, consisting of the SMC simulation plus a small exponential background. The difference in the two calibrations (solid line, right plot) are consistent to within uncertainties (dashed lines, which include the correlation between the slope and offset).

4.3.2 Phoswich Detectors

Before we can calibrate the phoswich detectors, we must first understand the E vs. ΔE 2D spectrum in order to pick out good β events. Figure 4.4 shows this 2D spectrum for one of the 3^+ runs; this later data set was chosen because during the $3\frac{1}{2}$ week break we lowered the threshold on the discriminator to be able to view the γ background (we kept a separate discriminator at a high threshold to continue to be able to effectively veto these events). The region labeled 'γ background' in the Figure was confirmed to be properly identified off-line using strong γ sources (^{137}Cs and ^{60}Co). The line of events at low CaF_2(Eu) energy (channel $\sim$ 20) correspond to events where only the plastic part of the phoswich fired and no energy was deposited in the CaF_2(Eu). It is the plastic's fast pulse which we use to trigger the data acquisition, so the corresponding line at $x_{\text{plastic}} \approx$ channel 0 for only CaF_2(Eu) events is barely visible. Above these 'ΔE only' events and, to a lesser extent, the island to the right are events where the LED pulser, used to monitor the gain of the β detectors, was not properly

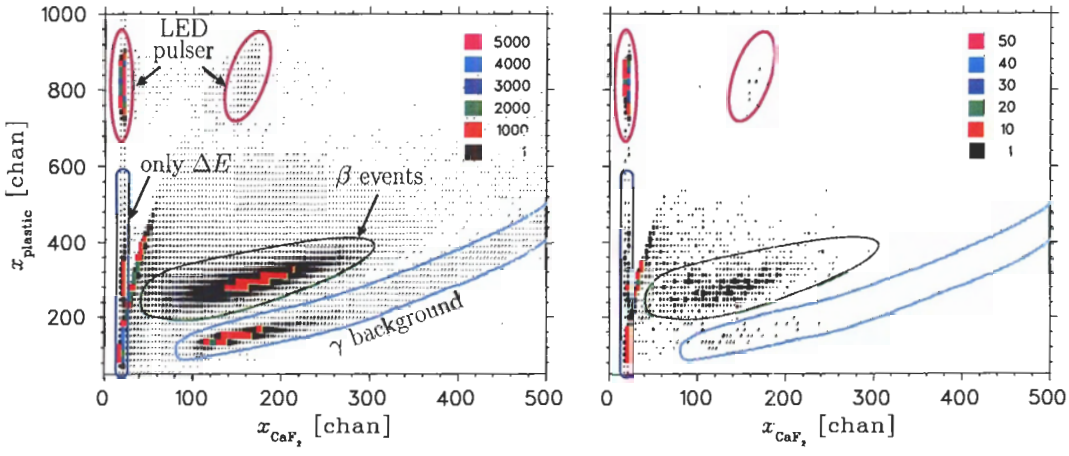

FIGURE 4.4: Phoswich singles (left) and Ar^+-coincident (right) E vs. ΔE spectra with major features labeled (see text). A recoil is defined here as an event where all four resistive anodes fired and and by cut in TOF to select ions.

flagged as a pulser in the DAQ; however, it is well-contained and separated in the 2D and so does not contaminate the rest of the spectrum.

One can clearly see the β events dominating the rest of this spectrum. The ΔE reading increases with the CaF_2(Eu) channel number not because of energy lost in the ΔE (which would have it decrease as the E reading increases), but because both signals are read out by the same PMT: the larger E signal adds to the ΔE pulse-height, even with a short gate. The β events are clearly separated from the other structures seen in this spectrum, allowing us to make a clean tag for β events by defining a region around this blob, as indicated in the Figure.

The plot on the right of Fig. 4.4 shows the same E vs. ΔE plot as the singles to the left, but this time only phoswich events in coincidence with the MCP detector are plotted. A TOF cut of $200 - 1000$ ns is made which picks coincidences with Ar ions, reducing γ backgrounds and other events not originating from decays from the trap. In this case, aside from the same line of events where the CaF_2(Eu) didn't fire, virtually all events are β events, as one would expect given the recoil coincidence condition. The distribution of events within the β-band is not the same as in singles due to kinematics, but clearly this is the region in the phoswich spectrum corresponding to β events.

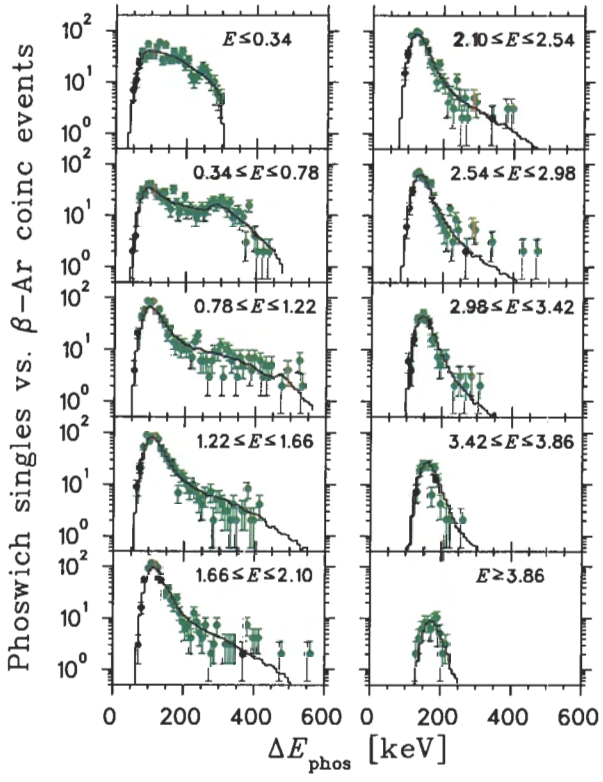

FIGURE 4.5: Phoswich ΔE singles projections and comparison to coincidences with the MCP. The points are the coincidences while the β singles are represented histograms.

A comparison of the recoil-coincident spectrum — which we know is very clean — to the singles helps us to get a handle on backgrounds in the phoswich spectra. For a given CaF_2(Eu) energy, the ΔE pulse-height corresponding to a β should be the same whether a recoil-coincidence is invoked or not because it will be given by the Landau peak of a transmitting β. We expect therefore that by projecting events onto the plastic axis for a given slice in CaF_2(Eu) pulse-height, that the ΔE spectra for singles and recoil coincidences will be the same up to an overall normalization; the degree to which this is true over all CaF_2(Eu) energies can be used to look for backgrounds in the phoswich 2D spectra. Such a comparison of the projections are shown in Fig. 4.5 for ≈ 0.44 MeV thick bands in CaF_2(Eu) up to about 4 MeV which is the largest β energy kinematics allows for a phoswich–MCP coincidence. At low energies, the projections are dominated by the 'ΔE only' events but as one gets out to $\gtrsim 1$ MeV, a clear Landau peak is seen. Agreement between the singles (histogram) and coincidences (points) is quite reasonable to within the poor statistics of the coincident events (a little less than one in a thousand of the singles). This indicates that the background levels in the β part of the spectrum are small and that the phoswich detectors therefore provide a good β tag.

Now that we understand the phoswich 2D spectrum, we can cut away non-β events and make a projection onto the CaF_2(Eu) axis to fit the β spectrum to an SMC simulation. Such a fit is shown in Fig. 4.6 where again the points are data and the solid line is the fitting function consisting of the MC and exponential background (dashed lines). The low-energy backgrounds in this detector are larger, and this time we do not have a 511 Compton edge to clamp down the calibration; just the end-point. The correlation between the offset and slope are therefore 100%, and we have much more freedom in varying the two to attain a good fit (*c.f.* discussion surrounding Fig. 4.3). As we will see, however, the E_β dependence on extracting physics results is weak, and (at least for this thesis) we are mostly interested in tagging good β events, so this rough calibration suffices. One should not, however, take the uncertainties seen in the Figure too literally, because they are purely statistical and a proper calibration would have to include systematics which would surely dominate.

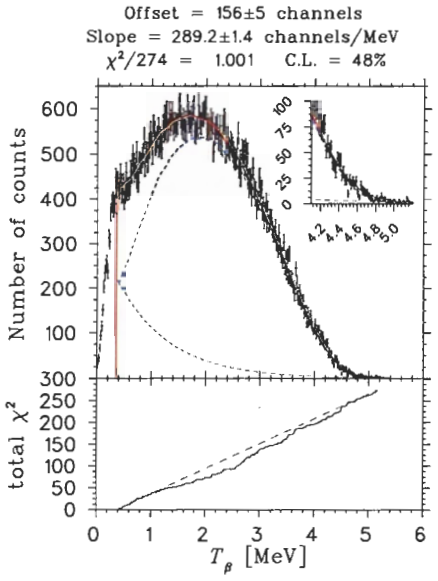

FIGURE 4.6: Sample calibration of the phoswich 'A' detector. The points are the $CaF_2(Eu)$ energy spectrum with a plastic ΔE coincidence, and the line is the fitting function consisting of a SMC simulation plus an exponential background.

4.4 Recoil Detection

4.4.1 TOF and Electric Field

The timing between the microchannel plate and either a β detector or the photoionization laser provides us with a lot of information. In both cases, the uniform electric field plays an important role because it separates different charge states, enhances collection efficiency of the charged recoils and defines, in a large part, the TOF of the event (see Eqs. 4.1).

Photoions

Let us first consider events where the MCP event is correlated with a pulse of the photoionization laser. In this case, the once neutral ^{37}K loses the valence electron essentially at rest, acquiring a charge of $q = +1$; the electric field then sweeps this ion onto the microchannel plate. These events provide a direct image of the trap/cloud in all three dimensions because, in the limit of zero cloud temperature, these ions are

created with zero energy. The $\hat{x}$ and $\hat{y}$ position of the hit in the MCP are therefore given by the corresponding initial position when the atom was photoionized. Similarly (see Eqs. 4.1), given the electric field strength, the $\hat{z}$ position can be deduced from the TOF. In practice, due to the high repetition rate of the 355 nm laser and the low probability of photoionization, we do not have the laser pulse start events; if we did, our DAQ system would be overwhelmingly swamped with useless events. Instead, the MCP is the event trigger and starts the TOF for these events, and we delay the input of the laser pulse into channel 7 of our multi-hit TDC by about a microsecond using $\approx$ 310 m of delay cables. In the TOF spectrum, an example of which is shown in Fig. 4.7, this delay is manifest as a peak at $\approx$ 1040 channels since the TDC calibration is 1 channel/ns with an arbitrary offset. The start of these events is scattered light from the 355 nm laser which has fired the MCP directly and the stop is the delayed trigger from the laser, so that the peak centroid gives us an accurate measure of laser trigger's delay, and the width of $\approx$ 2.5 ns is inherent resolution of the laser–MCP timing. The other broader peak at about channel 280 are events where a photoion started the TDC, and again the delayed trigger from the laser stopped it. The TOF of the photoion is therefore given by the time difference between the two peaks as indicated in the figure; the transit time of the photoion delays the start of the TDC, and so the stop from the laser is less than when the 1040 ns delay. Given the electric field strength (see below) and using Eq. (4.1), the centroid and width of this TOF distribution determine the $\hat{z}$ cloud position and size:

$$L = \frac{eU}{2M}\Delta t^2 \qquad \text{and} \qquad \sigma_L = \frac{eU\,\Delta t}{M}\sigma_{\Delta t} \tag{4.2}$$

As a concrete example, let us consider the spectrum of Fig. 4.7. The difference of the two Gaussian fits gave a TOF of Δt = 752.61(22) ns and a width of $\sigma_{\Delta t}$ = 13.63(18) ns. Using our measured field strength of U = −810(10) V/cm (see below), we calculate the cloud–MCP distance to be 5.99(7) cm; relative to chamber centre, which is 6.125 cm from the MCP, this corresponds to a cloud offset of $z_\circ$ = −0.14(7) cm. The width of the cloud in $\hat{z}$ is similarly found to be 0.217(4) cm. Note that though the Gaussian fit is reasonable, the actual distribution is slightly asymmetric which indicates the cloud size is not exactly Gaussian. The $\hat{x}$ and $\hat{y}$ dis-

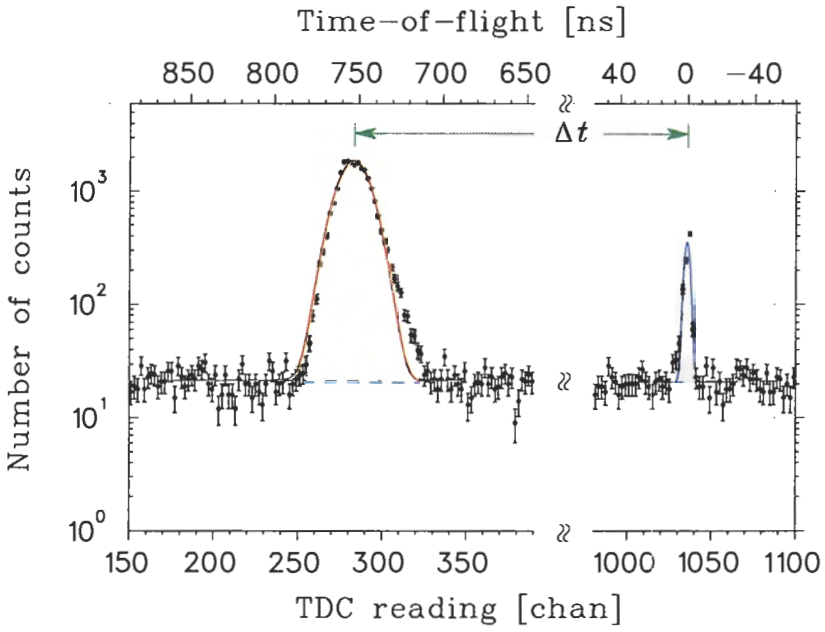

FIGURE 4.7: TOF spectrum of photoionized atoms. The peak centered on zero TOF are events where the 355 nm laser fired the MCP directly, while the peak at about 750 ns are from photoionized ^{37}K.

tributions of the cloud are given by direct fits of position of the hits in the MCP as mentioned earlier. Characterization of the trap/cloud in this manner will be discussed in greater detail in §4.6.

β decays

All three β detectors provide event triggers, so in the case where a recoil event is in coincidence with a β, the TOF spectrum is not reversed as it was for the photoion events; the βs are essentially prompt while the recoil takes > 350 ns to reach the MCP, so the β trigger starts the TDC and the recoil hit in the MCP stops it. The offset in the TOF spectrum is determined by the so-called 'prompt' peak, which are events where a photon or β fired the MCP directly; the start of the event will differ from the stop by the < 1 ns transit time of these particles, resulting in a sharp peak at short TOF. Figure 4.8 shows a typical TOF spectrum for the β−Ar coincidences — including this prompt peak — for the β-telescope (left) and one of the phoswich

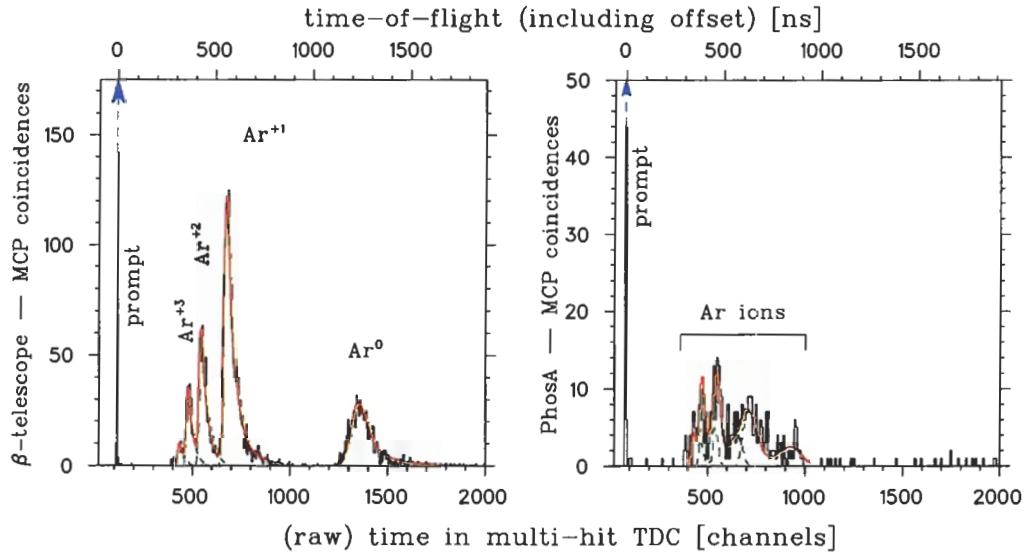

FIGURE 4.8: Typical time-of-flight spectra of the recoils with an event in the β-telescope (left) and one of the phoswich detectors (right). The β detectors start the multi-hit TDC and the MCP is the stop. The prompt peaks at $\approx$ channel 100 in both cases define the TOF offset, and the other peaks correspond to different charge states of the ions separated by the electric field.

detectors (right). The data (points) are compared to an SMC simulation (solid line); the dashed lines show the components of the simulation of the different charge states. The delays of both of these β detectors results in offsets of about 100 ns as seen by the non-zero timing of the prompt peak; this TOF offset is accounted for and subtracted in the top scale.

Let us first look at coincidences with β-telescope, which is in the back-to-back geometry (right plot of Fig. 4.8). In this case, we see the recoils at times-of-flight above $\approx$ 400 ns. The neutrals are unaffected by the electric field, while the $^{37}Ar^{+1,+2,...}$ ions are accelerated to shorter TOF. The electric field not only separates the different charge states in TOF, but also accelerates the ions to velocities ($>$ 4.8 keV) where we have measured the MCP efficiency to be flat as a function of energy [9]. The efficiency for neutrals, on the other hand, has a significant energy dependence as we noted and estimated in [13]. Throughout this thesis, the ions are used for physics results, and they are chosen based on their TOF. Specifically, the Ar^{+1} ions are taken to be those with a β-telescope–MCP TDC reading between channels 640–1100, the Ar^{+2}s between

525–639, and the Ar^{+3}s between 470–524. Higher charge states are barely resolved and represent but a tiny fraction of all $\beta-$Ar coincidences, and so are not used.

Comparisons of our simulations to the TOF spectrum for the β-telescope coincidences with the recoil were used to estimate the electric field strength. From the ^{38m}K experiment [9] and since we did not change the electrostatic hoop system in any way,* we expect that the field strength ($U = -807.7 \pm 0.2$ V/cm) and limits on the non-uniformity (< 1 V/cm^2) will carry over to the ^{37}K experiment. Fits of the leading edges of the $Ar^{+1,+2,+3}$ TOF spectrum to SMC simulations were done with field strengths of $U = -830, -826, \ldots, -790$ V/cm and a χ^2 map performed. The fits are shown in left panel of Fig. 4.9 for the 1^a and 1^b data sets where the data (points) are compared to the best field (blue solid line) as well as ± 4 V/cm (red dashed line). The solid green line shows the best field results over times which are not included in the fit, and can be seen to reproduce well the entire TOF spectrum (including the Ar^{+4} data, which has too few counts to add meaningfully to the fit of the electric field strength). With the exception of the σ^- polarized case in the 1^b data set, the χ^2 of the fit summed over all three charge states indicates good fits with $\chi^2/\nu < 1.2$. The χ^2 map of the six fits ($\sigma^\pm$ for each charge state separately) is shown in the right panel of Fig. 4.9. The filled circles are the points from the σ^+ polarization, and open from σ^-. The steepness of the χ^2 is of course greatest for the Ar^{+1} charge state (red) because it has more counts than the Ar^{+2} (green) and Ar^{+3} (blue) charge states. The solid curve with no points represents the sum of all six χ^2 maps (divided by two for ease of comparison); it is the location of this minimum which is quoted in the top of the two graphs of the χ^2 maps.

It is clear that there is some discrepancy between the minima between the two polarization states, most easily seen by the Ar^{+1} χ^2 functions. The minima of the individual χ^2 maps can differ from the average by ± 10 V/cm, which is much larger than the ± 1 V/cm (statistical) uncertainty quoted in the plots. As we will see in §5.2.4, our measurement of the neutrino asymmetry is only very weakly dependent on the magnitude of the electric field strength, and so a more detailed analysis to quantitatively understand the observed discrepancies was not pursued. Qualitatively,

*Admittedly, the addition of the dielectric mirrors may have a small effect on the field uniformity.

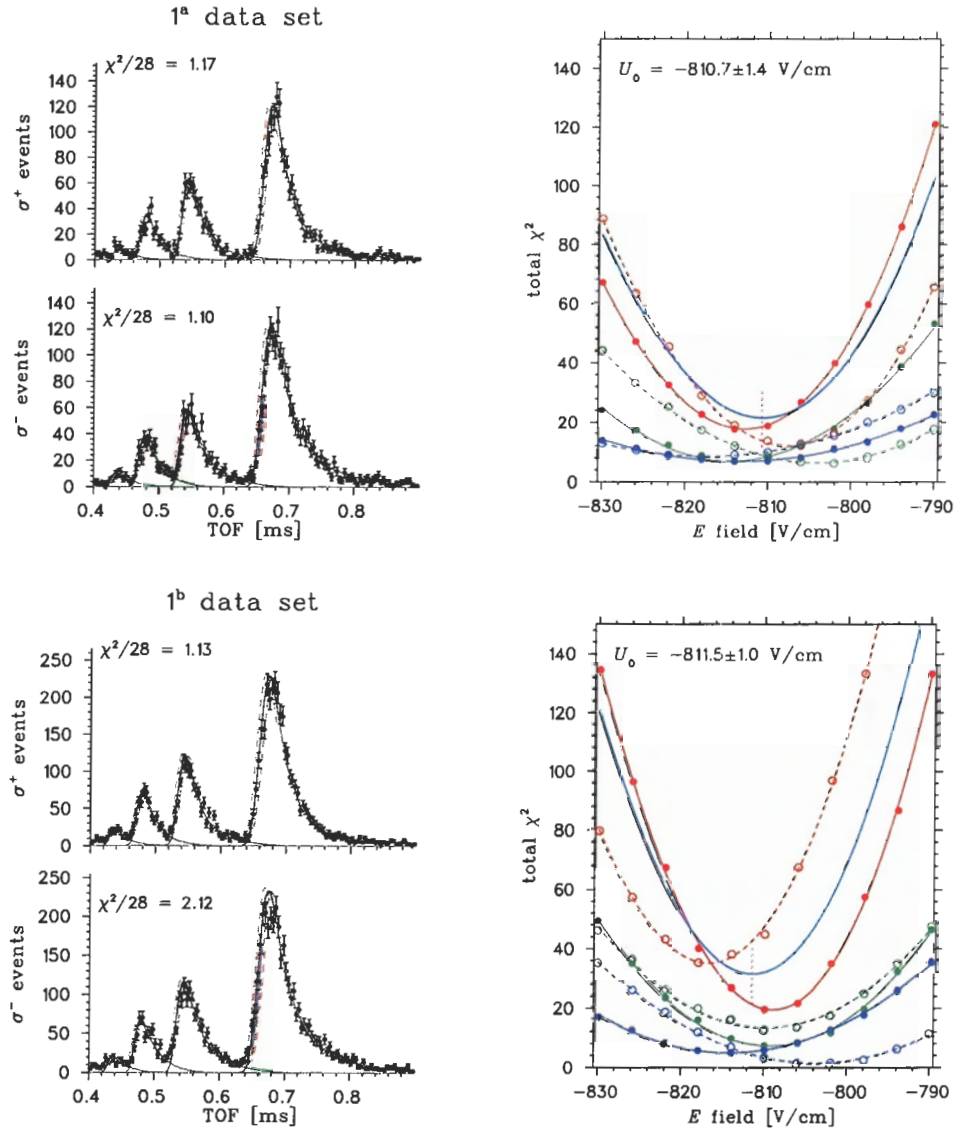

FIGURE 4.9: Fits of $Ar^{+1,+2,+3}$ TDC spectrum to deduce the electric field strength (see text). On the left we plot the TOF data (points) for β-Ar coincidences for $\sigma^{\pm}$ events for the $1^{a,b}$ data sets. Overlaid is a simulation with the best fit field strength for the $+1, 2, 3$ charge states. On the right we show a χ^2 map of these fits as the field strength is varied. One can see reasonable, but not perfect, agreement between the minima of the charge states. All minima of all data sets (including $3^{\pm}$ and on) is spanned if we take the field strength to be $U = -810 \pm 10$ V/cm.

we do *not* believe that the electric field is changing between polarization states — it is very difficult to imagine how it possibly *could* — but rather a symptom of making an absolute measurement with the damaged MCP. The two polarization states have different distributions on the plate and it seems likely that this apparent field shifting is a consequence of the position efficiency of the MCP. Once again, a detailed investigation into the electric field was not pursued and instead we took the variation of all of the individual minima (including similar fits to the $3^{\pm} - 6^{\pm}$ data sets) and assigned an uncertainty which encompassed all fit values. The result is an average field strength of $U = -810 \pm 10$ V/cm.

If we now look at the TOF of the phoswich coincidences (left plot of Fig. 4.8), we of course see a very different structure because the kinematics is drastically changed; instead of a back-to-back geometry, the phoswich detectors are at 90° with respect to the MCP. βs that fire the phoswich tend to give a momentum kick to the recoil in the opposite direction towards the opposing phoswich. By virtue of the electric field, the slower of these recoiling ions may get accelerated onto the MCP before their transverse momentum moves them outside the active area of the MCP. Neutral recoils, on the other hand, are extremely unlikely to hit the MCP, and indeed the TOF spectrum of Fig. 4.8 shows no indication of neutral recoils above the small background seen. The ions, though they have a rather different structure (which, even with the poor statistics, *seems* to be reproduced by the SMC simulations), do arrive at about the same TOF as in the back-to-back geometry, as one would expect given that the electric field accelerates them the same as it does for coincidences with the β-telescope. The different charge states are not resolved as well in TOF in this case due to the change in kinematics; however, the structure remains approximately the same, with most events between channels $600 - 1000$ being Ar^{+1}'s, and those between $500 - 600$ predominantly Ar^{+2}'s, etc.

4.4.2 MCP $\hat{x} - \hat{y}$ Position Information

Due to many off-line tests using photoions, a great many ions were accelerated and detected on the MCP within two small spots. This resulted in a degradation in the

efficiency of the plates to generate secondary electrons, which has to be modeled and accounted for. Below we discuss the position calibration and how the efficiency was calculated.

Position Calibration

As part of the ^{38m}K experiments, the position calibration of the recoil detector has been well-characterized. Off-line calibrations using an α source and a mask provided a good understanding of the absolute position spectrum as described in Ref. [11]. The 2.4 cm diameter collimator in front of the MCP defined the active area, and the initial α source calibration was adjusted so that the observed ^{38m}K online events reproduced the circular collimator.

The calibration deduced from the ^{38m}K experiments was carried over when analyzing the ^{37}K data. The gains of the four resistive anodes were adjusted according to the change in pulse-height of the pulser ($\lesssim 1\%$ variations), but otherwise the same calibration was used. As one can see from Fig. 4.11, the raw MCP position spectra using this calibration, the circular collimator is well-reproduced, though one can clearly see inefficient regions which will be discussed in the next section. To estimate how well the collimator was reproduced, we divided the MCP position spectra into bins of $\Delta\phi = 30$ and looked the radius at which the online data went to zero. We fit for each of these bins the half-height and plotted the results as a function of angle in Figure 4.10 for the 1^b and 6^+ data sets. The variation of $R_{\max}$ found this way is consistent over all of the data sets and is found to be $^{+0.11}_{-0.20}$ mm. Since the deviations seen in the mask data were strongest at the edges, we assume that the deviations at smaller radii are below this variation and that our uncertainty in the position of the MCP is ± 0.1 mm.

As we will see later when fitting the $\hat{x}$ asymmetry, a error in the scale factor of the $\hat{x}$ MCP position will translate into a corresponding uncertainty in B_ν. Without the collimator to define the active area, this uncertainty would have been extremely difficult to estimate; as it is, we have no concrete data regarding the inner part of the MCP position calibration but based on the mask data, we can be confident that it is

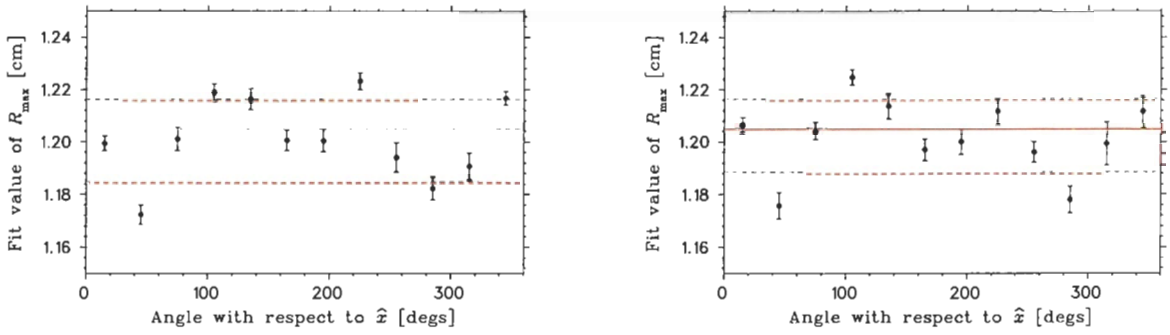

FIGURE 4.10: Calculated $R_{\max}$ of the MCP as a function of the angle with respect to the polarization axis.

known at least as well as at the edges. In future experiments, we will want an online calibration of the MCP position to better define the position calibration. This can be done by installing a permanent mask with a large open area as discussed in §6.1.

Position efficiency

In order to determine the MCP position efficiency, we use the unpolarized data of β-telescope–MCP coincidences. The basic idea is to first find an area in the 2D plot of scintillator energy vs. TOF which result in a flat position distribution using MC simulations (to account for kinematic and focusing effects), and to then compare the observed and expected number of counts; the ratio of the two as a function of MCP position is then taken to be the efficiency. As with the absolute position calibration, the physics results obtained in this thesis are only weakly dependent on this efficiency by virtue of the fact that we are taking asymmetries. The efficiency is common to both polarization states and so to first order, systematics arising from determination of the efficiency cancels. For absolute position measurements, however, such a variation in efficiency as seen in Fig. 4.11 would have a very large effect, and it is unlikely that the efficiency could be adequately accounted for*.

Figure 4.12(a) plots the β-telescope–Ar coincidence data as a 2D plot of the time-

*It should be noted that the damaged MCP plates were replaced before an experiment on ^{80}Rb was done, and the efficiency is now flat. Therefore, a future ^{37}K experiment will not have such drastic variations in its position efficiency.

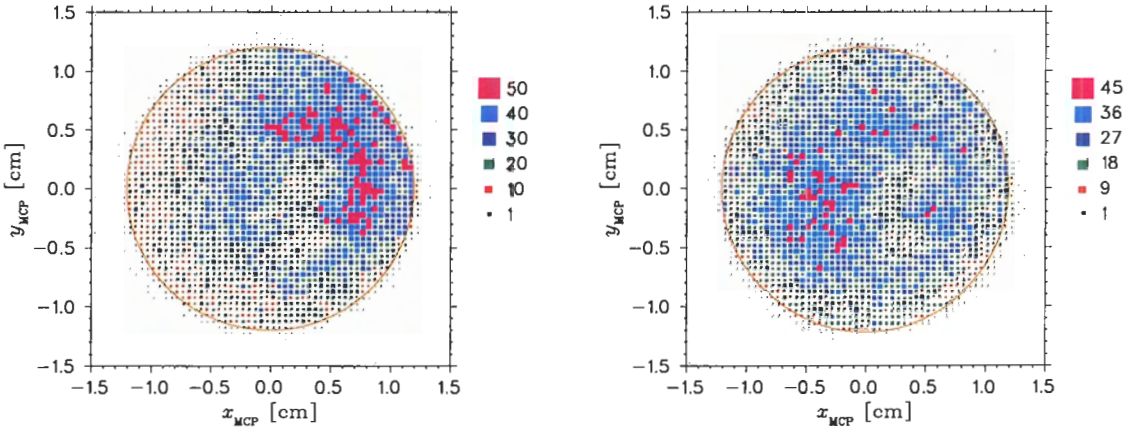

FIGURE 4.11: MCP position spectra for β-telescope–Ar coincidences. The data is taken from the 1^b (left) and 6^+ (right) data sets; the position distributions differ because of their cloud positions: $(x_\circ, y_\circ) = (+2.7, +0.1)$ and $(-1.1, +0.2)$ mm respectively. In both cases, the position calibration reproduces the fixed 24 mm wide diameter circular collimator. One can also see, independent of the data set, that the damaged plates have two particularly inefficient areas at $x_{\rm MCP} \approx +3$ mm and $y_{\rm MCP} \approx (0, -4)$ mm.

of-flight of the recoil ions versus the β-telescope's scintillator energy reading. Also depicted on this coincidence spectrum are the cuts used to pick events which result in an approximately flat spatial distributions on the MCP. As shown by the box at longer TOF, we choose events with TOF between channels 625 and 720 and with a scintillator energy between 0.85–2.4 MeV for the Ar^{+1} coincidences. Referring to the upper-left plot of Fig. 4.12(b), which shows an SMC simulation* of the position of these events (2D and both $\hat{x}$ and $\hat{y}$ projections), we see that the distribution is roughly flat. The active area of the MCP was broken up into 479 pixels of 1×1 mm^2 area as shown by the grid overlaying the 2D position spectrum. The total number of counts in a pixel, normalized to the maximum, is shown as a function of its radial coordinate on the MCP in the bottom plot of Fig. 4.12(b). Using the aforementioned cuts and assuming a uniform position efficiency, one can see that the spatial distribution of Ar^{+1}s is expected to be flat to $\lesssim 20\%$ for $r \lesssim 12$ mm. The sharp decline at radii above 12 mm arises from the fact that the active area only covers part of a pixel for

*These simulations are a weighted sum of all of the data sets, and include the offsets of the cloud positions.

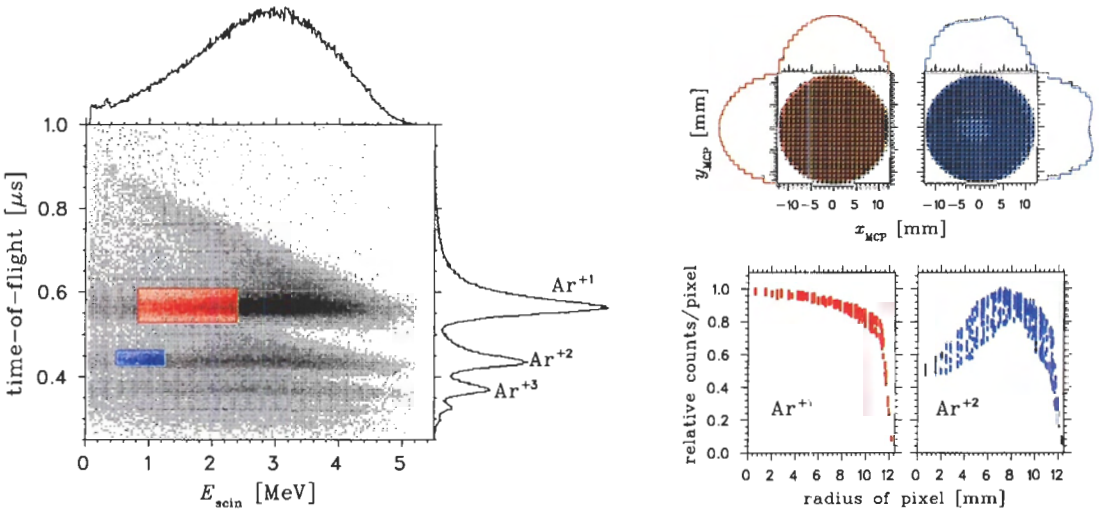

(a) E_{scin} and TOF cuts on data and MC (b) Simulation of spatial distributions

FIGURE 4.12: E_{scin} and TOF cuts used to generate flat spatial distributions on the MCP. On the left is a plot of unpolarized $\beta-$Ar ion coincidences and the cuts imposed. On the right is a simulation of the expected spatial distributions assuming perfect efficiency for recoil detection.

these points.

For the Ar^{+2}s, it was not possible to find a region in the E_β vs. TOF spectrum which resulted in as flat a distribution (and still had reasonable statistics). In this case, we took events with TOF between $540-575$ and scintillator energies of $0.5-1.25$ MeV (again, outlined by the box in Fig. 4.12(a)). The simulations with these cuts (top right plot in Fig. 4.12(b)) clearly show that this distribution is not flat, but has a dip in the centre of the MCP. Again, the number of counts for each pixel is shown in the lower plot; here, the variations are as large as 50%. Clearly, and especially when using the Ar^{+2}s, the simulations are essential to include these spatial variations due to kinematics, focusing by the electric field and the cloud position before one uses this data to extract a position efficiency.

The MCP active area was divided up by the same 479 pixel grid and the unpolarized events of Fig. 4.12(a) we binned accordingly. The resulting 2D MCP position spectra for the two charge states are shown in Fig. 4.13(a). The $\hat{x}$ and $\hat{y}$ projections of both are also plotted in the Figure and are normalized to the data such that both

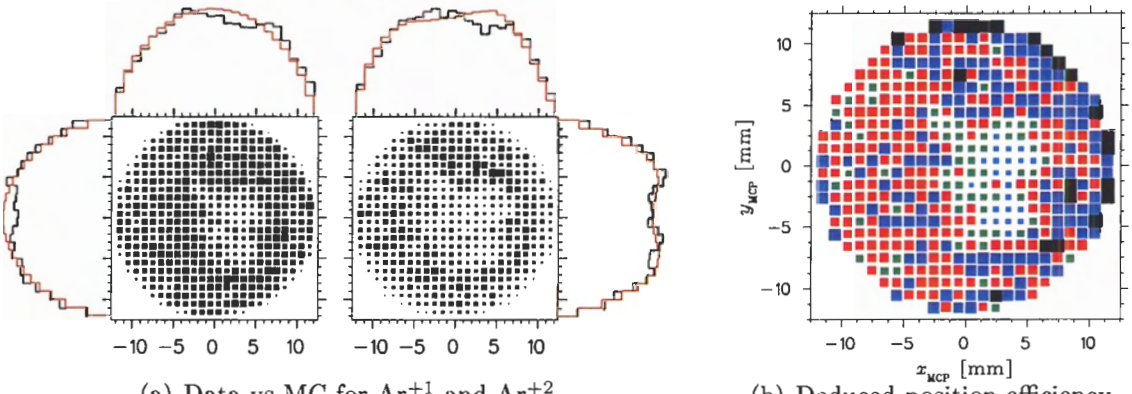

(a) Data vs MC for Ar^{+1} and Ar^{+2} (b) Deduced position efficiency

FIGURE 4.13: MCP position efficiency using a subset of the $\beta-Ar^{+1,+2}$ coincidences. A comparison of the position spectra for the data to a simulation assuming perfect efficiency is shown on the left. The MCP efficiency, plotted on the right, is taken to be the ratio of the observed to expected counts.

have unit area. From the normalized spatial distributions, we calculated the MCP position efficiency to be:

$$\epsilon_{\mathrm{MCP}}(p_i) = \frac{N_{\mathrm{obs}}(p_i)}{N_{\mathrm{sim}}(p_i)} \tag{4.3}$$

where $p_i = (x_i, y_i)$ is the pixel number corresponding to the 479 grid points of the MCP position. This efficiency was separately calculated for each charge state for the 1^{st} (1^a and 1^b) and 2^{nd} ($3^{\pm} - 6^{\pm}$) data sets, giving four results. As a measure of the difference between the efficiencies from the two charge states within a group of runs, a "reduced χ^2" was defined by:

$$\chi^2 = \sum_{\mathrm{pixels}} \frac{\left|\epsilon(\mathrm{Ar}^{+1}) - \epsilon(\mathrm{Ar}^{+2})\right|^2}{\sigma^2_{\mathrm{Ar}^{+1}} + \sigma^2_{\mathrm{Ar}^{+2}}} \tag{4.4}$$

The reduced χ^2 of this comparison was 1.015 when looking at only the 1^a and 1^b data sets; for the later data sets (which contains much more data), the χ^2 was higher at 1.248. These results indicate reasonable, but not perfect, agreement between the two charge states. The uncertainties used in this χ^2 are purely statistical, and don't reflect serious systematics due to, e.g. the cuts used to generate the position spectra (particularly with the Ar^{+2}'s), the pulse-height differences, uncertainties in the cloud

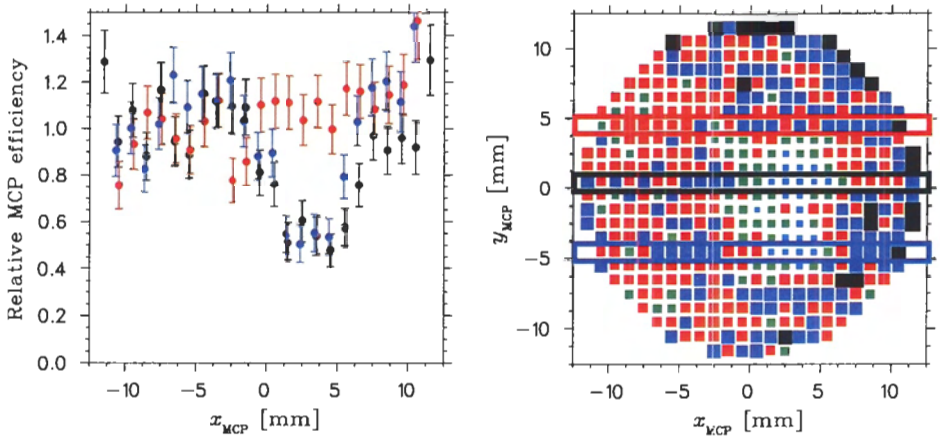

FIGURE 4.14: 1D slices of the MCP efficiency for $y_{\mathrm{MCP}} = -4.5, 0.5$ and $+4.5$ cm (left). These slices are overlaid on a copy of the 2D of Fig. 4.13(b) (right).

position, etc. For example, the corresponding χ^2 using a high-energy scintillator threshold of 2500 keV in the Ar^{+2}s for the 1st data sets raises the reduced χ^2 to 1.555.

A similar χ^2 was defined to compare the efficiencies deduced from the two groups of runs. After averaging the charge states for both the 1st and 2nd data sets, this comparison gave a reduced χ^2 of 1.047, which indicates good agreement even though the cloud positions are considerably different (see, for example, Table 4.3).

The final efficiency averaged over all charge states and all the data is shown graphically as a 2D in Fig. 4.13(b). Figure 4.14 shows the results as a 1D for a few slices in $\hat{y}_{\mathrm{MCP}}$. It can be seen to reproduce the two major inefficient areas noted earlier (as low as 50% efficiency), with a more or less uniform efficiency elsewhere. The pixels near the edge, especially in the upper-right corner, show an enhanced efficiency; this is not thought to be real, but is due to the fact that there are fewer events at the edges with which to deduce an efficiency, and furthermore the pixels at the edge are not fully filled and are therefore very sensitive to the position calibration of the MCP. So though the efficiency deduced this way produces the dominant inefficiencies, it should be considered rough at best, particularly because nothing has been mentioned regarding the pulse-heights in the resistive anode. For the analysis outlined above, the minimum (hardware) threshold was used in order to maximize the number of ions observed; a modest cut in the resistive anode pulse-height would greatly accentuate

the efficiency variations. This fact makes using the neutral recoils impossible, because their pulse-heights are already much lower than for the ions. Previously, for the ^{38m}K experiments, we were able to use the pulse-height information to reduce backgrounds in the MCP from γs and βs, but again this is not possible given the damaged plates. As noted earlier, we have since replaced the MCP and a uniform efficiency has once again been seen with good pulse-heights in the resistive anode (which proves that only the plates were damaged, and not the resistive anode itself). Therefore, the next time the ^{37}K experiment is performed, the non-uniform efficiency will not be so dramatic and we will be able to use the pulse-height information.

4.5 Lifetime measurements

As mentioned at the beginning of this chapter, the number of atoms in the 2nd trap are replenished every 700 ms when we transfer atoms from the first trap. Though this is less than the 1.2 sec half-life of ^{37}K, we can make rough estimates of the trap losses and β backgrounds based on the observed lifetime from activity in the detectors.

With each transfer, a scalar clock running at 100 MHz is reset. This gives each event a timestamp corresponding to the time after the 2nd trap had been replenished with new atoms. By generating lifetime spectra — the number of β and $\beta-$Ar coincident events as a function of this push-time — we can fit the decay curve to estimate* losses and backgrounds.

4.5.1 Trap losses

As seen from the TOF spectra, the $\beta-$Ar coincidence spectrum has a very low background, and so a deviation from the literature value of the lifetime of ^{37}K must be predominantly due to trap losses. These losses may arise, for example, from incomplete re-trapping of atoms after the optical pumping or from a poor vacuum. We therefore fit the sum of all $\beta-$Ar coincident lifetime spectra (dominated by the β-

*These estimates will not be very precise because we can only fit less than 60% of a half-life; for precise lifetime measurements, one needs to measure over many half-lives.

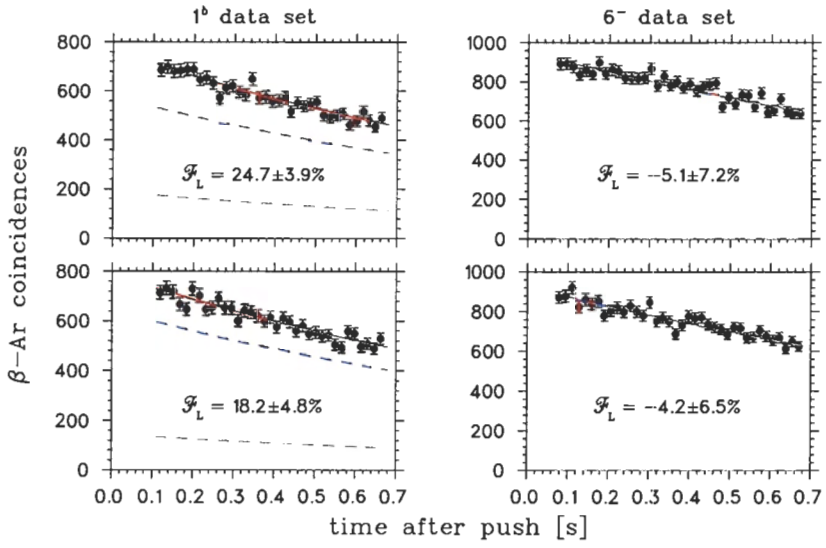

FIGURE 4.15: Recoil coincidences as a function of time after the $1^{st} \rightarrow 2^{nd}$ MOT transfer used to deduce trap losses for the 1^b (left) and 6^- (right) data sets for σ^+ (top) and σ^- (bottom) polarizations. The points are the sum of all $\beta-$Ar coincidences, including both polarized and unpolarized times within the MOT/OP cycle. The solid line is a fit to Eq. (4.5) and the dashed lines are a breakup of the decay and loss components.

telescope since the number of recoil coincidences with the phoswiches are relatively small) to a function of the form:

$$N_{\beta-\mathrm{Ar}}(t) = N_\circ \exp\Big((t_\circ - t)\Gamma\Big) \tag{4.5}$$

where the total decay rate, $\Gamma \equiv \Gamma_\mathrm{D} + \Gamma_\mathrm{L}$, is broken up into two decay constants: Γ_D which describes the radioactive decay rate, and Γ_L which is an effective decay constant accounting for trap loss mechanisms. The value of Γ_D is fixed at $\ln 2/1.226\ \mathrm{s}^{-1}$ from the known lifetime of ^{37}K [100]. Thus the only free parameters of the fit are $N_\circ$ and Γ_L. Once we fit a value for Γ_L, the fraction of atoms lost from the trap before they decay is given by:

$$\mathcal{F}_\mathrm{L} = \frac{\Gamma_\mathrm{L}}{\Gamma_\mathrm{D} + \Gamma_\mathrm{L}} \tag{4.6}$$

A fit of the $\beta-$Ar coincidence lifetime spectra for the 1^b data set is shown in the left panel of Fig. 4.15. The timing information was only introduced into the nuclear DAQ after the 1^a data set, so we do not have lifetime spectra for this group of runs.

We are therefore not able to obtain quantitative estimates of losses and backgrounds for these runs, however we can extend general trends seen in the 1^b data set to 1^a since both use the same optical pumping scheme. As a comparison to a data set where the cloud was optically pumped using the Helmholtz coils to generate the 2 G holding field instead of the trim coils, lifetime fits are also shown for the 6^- data set. As one can see, the trap losses in the 1^b data set is considerable at the 20% level; though the two polarization states are in agreement to within uncertainties, it may be that σ^+ may have slightly higher losses than σ^- polarization. Typically, the later data sets (after the new polarization scheme was introduced) showed considerably smaller losses and in fact are generally consistent with zero. In the 6^- data set, the comparative example shown in Fig. 4.15, the loss can be seen to actually be negative or, said another way, there is a gain. This corresponds to a fit lifetime that is *larger* than the literature value, which may occur due to backgrounds in the $\beta-$Ar coincidences which we have assumed were negligible.

4.5.2 Backgrounds in the β detectors

Armed with a reasonable estimate of the effective trap lifetime from the previous section, we now fit each β detector's lifetime spectra in singles to estimate their backgrounds. Unlike the previous section, we fix the decay constant to be Γ, the result from the $\beta-$Ar coincidences, and fit the lifetime with a background as a free parameter. For cases when there was found to be gain instead of a loss ($\Gamma_L < 0$), we assume the longer lifetime observed in the $\beta-$Ar coincidences was due to backgrounds — which is what we hope to extract from the β singles spectrum — and therefore fix it to be zero so Γ is the radioactive decay constant, Γ_D.

If one assumes the losses are the source of the background, and furthermore that they are not time-correlated with the dominant exponential decay, then in the limit that $\Gamma_D(t - t_\circ) \ll 1$, the time-dependence of the background drops out and one is left with an exponential plus a constant background. With $T \equiv (t_{\max} - t_\circ) \sim 680$ ms the time over which the lifetime is measured, $\Gamma_D T \sim 0.4$ which is not *much* less than one. Including terms up to 2^{nd} order adds small corrections, with the result being a

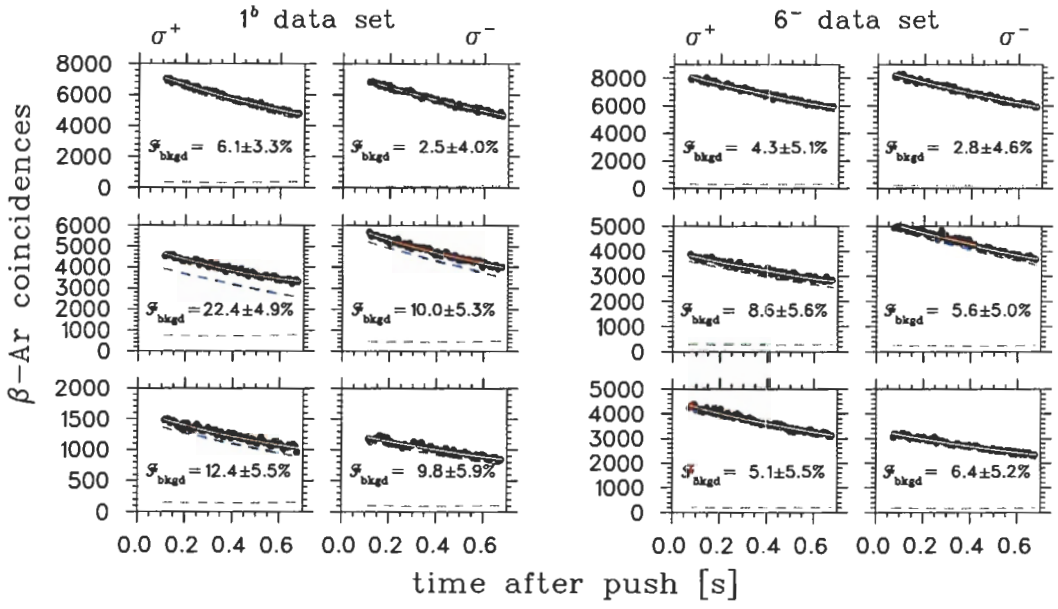

FIGURE 4.16: Backgrounds in the β detectors based on lifetime fits of the 1^a and 6^- data sets. Shown are the singles spectra and fits for the β-telescope (top), phoswich A (middle) and phoswich B (bottom).

fitting function of the form:

$$\frac{N_\beta(t)}{N_\circ'} = \exp\Big((t_\circ - t)\Gamma\Big) \; + \; b\Big[1 - \Gamma_D(t-t_\circ) + \frac{\Gamma_D(t-t_\circ)^2}{T-t_\circ}\big(1 + \tfrac{1}{2}\Gamma_D(T-t_\circ)\big)\Big] \quad (4.7)$$

In this case, the free parameters of the fits are the normalization $N_\circ'$ (as before) and the background b (instead of Γ_L).

Results for the 1^b and 6^- data sets are shown in Fig. 4.16 for each of the three β detectors. In all cases, the radioactive (exponential) decay of the fit (the higher dashed line) uses the results from Fig. 4.15, thereby accounting for the losses from the trap. The lower dashed line corresponds to the background term weighted by b in Eq. (4.7). The fraction of background events in the lifetime is calculated by comparing the integrated number of counts of these two components. The uncertainty quoted in this fraction includes, and in fact is dominated by, the uncertainty in the effective decay constant deduced by the fits to the β−Ar coincidences.

We expect that the 1^b data set will have larger β backgrounds than subsequent data sets because, from the results of the previous section, we know that more atoms

are lost from the trap before they decay. This is reflected by the results of Fig. 4.16 where again the 6^- data set is a respective example of all of the data sets using the second optical pumping scheme. The fact that the backgrounds in the σ^+ lifetimes are significantly larger than σ^- for the 1^b data set complements the hint from the $\beta-$Ar lifetime fits that the losses are larger for the σ^+ polarization in the 1^{st} data sets.

Comparison of the backgrounds in each of the β detectors also gives us an idea, at least qualitatively, as to how the atoms are lost spatially: are the losses homogeneous into 4π, or are they concentrated in certain spots? Considering the 1^b data set, we see that phoswich A has significantly larger backgrounds than the other two — at least for σ^+ polarization — which indicates more of the atoms get deposited onto the mirror in front of this detector. Referring back to Fig. 4.1(b), we see that the D_1 optical pumping light is initially directed toward and then retroreflected by this mirror. Considering that the beam is divergent, one might expect that this beam is preferentially pushing atoms towards phoswich A. However, because the heating from these photons is only 1 μK/photon and an atom typically absorbs less than a hundred photons, as well as the fact that both phoswiches have about the same backgrounds in σ^-, this is likely not (the whole) explanation.

The results of this and the previous section allow us to conclude that the 2^{nd} polarization scheme reduces the loss of atoms during the trap/optical pumping cycle. The estimates for the β backgrounds, specifically for the phoswiches, will be used when we analyze the β asymmetry in §5.1.

4.6 Cloud characterization

This section uses the photoion events to characterize the atom cloud. From these events, we can measure the cloud size and position as a function of time throughout the trap/optical pumping cycle. In addition, we will be able to estimate backgrounds during polarized times, which is crucial when we fit the vanishing of the fluorescence to deduce the cloud polarization in §4.7.

4.6.1 The fitting function

We are interested in fitting the photoion yield as a function of the optical pumping pine. We begin by breaking up the total number of events in the photoion spectrum, N_{tot}, into two parts: a signal, S and a noise, N. By definition, the two sum up to equal all events, so that $N_{\text{tot}} = S + N$. The two are obviously not independent, and so we only need one parameter to characterize the spectrum, the *integrated* signal-to-noise ratio, S/N. In terms of this, the integrated number of signal and noise events are:

$$S = N_{\text{tot}} \cdot \frac{S/N}{1 + S/N} \qquad \text{and} \qquad N = N_{\text{tot}} \cdot \frac{1}{1 + S/N}. \tag{4.8}$$

If we now assume that our signal is a Gaussian centered on position $x_\circ$ with a width of σ:

$$G(x) = \frac{\mathcal{A}}{\sqrt{2\pi}\sigma} \exp\left(-\frac{(x - x_\circ)^2}{2\sigma^2}\right), \tag{4.9}$$

we can fix the normalization such that we get the correct total number of signal events:

$$\mathcal{A} = S\,\Delta x = \frac{N_{\text{tot}}\, S/N}{1 + S/N}\Delta x, \tag{4.10}$$

where Δx is the bin size per unit of measure, either mm ($\hat{x}$, $\hat{y}$) or ns (TOF). For a background that is random with respect to the optical pumping time, the background level is simply the total number of background events divided by the number of bins:

$$b = \frac{N_{\text{tot}}}{1 + S/N} \cdot \frac{1}{n_{\text{bins}}}. \tag{4.11}$$

Thus we fit a function of the form:

$$\begin{aligned} F(x) &= G(x) + b \\ &= \frac{N_{\text{tot}}}{1 + S/N}\left[\frac{S/N\,\Delta x}{\sqrt{2\pi}\sigma} \exp\left(-\frac{(x - x_\circ)^2}{2\sigma^2}\right) + \frac{1}{n_{\text{bins}}}\right] \end{aligned} \tag{4.12}$$

where the only free parameters in the fit are the centroid, $x_\circ$, the width, σ, and the signal-to-noise, S/N. The range of the fits is large in order to reliably fit the S/N; for the $\hat{x} - \hat{y}$ position spectra, it is done over the whole of the MCP and for the TOF it is over a range of 100 ns.

The main motivation for deducing the signal-to-noise of these photoion spectra is to know what backgrounds we are admitting when generating the fluorescence spectra to fit the cloud polarization in the next section. These spectra are the total number of photoion events as a function of the optical pumping time, after events beyond 3σ of the central value have been rejected in each of $\hat{x}, \hat{y}$ and TOF. Therefore, the signal-to-noise quoted throughout this section is the integrated number of signal vs. background events only over 3σ, though the fit range is much larger. We can then use the same integrated S/N ratio to define the background in the time spectra of the photoion yield: assuming the background is constant, its level will be again be given by Eq. (4.11), where N_{tot} will be the total number of photoion events in the time spectrum and n_{bins} is its number of bins. This is very important as the background level has a very strong effect on the deduced polarization. Because we are able to fit over a wider range in TOF, the final signal-to-noise is taken to be that deduced from the TOF fits, rather than the $\hat{x} - \hat{y}$ positions which are cut off by the active area of the MCP.

4.6.2 Position and TOF cuts

Now that the fitting function has been defined, we need to sort the data — particularly during optical pumping times where we have much fewer photoion events — and try to reduce the backgrounds as much as possible by making judicious cuts which maximize the signal-to-noise. As mentioned earlier, we have an image of the trap from photoion events, and can make cuts in $\hat{x}$, $\hat{y}$ and TOF$\leftrightarrow \hat{z}$ to help pick out signal events.

To begin, we make no position cuts, requiring only that a photoion event was within the active area of the MCP, and apply a very generous cut on the TOF of photoion events. Referring back to Fig. 4.7, the initial cut used to define photoion events are ones where $700 \leq \Delta t \leq 800$ ns. This timing cut on the photoion TOF spectrum is quite generous as the centroid appears around 750 ns and has a width of $\sigma \leq 10$ ns. With these loose conditions, the data was sorted and spectra generated for the $\hat{x}$ and $\hat{y}$ positions in the MCP. We then fit Eq. (4.12) to these position spectra and obtained initial centroids $(x_\circ, y_\circ)$ and widths (σ_x, σ_y) of the photoion events on the MCP. As mentioned in §3.3.3, these positions correspond directly to the $\hat{x} - \hat{y}$

position and size of the cloud. Using these initial values, we can define an area on the MCP which corresponds to photoion events:

$$R^2 = \left(\frac{x - x_\circ}{\sigma_x}\right)^2 + \left(\frac{y - y_\circ}{\sigma_y}\right)^2. \tag{4.13}$$

The data was then re-sorted with the TOF condition being replaced by a requirement that $R \leq 3$, corresponding to a 3σ cut in position. We then would go back and fit Eq. (4.12) to this now cleaner TOF spectrum. This time we obtain a centroid $t_\circ$ and width σ_t in TOF, as well as an estimate of the signal-to-noise. These values were then used to define a tighter TOF condition: $|\text{TOF} - t_\circ| \leq 3\sigma_t$. Releasing the position condition and imposing this TOF cut, we went back and re-sorted the data to get even cleaner $\hat{x} - \hat{y}$ position spectra, which we again fit to Eq. (4.12) to obtain new transverse positions and widths. These cleaner position spectra yielded slightly different cloud centroids and smaller sizes, and of course a greater signal-to-noise. Once again, we'd re-sort the data with the position cut to generate a cleaner TOF spectrum. This process was iterated until none of the positions or widths changed. Once this was done, we obtained the average cloud size and position in all three dimensions throughout the trap/optical pumping cycle as well as the signal-to-noise of photoion events.

Figure 4.17 shows typical results of these fits for the 1^a data set as well as the effect of making the aforementioned cuts in position and TOF. Let us first consider times during which the atoms are trapped, with no position/TOF cuts imposed. This is shown as the dashed histogram and is $\div 100$ so it is on scale with the spectra during optically pumped times. The *differential* signal-to-noise during these times is very good because the MOT beams continually excite the atoms and we see many photoion events. Though difficult to see in Fig. 4.17 because of the overlaid spectra, the constant background below the main peak of these MOT photoions is negligible, with a signal-to-noise of typically 100-200. The non-Gaussian shape and large width of these MOT distributions is due to the movement of the cloud throughout the cycle (discussed in the next section). In this case, the cuts described above have very little effect due to the originally large signal-to-noise ratio.

The same spectra during optical pumping times is shown as the solid histogram.

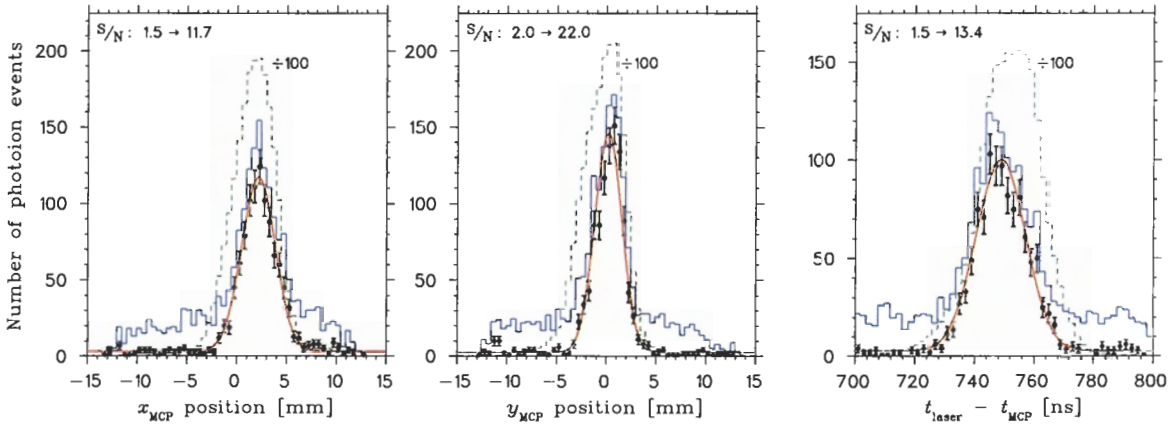

FIGURE 4.17: Photoion MCP position and TOF spectra used to deduce the cloud position and size. The solid histogram and points are the data during optically pumping times, before and after cuts have been made respectively (see text); the curve is a fit to the latter. The dashed histogram shows photoion events during trap times and because there are many more photoions with the D_2 light on, it is divided by 100 to be on scale with the other spectra.

Here we still see a large signal, but the background level has become quite appreciable: 50%–100% of the signal. After all iterations of fitting the peaks and making cuts, the final photoion spectra for the optically pumped data is shown as the points, along with the fit result (solid line). One can clearly see that the noise is greatly reduced, with essentially no signal events lost in doing so. As indicated in the top-left of the three plots, the signal-to-noise is increased by an order of magnitude after invoking the cuts described above. This drastic increase is realized because the photoion signals are well localized in space ($\hat{x}$ and $\hat{y}$ on the MCP) and in time (TOF). The initially poor signal-to-noise ratio of the raw data is due to the fact that given our laser intensity of $\approx$ 150 mW/cm^2; for the sum of all the runs in the 1^a and 1^b data sets, we only have $\approx$ 2700 identified photoion events. The background is random in (x, y, t), and the level is reasonable given the 10 kHz repetition rate of the pulsed laser and the $10-20$ Hz singles rate in the MCP detector. βs emitted from untrapped atoms have a non-negligible probability of registering an event in the MCP as do low-energy γ rays. These backgrounds could not be vetoed based on the pulse-height in the MCP as we had hoped to do because of the damaged plates used in this experiment (however the pulse-heights will make an additional filter for future experiments with the plates

repaired).

4.6.3 Position as a function of time

The average cloud size and position are now determined, but we are also interested in the time-dependence of cloud parameters. By breaking up the photoion spectra according to the time within the trap/optical pumping cycle, we can image the cloud throughout this cycle. During the MOT times, when atoms are continually being excited into the P state, there are a lot of photoions, and we can generate spectra with enough statistics to provide a reliable fit every 60 μs. We have seen that during OP (optical pumping) times, however, there are much fewer ($\approx$ 100$\times$ less) and we cannot make such fine a binning; during the 1.4 ms of this part of the cycle, we found that we could only break up the data into four bins: the first 40 μs long, the second 80 μs, the last two 600 μs. This choice of binning reflects the fact that there are more photoion events at the start of the optical pumping process before it dies away as the cloud becomes highly polarized.

The cloud was imaged throughout the trap/optical pumping cycle by fits similar to the ones described in the previous subsection. The results are shown graphically for each data set in Figs. A.1 – A.10 of Appendix A. In these plots, the cycle starts at $t = 0$ with the atoms being collected and trapped, e.g. 4.22265 s in Fig. 4.2. After 2.6 ms, the MOT is turned off and the atoms are optically pumped for 1.4 ms, at which point the MOT is turned back on, returning us to $t = 0$ in these plots.

Considering for now only the cloud position as a function of the cycle time (1st and 3rd panels), one can clearly see the atom cloud moving in all directions during the trap times. As expected, because the MOT photoions are independent of the polarization state when optically pumping, the cloud positions for σ^+ and σ^- are the same. Also note that, though the absolute positions may differ, the general trends of the cloud movement are consistent between data sets which have the same $\boldsymbol{B}$-fields for optically pumping the atoms and nominal cloud positions, *i.e.* between 1^a and 1^b, and similarly between all subsequent data sets. Note the increased uncertainties and coarser binning during optical pumping times which again is due to the reduced

statistics.

During these pumping times, we cannot image the cloud as well; this is 'unfortunate' (but only in the limit that we don't care about attaining high polarization!) because it is during these polarized times that we are making our asymmetry measurements and require the cloud characteristics in order to include them in our MC simulations. Even with only four points and with relatively large uncertainties in the positions, one can see that the cloud position is not varying as erratically as compared to when the cloud is subjected to trapping forces and is being recollected. This makes sense because there are no significant forces acting on the cloud during 2.6 ms optical pumping times. The only two are: (1) gravity, which generates a downward velocity of $gt \leq 2.6$ cm/s; and (2) the optical pumping light, where an absorption of a 755 nm photon has a 1.3 cm/s effect on the atom's velocity.* Note that both of these forces are negligible compared to the typical cloud temperature of a few mK, which gives thermal velocities on the order of 100 cm/s randomly distributed in direction. Thus we expect that during the optical pumping times, the cloud moves (as it thermally expands) with a *constant* 'sail' velocity†, $\boldsymbol{v}_{\text{sail}}$, defined by the group velocity of the cloud at the moment the trapping light is turned off:

$$\boldsymbol{x}(t) = \boldsymbol{x}_\circ + \boldsymbol{v}_{\text{sail}} \cdot t. \tag{4.14}$$

Here $\boldsymbol{x}_\circ$ is the cloud position at the start of the optical pumping (or, equivalently, the end of the MOT) part of the cycle. The last four bins of the MOT positions (the last 240 μs) have been fit‡ to a straight line in order to extrapolate the initial

*Multiple absorptions from the same laser beam can add to generate a stronger effect, but counter-propagating beams and the few number of photons absorbed before becoming highly polarized both mean that the overall effect should stay on the order of a one-photon absorption.

†We are assuming no forces on the atoms during the optical pumping times. The D_2 light is fully extinguished during these times, and retroreflection of the D_1 laser beam through the system is reasonable considering the 0.01 mm thickness of the mirrors; the beam divergence may cause a slight imbalance between the primary and retro-reflected beams, however the atoms absorb $\lesssim 40$ photons during optical pumping, and so the effect will be small.

‡The uncertainties in the 1$^{\text{st}}$ and 2$^{\text{nd}}$ centroids were artificially increased by 50 and 25% respectively in order to ensure that the greatest weighting was given to the points closest to the end of the MOT cycle, though doing so had a negligible effect on the final answers.

TABLE 4.3: Results of fits to the MOT/cloud positions. Listed are the initial cloud positions, in mm, at the start of the optical pumping part of the cycle. Upper values are a result of fitting the MOT photoion spectrum just before optical pumping is initiated. Lower values are a result of fitting the OP photoions directly and are only listed if the fit χ^2/ν was less than that calculated using the MOT photoion fit results. If the MOT photoions had a $\chi^2/\nu > 1$, then the result is listed in red; otherwise (*i.e.* if the MOT photoion fit was "good" and had a $\chi^2/\nu \leq 1$) then the OP photoion fit results are listed in gold.

Data set	$x_\circ$		$y_\circ$		$z_\circ$	
	σ^+	σ^-	σ^+	σ^-	σ^+	σ^-
1^a	2.89(6)	2.83(6)	−0.58(5)	−0.55(5)	−2.36(5)	−2.29(6)
	2.59(15)	2.58(14)	−0.39(15)	−0.51(14)		−2.06(13)
1^b	2.62(6)	2.75(6)	0.09(7)	0.09(7)	−2.09(7)	−2.16(7)
		2.60(15)	0.12(16)	0.23(12)	−1.96(14)	−1.96(10)
3^+	−1.55(5)	−1.56(5)	0.13(2)	0.14(3)	−2.91(3)	−2.90(4)
	−1.91(7)	−1.95(8)	0.30(9)	0.25(7)	−2.50(15)	−2.63(7)
3^-	−1.63(5)	−1.59(5)	0.55(4)	0.49(4)	−2.84(5)	−2.90(4)
	−2.11(10)	−2.05(11)	0.52(14)	0.71(12)	−2.44(13)	−2.25(12)
4^+	−1.50(8)	−1.47(7)	0.08(6)	0.17(5)	−2.82(6)	−2.77(5)
	−1.71(23)	−2.12(16)			−2.37(19)	−2.31(25)
4^-	−1.55(4)	−1.56(6)	0.53(4)	0.57(4)	−2.83(4)	−2.78(4)
	−2.09(9)	−1.52(19)	0.88(15)	1.05(14)	−2.47(11)	−2.09(16)
5^-	−1.46(6)	−1.43(6)	0.64(8)	0.69(5)	−2.72(4)	−2.65(9)
	−1.92(19)		0.77(25)	1.01(15)	−2.12(22)	−2.39(13)
6^+	−1.15(6)	−1.14(5)	0.25(3)	0.25(4)	−2.13(3)	−2.08(3)
	−1.50(7)	−1.50(7)	0.56(9)	0.52(12)	−1.75(6)	−1.82(6)
6^-	−1.37(5)	−1.35(6)	0.81(4)	0.63(8)	−2.55(3)	−2.60(3)
	−1.76(8)	−1.56(9)	1.07(10)	1.09(10)	−1.86(10)	−2.19(8)

position at the start of the optical pumping part of the cycle. We feel confident that the D_2 MOT beams have been fully extinguished based on the lack of events in the 100 μs between 'D_2 off' and 'OP on' (recall Fig. 4.2 of §4.1.2. We started turning off the quadrupole trapping field 400 μsec before turning off the D_2, so we are sure the current to the Helmholtz coils is zero, however eddy currents could persist and bias our position measurements. As measured with a Hall probe after the online experiment, the quadrupole field was found to falls to 5% of its value in 120 ± 50 μs.

Table 4.3 lists* the results of these fits for both polarizations of all of the data sets. The results are also listed at the bottom of each plot in Figs. A.1 – A.10, and as a summary, Fig. 4.18 shows the results graphically as a function of the data set (1st and 3rd columns; filled points). The large difference between the 1st and subsequent data sets (particularly in x_o) was intentional on our part; we realized the cloud position for the earlier data sets was right about where the plates were damaged, and so we moved the cloud to where the MCP position was not as inefficient as well as to have the cloud better centred in the chamber. Aside from this large difference, the initial cloud position is seen to be rather stable throughout the experiment and furthermore that there is no obvious correlation with the sign of either the optical pumping field nor the polarization state. This is not a coincidence because we checked that the length of the trapping part of the cycle time was optimal in that it fully recollected the atoms after optical pumping (*cf.* continuity of the fluorescence spectrum in top of Fig. 4.2). If we had made the trapping time too short, the atoms would likely have shown correlations with the field/polarization states and/or had larger losses because the cloud would not have been equilibrated with the trapping forces and not fully recollected. If we had made it longer, we *may* have been able to better diagnose the origin of the sail velocity, but this would have come at the cost of a reduced duty cycle.

After optically pumping for Δt_{op} seconds, the cloud centroid will have moved:

$$\boldsymbol{x}_{\text{final}} = \boldsymbol{x}_o + \boldsymbol{v}_{\text{sail}} \Delta t_{op}. \tag{4.15}$$

*To properly interpret this table, please read the caption carefully as well as the discussion surrounding it later in this section (pg. 110).

In a manner similar to estimating $x_\circ$, we fit the first four MOT bins and extrapolated the position of the cloud to the end of the optical pumping cycle, giving us x_{final}. With the initial and final positions, we can rearrange the above equation to solve for the sail velocity. These results are listed in Table 4.4 and, like the $x_\circ$, are quoted in the figures of Appendix A. The graphical summary of Fig. 4.18 shows the x_{final} positions as open circles on the same plots as the $x_\circ$, as well as the deduced sail velocity (columns 2 and 4). The cloud velocities in the $\hat{x}$ direction are reduced after the field-switching was enabled, but the $\hat{z}$ component was increased. As with the initial positions, there does not appear to be any correlation of the sail velocity with the sign of the magnetic holding field. It would have been surprising if there was a correlation between v_{sail} and the sign of the holding field because, even though the atoms' memory of the final position is not cleared by the trapping forces like it is for the initial position, there should not be any forces during the pumping times that would add a velocity component. Additionally, we note there there is no obvious correlation with the sign of the polarization state, which is very gratifying because if there were a correlation in this case, it would also prove that we were wrong in our assumption that there are no significant forces during optical pumping.

The figures of Appendix A show two fits of the position during OP times to Eq. 4.14. One is to the four points of the optically pumped photoions directly (red line with relatively large uncertainties), and the other is an interpolation between the beginning and end of the MOT times (blue line). The latter have significantly smaller uncertainties due to the much greater statistics in the photoion spectra and, since we know the cloud must move continuously between them, provide us with a reliable measure of the initial cloud size and group movement during the optical pumping process. In the top of each plot, the reduced χ^2 of the fits are quoted. The top refers to a comparison of the interpolated MOT position and velocity to the four optical pumping centroids (no free parameters, so there are $\nu = 4$ degrees of freedom). The lower χ^2 is the result of a direct fit to the optical pumping points; this entry is absent if its χ^2 was greater than that deduced by the MOT photoions. If the MOT χ^2 was 'good,' meaning less than or equal to one, then the OP fits are shown by the orange line with a yellow band representing its fit uncertainties; even if the OP χ^2 was greater

TABLE 4.4: Results of fits to the MOT/cloud positions (continued). Listed are the sail velocities of the cloud, in cm/s, during the optical pumping part of the cycle. The convention used (format, colours, etc.) is the same as in Table 4.3.

Data set	v_x		v_y		v_z	
	σ^+	σ^-	σ^+	σ^-	σ^+	σ^-
1^a	−75(8)	−70(8)	−22(6)	−32(6)	6(5)	5(6)
	−40(37)	−81(26)	10(36)	48(23)		9(23)
1^b	−94(7)	−93(7)	−19(9)	−20(6)	21(7)	30(7)
		57(28)	16(32)	5(21)	59(31)	11(21)
3^+	−35(5)	−26(6)	−1(5)	−11(5)	−71(8)	−69(5)
	−95(25)	−69(36)	18(26)	7(26)	10(52)	24(36)
3^-	−28(7)	−24(8)	−38(10)	−25(6)	−73(6)	−65(8)
	62(26)	−103(67)	98(43)	−61(68)	−126(71)	−121(128)
4^+	−37(8)	−41(13)	−23(10)	−24(11)	−55(8)	−70(14)
	−135(70)	28(70)			48(59)	−95(74)
4^-	−24(5)	−22(6)	−20(6)	−24(6)	−52(5)	−61(6)
	−12(32)	−193(46)	−105(55)	−187(73)	53(56)	−2(62)
5^-	−28(7)	−37(7)	−4(16)	−14(7)	−60(6)	−59(8)
	−80(121)		−127(72)	−132(67)	50(109)	−56(72)
6^+	−32(5)	−34(5)	8(5)	11(5)	−56(4)	−56(4)
	−72(17)	−60(15)	9(24)	−13(31)	0(19)	18(16)
6^-	−13(5)	−20(5)	−20(4)	−6(7)	−60(4)	−54(4)
	−105(28)	−55(42)	−65(35)	−9(46)	−47(46)	−25(58)

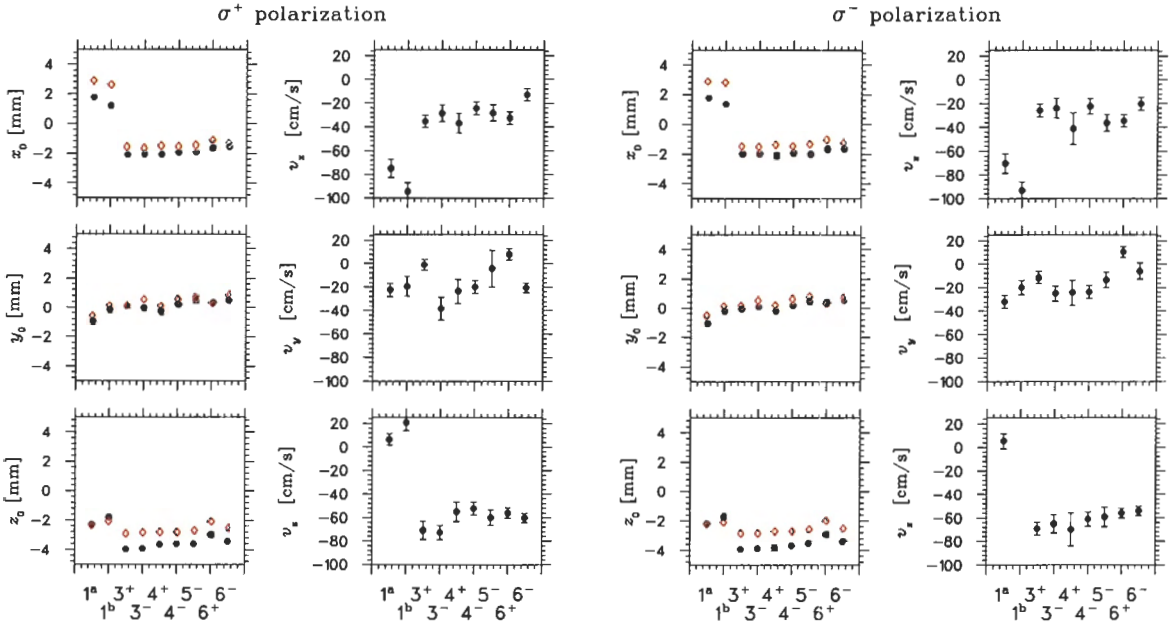

FIGURE 4.18: Graphical representation of the results ($\boldsymbol{x}_\circ$ and $\boldsymbol{v}_{\text{sail}}$) listed in Tables 4.3 and 4.4. In addition, the final positions, $\boldsymbol{x}_{\text{final}}$ are plotted as open circles.

than the MOT χ^2, it is still entered in these cases as long as it is also 'good' (less than one). Otherwise, if the MOT χ^2 was greater than one and the OP photoion fit gave a better χ^2, the results are shown in red with a magenta uncertainty band. A quick glance at the results shows many more OP results shown in red, which shows that the MOT results are generally not consistent with the OP results. This is particularly true of the later data sets using the Helmholtz coils to provide the optical pumping holding field.

Numerically, and again in a colour-coded manner, we can see the same trends in Tables 4.3 and 4.4. The top row for a given data set are the results using the MOT photoions and the lower are the corresponding results using the four OP points (if absent, these fits had a worse χ^2 than the MOT fits). The OP points listed in red correspond to the same as the figures of Appendix A; if the reduced χ^2 of the MOT was less than one, the results are shown in gold. Once again, one sees most OP entries are filled, and that they are in red.

Whether these plots and/or tables are viewed glancingly or scrutinized in great

detail, one sees there there are some serious discrepancies between the two methods of deducing the cloud position during optical pumping times. As an extreme example, consider the $\hat{x}$ positions of the 3^- data set for σ^+ polarization (top left of Fig. A.5): in this case, the optical pumping photoion points not only indicate a drastically different initial cloud position, but even a significant difference in the *sign* of the sail velocity! One's first reaction is to inquire about the quality of the OP fits of the photoion position/TOF spectra, and whether some bias has been introduced. This was investigated in great detail and in fact was one of the first reasons we pushed to improve the signal-to-noise ratio and make the position/TOF cuts on the photoions. Figure 4.19 shows a comparison for this 3^- discrepancy for the four OP bins. The data (histogram) is fit to Eq. (4.12) with the S/N fixed according to those determined from the TOF spectra; it is only significant for the last two bins where the signal is small (highly polarized by then) and the time bin is longer (600 μs vs. 40 and 80 μs). This fit result is overlaid as the solid line. For comparison, the expected signal based on the MOT fit results is shown as a short dashed line. The means of both distributions are depicted by long dashed lines. In the first three time bins, the MOT results clearly do not reproduce the data, and even with the limited statistics, the direct fits are significantly different. One must concede, in this particular case, that the last time bin has too few counts to say that the centroid should be so far to the right, however this is reflected by the large uncertainty in the centroid visible in Fig. A.5.

The general trends observed are that the MOT interpolations and the direct fits to the optical pumping data disagree more severely for data sets after the Helmholtz coils were installed and the polarization scheme changed. The effect is greatest in the $\hat{x}$ and $\hat{z}$ directions, with agreement generally not too bad in the $\hat{y}$ direction.

The question becomes "Why are they different, and which result is to be believed?" As mentioned earlier, it is hard to imagine how the MOT photoions could be wrong, because we know that the cloud must move continuously and that there are no significant forces acting on the atoms during optical pumping times. On the other hand, we know that the direct fits are significantly different in many cases, even considering their small statistics.

One possibility is that the photoionization laser beam ($\approx$ 24 mm FWHM as seen by

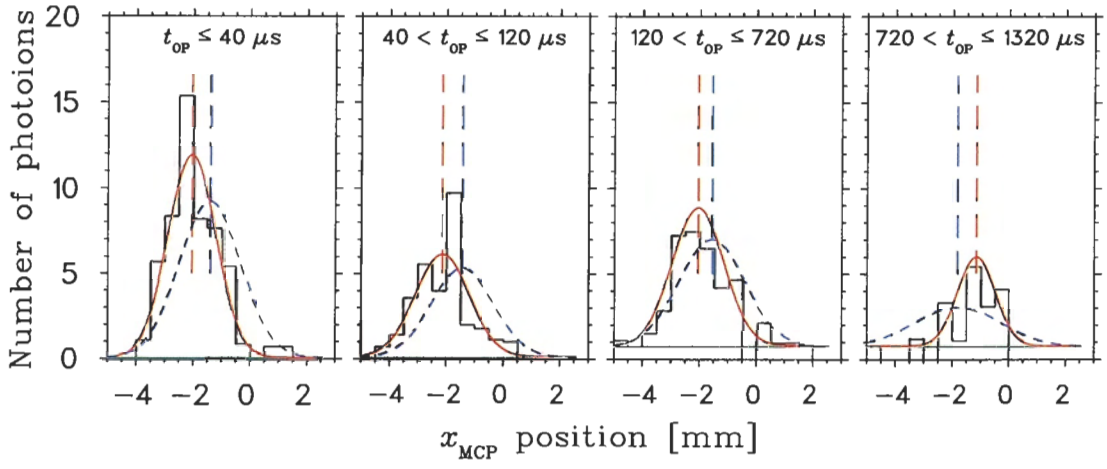

FIGURE 4.19: Photoion position spectrum during OP times and comparison to MOT interpolation. Shown as a histogram is the data for the 3^- data set with σ^+ polarization. The solid line is a fit to these points while the dashed line is the expected position and size based on the MOT interpolation (see text).

eye on a 1" diameter mirror) is not interrogating the whole cloud; if it only illuminated part of it, then biases could easily be seen. The fact that this laser beam is brought into the chamber from the vertical direction (which is mostly aligned with $\hat{y}$ in the optical pumping frame used here) would explain why the $\hat{y}$ direction does not show as big a discrepancy. However, when one considers the size and varied position of the MOT photoions as seen in the figures of Appendix A, this is quickly seen to be impossible, because we otherwise would have observed even larger biases in the MOT photoion spectra; there would be no signal when the trap moved out of the 355 nm laser beam and we would expect to see very distorted photoion spectra. Furthermore, a photoion–cloud misalignment would not explain the discrepancy between the last MOT points and the initial optical pumping point. The Gaussian nature of the laser beam may have biases from non-uniformity of the intensity, however the large beam profile means the intensity variation over the cloud volume will be small.

Another possibility is that the optical pumping beam is not fully overlapping the cloud of atoms. In this case, the atoms in the portion of the cloud that is not illuminated will not be excited into the P state, and therefore cannot be photoionized resulting in a bias of the photoion spectra during only optical pumping times. In this

case, the beam ($\approx$ 9 mm FHWM) is brought in along the $\hat{x}$ direction, so one would expect this direction to show little or no discrepancy, not the $\hat{y}$ direction. However, one must think in three dimensions: if the beam is missing the cloud in the $\hat{z}$ direction, and the cloud's group movement is in the $\hat{x} - \hat{z}$ plane, then the $\hat{y}$ distribution will not be affected (recall the sail velocity in $\hat{y}$ was relatively small) but *both* the $\hat{z}$ and $\hat{x}$ distributions would become biased.

To test this hypothesis, we look at the TOF spectra of the polarized β decay data. With the two methods of fitting the cloud position and sail velocity giving much different $\hat{z}$ positions and velocities, we expect that peaks in the timing of the β-telescope–Ar coincidences will be able to discern between the two characterizations. In order to avoid correlations with the uncertainty in the electric field as well as to maximize the sensitivity*, we look at the rising edge of the neutral ^{37}Ar peak even though we realize it is highly susceptible to not only the position efficiency described earlier, but it is also hard to model the energy dependence of the neutrals. However, as we only require use of the fastest neutrals, this will not preclude us from discerning between the two characterization schemes. Due to the time-walk of the MCP with low pulse-heights, the inefficient regions will be pushed to longer TOF, and the fastest recoils should be relatively clean. The result of comparing this data to two MC simulations is shown in Fig. 4.20 where the positions and sail velocities of the cloud input into each of the simulations was based on the MOT (solid line) and OP (dashed line) characterizations. In the 1^a data set (left panel), the agreement between the two characterizations is very good, which is what we expect because the cloud characterizations are very similar. The same comparison using the 6^+ data set, where the characterizations — in particular both z_o and v_z — are significantly different between the two, and give rise to a correspondingly significant difference in the simulated TOF spectrum. The simulation using the OP characterization is clearly too long in TOF, while the MOT characterization continues to do a good job of reproducing the data. Similar comparisons to other data sets continued to show the same results, and thus we conclude that:

*The neutrals, since they are not accelerated by the E-field, have the longest TOF and hence the finest binning.

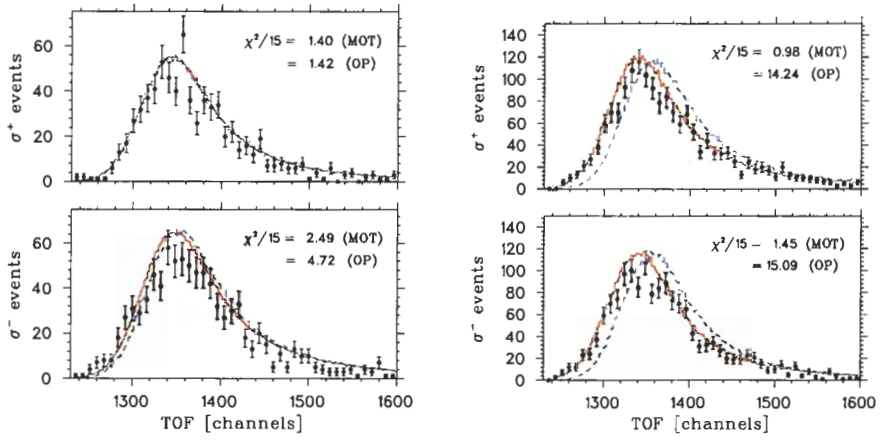

FIGURE 4.20: TOF comparison of the data to SMC simulations using the optical pumping and MOT cloud characterizations for the 1^a (left) and 6^+ (right) data sets. The points are the data, the solid line is the simulation using the MOT interpolation, and the dashed line represents the MC where the input position and sail velocity were from the fits to the four optical pumping bins directly.

1. agreement between the MOT and OP characterizations is reasonable when the trim coils were used when optically pumping, but there is serious disagreement in subsequent data sets using the Helmholtz coils.

2. for these later data sets, we believe the MOT characterization over the direct fits because indications are that the optical pumping beam was not illuminating the whole atom cloud in these cases.

This conclusion has great implications for the polarization of the cloud for all runs after the Helmholtz coils were installed. Our comparisons of MOT vs. OP cloud characterization have indicated strongly that our optical pumping beam was misaligned with the cloud; given that, it necessarily follows that *not all of the cloud was being optically pumped*, and we have no means to quantitatively estimate what fraction is being missed. Obviously with some fraction of the cloud unpolarized, the overall average of the cloud polarization is reduced. Furthermore, since we determine the polarization by fitting the photoion data to our atomic model of the vanishing of the fluorescence, and the unpumped atoms are not probed by this diagnostic, we have a large, entirely inestimable systematic uncertainty in the polarization of these data

sets; if some portion of the cloud was not being polarized, we can not know with any precision what fraction were unpolarized, nor how many were initially optically pumped before sailing out of the laser beam, etc. In short, we cannot use these data sets for any asymmetry measurement, and must restrict ourselves to the 1^a and 1^b data sets where the MOT and OP characterizations agree, and all indications are that the entire cloud was being optically pumped; only then can we believe that our photoion diagnostic actually probed all of the atoms.

4.6.4 Cloud temperature

As the cloud is being optically pumped, the (now untrapped) atoms ballistically expand due to their small (yet finite) thermal velocity. In order to describe this process physically, we turn to the kinetic theory of ideal gases which states that an ensemble of atoms at a temperature, T, will have a Maxwell-Boltzmann distribution of velocities [101]:

$$P(v)dv = \frac{4}{\sqrt{\pi}} a(av)^2 e^{-a^2v^2}, \tag{4.16}$$

where $v = |\boldsymbol{v}|$ is the magnitude of a given atom's velocity and a is the inverse of the most probable velocity, *i.e.* the velocity at which this distribution is maximized:

$$a \equiv \frac{1}{v_o} = \sqrt{\frac{M}{2k_BT}}. \tag{4.17}$$

Eq. (4.16) describes the probability that a given particle within a thermal ensemble will have a velocity between v and $v + dv$. Strictly speaking, and something that should be included in the future, one should calculate the distribution for an ensemble of atoms in a trapping potential. The 'temperature' deduced this way will in general differ from the Maxwell-Boltzmann distribution, especially for small temperatures. However, in this thesis we only consider a thermal ensemble.

Suppose for the moment that we truly have a point-like source and that it is centered at the origin. In a time, t, an atom with thermal velocity, $\boldsymbol{v}$, will move $\Delta\boldsymbol{x}(t) = \boldsymbol{v}t$. Assuming that the direction is homogeneous in space ($\langle v_x^2\rangle = \langle v_y^2\rangle = \langle v_z^2\rangle = \frac{1}{3}\langle v^2\rangle$), the velocity will have an average magnitude of $|\boldsymbol{v}| = v_o$ and the

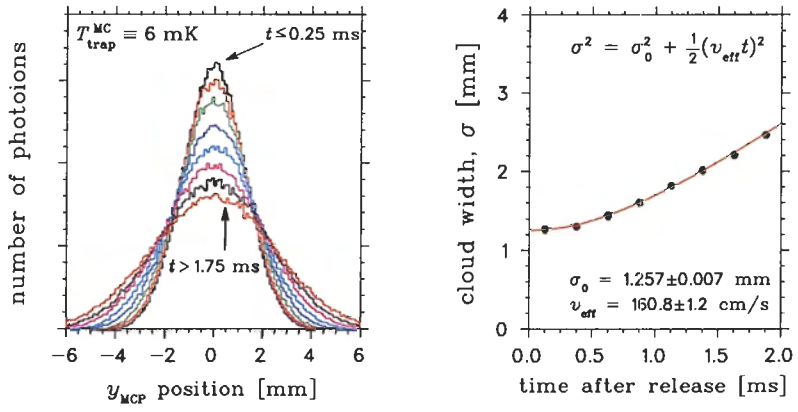

FIGURE 4.21: Example of MC analysis to determine how v_{eff} is related to the growth of the cloud size. The left panel shows the simulated photoion $\hat{y}$-MCP position spectrum for different bins of time after the atoms begin expanding due to their thermal velocity distributions. Gaussians are fit to each of these spectra and the time-dependence of σ is calculated. These results are plotted in the right plot, as well as the fit of the width to Eq. (4.19).

ensemble will ballistically expand as a three-dimensional Gaussian. Considering the argument of the normal distribution, we expect the width to grow according to:

$$\sigma^2(t) = \frac{1}{2} v^2 t^2. \tag{4.18}$$

If we start with a finite cloud size, $\sigma_\circ$, the width will initially be larger, however the expansion rate remains the same:

$$\sigma^2(t) = \sigma_\circ^2 + \frac{1}{2} v^2 t^2 \tag{4.19}$$

Though intuitive, this is by no means a rigorous derivation. To check that this is the correct expression, a MC analysis was performed. For a given temperature, the expansion of a finite-sized cloud was simulated over a 2 ms time scale by randomly and homogeneously distributing the atoms' velocity according to Eq. (4.16). The initial size was taken to be $\sigma_\circ = (1.410, 1.249, 1.062)$ mm, which are typical cloud sizes observed in the experiment. Simulated photoion events were tracked through the electric field in order to generate MCP position and TOF spectra; the time after the release was divided into 8 bins of 0.25 ms and, for each of these bins, the position/TOF distributions were fit to Gaussians. As an example of these distributions,

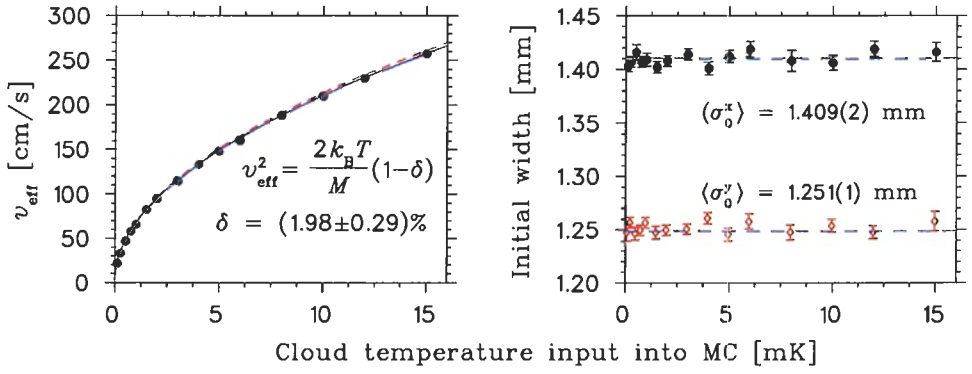

FIGURE 4.22: Relationship between fit v_{eff} and temperature as deduced by MC analysis (left). The points are the best fit v_{eff} for a given T, and the solid line shows the fit to the Eq. (4.20). The dashed line shows the case $v_{\text{eff}} = v_o$ for comparison. The fit values of the $\hat{x}$ and $\hat{y}$ widths are shown on the right, and agree with the values input into the simulations.

the $\hat{y}$ distributions are shown in the left plot of Fig. 4.21 where the initial cloud temperature input into the MC was 6 mK (again, a typical cloud temperature seen in the data). The sharpest peak is of course the first 250 μs after the atoms being their thermal expansion; by the time we get to the last time bin ($1.75 < t \leq 2$ ms), the width has approximately doubled. Note that this MC analysis exactly parallels how we will deduce the cloud temperature, and thus also accounts for minor corrections arising from the spatial resolution of the MCP and the small additional transverse movement of the photoions during their transit time in going from where they are photoionized to the MCP through the electric field.

After fitting these eight distributions, we plot on the right of Fig. 4.21 the deduced widths as a function of the time after the atoms were released and began their thermal expansion. Overlaid is the result of fitting these widths to a function of the form of Eq. (4.19). As one can see, the fit using this function describes the time dependence of the simulated widths very well. Ideally, we would expect that the parameter describing the time-dependence, let us call it 'v_{eff},' corresponds to v_o of the Maxwell-Boltzmann distribution. For a temperature of 6 mK, $v_o = 164.3$ cm/s which is very close, but slightly larger than, the fit value for v_{eff}.

The above analysis was done for a number of cloud temperatures ranging from 0.1 to 15 mK. For each of these, the initial widths and effective thermal velocities were

TABLE 4.5: Results of fits to the MOT size. Listed are the initial cloud widths as deduced by fitting the Gaussians to the distributions at the end of the MOT part of the cycle.

Data set	Initial cloud width [mm]					
	$\hat{x}$		$\hat{y}$		$\hat{z}$	
	σ^+	σ^-	σ^+	σ^-	σ^+	σ^-
1^a	1.268(53)	1.231(37)	1.418(36)	1.347(33)	1.105(61)	1.109(38)
1^b	1.413(41)	1.251(39)	1.556(96)	1.563(86)	1.265(63)	1.230(58)
3^+	1.018(33)	1.014(29)	1.123(42)	1.164(26)	1.003(22)	0.994(18)
3^-	0.941(30)	1.004(33)	1.222(24)	1.198(22)	1.012(23)	1.003(23)
4^+	1.059(69)	1.019(40)	1.263(36)	1.197(01)	1.057(62)	1.071(34)
4^-	1.013(27)	1.016(36)	1.332(51)	1.268(27)	1.075(25)	1.072(31)
5^-	1.056(38)	0.990(37)	1.307(28)	1.227(25)	0.994(41)	1.048(21)
6^+	1.115(42)	1.110(32)	1.354(36)	1.370(26)	1.074(42)	1.080(21)
6^-	1.051(31)	1.082(48)	1.394(25)	1.406(52)	1.057(19)	1.024(24)

calculated as described above. The temperature dependence of the v_{eff}, averaged over the three dimensions, is shown in the left plot of Fig. 4.22. Again, because we expect v_{eff} to be close to $v_\circ$, these points were fit to a function of the form:

$$v_{\text{eff}}^2 = \frac{2k_B T}{M}(1-\delta) = v_\circ^2(1-\delta) \tag{4.20}$$

where the only variable free to vary in the fit was δ, a small correction parameter accounting for the tracking, MCP spatial resolution, etc. The temperature dependence of the velocities is well-reproduced, with the fit giving a 2% value for the correction factor. On the right of Fig. 4.22 are plotted the initial widths fit for each temperature in the $\hat{x}$ and $\hat{y}$ directions. It is worth noting that the fit for each temperature reproduced the values input into the MC.

Now that we know how to relate the cloud expansion to its temperature when released, we can fit the photoion data to estimate the temperature of the cloud during the ^{37}K experiment. In fact, we use the exact same fits as §4.6.3 except instead of analyzing the time dependence of the means to get the initial cloud position and sail

velocity, we consider the widths of our Gaussian fits to get the initial cloud size and temperature. The initial width is given by the averaging the same four MOT time bins used to deduce the initial cloud position. The results are listed in Table 4.5 and shown graphically in Fig. 4.23. Unlike Table 4.3 for the initial positions, there are no entries from fits to the optically pumped photoions because no initial widths were estimated from this data; due to the low number of photoions during optical pumping times, in this case we are not to be able to reliably fit the time dependence of the widths and extrapolate the size to when they were released.

Referring again to Figs. A.1 – A.10, one can see that the widths during OP times are erratic and follow less of a trend than that of the centroid. In particular, the last bin (which has the smallest statistics) is needed because it would almost entirely define the cloud temperature if we attempted a fit using Eq. 4.19. The results of such attempts, if they converged at all, were extremely varied and often non-sensical, even giving negative temperatures. We therefore relied on the continuity of the cloud size and again used the fits of the MOT photoions just after the optical pumping part of the cycle to define the final cloud size. One can see that once the trap is enabled, the cloud expansion is halted and the atoms are recompressed by the time we release them and begin optically pumping again. Instead of a linear interpolation, we expect a quadratic dependence of the width with time, and so we define the cloud's effective thermal velocity by:

$$v_{\text{therm}} = \sqrt{\frac{2}{\Delta t_{\text{op}}}\left(\sigma^2_{\text{final}} - \sigma^2_{\circ}\right)}. \tag{4.21}$$

where $\Delta t_{\text{op}} = 1.4$ ms is the time between the measurements of the widths. Rearranging Eq. (4.20), we are able to relate this calculated velocity to the cloud's average temperature.

The temperatures deduced in this manner are listed in Table 4.6 and are shown graphically in Fig. 4.23. Typical temperatures are in the range of $3 - 8$ mK which is significantly higher than the 150 μK Doppler limit for ^{37}K (see pg. 49). We have typically seen temperatures above the Doppler limit in the ^{38m}K experiments such that we expected ^{37}K temperatures of ~ 1 mK; the observed temperatures are several

TABLE 4.6: Results of fits to the MOT expansion. Listed are the cloud temperatures as deduced by fitting the cloud expansion over the optical pumping time.

Data set	Cloud temperature [mK]					
	$\hat{x}$		$\hat{y}$		$\hat{z}$	
	σ^+	σ^-	σ^+	σ^-	σ^+	σ^-
1^a	7.46(0.61)	5.93(0.71)	5.42(0.50)	4.78(0.46)	3.19(0.41)	3.29(0.40)
1^b	8.19(0.69)	8.75(0.67)	6.51(0.80)	6.42(0.72)	4.25(0.55)	3.29(0.50)
3^+	5.61(0.49)	5.96(0.35)	8.26(0.50)	7.54(0.51)	4.41(0.39)	4.22(0.35)
3^-	4.43(0.36)	4.83(0.38)	6.42(0.51)	7.36(0.56)	4.11(0.41)	4.51(0.48)
4^+	2.87(0.65)	5.70(0.81)	8.77(1.17)	7.94(1.27)	3.25(0.69)	4.69(0.89)
4^-	5.22(0.36)	5.04(0.39)	6.06(0.77)	5.88(0.50)	4.28(0.40)	3.88(0.47)
5^-	3.71(0.40)	4.92(0.49)	5.05(0.56)	5.83(0.61)	4.15(0.48)	3.83(0.45)
6^+	3.81(0.32)	4.18(0.31)	5.71(0.48)	5.56(0.48)	3.06(0.32)	3.59(0.28)
6^-	3.78(0.29)	3.30(0.35)	3.64(0.34)	4.19(0.49)	2.68(0.27)	2.96(0.26)

times larger than we had expected. This is likely due to the MOT $\leftrightarrow$ optical pumping cycling of the atoms and the turning on and off the magnetic fields. It does appear, from Fig. 4.23 that the $\hat{y}$ temperatures are generally higher than the other directions. This indicates field effects because the quadrupole field in this direction is twice as strong as the $\hat{x}$ and $\hat{z}$ directions, and thus effects from turning it on and off are likely enhanced. It also appears that, at least in the $\hat{x}$ direction, the Helmholtz coils of the later data sets resulted in lower temperatures, but this is far from conclusive (a clear trend is only observed in the $\hat{x}$ direction with σ^+ polarization) and certainly not the dominant source of high cloud temperatures. As with the position and sail velocity, there are no blatant correlations of the initial widths with the sign of the holding $\boldsymbol{B}$-field nor the polarization state.

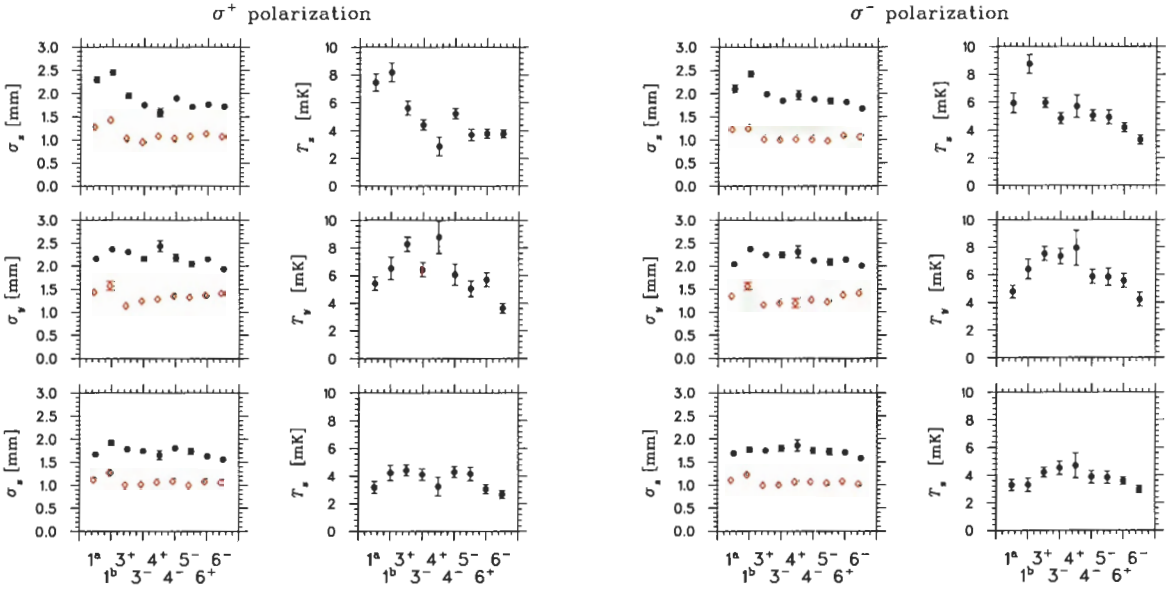

FIGURE 4.23: Graphical representation of the deduced cloud sizes and temperatures listed in Tables 4.5 and 4.6. The filled (open) circles represent the cloud widths at the start (end) of the optical pumping part of the cycle. The difference between the final and initial cloud width is used to calculate the cloud's average thermal velocity which in turn is used to calculate the mean cloud temperature .

4.7 Atomic Fits to the Polarization

In the previous sections, we have deduced the cloud size and position throughout the trap/OP cycle. In this section, we will use this information to make clean MCP position and TOF cuts on the photoion spectra; the number of photoion events as a function of the optical pumping time, as mentioned earlier, is directly related to the atomic fluorescence because only atoms in the excited P state can be photoionized. We will fit these spectra to our model of the optical pumping process and thereby fit the average polarization of the atomic ensemble.

4.7.1 Fits to the Time Spectra of the Photoion Yield

The physics going into our model of the optical pumping process has been outlined in §3.3.2, the kernel of which is based on the rate equations for a multi-level atom, Eqs. (3.44). By fitting the photoion spectra to this model, we are able to estimate the average atomic sublevel populations as a function of the optical pumping time. Using Eqs. (3.25) and (3.26), and given the sublevel populations from the fit results (including the negligible excited state populations), we are able to estimate the the polarization and alignment of the atom cloud; both will be subject to uncertainties arising from the different population distributions among all of the ground (and excited) state sublevels that give the same steady-state photoion yield. The polarization and alignment are averaged over the same times as used online when defining 'polarized' events, namely 200 μs after the optical pumping process is initiated.

As seen by Eq. (3.39), the transition probability, W_{ij}, depends on a few parameters which we allow to vary freely in the fits: I_L, the laser light intensity; Δ, the detuning of the optical pumping laser with respect to the $F = 2 \rightarrow F' = 2$ transition; and γ_L, the FWHM of the laser beam. The transition probability affects the rate at which the cloud becomes polarized, but does not affect the asymptotic value of the final polarization; given enough pumping time, perfect circular polarization and a perfectly aligned holding field, the cloud will become 100% polarized even if W_{ij} is relatively small. The depolarizing mechanisms included in our model are given by: S_3, the Stoke's parameter which characterizes the purity of the circular polarization

of the optical pumping laser light [102]; and $B_\perp$, the unwanted component of $B_{\rm op}$ perpendicular to the $\hat{x}$ or polarization axis. If $S_3 \equiv |\hat{\mathcal{E}} \cdot \hat{\epsilon}_{+1}|^2 - |\hat{\mathcal{E}} \cdot \hat{\epsilon}_{-1}|^2 \neq \pm 1$, then the polarization of the laser light is not pure, and there will be a small component of the wrong polarization which will quickly pump atoms out of the stretched state. If the optical pumping field is not perfectly aligned with the quantization axis of the laser beam, then the $|F\ M_F\rangle$ states will mix and again atoms may be able to leak out of the stretched state, resulting in imperfect polarization.

The two (de)polarizing mechanisms, S_3 and $B_\perp$, are completely correlated and cannot be simultaneously fit. Similarly, I_L and Δ are also 100% correlated. Thus fits were performed with each of the possible combinations of free parameters: (S_3, I_L), (S_3, Δ), $(B_\perp, I_L)$ and $(B_\perp, \Delta)$. Other parameters were fixed:

- $t_{\rm offset} = 0$ – assumes that the optical pumping process starts at zero time. The time resolution of the online data is 10 μs, and it is possible for the process to start anywhere within the bin, not necessarily at $t = 0$.

- $b = b_\circ$ – the background level as determined from S/N results from the position/TOF fits of the photoions in the MCP in §4.6.2.

- $B_{\rm op} = \pm 2$ G – for the 1^a and 1^b data sets, $B_{\rm op} = -2$ G; for subsequent data sets, the sign is that indicated by the name, *e.g.* $3^\pm$ had a field of ± 2 G.

Examples of the fits of the rate equation model to the $1^{\rm st}$ data sets are given in Fig. 4.24. In the cases shown, we have fixed the circular polarization of the laser light to be perfect ($S_3 = \pm 1$) and have left $B_\perp$ and I_L free to vary in the fits. The polarizations quoted in the Figures are averaged from 0.2 s $\leq t_{\rm op} \leq$ 1.3 s. Results with S_3 free to vary instead of $B_\perp$ were very similar, with the small differences considered below when including systematic uncertainties. One can see the large initial spike in fluorescence which is expected because at the start of the optical pumping process, the cloud is unpolarized. The fluorescence quickly dies away, but does not entirely vanish to the background level expected based on the position/TOF fits (cyan line barely visible above the $\hat{x}$-axis); hence the fits to our optical pumping model indicate that the polarization — though quite high at $95 - 98\%$ — is not complete.

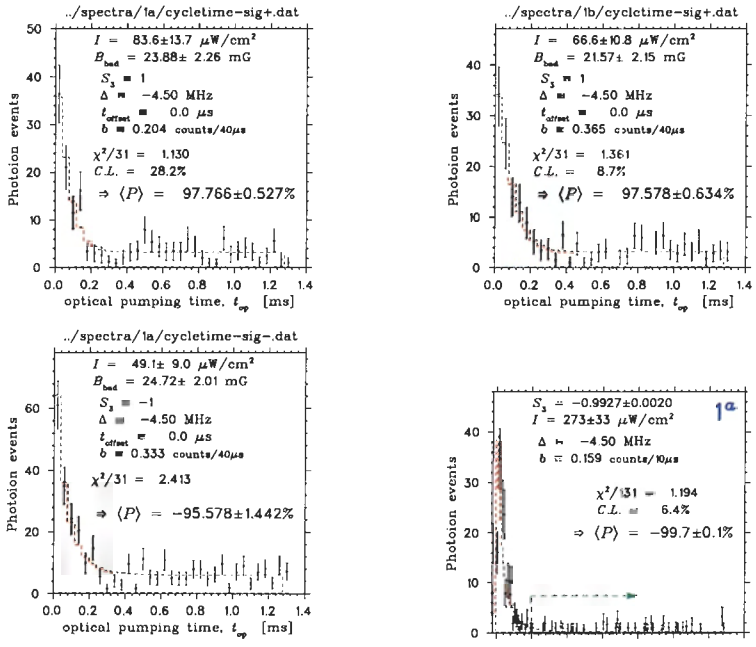

FIGURE 4.24: Fits to the vanishing of the fluorescence for the 1st data sets where the field was -2 G: 1^a (left) and 1^b (right). The top row is σ^+ polarization and the bottom σ^-.

For the data sets where the Helmholtz coils generated the optical pumping field, examples of fits to the fluorescence curves are shown in Figs. 4.25 and 4.26. In these cases, as predicted by the position/TOF fits, the background level is smaller, but one also sees that the extinguishing of the fluorescence is better than the $1^{a,b}$ data sets. The resulting fit polarization is therefore higher than the 1st data sets at $98 - 99.5\%$. However, as mentioned earlier, this method of deducing the atomic cloud's average polarization only probes atoms that are overlapped with the optical pumping laser beam. As we explained at the end of §4.6.3, we have evidence that not all of the cloud was being optically pumped, although our diagnostics at this stage are limited. The true *total* cloud polarization is actually lower than these fits indicate; furthermore, it is lower by an amount that we *cannot* estimate. The point of showing these plots and calculating the polarization is to indicate how the Helmholtz coils improve the optical pumping method. The Helmholtz coils generate a better defined $\boldsymbol{B}$-field compared to using the trim coil fields and therefore there will be less gradient magnetic fields which disrupt the optical pumping process. The fits of the parts of the cloud that were

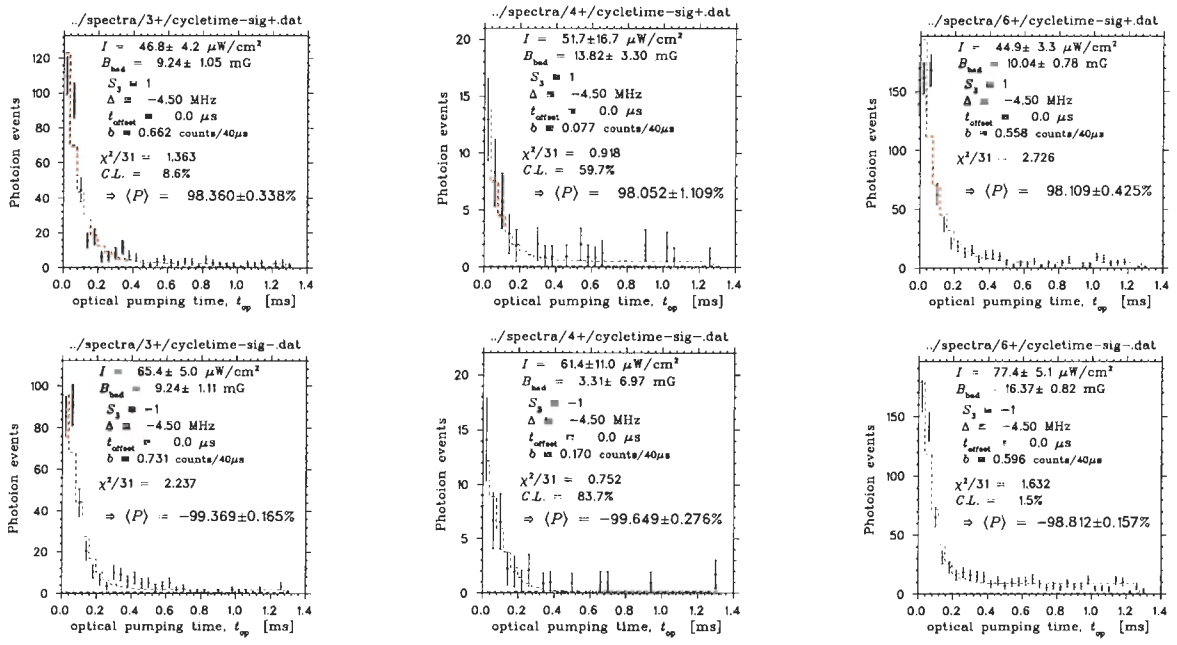

FIGURE 4.25: Fits to the vanishing of the fluorescence for the 2^{nd} data sets where the field was +2 G: $3^+, 4^+$ and 6^+ (left to right). The top row is σ^+ polarization and the bottom σ^-.

efficiently pumped give us an idea as to the polarizations we can expect to achieve next time we run and are absolutely sure that we are pumping the entire cloud.

The results of the fits to all of the data sets is given in Table 4.7.

4.7.2 Systematics

This section explores the potential sources of systematic uncertainties in the fits of the vanishing of the fluorescence. Generally speaking, each of the input parameters of the model was varied by its uncertainty, and then the systematic taken to be the change in the fit values of P and T. As outlined in §B.2.2, we follow [103] in our analysis of systematic (Type B) uncertainties. The largest source of error is the fitting range, which corresponds to normalizing the initial spike in the fluorescence. Tables 4.8 and 4.9 list the identified sources of systematic errors and estimates of their magnitude. Below we discuss each of the sources in some detail.

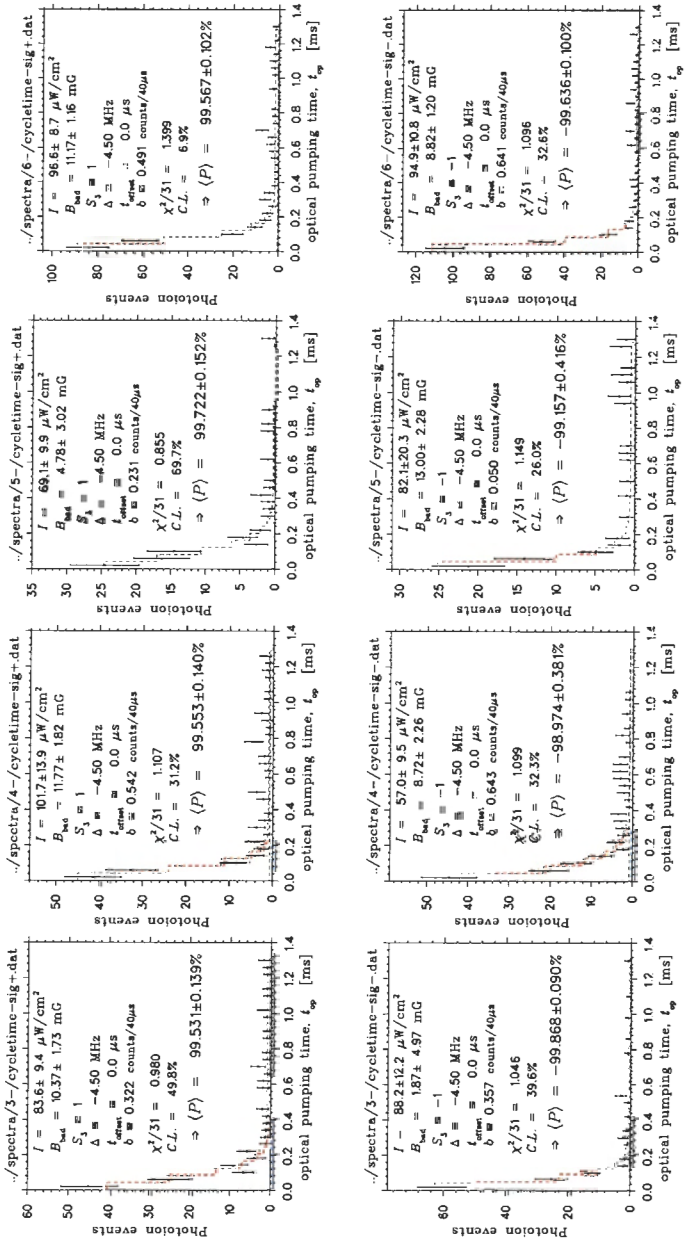

FIGURE 4.26: Fits to the vanishing of the fluorescence for the 2nd data sets where the field was -2 G: $3^-, 4^-, 5^-$ and 6^- (left to right). The top row is σ^+ polarization and the bottom σ^-.

TABLE 4.7: Results of fits of the photoion spectra to the optical model from which the average polarization and alignment of the cloud is calculated. All values are in percent, and the quoted uncertainties are purely statistical at this stage.

Data set	P_+	P_-	T_+	T_-
1^a	97.8 ± 0.5	-96.0 ± 1.3	-94.2 ± 1.3	-90.7 ± 2.6
1^b	97.6 ± 0.6	-95.5 ± 1.5	-93.8 ± 1.5	-91.7 ± 2.2
3^+	98.4 ± 0.3	-99.4 ± 0.2	-97.4 ± 0.5	-98.4 ± 0.3
4^+	98.2 ± 1.0	-98.5 ± 0.5	-97.8 ± 2.2	-97.6 ± 1.4
6^+	98.2 ± 0.4	-98.8 ± 0.2	-96.8 ± 0.6	-96.8 ± 0.4
3^-	99.5 ± 0.1	-99.9 ± 0.5	-98.7 ± 0.4	-99.7 ± 0.8
4^-	99.5 ± 0.1	-99.2 ± 0.4	-98.9 ± 0.3	-98.2 ± 0.6
5^-	99.6 ± 0.4	-99.2 ± 0.4	-99.3 ± 2.4	-98.1 ± 0.7
6^-	99.6 ± 0.1	-99.7 ± 0.1	-98.8 ± 0.2	-99.2 ± 0.2

The Fitting Range

The overall normalization of the rate equation model we are comparing the photoion data to is fixed such that the total number of counts are equal in the two spectra. This normalization is actually crucial to remove large systematic dependences of the normalization on the sometimes very low-statistics of the initial spike in the fluorescence (versus, for example, allowing the normalization to be a free parameter). Therefore, we do not actually need to *fit* the very initial part of the optical pumping process, at least to within the first 60 μs; if taken to extreme, we will only fit the flat background and have *no* information on the pumping process. We are sensitive to the details of the optical pumping process (*i.e.* the exact mechanism by which the cloud is polarized) only in so far as we need to define the normalization of the initial spike in the fluorescence. At times greater than 200 μs, a steady-state is achieved and, regardless of the process by which the atoms got there, the baseline of fluorescence is a sensitive probe of atoms not in the stretched state. If we instead let the normalization become a free parameter, then we become more sensitive to the pumping process

and the details of how the fluorescence decays away; a more detailed model of the pumping process (e.g. including perpendicular field components in a more rigourous manner) and off-line tests with stable species may help improve our fits and reduce this (currently dominant) source of systematic uncertainty.

This systematic was estimated by fitting the fluorescence spectra as we successively cut the first $10, 20, \ldots, 60$ μs. The assigned uncertainty was taken to be the maximum and minimum differences from the nominal fit result using the entire spectrum.

(De)Polarizing Mechanisms

In the atomic model, incomplete polarization of the atoms can occur in two dominant ways: either through imperfect circular polarization of the optical pumping laser light, or the magnetic holding field may be mis-aligned with the quantization axis. In the case of the polarization of the laser light, a small component of the opposite handedness will quickly pump atoms in the wrong direction, thereby spoiling the polarization. The Stokes' parameter, S_3, characterizes how well the light is polarized; the further from unity this parameter is, the less atoms accumulate into the stretched state. The atoms equilibrate early in the cycle, so the result is a baseline of fluorescence above the background.

A small component of a $\boldsymbol{B}$ field not aligned with the optical pumping axis will cause the atoms to Larmor precess about that axis, which also induces transitions between the sublevels and can result in an incomplete polarization. The effect is very similar to a poor S_3, and indeed the fits cannot converge if both left free to vary due to the complete correlation between these parameters.

A systematic uncertainty arises from the difference in the fit value of the polarization according to which depolarizing mechanism we include in our model: in one case, we set $S_3 = \pm 1$ and let $B_\perp$ be free to vary; and in the other we fix $B_\perp = 0$ G and let fit S_3. The difference arises mostly in how the pumping process achieves the steady-state and the final distribution of atoms left in sublevels outside of the stretched state (e.g. the relative amounts of $|2\ 1\rangle$ versus $|1\ 1\rangle$). Because these two mechanisms are highly correlated and result in very similar sublevel populations, this systematic is

not very large.

Laser Beam Intensity/Detuning

These two parameters are extremely correlated, and both are difficult to know with absolute precision. Estimates are that the detuning was 4.5 MHz to the red of the D_1 transition, and the total average beam intensity was 500 μW/cm^2. The detuning is thought to be known to within half a MHz, but the intensity overlapping the atom cloud is more difficult to estimate. A power meter measured the total beam intensity, $I_{\text{tot}} = 1.5$ mW, and the density was estimated by dividing by the area, $\pi(1 \text{ cm})^2 = 3.1 \text{ cm}^2$. A reduced apparent power density in the fit may be due to the Gaussian nature of the beam and cloud, but most likely it is accounting for inefficiencies in the optical pumping process or loss channels not present in our model.

Due to the complete correlation between the detuning and intensity, the two parameters could not be independently fit. To estimate the effect of using one over the other, all fits were done with the detuning fixed at its best value, and the intensity free to vary; this was then compared to a fit with the intensity fixed at its best value, and the detuning free to vary. The difference in the fit results is taken to be a systematic uncertainty in our measurement of the polarization.

Dependence on Binning

Although Poisson statistics are used throughout, and low statistics in the photoion spectra should be properly accounted for, the resulting answer for the polarization will depend on the choice of binning of the spectra. In particular, the dependence arises from two affects:

1. the estimate of the size of the initial spike in fluorescence

2. the estimate of the flat background in steady state (long times)

In the first case, too fine a binning makes the normalization subject to large (relative) statistical fluctuations, while too coarse a binning makes one sensitive to times when the fluorescence has already diminished by a large fraction. In the second case, too

fine a binning makes one encounter many zero-count bins and again, more sensitive to statistical fluctuations; in this case, coarse binning poses no problem.

This systematic was taken to be the variation in the fit value of the polarization for binning factors of 1 bin/10 μs, 1 bin/20 μs, ..., 1 bin/50 μs.

The Time Cut-off

The clock scaler (cleared with each duty cycle and read with each event) measuring the cycle time has a bin width (resolution) of 10 μs, so we can not be sure of when — within this bin — the optical pumping beams were on. Indeed, some of the spectra show indications that a build-up of the fluorescence is present within the first time bin, *i.e.* the second bin has more counts than the first, and then the normal vanishing of the fluorescence occurs. This effect may be manifest through the unknown 'start time' of the optical pumping process, or may also be a result of inefficient atom excitation by the OP beams. For example, if the OP beams take some finite time to come to full intensity, a discernible rise the initial fluorescence spike may be expected. No matter the mechanism, the answer will clearly be a poorer polarization than if the first bin had the most number of counts. As an estimate of the effect, we assume it is due only to the unknown start of the OP process within the first bin, which we leave as a free parameter of the fit.

In estimating the systematic, we compare the fit value for $t_o = 0$ to that of the best fit time-offset. This difference is called the systematic error due to the time cut-off.

Random Background

The background was estimated from the position spectra of the photoions in the MCP (see §4.6.2). In the fits to the fluorescence, this background is a fixed parameter, however its magnitude is subject to statistical uncertainties which will have a direct effect on the deduced polarization. This is because the steady-state of the pumping process which almost entirely determines the final polarization is defined entirely by the magnitude of the flat tail at long times.

These photoion spectra are the same events that defined our cuts early; this time

however we look at the number of photoion events during the optical pumping time (rather than position/TOF). Of the $\sim$ 2700 events in the $1^{a,b}$ data sets, 1800 were associated with either $\sigma^{\pm}$ polarization. We are justified in fixing the background level in these time-spectra of the photoion events based on the S/N determined from other information (position/TOF) about the same photoion events.

To estimate the systematic uncertainty due to the background, the level was varied by $\pm 1\sigma$ of its best fit value, and the polarization re-fit. The change in the fit result is taken to be the systematic. Note that this systematic is never the dominant one because the backgrounds are so small; the position and TOF cuts made on the photoions produces a very clean spectrum of the fluorescence. By allowing events within 3σ of the central value, we have a 95% acceptance efficiency if the cloud were Gaussian and the atoms are thermalized.

It should be noted that the position cuts were relaxed a great deal and the polarization fit to check that the cuts were not biasing the data. Specifically, we made a 10σ cut in TOF to define a very loose condition on photoion events and required only that the position of the hit was anywhere within the MCP's active area. This of course gave much larger backgrounds and poorer signal-to-noise ratios. The fit polarizations were entirely consistent with earlier estimates when tighter cuts were made*, however the systematic due to the background level became quite significant at $\pm 0.4\%$.

4.7.3 The Combined ($\sigma^{\pm}$) Polarization

The relevant quantity for any asymmetry measurement will be the combination of both polarization states. We therefore define an "effective polarization" to be the average magnitude of the two polarization states:

$$\mathcal{P} \equiv \frac{1}{2}\Big(P_{+} - P_{-}\Big). \tag{4.22}$$

*For example, the fits to 1^{a} gave $P(\sigma^{+}) = 97.9 \pm 0.6\%$ and $P(\sigma^{-}) = -95.9 \pm 1.3\%$ which are in good agreement with the results listed in Table 4.7. Similarly, for 1^{b} we found $P(\sigma^{+}) = 98.1 \pm 0.8\%$ and $P(\sigma^{-}) = -95.8 \pm 2.0\%$ with the looser cuts.

TABLE 4.8: Systematic uncertainties in the fits to the vanishing of the fluorescence for the 1st data sets, before field switching was enabled. The variance and shift from the potentially asymmetric uncertainty range, Δ and δ, are described in Appendix B.2.2. All values are in percent, and the dominant systematics are identified by a **boldfaced** font.

$B = -2$ G		σ^+			σ^-	
Source	σ_P^+	$\bar{\Delta}$	δ	σ_P^-	$\bar{\Delta}$	δ
S_3 vs. $B_\perp$	$^{+0.01}_{-0.01}$	± 0.01	0.00	$^{+0.30}_{-0.30}$	± 0.30	0.00
background	$^{+0.05}_{-0.03}$	± 0.04	$+0.01$	$^{+0.06}_{-0.12}$	± 0.09	-0.03
binning	$^{+0.05}_{-0.05}$	± 0.05	-0.00	$^{+0.17}$	± 0.09	$+0.09$
time offset	$^{+0.07}_{-0.07}$	± 0.07	-0.00	$^{+0.20}_{-0.20}$	± 0.20	0.00
fitting range	$^{+0.01}_{-0.34}$	$\pm\mathbf{0.18}$	$\mathbf{-0.17}$	$^{+0.89}_{-0.08}$	$\pm\mathbf{0.49}$	$\mathbf{+0.41}$
I_L vs. Δ	$^{+0.01}$	0.00	$+0.00$	—		
MCP efficiency	$^{+0.05}$	± 0.03	$+0.03$	$_{-0.06}$	± 0.03	-0.03
Sum systematics		± 0.32	-0.13		± 0.85	$+0.42$

Due to the fact that we are unable to determine which depolarizing mechanism dominates (S_3 or $B_\perp$), the individual polarizations, $P_\pm$, are taken to be the average of the two fits where one or the other was a fitting parameter. Thus we assume that both contribute roughly equally which is a reasonable assumption; and, at any rate, the systematics as deduced above account for the difference between the two fits.

As a concrete example of how the effective polarization is deduced, let us consider the 1^a data set. With S_3 free to vary, the fits to the vanishing of the fluorescence gave nuclear polarizations of $P_+ = 0.978(5)$ and $P_- = -0.965(12)$, while the fits with $B_\perp$ free to vary* gave $P_+ = 0.978(5)$ and $P_- = -0.956(14)$. Averaging the magnitude *and* statistical uncertainties for both σ^+ and σ^- yields $\langle P_+ \rangle = 97.8(0.5)\%$ and $\langle P_- \rangle = -96.0(1.3)\%$. Evaluating Eq. (4.22) using these values yields $\mathcal{P}_{1^a} = (96.9 \pm 0.7)\%$ for the combined polarization. Similar analyses were done for the other data sets, resulting in the combined polarizations listed in Table 4.10.

*These results are shown in Fig. 4.24

TABLE 4.9: Systematic uncertainties in the fits to the vanishing of the fluorescence for the 3rd–6th data sets. The systematics are estimated separately for both negative (left) and positive (right) signs of the optical pumping field. All values are in percent, and the dominant systematics are identified by a **boldfaced** font.

	$B = -2$ G				$B = +2$ G			
	σ^+		σ^-		σ^+		σ^-	
Source	$\bar{\Delta}$	δ	$\bar{\Delta}$	δ	$\bar{\Delta}$	δ	$\bar{\Delta}$	δ
S_3 vs. $B_\perp$	±0.01	0.00	±0.03	0.00	±0.08	0.00	±0.00	0.00
background	±0.03	+0.01	±0.03	−0.01	±0.03	+0.00	±0.03	−0.01
binning	±0.01	−0.00	±0.01	+0.00	±0.04	+0.02	±0.03	+0.00
time offset	±0.01	−0.00	±0.02	+0.00	±0.04	−0.00	±0.04	+0.00
fitting range	**±0.02**	**−0.02**	**±0.05**	**+0.04**	**±0.14**	**+0.14**	**±0.06**	**−0.06**
I_L vs. Δ	±0.00	+0.00	±0.00	−0.00	±0.00	+0.00	±0.00	−0.00
MCP efficiency	±0.00	−0.00	±0.00	−0.00	±0.00	−0.00	±0.01	−0.01
Sum systematics	±0.05	−0.02	±0.09	+0.04	±0.25	+0.17	±0.11	−0.08

TABLE 4.10: Effective (combined $\sigma^\pm$) polarizations for the data sets. The systematic uncertainties were deduced using combinations of data sets (see Tables 4.8 and 4.9), and so are only included after averaging similar data sets. All values are given in percent.

Data set	$\mathcal{P}$	Data set	$\mathcal{P}$	Data set	$\mathcal{P}$
1^a	96.89 ± 0.71	3^-	99.69 ± 0.25	3^+	98.90 ± 0.19
1^b	96.55 ± 0.80	4^-	99.29 ± 0.20	4^+	98.35 ± 0.59
		5^-	99.46 ± 0.26		
		6^-	99.62 ± 0.07	6^+	98.51 ± 0.22
$\langle\mathcal{P}\rangle_{\text{stat}}$	96.74 ± 0.53		99.58 ± 0.06		98.72 ± 0.14
Systs	$\bar{\Delta} = \pm 0.46$ $\delta = -0.27$		$\bar{\Delta} = \pm 0.05$ $\delta = -0.03$		$\bar{\Delta} = \pm 0.14$ $\delta = +0.12$
$\langle\mathcal{P}\rangle$	96.47 ± 0.80		99.55 ± 0.09		98.84 ± 0.26

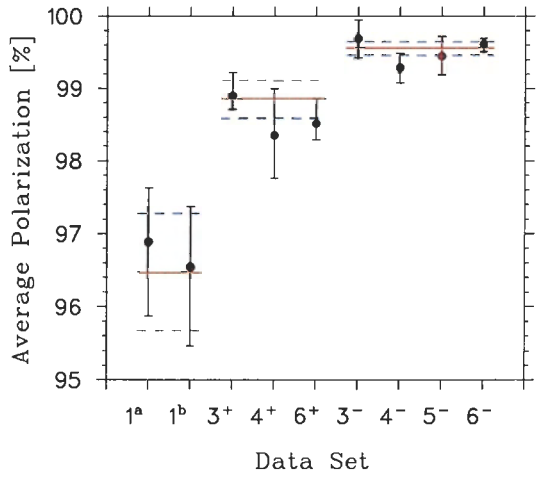

FIGURE 4.27: Average value of the combined polarization, $\mathcal{P}$, as a function of data set. These are simply a graphical representation of the results presented in Table 4.10.

Now we must factor in systematic uncertainties. As mentioned earlier, in order to obtain reasonable statistics to estimate these uncertainties, all comparable data sets were combined, and so we do not have an estimate for the individual data sets (e.g. just the 1^a data set; we only have systematics for the combination of the 1^a and 1^b data sets). This is not a problem, however, because it simply means that we must defer inclusion of systematic uncertainties in all measurements involving the polarization until we sum up similar data sets, which we will do anyway when extracting physics results. Thus, we only have three combined polarization measurements: one for the 1^a and 1^b data sets; another for the $3^+, 4^+$ and 6^+ data sets; and a final one for the $3^-, 4^-, 5^-$ and 6^- data sets.

Systematics from Tables 4.8 and 4.9 are included in Table 4.10 and added in quadrature to the combined polarizations of compatible data sets. The results are also shown graphically in Fig. 4.27 and emphasize the fact that the different polarization schemes result in different average polarizations. The bottom line in Table 4.10* shows the final estimate of the combined polarization for the three groups of data sets, including all uncertainties. In all cases, the statistical and systematic uncertainties are about equal, although the magnitude of both is much larger in the 1^{st} data sets.

*More than figuratively!

We must re-iterate again, however, that there is a systematic associated with the 3^{rd}–6^{th} data sets which we cannot estimate because as discussed in §4.6.3, we have indications that not all of atom cloud was being probed by the OP beam. The higher polarizations quoted and smaller uncertainties do indicate, however, that the next time the experiment is performed — and we are absolutely confident that the beam is fully overlapping the cloud — we can expect to achieve higher polarizations using the Helmholtz coils to provide the weak bias field for optical pumping.

CHAPTER 5

Angular Correlations

5.1 β Asymmetry, A_β

This section describes analysis of the β-singles data from the phoswich detectors as a measurement of the β asymmetry parameter. As was shown in §4.5, backgrounds from lost atoms introduce large corrections which are estimated from limited lifetime measurements and so are not known very well. Therefore, we are not able to use the current data to extract a precise measurement of A_β; however, this run has shown that we can considerably improve the measurement the next time we perform a ^{37}K experiment.

5.1.1 Introduction

As shown in Fig. 4.1, the geometry of our experiment includes two phoswich β detectors arranged to optimize a measurement of the β asymmetry parameter. The detection axis defined by these detectors was made to overlap the polarization axis (defined by the optical pumping beam) by placing the detectors behind the mirrors which reflect the optical pumping beams. We polarize our trapped atoms and compare the β rate in these detectors when the polarization is aligned vs. anti-aligned with their detection axis.

Recall from Eq. (2.6) that the β asymmetry comes into the decay rate as:

$$\frac{d^4W(\boldsymbol{p}_e,\boldsymbol{p}_\nu,\boldsymbol{I})}{d\Omega_e\,d\Omega_\nu} \sim 1+\ldots+\frac{\boldsymbol{I}}{I}\cdot\left[A_\beta\frac{\boldsymbol{p}_e}{E_e}+\ldots\right]+\ldots \tag{5.1}$$

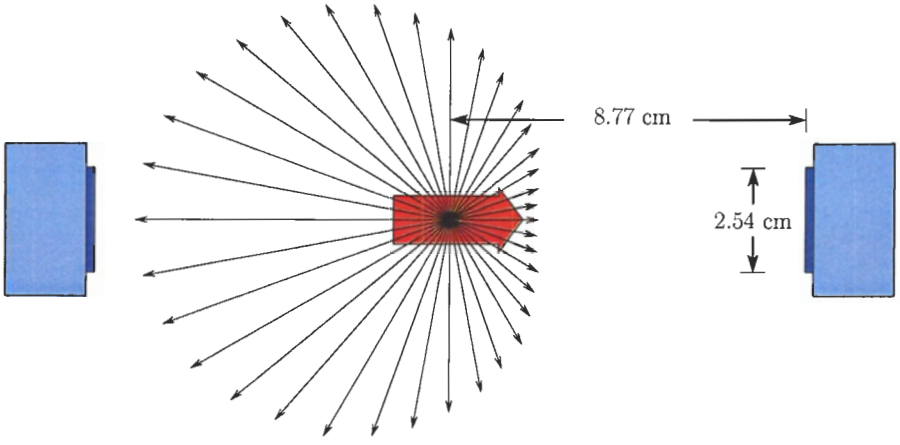

FIGURE 5.1: Schematic diagram of geometry used for the A_β measurement. Shown are the two phoswich detectors with the laser-cooled ^{37}K in the centre, polarized along the direction indicated by the fat arrow. The length of the thin arrows indicate the expected angular distribution assuming $A_\beta = -0.57$ and $P = +1$.

so one can see A_β is the relative strength of the correlation between the emitted positron and the initial nuclear polarization, $\boldsymbol{I}$. Figure 5.1 schematically shows the situation, with the expected angular distribution according to Eq. (5.1) of βs assuming the Standard Model and perfect polarization. The sign of A_β is negative, so one expects an anti-correlation with the polarization, so that the phoswich detector along $-\boldsymbol{P}$ will see a higher β rate than the one along $+\boldsymbol{P}$. By flipping the sign of the polarization, the phoswich detector will see a change in the β rate, which to first order equals $\mathcal{P}A_\beta$. With our independent measurement of $\mathcal{P}$ from §4.7.3, we are able to extract A_β from such a measurement.

For the ideal case of perfect polarization, point-like detectors and assuming the SM-based value of $A_\beta = -0.5702(5)$, we would expect to see an asymmetry of -57% in phoswich A and $+57\%$ in phoswich B. A MC simulation of this ideal case shows that finite detectors and their response functions (including energy loss through the mirrors), the finite cloud size and its position, and β (back)scattering reduces the expected asymmetry to $\pm 55\%$. Note that though the positrons are generally relativistic because of our 500 keV detection threshold, the energy dependence in Eq. (5.1) cannot be neglected.

5.1.2 Raw Asymmetries

Here we present the raw β asymmetries in the phoswich detectors. The asymmetry at this point is based on the number of accepted $E-\Delta E$ events in the phoswich detectors with conditions that: (1) there is an acceptable energy reading in both the plastic ΔE and $CaF_2(Eu)$ E detectors (see Fig. 4.4); and (2) optical pumping of the cloud had proceeded for more than 200 μs, the same condition used to deduce the cloud polarization earlier. Furthermore, because the DSSSD-scintillator telescope is perpendicular to the polarization axis and insensitive to the direction of the polarization, the number of counts in the phoswiches for each polarization state was normalized according to the counts in the β-telescope to account for differences in the number of atoms decaying. This renormalization resulted in $1\% - 2\%$ corrections to the raw rates in the phoswich detectors.

With these cuts, the number of counts in each phoswich detector for each polarization state directly give a measure of the β asymmetry:

$$A_\beta = \frac{1}{\mathcal{P}} \frac{N^{\sigma^+}_{\text{phos}} - N^{\sigma^-}_{\text{phos}}}{N^{\sigma^+}_{\text{phos}} + N^{\sigma^-}_{\text{phos}}} \tag{5.2}$$

where $N^{\sigma^\pm}_{\text{phos}}$ is the number of counts in the phoswich detector for a given polarization state normalized by the β-telescope rate, and the values of Table 4.10 were used to account for the finite polarization of the cloud. In Fig. 5.2 we show the asymmetries in the two phoswich detectors as a function of the trap/optical pumping cycle time for the 1^a data set. One can see that during the trapping times, the asymmetry is consistent with zero at the 1% level which is expected because the MOT does not generate bulk polarization of the trapped atoms. Once the optical pumping is turned on (depicted by the dotted line at $\sim$ 2.6 ms), the asymmetry quickly rises to $\gtrsim 0.4$. Once the polarization part of the cycle is finished at $\approx$ 4 ms, the MOT is reactivated to recollect atoms and we start the cycle over again.

The vacuum in the detection chamber was very good, but not perfect; this may have an effect on the observed asymmetries by shortening the trap lifetime and producing a background from atoms that decay on the chamber walls. Based on the observed 2^{nd} MOT lifetime of 30 s, the vacuum in the detection chamber was calculated to be

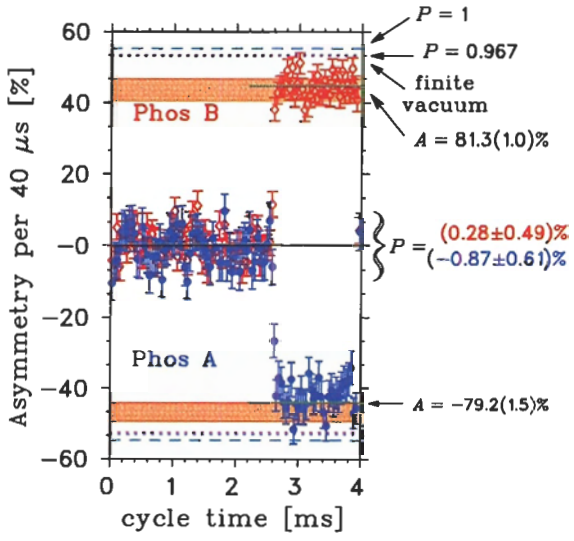

FIGURE 5.2: Asymmetry in the phoswich detectors as a function of the cycle time for the 1^a data set. The bands represent the expected asymmetries given the background deduce in §4.5 (see also §5.1.3).

3×10^{-10} Torr. To investigate the effect of the finite vacuum, we intentionally worsened it to 1×10^{-8} Torr to see how much the observed asymmetry in the phoswich detectors was reduced. We have fit the dependence of the asymmetry as a function of pressure, and estimate that there is a 0.004 attenuation due to the actual pressure of 3×10^{-10} Torr.

Referring back to Fig. 5.2, we show the expected asymmetries assuming the Standard Model and perfect polarization (dashed line with the highest asymmetry). Even once we factor in the observed polarization of 96.7% and the finite vacuum, we still expect to have a higher asymmetry than is observed. If the polarization was the source of the discrepancy, we would need a much lower polarization to agree with the fit asymmetries during polarized times. Based on the rough calculation of backgrounds in the β detectors in §4.5 and as discussed shortly in §5.1.3, we can estimate what effect untrapped atoms has on this singles measurement; this is shown as the horizontal bands in Fig. 5.2. Though the uncertainties in our background correction are large and so the band width is large, we find much better agreement with the observed asymmetries once they are included.

Figure 5.3 shows the average asymmetry over polarized times for each run. The data sets are distinguished by colour, with the average for each set listed. First is the 1^a data set, and then 1^b; following these are the subsequent data sets where the OP field switching was implemented. The first of these is the 2^+ data set which is otherwise not considered in this thesis because the trap location was being moved around and the optical pumping process was being optimized, making a quantitative analysis effectively impossible. Following in order are the 3^-, 3^+, 4^-, 4^+, 5^-, 6^- and finally 6^+. β energy cuts of 1, 2 and 3 MeV are shown in the Fig. 5.3. As one can see, the higher E_β cuts do slightly increase the observed asymmetry. However the change is not drastic, indicating that low-energy backgrounds are not overwhelmingly significant.

The most striking data sets are 1^b and 2^-, which clearly have a reduced asymmetry compared to the rest. As mentioned earlier, this is expected for the 2^- data set because these runs were used for optimization, however the 1^b data set is expected to have high polarizations based on the fits to the vanishing of the fluorescence. We will see in the next section that a large part of this discrepancy arises from atoms leaving the trap and getting sprayed onto the walls and mirrors in front of the phoswich detectors, where they (likely) depolarize and hence give a reduced asymmetry.

5.1.3 Background corrections

The phoswich detectors are not able to distinguish decays from atoms on the optical pumping mirrors from atoms from the trap region. Since atoms implanted on the mirrors likely depolarize, they represent a significant background to the A_β measurement. When these atoms β decay, they do so with no correlation with the polarization axis and so the phoswich detectors will see a suppressed asymmetry, depending on how many decays it observes from the trap region versus atoms from the mirrors.

The results of §4.5 give us an idea as to how many atoms are lost and may have been deposited onto the mirrors. We can correct the observed asymmetry assuming these lifetime measurements give an accurate estimate of this background. Figure 5.4 is the same as Fig. 5.3, but this time the β asymmetries are corrected for atoms

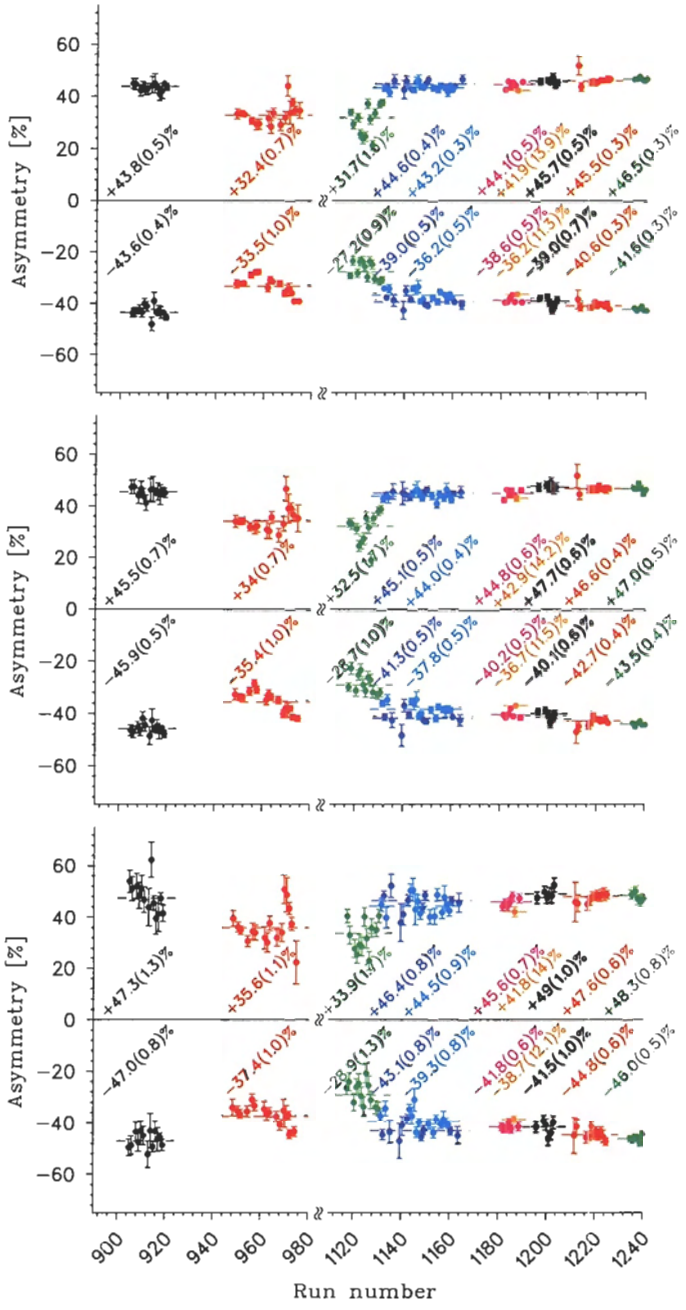

FIGURE 5.3: β asymmetries deduced from the phoswich detectors using a $E_\beta = 1$ MeV (top), 2 MeV (middle) and 3 MeV (bottom) cuts. In this case, the only correction applied is a renormalization based on the counts in the β-telescope for the $\sigma^\pm$ polarization states.

lost based on the lifetime measurements. The 1^a data set, for which we do not have lifetime measurements, has been corrected based on the lifetime measurements of the 1^b data set because they both share the same optical pumping scheme. The extremely high asymmetries of the 1^a data set seen in Fig. 5.4 indicates that the losses were greater in the 1^b data set, and that we have likely over-corrected the 1^a data set. The 1^b and subsequent data sets all have improved asymmetries, but are generally still slightly below the $\pm 55\%$ asymmetry expected for the Standard Model prediction of $A_\beta = 0.5702(5)$.

5.1.4 Discussion

The phoswich detectors in the present system are clearly prone to a large background due to lost atoms from the trapping region, making a precise measurement of A_β impossible. The deduced backgrounds in the β detectors from the lifetime measurements prove that these backgrounds exist; however, since we only measured the rates in the detectors under one half-life, our measurements of the backgrounds are not good enough to make a precise correction possible. Qualitatively, though we know from §4.7 that the $3^{\text{rd}} - 6^{\text{th}}$ data sets did not polarize the entire cloud, the lifetime measurements show that these backgrounds are reduced when the Helmholtz coils were used to optically pump the atoms. This implies that a subsequent experiment with this optical pumping scheme optimized will require a smaller correction.

Table 5.1 shows the backgrounds needed to obtain the SM prediction with and without the corrections from the lifetime measurements. Without the corrections, one can see that the asymmetries fall well below the Standard Model prediction. Once the corrections are applied, the asymmetries become much closer to agreeing with predictions. The uncertainties are significantly increased because our estimates of the backgrounds are coarse. It is encouraging to note that we have not overestimated the backgrounds because there are no significantly negative values once the corrections are applied. It does seem, however, that we may have underestimated the backgrounds in Phos A where agreement with the SM would require statistically significant extra backgrounds than are accounted for; Phos B is generally consistent with the SM,

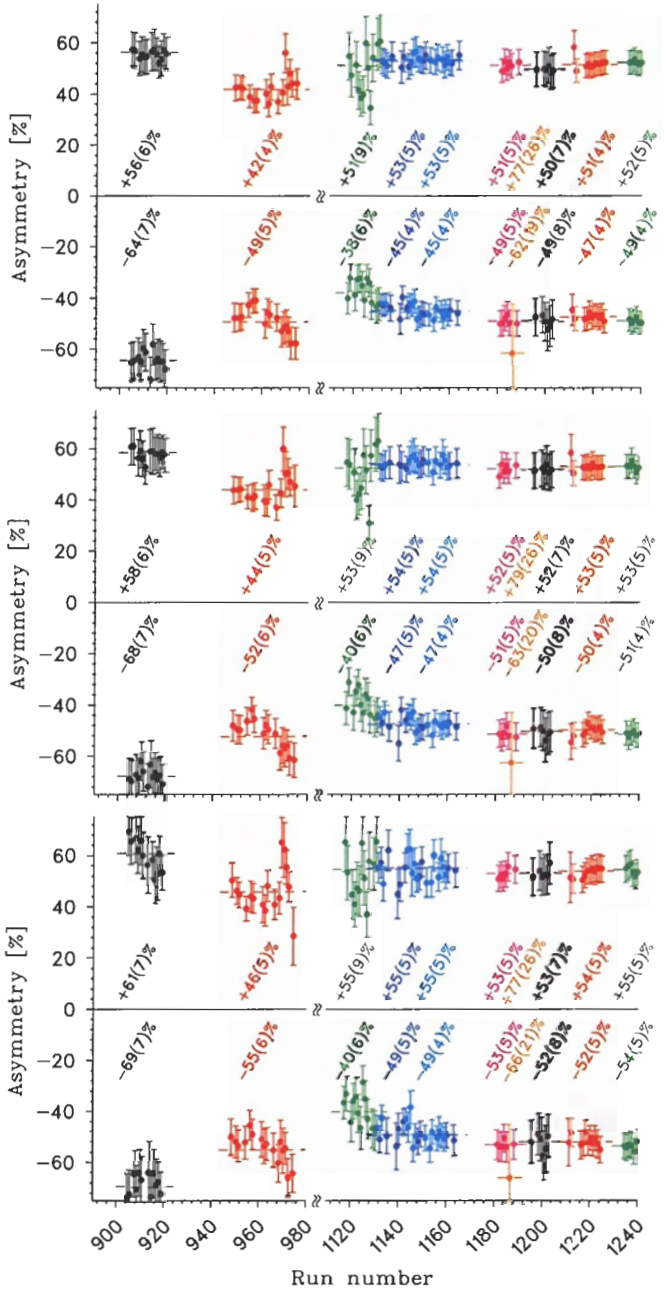

FIGURE 5.4: β asymmetries deduced from the phoswich detectors using a $E_\beta = 1$ MeV (top), 2 MeV (middle) and 3 MeV (bottom) cuts. In this case, corrections for both the normalization of $\sigma^\pm$ in the scintillator and the backgrounds based on the lifetime fits are applied.

TABLE 5.1: "Extra backgrounds" needed for the observed asymmetries in the phoswich singles β spectra in order to agree with the expected asymmetry of $\pm 55\%$ based on the Standard Model prediction of $A_\beta = 0.57$. The β energy cut in this case is 1 MeV. All values are in percent, and the "non-extra backgrounds" in the phoswich detectors are taken from the results of §4.5.

Data set	no background correction		including lifetime results	
	Phos A	Phos B	Phos A	Phos B
1^a	10.4± 0.4	10.2± 0.4	−8.6± 6.2	−1.1± 5.3
1^b	19.6± 0.9	20.5± 0.6	5.0± 4.9	12.1± 4.0
2^-	25.3± 0.8	21.2± 1.4	15.5± 5.1	3.4± 8.0
3^+	14.5± 0.5	10.7± 0.3	9.3± 3.6	1.4± 4.3
3^-	14.5± 0.4	9.5± 0.4	9.3± 3.9	1.8± 4.5
4^+	17.1±10.3	11.9±12.6	−6.2±17.5	−20.4±23.3
4^-	14.9± 0.4	9.9± 0.5	5.3± 4.5	3.5± 4.3
5^-	14.5± 0.6	8.4± 0.5	5.8± 6.9	4.7± 6.0
6^+	12.1± 0.3	7.8± 0.3	5.9± 3.9	2.3± 4.1
6^-	13.1± 0.3	8.6± 0.3	7.0± 3.8	3.2± 4.0

although the large uncertainties mean that we cannot extract a test of the SM or place any interesting limits on new physics using the β asymmetry.

In future experiments, it will be necessary to understand and remove the loss of atoms. Assuming the loss is correlated with the violent cloud movements throughout the optical pumping/trap cycle, this can be developed off-line using stable potassium species. Longer lifetime measurements would be useful to test how well the fit half-life agrees with the measured value, but attempting to make corrections based on these measurements will never result in a precise measure of A_β; we have had to make too many assumptions (like the homogeneity of the losses, that the atom fully depolarizes when implanted on the mirror/wall, etc.), and it is unlikely we would ever measure the background to less than a percent using the lifetime. Therefore, if a precise measurement of A_β is to be feasible, we *must* develop our optical pumping techniques such that atoms are not lost during the MOT/OP cycling.

5.2 The Neutrino Asymmetry, B_ν

This section describes how we use our clean β–Ar coincidences in the back-to-back geometry to measure the neutrino asymmetry. The detectors involved have been well-characterized and understood in great detail from the $0^+ \rightarrow 0^+$ scalar [11, 9] and massive neutrino [12, 13] searches.

5.2.1 Introduction

We begin by looking at the angular distribution of the β decay and noting that one is sensitive to the neutrino asymmetry, B_ν, in the back-to-back geometry.

Consider the set-up of the MCP and plastic scintillator with the polarization axis perpendicular to the detection axis as depicted by the schematics in Fig. 5.5. In order to intuitively understand the situation, let us take the limit of a point-like β detector (so that $\boldsymbol{p}_e = p_e\hat{z}$) and assume that the neutrino is emitted perpendicular to the detection axis (*i.e.* $\boldsymbol{p}_\nu \cdot \boldsymbol{p}_e = \boldsymbol{p}_\nu \cdot \hat{z} = 0$).

For a given nuclear polarization along $\hat{x}$, the neutrino will be preferentially emitted

along or against it. As the name of this correlation implies, this is akin to the β asymmetry, the only difference being which lepton is correlated with the initial nuclear spin. The sign of B_ν determines the direction, and the magnitude gives the degree of this correlation. For ^{37}K, the SM predicts that the sign is negative, and that the magnitude is large, ≈ 0.75 (see §2.1.2). Thus if the optical pumping beam is σ^+ so that the nucleus is polarized along $+\hat{x}$, then case (a) in Fig. 5.5 will be highly suppressed relative to case (b). Conservation of momentum — and the fact that the laser-cooled ^{37}K decays from rest — allows us to relate the unobserved neutrino momentum in terms of that of the positron and recoil: $\boldsymbol{p}_\nu = -\boldsymbol{p}_e - \boldsymbol{p}_{\rm Ar}$. In the idealized scenario outlined here, the recoil momentum in the $\hat{z}$ direction is $-p_e$, while in the $\hat{x}$ and $\hat{y}$ directions, $\boldsymbol{p}_{\rm Ar} = -\boldsymbol{p}_\nu$. Therefore, the suppression of (a) and enhancement of (b) translates into a greater number of recoils striking the MCP at $x > 0$. The collection efficiency of the Ar ions — even those with a relatively high transverse momentum, which of course are most sensitive to B_ν — are enhanced by the focusing effect of the electric field. If the optical pumping beam is instead σ^- polarized, the nuclear polarization will be along $-\hat{x}$ and so the situation is reversed; in this case, scenario (b) is suppressed and one would see more events at $x < 0$.

In terms of the decay rate, Eq. (2.5), one can easily show that flipping the polarization direction will give rise to an asymmetry in the decay rate that goes like:

$$\frac{dW(\sigma^+) - dW(\sigma^-)}{dW(\sigma^+) + dW(\sigma^-)} = \mathcal{P}B_\nu \cos\theta_{\nu i} - \mathcal{P}D\left(\tfrac{p_e}{E_e}\right)\sin\theta_{\nu i} \tag{5.3}$$

Here $\mathcal{P} \equiv \langle \boldsymbol{I} \rangle / I$ is the average effective nuclear polarization for both signs of the optical pumping light, as defined in §4.7.3, and $\theta_{\nu i}$ is the angle between the neutrino and the polarization axis, which we assume lies exactly along $\hat{x}$. Thus the recoil asymmetry in the $\hat{x}$ direction is:

$$\left.\frac{dW(\sigma^+) - dW(\sigma^-)}{dW(\sigma^+) + dW(\sigma^-)}\right|_{\hat{x}} = -\mathcal{P}B_\nu \left(\hat{p}_{\rm Ar} \cdot \hat{x}\right) \tag{5.4}$$

If we consider the cases where the neutrino was emitted in the $\pm\hat{x}$ direction, then the magnitude of the recoil asymmetry will be $\mathcal{P}B_\nu$. A precise measurement of the recoil asymmetry therefore translates into a direct measurement of the combination

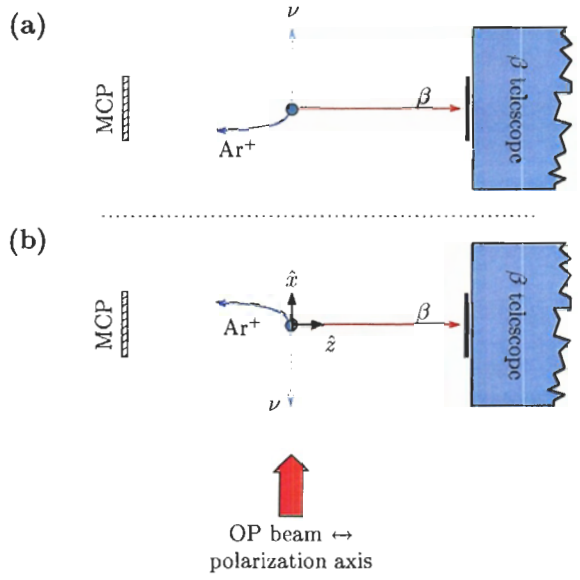

FIGURE 5.5: Schematic diagram of the geometry used to measure the neutrino asymmetry.

$\mathcal{P}B_\nu$ which, since the polarization is measured independently, allows us to measure the neutrino asymmetry parameter. The position of recoil events in the MCP along the polarization axis will be related to the $\hat{x}$ component of the recoil momentum. Inclusion of finite detector sizes and allowing the daughter products to be emitted into 4π means that Eq. 5.4 is no longer true, and that the asymmetry cannot be expressed as an analytic function of the MCP position; however, MC techniques can be used to extract the value of B_ν from the observed recoil asymmetry.

Figure 5.6 shows the MCP position spectra for β–Ar coincidences for the 1^a data set. The charge states $+1, +2$ and $+3$ were selected based on the TOF between the scintillator and MCP and then summed. The neutrals cannot be used in this data because the MCP energy and (especially) position efficiencies are prone to large systematics. The top panel shows both the 2D and the corresponding 1D projections for both σ^+ (left) and σ^- (right) polarized optical pumping light. As one can see from the bottom-left plot, there is a clear asymmetry between the two in the $\hat{x}$ direction. The red lines are a MC simulation assuming the SM and as mentioned above, relates Eq. 5.4 to the observed position asymmetry.

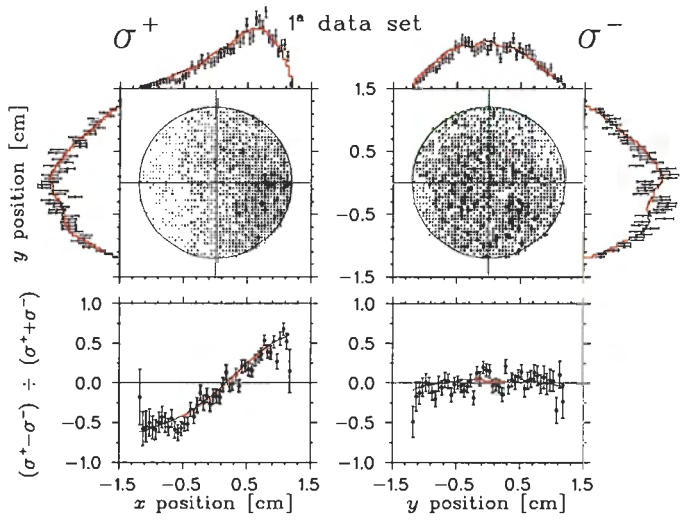

FIGURE 5.6: MCP $Ar^{+1,2,3}$ β-coincident position spectra. The black points are data and the solid red line is a MC simulation (see text).

The $\hat{y}$ asymmetry is shown in the bottom-right plot, and in this case, the recoil asymmetry is given by:

$$\left.\frac{dW(\sigma^+) - dW(\sigma^-)}{dW(\sigma^+) + dW(\sigma^-)}\right|_{\hat{y}} = -\mathcal{P}D\,\frac{p_e}{E_e}\left(\hat{p}_{\mathrm{Ar}} \cdot \hat{y}\right), \tag{5.5}$$

A finite asymmetry will ideally only be observed if the time-violating correlation parameter D is non-zero (up to final-state effects, of course). Note, however, that systematics may also provide a false signal; for example, even a small $\hat{y}$ component of polarization can give rise to an asymmetry through the B_ν term, and thus this asymmetry is very sensitive to the direction of the nuclear polarization. An asymmetry can also arise if the cloud position differs between the two polarization states.

5.2.2 Method of Fitting the Data to MC Simulations

The predicted shape of the $\hat{x}$ asymmetry is generated using MC simulations of the experiment, where the tracking of the βs is done using GEANT. This 'theory curve' is then fit to the data in order to determine the experimental value for B_ν. Incorporated in the MC are: the finite sizes of the detectors; the detector response function, including β scattering and annihilation-in-flight; the electric field; the effective polarization

of the atomic sample; and the finite size and position of the expanding, polarized cloud. Input into all simulations are the measured value of the ratio of Fermi to Gamow-Teller matrix elements, and the resulting Standard Model prediction for the neutrino asymmetry, *i.e.* $B_\nu^{\rm SM} = -0.7692(14)$ (see §2.1.2).

Referring back to Fig. 5.6, the simulations for $\sigma^\pm$ polarization are first separately fit to the 1D $\hat{x}$ projections with an overall scaling factor free to vary. This ensures that the relative normalization of the spectra for two polarization states are optimal before generating the simulated asymmetry. In general, these fits produced normalization factors such that the number of counts in both the data and the MC were equal. All simulations were generated with at least 100× more events than the data so that the statistical uncertainty in all of the fits were not biased by the finite statistics of the simulations. Once the MCs were normalized, a simulated asymmetry curve was generated in exactly the same way as the data, *i.e.* for both the data and the MC, we define the MCP position asymmetry as a function of the x_i coordinate (either $\hat{x}$ or $\hat{y}$) as:

$$\mathcal{A}(x_i) = \frac{N^+(x_i) - N^-(x_i)}{N^+(x_i) + N^-(x_i)} \tag{5.6}$$

where $N^\pm(x_i)$ is the number of counts in the $i^{\rm th}$ bin for which the optical pumping light was $\sigma^\pm$ polarized.

The obvious approach to fitting the data is to generate a number of MCs with various values of B_ν, and then to fit the data directly by making a χ^2 map as a function of the value of B_ν input into the MC. This approach, though simple and valid, was not used due to the exorbitant computing resources required, especially when investigating potential systematics*.

Instead, the method used to extract B_ν from the data was to exploit the fact that the magnitude of the asymmetry scales like $\mathcal{P}B_\nu$. With an overall scaling factor, κ, free to vary, we fit the data to a MC by minimizing the χ^2 between the two asymmetry curves. This scaling factor represents the ratio of the best fit $\mathcal{P}B_\nu$ to that input into the simulation. This way, we only need to generate one reference value for the polarization and the neutrino asymmetry; in all cases, the Standard Model

*For each of the nine data sets, we require over 150 MCs *for each value of* B_ν simulated!

prediction for B_ν is used for the neutrino asymmetry, while the polarization is taken to be the best estimate for each data set. If we let $\mathcal{B}_\nu$ represent these reference values for the polarization and asymmetry parameter:

$$\mathcal{B}_\nu \equiv \mathcal{P}_{\rm ref} B_\nu^{\rm SM}, \tag{5.7}$$

then based on the decay rate (see Eq. (5.4)), the scaling factor should be given by:

$$\kappa = \frac{\mathcal{P}B_\nu}{\mathcal{B}_\nu}. \tag{5.8}$$

The shape of the asymmetry curve is determined primarily by the acceptance of the detectors and the strength of the electric field, while the magnitude of the asymmetry will be defined by the value of $\mathcal{P}B_\nu$. Fitting a value for κ by scaling the normalization of the asymmetry curve is therefore equivalent to fitting the combination $\mathcal{P}B_\nu$. If the true value of $\mathcal{P}B_\nu$ is less than the reference values, our fit value for κ would be less than unity; conversely, if $\mathcal{P}B_\nu > \mathcal{B}_\nu$ then we would find $\kappa > 1$. Of course if our input $\mathcal{B}_\nu$ exactly reflects reality, our fit would return $\kappa = 1$. Note that because the value of $\mathcal{B}_\nu$ simply represents a reference point, the actual value input into the MC is arbitrary, at least for small deviations from the true value. In order to confirm that this is true, simulations with varying values of B_ν were compared to each other, and it was found that the asymmetry curves did in fact scale linearly over a wide range ($\pm 15\%$) to within the MCs statistical uncertainties ($\lesssim 0.2\%$).

Once a value for κ is fit, we rearrange Eq. (5.8) to get:

$$B_\nu = \frac{\kappa \mathcal{B}_\nu}{\mathcal{P}}, \tag{5.9}$$

and since the reference value of the effective polarization input into the MC is $\mathcal{P}_{\rm ref} = \mathcal{P}$, the one we measured using the photoions, the polarizations cancel and we are left with:

$$B_\nu = \kappa B_\nu^{\rm SM} \tag{5.10}$$

when evaluating the neutrino asymmetry. The uncertainty in this value of B_ν will have contributions from both the fit result of κ as well as the uncertainty in the fit polarization. From Eq. (5.9):

$$\frac{\sigma_{B_\nu}^2}{B_\nu^2} = \frac{\sigma_\kappa^2}{\kappa^2} + \frac{\sigma_\mathcal{P}^2}{\mathcal{P}^2} \tag{5.11}$$

Note that there is no contribution from $\mathcal{B}_\nu$ because as mentioned before, this is simply a reference point; it can be taken to be any value — at least any one reasonably close to the fit result — and hence, no uncertainty is associated with it. The correlation between κ and $\mathcal{P}$ is zero because of the way we have defined κ: polarizations cancel, even if they are improperly estimated, *i.e.* if our estimated polarization, $\mathcal{P}$, is $\mathcal{P}_{\text{true}} \pm \delta\mathcal{P}$, then the reference polarization will similarly be $\mathcal{P}_{\text{ref}} = \mathcal{P}_{\text{true}} \pm \delta\mathcal{P}$ and the bias cancels. In the end, then, κ remains unchanged, and so $\text{cov}(\kappa, \text{P}) = 0$.

Recall that evaluation of the systematics in $\mathcal{P}$ for introduces small shifts in the best estimate of the combined polarization, and that this shift is *not* included in the simulations; this bias, then, will not cancel with the reference value in $\mathcal{B}_\nu$. When evaluating the final value of B_ν, a shift of $\delta\mathcal{P}$ must be propagated through to B_ν according to:

$$\begin{aligned} B_\nu &\rightarrow \frac{\kappa\mathcal{B}_\nu}{\mathcal{P} + \delta\mathcal{P}} \\ &\approx B_\nu(1 - \delta\mathcal{P}/\mathcal{P}) \end{aligned} \tag{5.12}$$

5.2.3 Fit results

Using the method outlined above, and the numerical fitting techniques described in §B.1, we have fit each of the data sets to obtain a value for κ. Using the best estimates of the cloud characteristics, the polarization, the electric field, etc., as given in §4.4–§4.7, we generated MC simulations and analyzed the MCP position spectra in the exact same manner as the data: The atoms are given the average polarization as deduced by the photoion fits and move/expand according to the deduced positions, velocities and temperatures. Decays are generated after the atoms have been released for 200 μs, and the decay products are tracked. GEANT is utilized to track the βs while the simple Ar–recoil tracking in the constant electric field provides us with the TOF. The MC generates βs with kinetic energy as low as 50 keV, but — like the data — has a T_β threshold of 500 keV imposed after all tracking is completed. Our best estimate of the MCP position efficiency and the charge states (generated randomly at the time of the decay) are determined from their TOF, as is done with the data.

The plots in Fig. 5.7 show the results of fits for the 1^a (left) and 1^b (right) data sets. The top panel shows the σ^+ (filled circles) and σ^- (open circles) projections for the Ar^{+1}'s ($640 \leq \texttt{mh5} \leq 1100$ ns, where recall that $\texttt{mh5} = \text{TOF} + t_{\text{offset}}$) as well as the comparison to the MC simulation (green and blue lines, respectively). The difference in shape of the two polarization states is due to the kinematic acceptance of the system with the trap offset from the centre of the MCP. Below these position spectra we plot the asymmetry and overlaid as a histogram is the fit result for κ. In the case of the Ar^{+1} data, the position spectra are binned such that there are 1.5 mm/bin for the 1^a data set, and due to the greater statistics, 1 mm/bin for 1^b. As one can see, the agreement between the MC and the data in the projections is rather poor, but once the asymmetry is taken, the fit gives a reasonable χ^2. The beauty of the relative measurement is now made clear: many systematic problems which would plague an absolute measurement (*i.e.* the projections) cancel to first order once the asymmetry is taken, and thus a relatively much cleaner measurement may still be made of the neutrino asymmetry. The most significant culprit in the discrepancies of the projections is the MCP position efficiency; however, since both σ^+ and σ^- are equally affected and we are taking the asymmetry in each position bin, the (in)efficiencies largely cancel resulting in a well-behaved asymmetry curve.

Also shown in Fig. 5.7 are the fit results for the Ar^{+2} ($525 \leq \texttt{mh5} < 640$ ns) and Ar^{+3} ($470 \leq \texttt{mh5} < 525$ ns) position spectra. When calculating the asymmetry, Gaussian statistics is assumed in order to be able to assign uncertainties to the asymmetry points; in order to ensure that this assumption is valid, we have rebinned the data until most bins have $\gtrsim 65$ counts. If we retained 1 mm wide bins for the Ar^{+3} spectrum, for example, our calculated weights when fitting the asymmetry curve would be highly biased since in fact each projection follows Poisson statistics, which only approaches Gaussian as the number of counts gets large*.

Once all three charge states were fit, the final value for κ was calculated by taking a weighted average of the three. Clearly, with the Ar^{+1} data having the most events, the κ deduced for a given data set will be dominated by these events. The +4 and higher charge states were not used because, in order to validate the Gaussian approximation

*This will be further discussed as a source of systematic uncertainty in κ shortly.

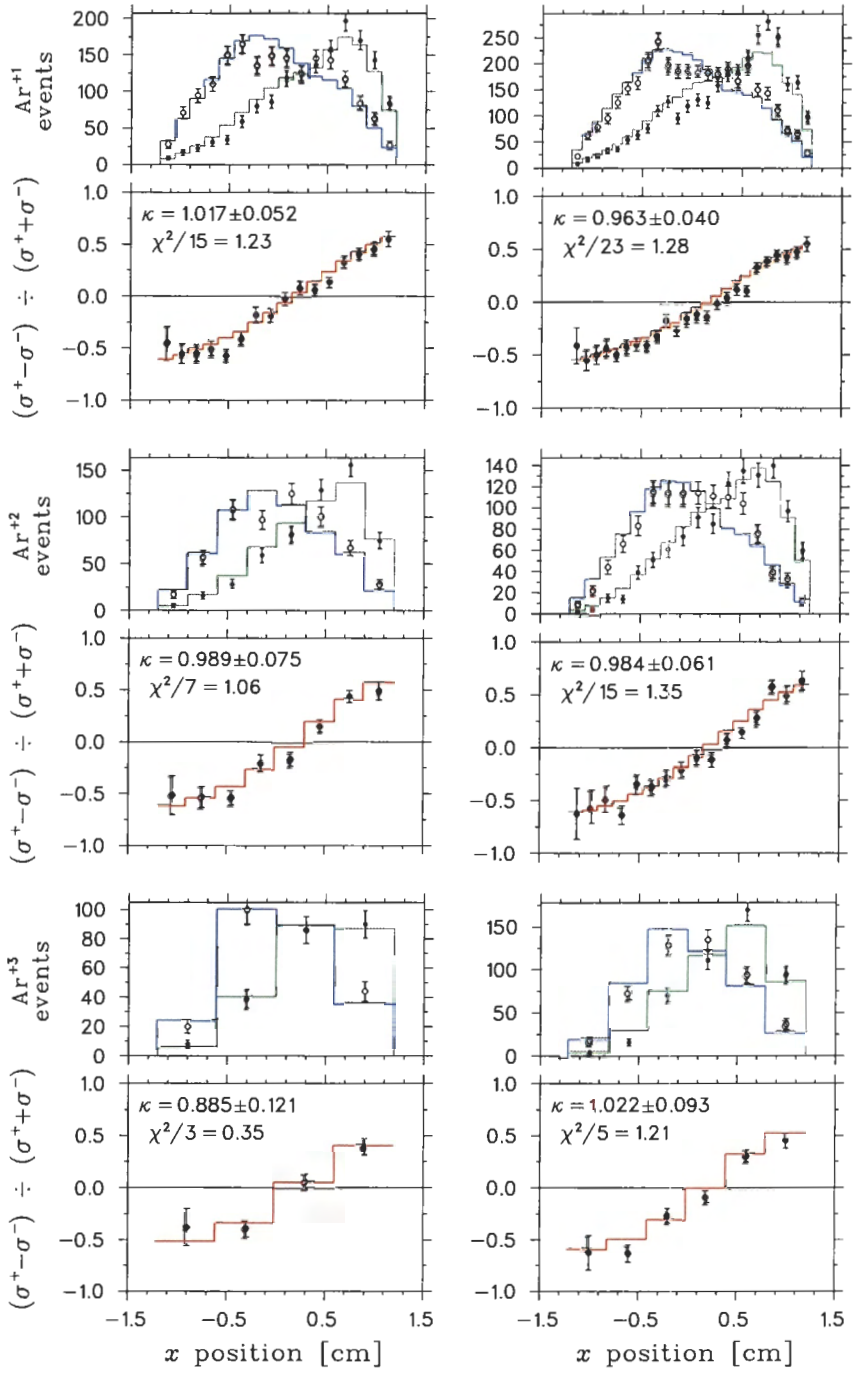

FIGURE 5.7: Best fit of κ using the Ar–β coincidences for the 1^a (left) and 1^b (right) data sets (see text).

TABLE 5.2: Fit results to the scaling factor, κ, using the best estimates of all input parameters. The uncertainties quoted here are purely statistical.

Data set	$\kappa = \frac{B_\nu}{B_\nu^{\rm SM}}$	Data set	$\kappa = \frac{B_\nu}{B_\nu^{\rm SM}}$	Data set	$\kappa = \frac{B_\nu}{B_\nu^{\rm SM}}$
1^a	0.995 ± 0.040	3^-	0.966 ± 0.031	3^+	0.993 ± 0.031
1^b	0.975 ± 0.031	4^-	0.912 ± 0.023	4^+	0.900 ± 0.069
		5^-	0.889 ± 0.042		
		6^-	0.915 ± 0.024	6^+	0.935 ± 0.028
$\langle\kappa\rangle = 0.983 \pm 0.025$		$\langle\kappa\rangle = 0.921 \pm 0.014$		$\langle\kappa\rangle = 0.956 \pm 0.020$	

when calculating the asymmetry, we would have to use 1.2 cm wide bins, which would not give an asymmetry "curve".

The best fit κ's averaged over the three charge states for all of the data sets are listed in Table 5.2. From this, one can see that the data sets where the field switching was implemented have, on average, a significantly smaller value for κ than in the $1^{a,b}$ data sets. As was discussed in §4.6.3, it was found by analysis of the TOF of the photoions that the optical pumping beam was likely not fully overlapped with the atomic cloud, resulting in an inestimable systematic on the cloud's polarization. The apparent neutrino asymmetry for these data sets is expected to be smaller since, if a part of the cloud was unpolarized, those decays will suppress the MCP position asymmetry. Therefore, in what follows, we will not consider these data sets and will only concentrate on 1^a and 1^b where the polarization is better understood.

5.2.4 Systematics in κ

This section explains how potential systematics to the asymmetry curve fits were estimated. As this section shows, our largest systematic uncertainties arise from our limited knowledge of the cloud position during the polarized part of the MOT/OP cycle. All other potential sources investigated affecting the fit value of κ are $\leq 50\%$ of this dominant systematic.

Cloud position during polarized times

Due to the finite statistics of the photoions, our knowledge of where the cloud was at the start of the polarization part of the cycle (*i.e.* at about 2.6 μs in Figs. A.1– A.10) has an uncertainty associated with it; not surprisingly, the observed asymmetry is extremely sensitive to systematic positional shifts between the $\sigma^{\pm}$ polarization states. Similarly, the position at the end of the optical pumping cycle, when the MOT is turned back on to re-collect the atoms, has an uncertainty. The mean position of the cloud throughout the polarized times over which we increment the MCP position spectra to make the B_ν measurement will have an uncertainty characterized by the initial cloud position, $x_\circ$, and the interpolated group movement of the cloud, v_{sail}. Below we discuss the uncertainties introduced by these potential systematics.

Initial cloud position As far was we can tell, the cloud did not shift between σ^+ and σ^-. However, we can only say that to the precision that the centroid of the photoion peaks are determined (see §4.6.3). If the position was different between the two — especially in the $\hat{x}$ direction — then the resulting asymmetry could be greatly affected and be either enhanced or suppressed (depending on which way the cloud shifted).

In fact, this scenario is difficult to imagine because the initial cloud position is determined entirely by the MOT, which is exactly the same in the two cases. The $\sigma^{\pm}$ optical pumping light is only applied *after* the cloud is released, and since the MOT destroys any 'memory' the atoms may have had from the previous optical pumping cycle, it seems unlikely that there could be a relative shift in the initial cloud position between the two polarization states. However, an apparent shift may arise due to the finite statistics in measuring the centroids; and perhaps more likely, it is conceivable that the re-collection of the expanded atoms from the previous cycle may not have attained equilibrium before releasing again. Also, small but possibly finite lingering $\boldsymbol{B}$ fields may cause a shift. Since the dependence on such a possibility is severe, we have investigated what effect it may have had on our fit value of κ in order to assign a uncertainty arising from this potential systematic.

To determine the potential effect on the fit value of κ, we compared fit results where the cloud position input into the MC was shifted by the uncertainty as deduced by fits to the photoions (see Table 4.3), with all other parameters fixed at their best values*. For example, consider the $\hat{x}$ positions of the 1^a data set; in this case, the best estimates of the average positions gave $x_\circ^{\sigma^+} = 2.89(6)$ mm and $x_\circ^{\sigma^-} = 2.83(6)$ mm. The difference of these nominal positions is consistent with zero, and so shows no significant indication of the cloud moving between polarization states. However, due to the limited precision in these measurements of the centroids, the cloud *may* have moved by 0.06 ± 0.008 mm. To account for that possibility, we generated MC simulations where the positions were at $x^{\sigma^+} = x_\circ^{\sigma^+} \pm \delta x_\circ^{\sigma^+}$ and $x^{\sigma^-} = x_\circ^{\sigma^-} \mp \delta x_\circ^{\sigma^-}$ (with y and z fixed at their best estimates, $y_\circ$ and $z_\circ$). Continuing with the $\hat{x}$ positions of the 1^a data as an example, the fit results for κ using these positions are listed in Table 5.3. As one can see from Fig. 5.6, when the MC has $x \gtrless x_\circ$ for $\sigma^\pm$, the simulated asymmetry will increase and we fit a smaller value for κ; conversely, for $x^{\sigma^\pm} \lessgtr x_\circ^{\sigma^\pm}$ the MC's asymmetry will be attenuated and the fit yields a larger scaling factor to reproduce the data's asymmetry.

As outlined in §B.2.2, we can estimate the uncertainty in our fit value of κ based on these points. Note however that the quantity of interest here is the mean difference between the centroids, so evaluating the points at their $\pm 1\sigma$ values is an overestimate by a factor of $\sqrt{2}$; hence $\bar{\Delta}$ and δ defined by Eq. (B.36) must be scaled to $\bar{\Delta} \to \bar{\Delta}/\sqrt{2}$ and $\delta \to \delta/2$, respectively. The three points in Table 5.3 yielded a Type B systematic of $\delta\kappa = {}^{+0.0114}_{-0.0108}$. In this case, the uncertainties are essentially symmetric†: δ adds only a +0.03% shift, and the symmetrized 1σ systematic uncertainty is $\bar{\Delta} = 1.1\%$. By Eqs. (B.38) and (B.39), the deduced expectation value is $E[\kappa] = 0.995$ with a Type B uncertainty of $\sigma_\kappa = 0.011$.

Systematics were estimated in this manner for each of the three directions ($\hat{x}$, $\hat{y}$ and $\hat{z}$) separately. For $\hat{y}$ and $\hat{z}$, the potential systematic is expected to be small because small shifts in these directions will have only little bearing on the $\hat{x}$ asymmetry via

*Correlations between this and other systematics (particularly v_{sail}, the cloud movement during optical pumping times) will be discussed later.

†Indeed, a third (in)significant digit has been retained in order to see *any* asymmetry at all.

TABLE 5.3: Fit results used to estimate the systematic due to the uncertainty in the cloud positions of the $\hat{x}$ direction for the 1^a data set.

$\hat{x}$ position (mm)				fit value
σ^+ polarization		σ^- polarization		of κ
$x_\circ^{\sigma^+} + \delta x_\circ^{\sigma^+}$	$= 2.95$	$x_\circ^{\sigma^-} - \delta x_\circ^{\sigma^-}$	$= 2.77$	0.9800
$x_\circ^{\sigma^+}$	$= 2.89$	$x_\circ^{\sigma^-}$	$= 2.83$	0.9951
$x_\circ^{\sigma^+} - \delta x_\circ^{\sigma^+}$	$= 2.83$	$x_\circ^{\sigma^-} + \delta x_\circ^{\sigma^-}$	$= 2.89$	1.0114

the finite acceptance of the detectors; however, it is not clear which variation will have the largest effect. In $\hat{x}$, it is obvious that if we increased/decreased both $\sigma^\pm$ centroids simultaneously, the effect would largely cancel and so in that case, we only compare opposite variations. In the case of $\hat{y}$ and $\hat{z}$, in addition to the comparisons made for $\hat{x}$, we also compared simulations where, e.g., $y^{\sigma^+} = y_\circ^{\sigma^+} \pm \delta y_\circ^{\sigma^+}$ and $y^{\sigma^-} = y_\circ^{\sigma^-} \pm \delta y_\circ^{\sigma^-}$. The final systematic was taken to be the larger of the two variations in κ.

The results for all directions (which were "independently varied") are listed in the error budget of Table 5.4 at the end of this section. As expected, the $\hat{x}$ direction overwhelmingly dominates the systematic due to the initial cloud position uncertainty, by a factor of more than five. Intuitively, one would not expect high correlations between the three directions, and especially since the systematics from $\hat{y}$ and $\hat{z}$ are inherently small, we neglect correlations and add the three contributions in quadrature to get the total systematic arising from the initial cloud position. As a check of this, we also made simulations where all three directions were simultaneously varied by their uncertainties and compared the resulting fit values of κ. Explicitly, we compared fits ("simultaneously varied") where the positions were $(x_\circ, y_\circ, z_\circ)^{\sigma^+} \rightarrow (x_\circ \pm \delta x_\circ, y_\circ \pm \delta y_\circ, z_\circ \pm \delta z_\circ)^{\sigma^+}$ and $(x_\circ, y_\circ, z_\circ)^{\sigma^-} \rightarrow (x_\circ \mp \delta x_\circ, y_\circ \mp \delta y_\circ, z_\circ \mp \delta z_\circ)^{\sigma^-}$. In both data sets, the systematic uncertainties deduced this way are consistent with the sum of the three independently varied estimates for each of $\hat{x}, \hat{y}$ and $\hat{z}$. This is consistent with the expectation that the three positions are independent variables. The shifts, δ, however, show larger variations than the $\bar{\Delta}$s, and it is unclear which estimate is to believed over the other; we therefore have opted to average the two shifts for each

data set, *i.e.* for 1^a, we take δ to be +0.001 due to the Type B uncertainties in the initial cloud position.

Cloud sail velocity In addition to the uncertainty in the initial cloud position just described, the movement of the cloud during optical pumping times introduces a potentially large source of systematic uncertainty. Recall from §4.6.3 that this 'sail velocity' was determined based on a linear interpolation between the cloud positions at the start and end of the optical pumping part of the cycle. Again — at least for the $1^{a,b}$ data sets — there do not appear to be significant differences in the sail velocities between σ^+ and σ^- (see Table 4.4) because the small shifts are within uncertainties (these shifts are included in the MCs. However, much like the initial cloud position, the fit value of κ is very sensitive to the uncertainty on our estimate of (particularly the $\hat{x}$ component of) v_{sail}.

In this case, a difference in v_{sail} between the two polarization states is not as difficult to imagine: the D_1 optical pumping light, though meant to only affect the internal degrees of freedom of the atoms, also has a slight effect on the atoms' external motion since they necessarily absorb some D_1 photons. However, it only takes an average of 6.2 absorptions of the D_1 light to optically pump an atom into the stretched state. Once there, it no longer absorbs any more $\sigma^\pm$ light (because there is no $M_F = 3$ state to get excited to). With such a small absorption rate of the optical pumping light, we do not expect that the D_1 laser beam is significantly heating the atoms. A D_1 photon imparts $\approx$ 1.5 eV/c of momentum per absorption*, which is small compared to the component of the cloud's sail velocity along the pumping beam axis (e.g. $\sim$ 70 cm/s, for 1^a, corresponding to a momentum of $Mv \approx 80$ eV/c). The fact that both σ^+ and σ^- absorb similar amounts of pumping light throughout the cycle further† reduces the difference between the sail velocities.

An analysis akin to that just used to estimate the uncertainty from the initial cloud

*Note that because we have counter-propagating beams that are of nearly equal intensity, the overall momentum imparted during optical pumping will not be much larger than the one photon absorption.

†However, based on the fits of the polarization, σ^- absorbs $\sim$ 50% more optical pumping light than σ^+ for the $1^{a,b}$ data sets.

position was similarly performed for $\boldsymbol{v}_{\text{sail}}$: with all other parameters fixed at their best values, a comparison made between simulations where the sail velocities were varied by $\pm 1\sigma$ of their nominal values. The results, also listed in Table 5.4, again show a large dependence in the $\hat{x}$ direction, with essentially negligible contributions from $\hat{y}$ and $\hat{z}$. This time, however, there is a slightly larger estimated uncertainty from the simultaneous variation of the three directions in the 1^a data set. This may indicate slight correlations between the directions; as indicated by the boldfaced font, we take this as our estimate of the systematic uncertainty instead of the one deduced from the independent variations.

Correlations between $\boldsymbol{x}_\circ$ and $\boldsymbol{v}_{\text{sail}}$ Recall that the sail velocity was determined by a linear interpolation between the initial and final cloud positions. Thus, it is clear that the systematic associated with $\boldsymbol{x}_\circ$ will be correlated with that determined for $\boldsymbol{v}_{\text{sail}}$, and that we should therefore not add the two simply in quadrature. This correlation can be deduced based on a geometrical argument: the two uncertainties from $\boldsymbol{x}_\circ$ and $\boldsymbol{x}_{\text{final}}$ form a right-angled triangle with $\boldsymbol{v}_{\text{sail}}\Delta t$ because they are uncorrelated, independent measurements:

$$(\sigma_{\boldsymbol{v}_{\text{sail}}}\Delta t)^2 = \sigma^2_{\boldsymbol{x}_\circ} + \sigma^2_{\boldsymbol{x}_{\text{final}}}, \tag{5.13}$$

where $\Delta t = 1.4\ \mu$s is the optical pumping time. Thus the correlation $\rho_{\boldsymbol{x}_\circ,\boldsymbol{v}_{\text{sail}}}$ is simply the projection of $\sigma_{\boldsymbol{v}_{\text{sail}}}\Delta t$ onto the $\sigma_{\boldsymbol{x}_\circ}$ axis:

$$\rho_{\boldsymbol{x}_\circ,\boldsymbol{v}_{\text{sail}}} = \frac{-\sigma_{\boldsymbol{x}_\circ}}{\sqrt{\sigma^2_{\boldsymbol{x}_\circ} + \sigma^2_{\boldsymbol{x}_{\text{final}}}}} \tag{5.14}$$

The same correlation is found if one propagates uncertainties starting from $\boldsymbol{x}_{\text{final}} = \boldsymbol{x}_\circ + \boldsymbol{v}_{\text{sail}}\Delta t$, solves for $\sigma_{\boldsymbol{v}_{\text{sail}}}$ — including correlations — and then requires that it agree with Eq. (5.13) above. The correlation is negative (as expected) because if, for example, we increase the initial position by δx, we would need to decrease v_{sail} by $\frac{-\delta x}{\Delta t}$ in order to arrive at the same final position. Note that if the initial and final positions are determined with the same precision, the correlation of the sail velocity with $\boldsymbol{x}_\circ$ will be 50%, as expected; this is more or less the case as can be seen at the bottom

TABLE 5.4: Systematic uncertainties in κ from the cloud position during optical pumping times. All values have been multiplied by $\times 100$ for clarity, and so (roughly) correspond to percent effects on the fit value of κ.

Source		1^a data set σ_κ	1^a data set $\bar{\Delta}$	1^a data set δ	1^b data set σ_κ	1^b data set $\bar{\Delta}$	1^b data set δ
Initial cloud position							
independently varied	$\hat{x}$	$^{+1.14}_{-1.08}$	± 1.11	$+0.03$	$^{+1.27}_{-1.25}$	± 1.26	$+0.01$
	$\hat{y}$	$^{+0.26}_{-0.08}$	± 0.17	$+0.09$	$^{+0.12}_{-0.09}$	± 0.10	$+0.02$
	$\hat{z}$	$^{+0.16}_{+0.03}$	± 0.07	$+0.10$	$^{+0.23}_{-0.13}$	± 0.18	$+0.05$
	sum		$\pm \mathbf{1.14}$	$+0.22$		$\pm \mathbf{1.28}$	$+0.08$
simultaneously varied		$^{+1.11}_{-1.15}$	± 1.13	-0.02	$^{+1.06}_{-1.42}$	± 1.24	-0.18
Cloud sail velocity							
independently varied	$\hat{x}$	$^{+1.17}_{-1.09}$	± 1.13	$+0.04$	$^{+1.29}_{-1.21}$	± 1.25	$+0.04$
	$\hat{y}$	$^{+0.20}_{-0.09}$	± 0.14	$+0.05$	$^{+0.10}_{-0.27}$	± 0.19	-0.09
	$\hat{z}$	$^{+0.16}_{-0.03}$	± 0.10	$+0.06$	$^{+0.01}_{-0.28}$	± 0.14	-0.13
	sum		± 1.15	$+0.15$		$\pm \mathbf{1.29}$	-0.18
simultaneously varied		$^{+1.46}_{-1.24}$	$\pm \mathbf{1.35}$	$+0.11$	$^{+1.20}_{-1.16}$	± 1.18	$+0.02$
$\rho_{x_o, v_{sail}}$ (in $\hat{x}$ direction):			-48.8%			-58.5%	
Combined systematic:			± 1.27	$+0.23$		± 1.17	-0.13

of Table 5.4. Here, only the correlation in the $\hat{x}$ direction is quoted because it is this systematic which totally dominates the uncertainty from the cloud position.

The final uncertainty is taken from the largest systematic calculated from $\boldsymbol{x}_\circ$ and $\boldsymbol{v}_{\text{sail}}$, be it from the independent or simultaneous variations of the positions. These are highlighted in Table 5.4 by a boldfaced font. The two are then added in quadrature including the $\hat{x}$ correlation; for example, for the 1^a data set, we calculate the total uncertainty in κ as:

$$\begin{aligned}\sigma_\kappa^2 &= (\sigma_\kappa^{\boldsymbol{x}_\circ})^2 + (\sigma_\kappa^{\boldsymbol{v}_{\text{sail}}})^2 - 2\,\rho_{\boldsymbol{x}_\circ,\boldsymbol{v}_{\text{sail}}}\,\sigma_\kappa^{\boldsymbol{x}_\circ}\sigma_\kappa^{\boldsymbol{v}_{\text{sail}}} \\ &= 1.27^2.\end{aligned}$$

The shifts are taken to be the average of the independent and simultaneous variations in the two cases, and then added together. This was done because the total uncertainties of the two methods are very similar, and so we expect their shifts to be as well; because the shifts are of the same order of magnitude as the fluctuations due to MC statistics, this averaging should reduce the possibility of over-estimating the shifts.

Cloud size during polarized times

The previous subsection dealt with the cloud position as a function of time over the optical pumping part of the experimental cycle. Below we now discuss the systematics arising from the width of the cloud over the same times. In this case, we do not expect as high sensitivities because the cloud sizes are similar between σ^+ and σ^-, and as the 2^{nd} moment of the position distribution, should not have a large effect on the asymmetry.

Initial cloud width The initial cloud width is determined from the same Gaussian fit to the photoion data used to obtain the centroids for the position of the cloud. It seems equally unlikely, therefore, that these initial widths would differ between $\sigma^\pm$ since it is again the MOT which defines the size of the cloud when it is released and the optical pumping is initiated. Regardless of the how unlikely the systematic is expected to be, we performed an analysis identical to that just done on the cloud

positions to estimate how large a systematic this may be. Again MC simulations were generated where this time the initial widths were varied by $\pm 1\sigma$ of their best-fit values, and the effect on the fit value of κ was tabulated (see Table 5.5). In this case, the independent variations gave a larger uncertainty compared to the simultaneous variations, indicating that the cloud size in the three directions may be anti-correlated. As in Table 5.4, we choose the larger of the two when assigning a systematic uncertainty and this is again indicated by a boldfaced font in Table 5.5.

Cloud temperature The width of the cloud as it is optically pumped was inferred from the difference in the width of cloud at the start and end of the optical pumping cycle (see §4.6.4). In the case of the sail velocity, it was pointed out that the optical pumping light could have a small heating effect, and change the group movement of the cloud; it seems less likely that the temperature of the two polarization states could be systematically different, since again this is defined by the end of the MOT cycle when the atoms are released and begin their ballistic expansion. Absorption affects the group movement of the cloud, rather than being a source of an increase in the random thermal motion of the atoms*, while de-excitation heats the atoms by an amount on the order of $T_{\text{recoil}} \approx 0.8\ \mu$K/photon, which is negligible.

The systematics were again deduced in the same manner as the other cloud characteristics described earlier, with the results listed in Table 5.5. The uncertainties deduced using independent and simultaneous variations are more similar than in the case of the initial cloud size, which indicates a smaller, essentially negligible, anti-correlation between directions. Again to be conservative, the quadratic sum of the independent variations is taken to be the uncertainty associated with the temperature of the cloud.

Correlations between σ_o and T A similar analysis to that outline for the correlation between the initial cloud position and the sail velocity shows that the correlation

*Since the atoms generally de-excite by spontaneous emission, however, there *will* be some randomness involved; the average effect will be biased towards the direction of the laser beam, though, and so should have a greater effect on the sail velocity.

TABLE 5.5: Systematic uncertainties in κ from the cloud size and temperature during optical pumping times. All values have been multiplied by $\times 100$ for clarity, and so (roughly) correspond to percent effects on the fit value of κ.

Source		1^a data set σ_κ	$\bar{\Delta}$	δ	1^b data set σ_κ	$\bar{\Delta}$	δ
Initial cloud size							
independently varied	$\hat{x}$	$^{+0.15}_{+0.04}$	± 0.05	$+0.09$	$^{+0.24}_{-0.40}$	± 0.32	-0.08
	$\hat{y}$	$^{+0.11}_{-0.03}$	± 0.07	$+0.04$	$^{+0.10}_{-0.22}$	± 0.16	-0.06
	$\hat{z}$	$^{+0.14}_{-0.02}$	± 0.08	$+0.06$	$^{+0.22}_{-0.31}$	± 0.27	-0.05
	sum		$\pm \mathbf{0.21}$	$+0.19$		$\pm \mathbf{0.48}$	-0.19
simultaneously varied		$^{+0.30}_{+0.01}$	± 0.14	$+0.15$	$^{+0.12}_{-0.10}$	± 0.11	$+0.01$
Cloud temperature							
independently varied	$\hat{x}$	$^{+0.05}_{+0.01}$	± 0.02	$+0.03$	± 0.08	± 0.08	0
	$\hat{y}$	$^{+0.15}_{-0.11}$	± 0.13	$+0.02$	$^{+0.21}_{-0.08}$	± 0.15	$+0.06$
	$\hat{z}$	$^{+0.26}_{-0.02}$	± 0.14	$+0.12$	$^{+0.02}_{-0.08}$	± 0.05	-0.03
	sum		$\pm \mathbf{0.26}$	$+0.17$		$\pm \mathbf{0.20}$	$+0.03$
simultaneously varied		$^{+0.14}_{-0.23}$	± 0.18	-0.05	$^{+0.12}_{-0.24}$	± 0.18	-0.06
$\rho_{\sigma_\circ, T}$ (average of $\hat{x}$, $\hat{y}$ and $\hat{z}$):			-43.5%			-55.1%	
Combined systematic:			± 0.25	$+0.23$		± 0.40	-0.10

between the initial cloud size and the thermal expansion is:

$$\rho_{\sigma_\circ,T} = \frac{-\sigma_\circ \Delta\sigma_\circ}{\sqrt{\sigma_\circ^2 \Delta\sigma_\circ^2 + \sigma_{\text{final}}^2 \Delta\sigma_{\text{final}}^2}} \tag{5.15}$$

where for clarity, instead of "σ_{σ_i}", $\Delta\sigma_i$ is used to represent the 1σ uncertainty in the measured width, σ_i. Unlike the $\hat{x}$ direction for $\rho_{x_\circ,v_{\text{sail}}}$, no one direction dominates the systematic uncertainty from the cloud size. Therefore, in accounting for the correlations in Table 5.5, we take the average of all three directions of both polarization states. The standard deviation of the individual correlations is less than 20%.

Binning of the data

The fit results depend on how finely binned the $Ar^{+1,+2,+3}$ position spectra are because, as mentioned earlier, the propagation of error used to derive the weighting of points in the asymmetry curve has been assumed to be Gaussian. Too fine a binning will bias events because there are too few events to validate the Gaussian approximation to the truly Poissonianly distributed number of counts per bin. Conversely, too coarse a binning removes positional dependence and overall sensitivity. This systematic is different for the two data sets because the 1^b data has $\approx 2\times$ more events than the 1^a set.

We began by binning the projections of the position spectra such that there was 0.5 mm/bin. We then calculated the mean number of counts per bin, $\bar{n}$, and if it was less than some threshold, $\bar{n}_{\text{min}}$, we rebinned the spectra by two so that there was 1 mm/bin. If the recalculated $\bar{n}$ was still less than $\bar{n}_{\text{min}}$, we again made the binning coarser; this process was iterated until $\bar{n} \geq \bar{n}_{\text{min}}$.

In order to find the optimal value for this threshold, the fit results for κ were plotted as a function of $\bar{n}_{\text{min}}$ as shown in Fig. 5.8. The points represent the fit values every time the increase in $\bar{n}_{\text{min}}$ resulted in a rebinning of any of the three charge states. The blue arrows indicate the values of $\bar{n}_{\text{min}}$ which caused the Ar^{+1} charge state spectrum to be rebinned; in both data sets, the first instance of the +1 rebinning can be seen to cause a relatively large step in the fit value of κ. This makes sense because the Ar^{+1}'s have the greatest statistics, and hence the greatest effect on the average value

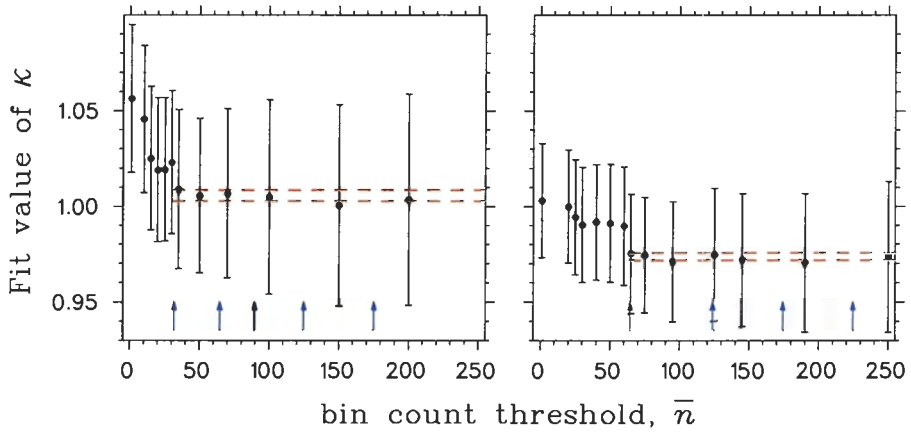

FIGURE 5.8: Systematic dependence of κ on $\bar{n}$ for the 1^a (left) and 1^b (right) data sets. The arrows point to thresholds which change the rebinning factor of the Ar^{+1} charge state.

of κ. After this first rebinning of the Ar^{+1}'s, there is only a small variation in the value of κ and there no longer is a systematic decline as $\bar{n}_{\min}$ increases.

All fits to the neutrino asymmetry have $\bar{n}_{\min} = 80$, which is well into the flat region of Fig. 5.8 for both data sets. As an estimate of the uncertainty on B_ν, we took the variation in the fit value of κ for all cases above the first rebinning of the Ar^{+1} charge state; this range and the variation is shown by the dashed red lines in Fig. 5.8. The numerical results are listed in Table 5.6.

Systematics common to 1^a and 1^b

The previous subsection dealt with the systematics related to the cloud characterization, which were different for the two data sets. Below we account for systematics that did not change between data sets, and so should be common to both 1^a and 1^b. The general scheme for estimating these systematics are similar to the that done for the cloud characterization, and is also done for each data set independently; in the end, however, since they should be common to both, we average the two estimates and apply the systematics only to the combination of κs from the two data sets.

MCP position calibration The position calibration of the MCP was based on the (α source + mask) data, and then adjusted slightly at larger radii in order to make

TABLE 5.6: Systematic uncertainties in κ separate for the 1^a and 1^b data sets. All values have been multiplied by $\times 100$ for clarity, and so (roughly) correspond to percent effects on the fit value of κ.

Source	1^a data set		1^b data set	
	$\bar{\Delta}$	δ	$\bar{\Delta}$	δ
Cloud position/velocity	± 1.27	$+0.23$	± 1.17	-0.13
Cloud size/temperature	± 0.25	$+0.23$	± 0.40	-0.10
Counts per bin threshold	± 0.43	-0.08	± 0.24	-0.04
Total systematics:	± 1.45	$+0.38$	± 1.28	-0.27

the collimator image of the online data become circular. Based on the linearity of the mask data and on how well the online calibration reproduces the $R_{\max} = 1.2$ cm collimator image on the MCP, we expect deviations to be below 1 mm. Due to the fact that we are fitting the asymmetry in this detector as a function of the $\hat{x}$ coordinate, we must be concerned about potential deviations in the position calibration of the MCP.

To investigate the effect of the position calibration, we varied the scaling of the calibration by $\pm 20\%$, *i.e.* $r'_{\rm MCP} = r^{\circ}_{\rm MCP}(1 \pm 0.005, \pm 0.01, \pm 0.015,$ and $\pm 0.02)$, and fit κ in each case. The dependence of κ on the scaling factor was fit to a straight line as shown in Fig. 5.9 for both data sets. The systematic uncertainty (see Table 5.7) was taken to be the average variation of the fit value of κ due to $^{+}0.8_{-1.7}\%$ changes in scaling the radius of the calibration.

Another effect which is likely correlated with the position calibration scaling is the overall active area of the MCP. Though this is well-defined by the collimator, non-linearities in the calibration are largest near the edges of the MCP, and may effect the fit value of κ since this is also where the asymmetries are largest.* Ideally, if one were to shrink the active area of the MCP by imposing radial position software cuts in the data (and of course the MC), the fit value of κ would not change and only the

*Though this is also where statistics are the most limited, and hence the weighting in the fit to κ are reduced relative to smaller radii.

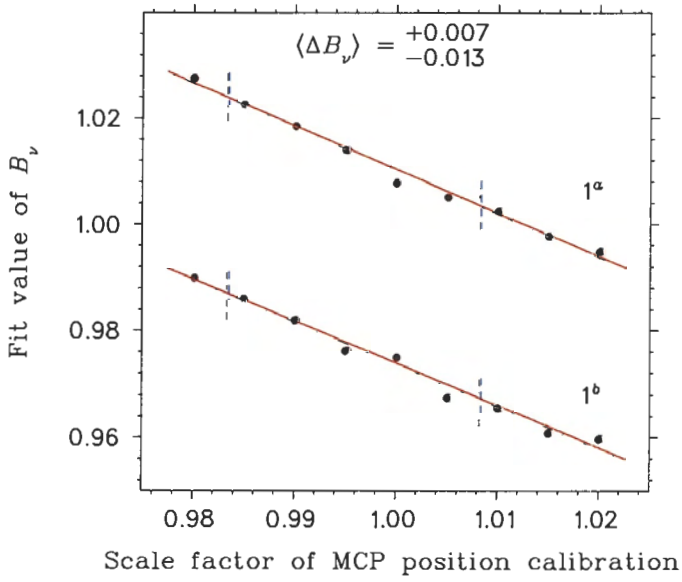

FIGURE 5.9: Effect of scaling the radial position calibration of the MCP on κ. The dashed blue lines indicate the limits on the scaling of the radial position as deduced in §4.4.2.

uncertainty would slightly increase due to the vetoing of the edge events. We tested the variation of κ for radii of $R_{\max} = 0.9, 1.0, 1.1, 1.2$ and 1.25 cm.

MCP position efficiency As discussed in §4.4.2, we have estimated the dependence of the MCP position efficiency for the recoil ions based on comparisons to simulations of what one would expect if it were perfect. By taking the asymmetry of the absolute position spectra, we significantly reduce our sensitivity to this systematic; however, it remains a cause for concern. To estimate the potential bias introduced by the efficiency, we generated MCs with varying amounts of the correction applied for the MCP efficiency to see the effect on the extracted value of κ. The variation of the correction applied is described by a factor, λ, in terms of the best estimate, $\epsilon_{\text{MCP}}(x, y)$:

$$\epsilon_{\text{MCP}}(x, y; \lambda) = \epsilon_{\text{MCP}}(x, y) + \lambda\big[\max\left(\epsilon_{\text{MCP}}(x, y)\right) - \epsilon_{\text{MCP}}(x, y)\big]. \tag{5.16}$$

With this parameterization, our best estimate is recovered at $\lambda = 0$. Positive values suppress the inefficiency, tending towards a uniform efficiency as $\lambda \to 1$; negative

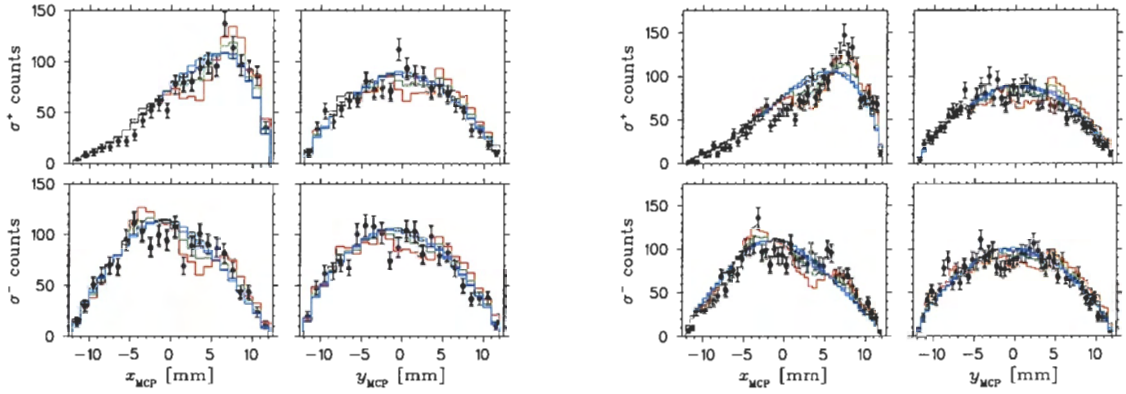

FIGURE 5.10: Position projections and effect of the MCP efficiency. Shown are the comparison of data (points) to simulations with $\lambda = -0.7, -0.1, +0.5$ and $+0.9$ for the 1^a (left) and 1^b (right) data sets.

values of λ enhance the estimation of the efficiency.

In order to see what range of λ values we should consider for the uncertainty in the efficiency, we compared the projections of the MCP position spectra for various values of λ. These plots are shown in Fig. 5.10 for the 1^a and 1^b data sets for a few values of λ. One can see how the projections become more uniform as λ approaches unity, and how the inefficiencies are most apparent at negative values (e.g. cyan versus red histogram). For the 1^a data sets, it is clear that $\lambda = -0.7$ is too much of an enhancement of the inefficiency, and similarly $\lambda = +0.9$ is too little. On the other hand, $\lambda = -0.7$ is not unreasonable for the 1^b data set (especially for the σ^+ $\hat{x}$-projection), and $\lambda = +0.5$ is already too smooth. The dichotomy in these absolute position spectra accentuates the fact that the accuracy of our deduced MCP efficiency is limited; as stated before, if we were not using the asymmetry of the two polarization states, the MCP efficiency would be a very serious systematic and would surely dominate the final uncertainty.

We have estimated the effects of the MCP position efficiency by investigating the dependence of κ on the value of ϵ_{MCP}, *i.e.* by letting $\lambda = \pm 0.1, \pm 0.3, \ldots, \pm 0.9$. This range of λ spans the efficiency values which give somewhat reasonable projections in Fig. 5.10, and represents a rather large variation of the overall magnitude of the MCP position efficiency. The results, listed in Table 5.7, separately for the 1^a and 1^b data sets. Naively, one would expect this systematic to be common between the two data

sets because the MCP did not change between the two, however because the trap position was not strictly constant, the effect of the position efficiency can be different between the two.

We stress again that if the absolute position was needed, this systematic would result in an uncertainty that far out-weighed the statistical uncertainty; the fact that this measurement uses the difference of the same position bins — differing only in polarization states — means that most of the efficiency effects drop out. We also note, however, that as of the fall of 2004, the damaged plates of the MCP have been replaced for an experiment involving ^{80}Rb, and the position efficiency has been found to once again be uniform. Therefore, the next time the ^{37}K B_ν experiment is performed, this inefficiency systematic will become negligible.

$\hat{x}-$OP alignment As made explicit in Eq. (5.3), the recoil asymmetry in the $\hat{x}$ direction only goes like $-\mathcal{P}B_\nu$ if the polarization axis is exactly along x-axis of the MCP. A small misalignment of these two directions will attenuate the asymmetry arising from B_ν and introduce a small component of the D term which would otherwise fully describe the $\hat{y}$ asymmetry. Similarly, the $\hat{y}$ asymmetry will increase because instead of being ≈ 0, it would acquire a finite asymmetry from the B_ν term.

The calibration of the MCP position, being carried over from the detailed work on the scalar search, is in the reference frame of the chamber. The transformation to the optical pumping frame is made by rotating the coordinates by 30°, the nominal angle defined by the ports housing the phoswich detectors and thin mirrors relative to the push beam axis. If either the MCP calibration is off or these ports are not at exactly 30°, then we may be introducing a bias in our B_ν measurement.

In order for the incident optical pumping light to be retro-reflected back out of the system as observed, the angle of the mirrors defining the polarization axis must not have been misaligned by more than about a degree. The absolute orientation of the MCP is also known very well from calibrations using an α source and a mask [104]. The relative orientation of the polarization and MCP's x-axis is likely less than 2°; however, to be conservative, we double that and assume that the reasonable range of this misalignment is within ±4°.

In order to estimate the systematic uncertainty, we varied the orientation of the MCP from $-10°, -7.5°, \ldots, +10°$ and fit κ to each angle, giving nine results for each of the 1^a and 1^b data sets. These results were then fit to a Taylor expansion of κ around $\sin\theta_{\hat{x}-\mathrm{OP}} = 1$ (*cf.* Eq. (B.26)):

$$\kappa(\theta_{\hat{x}-\mathrm{OP}}) \;=\; \kappa_\circ \;+\; c_1 \cdot \sin\theta_{\hat{x}-\mathrm{OP}} \;+\; \frac{1}{2}\, c_2 \cdot \sin^2\theta_{\hat{x}-\mathrm{OP}}, \tag{5.17}$$

where $\kappa_\circ, c_1$ and c_2 were free parameters. Unlike the dependence on the cloud parameters, since this time we have a number of fits to κ as a function of only one parameter, we are able to fit c_1 and c_2 (*i.e.* $\bar{\Delta}$ and δ) directly, instead of estimating them from only two points at $\pm 1\sigma$. $\kappa_\circ$ represents the best estimate of κ, which may or may not coincide with the result of fitting the asymmetry to the expected relative orientation of $\sin\theta_{\hat{x}-\mathrm{OP}} = 0$. We estimate the systematic uncertainty on κ by simply evaluating the Taylor expansion, Eq. (5.17), at $\theta_{\hat{x}-\mathrm{OP}} = \pm 4°$ using the fit values of $\kappa_\circ, c_1$ and c_2. This gave $\sigma_\kappa = {}^{+0.0040}_{-0.0011}$ and ${}^{+0.0030}_{-0.0006}$ for the 1^a and 1^b data sets respectively. These results are listed in Table 5.7. We average the upper and lower uncertainties for the two data sets since this systematic is common to both, giving a total uncertainty in κ from the alignment of the MCP position and the optical pumping axis of ± 0.0033.

As with the previous systematic estimates, we varied the orientation of the MCP by $\pm 10°$ and fit the Taylor expansion of κ around zero. This gave the systematics outlined in Table 5.7. Note that the uncertainties are both positive; this is because the misalignment suppresses the B_ν asymmetry, regardless of the direction. We therefore end up with a relatively large shift, and in fact the δ term in Eq. (B.39) dominates the total uncertainty of this systematic.

The electric field An improper estimation of the magnitude of the electric field can have an effect on the deduced value of κ in a number of ways: it will change the acceptance of recoil detection by collecting Ar^+ ions of higher transverse momentum with greater/lesser efficiency; it will change the shape of the asymmetry curve; and for a given set of TOF cuts bins used to choose the charge states, it will change the relative distributions $Ar^{+1,2,3}$ charge states. *I.e.* if the field is actually stronger than expected, then compared to our simulations, we will have more (slow) Ar^{+2} with

mh5 ≤ 640 channels, and similarly more Ar^{+3} will be in our Ar^{+2} TOF bin.

The electric field was determined to be -810 ± 10 V/cm based on the TOF spectra of the $Ar^{+1,2,3}$s as discussed in §4.4.1. The dependence of κ on the magnitude of the field was found by fitting the asymmetry with differing field strengths of $-790, -795, \ldots, -830$ V/cm. A Taylor expansion of κ around $E = -810$ V/cm evaluated at ± 10 V/cm gave $^{+0.0019}_{-0.0014}$ and $^{+0.0028}_{-0.0023}$ as the systematic uncertainties for the 1^a and 1^b data sets respectively.

E_β threshold The (kinetic) energy threshold on the β-telescope was set to $T_{\text{thresh}} = 500$ keV, above the Compton edge of the $e^\pm$ annihilation radiation, based on the calibration fit of §4.3.1. In the MC simulations, this threshold is set with no uncertainty, but if the calibration is slightly off, one may introduce a systematic uncertainty by having an effectively different threshold placed on the data.

To estimate the systematic effects on κ due to this threshold, simulations were generated with thresholds of $400, 450, \ldots, 600$ keV, and with the resulting asymmetry curves fit to the data. For both 1^a and 1^b, the fit value of $\kappa_\circ$ was consistent with the value of $\kappa(500 \text{ keV})$.

Using the uncertainties from the calibration fit, the energy at 500 keV is known to ± 12 keV. We estimate the systematic uncertainty on κ by simply evaluating the Taylor expansion at $T_{\text{thresh}} = T_{\text{thresh}} \pm 12$ keV using the fit results to $\kappa_\circ, c_1$ and c_2. This gave $\sigma_\kappa = \pm 0.0002$ for both 1^a and 1^b data sets; however, to account for systematics in the calibration and to be conservative, we assume an uncertainty of $\sigma_{T_{\text{thresh}}} = 50$ keV, which increased the deduced systematic on κ to those listed in Table 5.7. We average the upper and lower uncertainties for the two data sets since this systematic is common to both, giving an essentially symmetric, total uncertainty in κ from the β energy threshold cut of ± 0.0006. Even with a generous allowance for the uncertainty in the calibration, this systematic is negligible. This makes sense because the β-telescope is really only used to tag positrons that were emitted in a small pyramid around the $\hat{z}$ axis, and the recoil asymmetry is not directly dependent on the emitted β's energy.

TABLE 5.7: Systematic uncertainties in κ common to both 1^a and 1^b data sets. All values have been multiplied by $\times 100$ for clarity, and so (roughly) correspond to percent effects on the fit value of κ.

Source	$\sigma_\kappa^{1^a}$	$\sigma_\kappa^{1^b}$	$\langle\sigma_\kappa\rangle$	$\bar{\Delta}$	δ	σ_κ
MCP position calibration	$^{+0.68}_{-1.37}$	$^{+0.66}_{-1.32}$	$^{+0.67}_{-1.34}$	± 1.01	-0.33	± 1.11
MCP position efficiency	$^{+0.31}_{-0.39}$	$^{+0.51}_{-0.65}$	$^{+0.41}_{-0.52}$	± 0.46	-0.06	± 0.47
$\hat{x}_{\mathrm{MCP}}-\mathrm{OP}$ alignment	$^{+0.40}_{+0.11}$	$^{+0.30}_{+0.06}$	$^{+0.35}_{+0.08}$	± 0.13	$+0.22$	± 0.33
Electric field	$^{+0.19}_{-0.14}$	$^{+0.28}_{-0.23}$	$^{+0.23}_{-0.19}$	± 0.21	$+0.03$	± 0.21
E_β threshold	$^{+0.09}_{-0.05}$	$^{+0.04}_{-0.06}$	$^{+0.07}_{-0.06}$	± 0.06	$+0.00$	± 0.06
Total common systematics:					-0.14	± 1.27

5.2.5 The B_ν Result

In §4.7.2 we presented a breakdown of the uncertainties associated with our atomic measurements of the polarization via the vanishing of the fluorescence. Here we combine those results with the uncertainty estimates of κ above to determine the final uncertainty in our extracted value of B_ν.

Let us put all of the fit κ results together for the $1^{a,b}$ data. We start by adding in the separate systematics (both the variance, $\bar{\Delta}$, and the shift, δ) from Table 5.6 to the 1^a and 1^b data sets:

$$\kappa_{1^a} = 0.995 + 0.004 = 0.998 \qquad \sigma_{1^a}^2 = 0.040^2 + 0.014^2 = 0.043^2$$
$$\kappa_{1^b} = 0.975 - 0.003 = 0.973 \qquad \sigma_{1^b}^2 = 0.031^2 + 0.013^2 = 0.034^2$$

Now we take a weighted average of these two results, and then add in the common systematics from Table 5.7:

$$\left.\begin{aligned} \langle\kappa\rangle &= 0.983 - 0.001 \\ \sigma_\kappa^2 &= 0.026^2 + 0.013^2 \end{aligned}\right\} \quad \langle\kappa\rangle = 0.981 \pm 0.029 \tag{5.18}$$

Including the finite polarization from Table 4.10, the above result for $\langle\kappa\rangle$ and the SM prediction of $B_\nu^{\mathrm{SM}} = -0.7692$ with Eqs. (5.10) and (5.11), we arrive at our final

result for the neutrino asymmetry:

$$\boxed{B_\nu = -0.755 \pm 0.024}, \tag{5.19}$$

a 3.1% measurement in agreement with the Standard Model.

This result includes both Type A ("statistical") and Type B ("systematic") uncertainties; however, it can be instructive for future experiments to know how much of the final uncertainty is statistical and how much is due to systematics. The total statistical uncertainty can be calculated by combining the statistical uncertainties in κ and $\mathcal{P}$ for the 1^a and 1^b data sets combined; the former is given in Table 5.2 and the latter in Table 4.10. Adding these two statistical contributions in quadrature, we find:

$$\sigma_{B_\nu}^{\text{stat}} = 0.020. \tag{5.20}$$

The total uncertainty is the sum in quadrature of statistical and systematic uncertainties, so it follows that the total systematic uncertainty is*:

$$\sigma_{B_\nu}^{\text{syst}} = 0.013, \tag{5.21}$$

and so the result, Eq. (5.19), can be re-expressed as:

$$B_\nu = -0.755 \pm \underset{\text{(stat)}}{0.020} \pm \underset{\text{(syst)}}{0.013} \tag{5.22}$$

This explicitly shows that the present experiment is statistics limited, almost entirely from the fits to κ which bring in a statistical uncertainty almost $5\times$ larger than that arising from the polarization. We therefore expect that, even if we did not improve the system at all, we could achieve a 1.7% measurement by simply counting longer. Of course if we had a fully polarized cloud for all of our data sets, the statistical uncertainty would be much smaller (see Table 4.1) and we would have been systematics limited even with the run performed in the fall of 2002.

*Note that the same total systematic is found by taking the weighted average of the cloud systematics, and then summing that with the common (both in κ and $\mathcal{P}$) systematics.

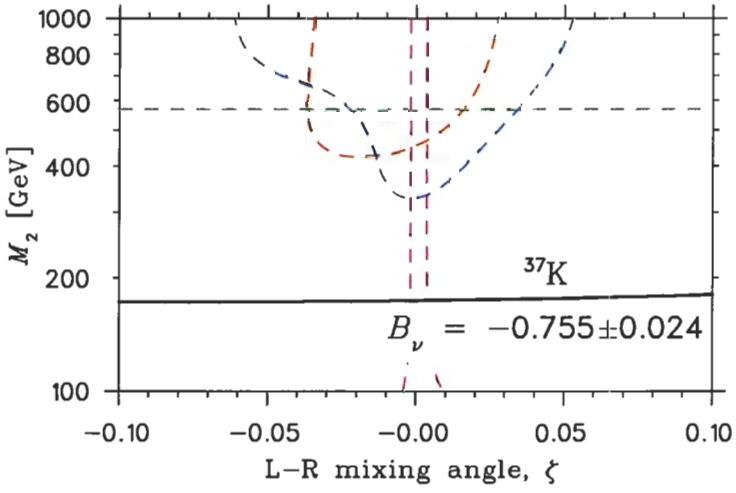

FIGURE 5.11: Exclusion plot of the left-right mixing angle, ζ, versus a possible right-handed boson mass, M_2 including the B_ν result. This is a reproduction of Figs. 2.3 and 2.5 (dashed lines) with the result, Eq. (5.19), included (solid line).

Fig. 5.11 depicts the impact of this 3% measurement of the neutrino asymmetry on right-handed current parameters within the manifest left-right symmetric model. This is a reproduction of the exclusion plots shown in §2.2.3 with this B_ν result added.

Clearly, our result is not competitive with the limits imposed by other experiments, however as this was a first attempt at a complicated measurement, we believe we will soon be able to vastly improve our precision and in our next running period, we expect to place limits that complement the variety of techniques used to search for right-handed currents.

5.3 Time-Reversal Violating Correlation, D

As has been alluded to earlier, the β-Ar coincidences in the back-to-back geometry can be used to time-violating currents in the weak interaction. The triple-vector product in the angular distribution weighted by the D parameter is only non-zero if time-reversal is not a good symmetry. Given our geometry, with the β emitted in the $+\hat{z}$ direction and the polarization along $\pm\hat{x}$, kinematics only allows $\boldsymbol{P}\cdot(\boldsymbol{p}_e\times\boldsymbol{p}_\nu)$ to be non-zero when neutrinos are emitted with a $\hat{y}$ component. Therefore, instead of

looking at the $\hat{x}$-asymmetry in Eq. (5.3) as we did for the B_ν measurement, this time we look at the $\hat{y}$-asymmetry leading to Eq. (5.5). Figure 5.6 shows the $\hat{y}$-asymmetry for the 1^a data set in the bottom-right panel. It is compared to a MC simulation where $D = 0$. If the value of D was allowed to vary, we found $D = +0.048 \pm 0.020$ where the uncertainty is purely statistical.

We did not pursue a detailed analysis of this correlation (*i.e.* including systematics) because we quickly realized how difficult it is to measure with great precision. One would expect that a null measurement would be very appealing because the only (physics) sources of a finite asymmetry are: (1) a SM-violating T-odd, (P-even) interaction, and (2) final-state effects, predicted [105] to come in at the 2×10^{-4} level — half as large as in ^{19}Ne. In the ideal case, this expectation is valid, however a number of serious systematics make such a measurement very difficult to do with the precision needed to complement current limits imposed by β decay experiments of the neutron [106] and ^{19}Ne [107], *i.e.* 1×10^{-3}. The large value of B_ν means that even a small misalignment of the polarization direction and the $\hat{x}$ axis will generate a significant asymmetry in $\hat{y}$. Furthermore, the cloud characteristics which were found to contribute a significant ($\gtrsim 1\%$) systematic to the B_ν measurement will also generate false signals. Not including our statistical uncertainty of $\approx \pm 0.02$, these two factors alone limit our D measurement to a precision of approximately $\pm 2 \times 10^{-2}$, which is already over an order of magnitude larger than present limits.

It seems very difficult for our experiment to achieve the precision needed to make an impact on T-violating interactions. Reaching the 0.1% level would likely be possible, but certainly would be extremely demanding. In addition to much more statistics, we would to minimize and understand the source of the cloud sail velocity, and would have to be very careful about the relative orientation of the optical pumping and MCP axes; much of the development needed for a precision experiment will be addressed in future efforts to improve the measurement on B_ν, so we expect to be able to extract D limits the next time we run.

The emiT collaboration is working at improving their measurement and expect to extend their sensitivity to the 3×10^{-4} level [106]. This raises the bar very high on experiments aimed at testing time-reversal invariance. Even a dedicated program

meant to be optimized for a D measurement might be able to compete at this level over the course of years of development; however, it will likely not be possible for us to achieve such sensitivities to D in parallel with our search for right-handed currents. It is therefore unlikely that we will pursue a D measurement, at least not vigourously and not until we have completed our right-handed current search using B_ν, R_{slow} and A_β.

5.4 The R_{slow} Parameter

The B_ν asymmetry, though the dominant part of this thesis, is not the only clean correlation sensitive to right-handed currents that we can measure in our present geometry with our polarized source of ^{37}K. Using the phoswich detectors in coincidence with the recoil detector, we have found [92] a new correlation which not only has a different sensitivity to M_2 and ζ, but is also rather insensitive to uncertainties in the measured value of λ, the ratio of Gamow-Teller to Fermi matrix elements.

5.4.1 Dependence on Right-Handed Current Parameters

The geometry of the phoswich and MCP detectors, depicted in Fig. 5.12, is such that fast Ar^+ recoil events are suppressed because the electric field of -810 V/cm is not large enough to significantly alter the ion trajectory, so recoils with large momenta along $-\hat{x}$ will miss the MCP. For slow recoils, however, the field is able to focus the ions within the active area of the MCP. In this way, the kinematics and geometry of these events helps to pick out slow recoil events. In the purely back-to-back geometry depicted in Fig. 5.12, this translates to events where the β alone goes along $\hat{x}$ into the phoswich, while the ν and recoil are both emitted in the opposite direction. In reality, however, the Ar^+ and ν are not constrained to be along $-\hat{x}$ and the differentiation of fast to slow recoils becomes less precise. We have shown that we can enhance selectivity of slow recoils based on the TOF. At the present time with current statistics this cut is not practical, however this can be employed in the future when we have more events.

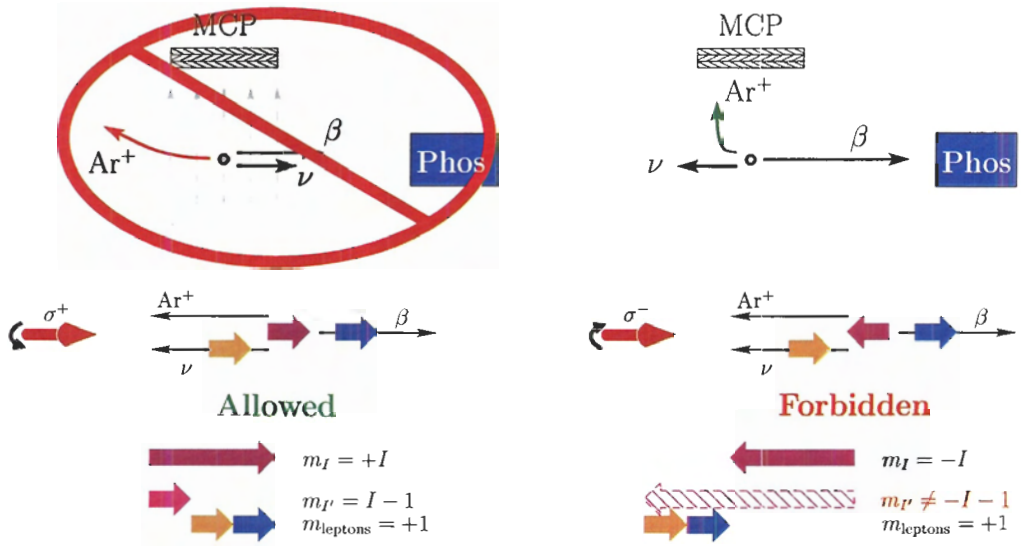

FIGURE 5.12: Geometry (not to scale) and kinematics of phoswich–MCP coincident events. The top panel depicts how the experimental set-up and kinematics of the decay accept slow recoils, while fast Ar^+ will not fire the MCP. The bottom panel shows how angular momentum can only be conserved for the slow recoils if the initial nuclear spin is aligned with the β direction.

Continuing to consider the back-to-back geometry for simplicity, it is easy to show that helicity arguments require that, for a purely $V-A$ interaction, the initial nuclear spin of the ^{37}K must be aligned with the β direction. If it were opposite, the initial spin projection of $m_I = -I$ could not equal the sum of the final state spins: $m_{I'} + m_{\text{leptons}} = -I + 1 > m_I$. We therefore define a vanishing observable, R_{slow}, to be the ratio of these phoswich–MCP coincidences:

$$R_{\text{slow}} \equiv \frac{N(\hat{i}\cdot\hat{p}_\beta = -1)}{N(\hat{i}\cdot\hat{p}_\beta = +1)}. \tag{5.23}$$

In the back-to-back geometry, this ratio vanishes as can be seen by looking at the decay rate and imposing $\hat{p}_\beta = -\hat{p}_\nu = -\hat{i}$:

$$dW(\hat{i}\cdot\hat{p}_\beta = -1) = dW_\circ\xi\Big[1 - (a_{\beta\nu} - \frac{2}{3}c\,c_p)\frac{p_\beta}{E_\beta} - P(A_\beta\frac{p_\beta}{E_\beta} - B_\nu)\Big]. \tag{5.24}$$

Taking the limits $P \to 1$ and $\frac{p_\beta}{E_\beta} \to 1$, we get:

$$dW(\hat{i}\cdot\hat{p}_\beta = -1) = dW_\circ\xi\Big[1 - a_{\beta\nu} + \frac{2c}{3} - (A_\beta - B_\nu)\Big], \tag{5.25}$$

which, after substituting $a_{\beta\nu} = 0.6684 \approx \frac{2}{3}$ and $c = (A_\beta - B_\nu) = 0.1990 \approx \frac{1}{5}$, is zero. The denominator, on the other hand, goes like:

$$dW(\hat{i} \cdot \hat{p}_\beta = +1) = dW_\circ \xi \Big[1 - a_{\beta\nu} + \frac{2c}{3} + (A_\beta - B_\nu)\Big] \tag{5.26}$$

$$\xrightarrow[c=1/5]{a_{\beta\nu}=2/3} \frac{4}{15} dW_\circ \xi, \tag{5.27}$$

and so does not vanish

We measure R_{slow} by looking at the $\hat{x}-$MCP asymmetry as per the B_ν measurement, except this time requiring that a β fired the phoswich detector instead of the (back-to-back) β-telescope.

Noting that the lepton spins are aligned in back-to-back decay, one can see that the Fermi component (*i.e.* where $a_{\beta\nu} = +1$) of this mixed F/GT decay is suppressed. To the extent that we measure only slow recoils, the Gamow-Teller part of the decay is singled out making us much less sensitive to the value of λ. Algebraically, it is a straightforward — albeit rather tedious — task to use Eqs. 2.19 and 2.20 to show that the dependence of R_{slow} on the right-handed current parameters goes like $(\delta + \zeta)^2$, where $\delta \equiv (M_1/M_2)^2$. Intuitively, this can be understood by considering how the matrix elements of a $V + A$ interaction couple to left-handed neutrinos:

1. directly through a new right-handed boson exchange: In this case, the matrix element with a W_R exchange is suppressed relative to the W_L by the $1/M_W^2$ mass-dependence of the propagator, resulting in a M_1^2/M_2^2 dependence.

2. weak eigenstate mixing of the left- and right-handed bosons. This time, the mixing goes like $\sin\zeta$ which, for small admixtures, is linear in ζ.

The overall probability of having a right-handed current goes like the square of the sum of these two matrix elements, namely $(\delta + \zeta)^2$.

5.4.2 Measurement Prospects

The R_{slow} observable has been shown to be a sensitive probe of the RHC parameters, and that it will depend only weakly on the accuracy of the measurement of λ. The

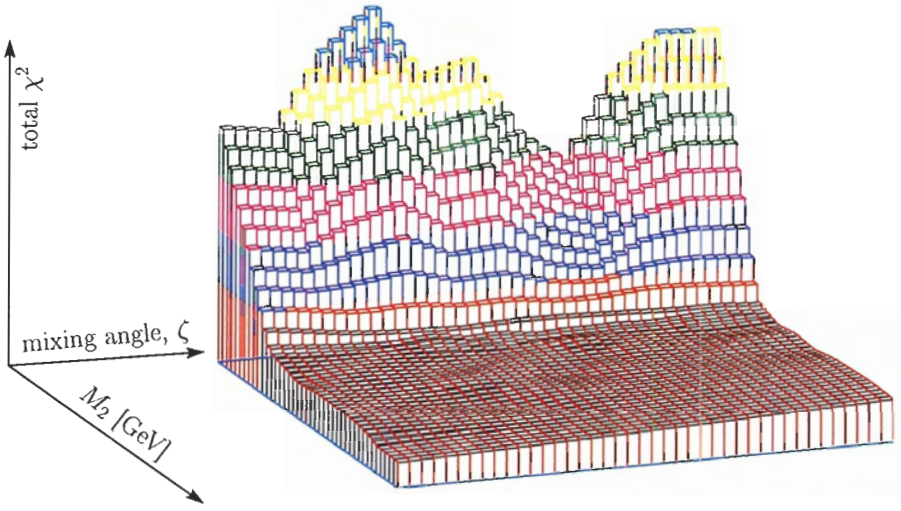

FIGURE 5.13: Exclusion plot of the right-handed boson mass, M_2, versus the left-right mixing angle, ζ, from a 'fit' to R_{slow}. Shown is the χ^2 surface of very rough fits to the MCP position spectra for phoswich–recoil coincident events. One can see very little sensitivity at large masses but that a wall quickly rises as one gets to $M_2 \lesssim 100$ GeV.

drawback is in the number of events: there are under 10× less events than our B_ν measurement due to kinematics and detector acceptances, and so R_{slow} is highly statistics limited. We plan to continue analyzing this observable in future experiments when we have sufficient statistics to warrant a detailed analysis. In particular, we would like greater statistics to be able to make additional TOF cuts to help pick slow recoil events, which should enhance our sensitivity.

As a foray into using the phoswich–MCP coincidences to measure R_{slow}, the data was filtered for all runs (not just $1^{a,b}$), and all phoswich A–MCP coincidences were recorded. A MC simulation was made for a wide variety of values of right-handed current parameters: 100 GeV $\leq M_2 \leq$ 300 GeV and $-0.25 \leq \zeta \leq 0.25$. The χ^2 map of the resulting fits is shown in Fig. 5.13. The minimum χ^2 is taken to be the average value over the plateau at high masses ($M_2 > 150$ GeV) and is found to be 25.5 for 24 degrees of freedom. This corresponds to — very roughly — a measurement of R_{slow} to ± 0.1. Comparing this exclusion plot to limits from the B_ν correlation, one sees the relatively enhanced sensitivity of R_{slow} because the same limit would require a 5% measurement of B_ν.

CHAPTER 6

Future Prospects and Directions

This first measurement of the β decay of polarized ^{37}K has produced a 3% measurement of the neutrino asymmetry parameter, which does not yet represent a stringent test of the Standard Model. This chapter discusses the sources of systematic uncertainties, what steps can be taken to minimize them and what sensitivities TRINAT expects in the future.

6.1 Reduction of Systematics

The B_ν measurement described in this thesis suffers from a few dominant systematics. In this section, we discuss the limitations of the current experiment and how we can improve them without drastic changes to the system.

6.1.1 Cloud polarization

First and foremost we must discuss the polarization of the atomic cloud. If we had been sure that the optical pumping beam was fully overlapping the cloud for all of the data sets, our B_ν measurement would not be statistics limited as it currently is; we likely would have been able to improve the precision of our B_ν measurement by a factor of two. The later data sets where the field switching was enabled have higher polarizations* and reduced systematics arising from the polarization of the cloud. The next time we run, we will have improved Helmholtz coils for applying the optical

*At least of the parts of the cloud that were optically pumped and probed using photoionization techniques.

pumping holding field, and we simply have to make certain that the optical pumping beam is large enough, and is well-centered on the atom cloud so that all of the atoms are certainly being polarized.

The TRINAT collaboration now has a D_1 laser which gives us $10\times$ the power of the optical pumping beams used in the experiment presented in this thesis. We will therefore be able to illuminate a much larger area with greater uniformity, which will make it easier to ensure that we are optically pumping the whole atomic sample.

A simple check that the lasers fully overlap the atoms is to move the cloud in space and ensure that the observed asymmetries do not change; however this would be an expensive use of valuable beamtime. Since photoionization can only occur from atoms that are being optically pumped, we can also check the absolute rate of the photoions as we move the cloud in space; we will change the cloud position until we see the rate decrease which will tell us when we have moved the cloud outside of the optical pumping laser beams. This method of checking the cloud–laser overlap can be investigated and optimized off-line with stable ^{41}K before we use it for the ^{37}K experiment.

We have attempted to develop non-resonant photoionization from the ground state directly using a high-power 266 nm laser. This photoionization scheme would be extremely useful for viewing the cloud position and size when the atoms are not being excited and the 355 nm laser produces no photoions, e.g. during optical pumping times when the cloud is highly polarized. There are two difficulties with this probe: the 266 nm laser photoionizes the P state $100\times$ more than the ground state, so any excited state populations would bias the probe of the ground state; and the 266 nm laser also fires the MCP with high efficiency which not only significantly reduces the signal-to-noise of the photoions, but also carries a high risk of damaging the recoil detector.

A clean probe of the ground state populations would be to use a 405 nm laser to resonantly excite atoms via the $4S_{1/2} \rightarrow 5P_{1/2}$ transition and to then photoionize atoms in this excited state using a 532 nm pulsed laser. Contamination from any atoms excited into the $4P$ state is suppressed in this technique because the 532 nm laser does not photoionize the $4P$ state. With a 0.67 MHz/G splitting of the $|2 + 2\rangle$ from the

$|2+1\rangle$ state and a $5P$ state linewidth of 1.1 MHz, a 5 G or greater optical pumping holding field would be needed to Zeeman-split the sublevels enough to resolve them. This technique of course would require that the 405 nm laser itself have a linewidth small compared to the $5P$ state, which is not a simple task; we have achieved laser linewidths of 3.5 MHz, which is already useful since one in principle deconvolve the laser linewidth, however a laser with a linewidth $\lesssim 1$ MHz would allow us to resolve the sublevel and allow us to be sensitive to small populations in the $|2 \pm 1\rangle$ next to the strongly populated stretched state. This technique can also be developed and tested off-line with stable ^{41}K.

Based on analysis of the polarization of the later data sets — again at least the part of the cloud that was being optically pumped — we expect to be able to achieve polarizations of $\gtrsim 99\%$ with systematic uncertainties that would be below the 0.3% level. At this level of precision we would need to develop our optical pumping model, in particular to properly include the effects of components of the magnetic field not aligned with the laser beam axis (*i.e.* to use the density matrix formalism instead of the rate equations). With these improvements implemented, we would expect uncertainties in the polarization to be reduced by nearly an order of magnitude.

6.1.2 Cloud characterization

The dominant systematic of the $1^{a,b}$ data sets after the polarization is the characterization of the cloud, particularly the position and sail velocity. This seems to have been improved in the latter data sets once the field switching was enabled, however at present it is not entirely clear how to minimize the cloud movement and the different positions between σ^+ and σ^-; this again should be developed off-line using ^{41}K. Our *diagnostics* of these characteristics, however, can be improved by simply* increasing the intensity of the photoionizing laser beam: more photoions will give us greater statistics with which to characterize the cloud. Assuming that our polarization is very high, it will still be problematic to obtain good statistics of the cloud location at long optical pumping times, unless of course we are able to develop the $4S \rightarrow 5P$

*Subject of course to real-life budget limitations.

photoionization technique described earlier. If we are only photoionizing from the excited state, it will be necessary to periodically destroy the polarization early and probe the cloud characteristics throughout the optical pumping times by shining in some D_2 light. For example, once or twice a run, we could take a few cycles and turn the MOT light on after 25, 50, ..., 400 μs and obtain photoion images of the cloud with good statistics, allowing us to view the expansion and movement directly. It is very important to actually *see* the cloud expand and move, not only online to include the cloud characteristics in our Monte Carlo, but also off-line when learning how to minimize the cloud movement using stable ^{41}K.

We are also planning to implement double-pass AOMs which will allow us to shift the laser frequency of the trapping light (without a corresponding shift in the direction of the beam). This is a technique we have used in the ^{38m}K experiment to minimize the size of the cloud. Additionally, by shifting the D_1 frequency to compensate for the Zeeman shift from the optical pumping holding field, we will be able to minimize the cloud's sail velocity and shifts in the cloud position. This can be tested off-line, especially in conjunction with learning to view the cloud throughout the optical pumping process.

With the above improvements and diagnostics, we expect to be able to greatly reduce the cloud movement and position shifts so that our uncertainties in the cloud characteristics will no longer be a dominant systematic. A quantitative estimate is impossible at this time until the techniques are developed, however we expect it will be feasible to control and measure the cloud position with $\approx 10\times$ the present accuracy, which would bring down the systematics on B_ν to the 0.1% level.

6.1.3 MCP Position Information

The recoil detector's position efficiency and calibration were found to have a considerable contribution to the overall systematic uncertainty. We have already replaced the damaged micro-channel plates and proven that the detector once again has a very uniform efficiency. This improvement immediately reduces the systematics from recoil detection considerably, however it does not improve our knowledge of the ab-

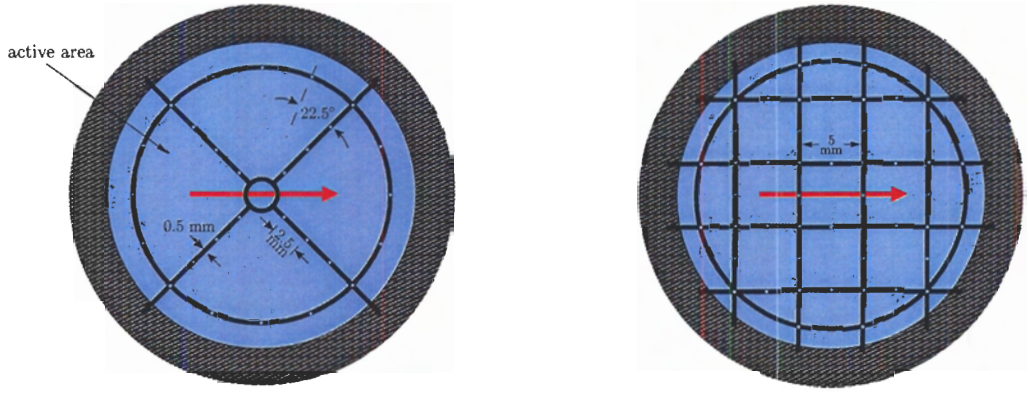

(a) Large open area mask (b) Grid mask

FIGURE 6.1: Schematic diagrams of potential mask designs for online calibration of the micro-channel plate's position and active area.

solute position calibration of the MCP. Our plan is to add a permanent mask, one with a large open area, in order to have an on-line calibration of the recoil detector's position and active area. This would also be a useful upgrade of the system for an improved measurement of $a_{\beta\nu}$ in ^{38m}K [11], so we will have to consider both experiments when designing this mask. In terms of the right-handed current search, Fig 6.1 shows schematics of two potential mask designs which have the characteristics required to improve the experiment presented in this thesis, and which would also be compatible with the ^{38m}K experiment. First and foremost, the mask should have a large open area so as not to block many of the recoils we are measuring. The hatched area shown in Fig. 6.1 represents the inactive region of the MCP, *i.e.* beyond the 2.5 cm diameter of the current detector. In both designs there is a circular component of the mask at $R \approx 0.9R_{\text{max}}$ with small ($\varnothing$0.25 mm) holes spaced throughout which would be used to define the position calibration near the edge of the MCP. Furthermore, this part of the mask can be used to accurately define the active area of the detector with better position information that the current collimator.

In design (a), four arms come in from the edges and connect to a small circular piece centred on the MCP. The idea here is to leave as much open area as possible,

especially along the polarization axis (depicted by the thick red arrow). It is important to leave the actual centre of the detector open because this is where the photoions from the trap will be hitting the MCP, and so the inner circle must be larger than the cloud size in $\hat{x} - \hat{y}$ in order to keep this cloud position measurement clean. The arms have small holes throughout to define the position calibration over most of the MCP's active area; the drawback in this design is that the position calibration along the polarization axis (as well as perpendicular to it) will require the greatest amount of interpolation. Obviously, there is a trade-off between having a open area and knowing definitively the position calibration along the polarization axis. In this design, the mask covers less than 10% of the active area of the detector. One might consider as a spin-off of this design arms which would come in at $\pm 30°$ rather than $\pm 45°$ to the polarization axis so that the calibration is better defined along $\hat{x}$.

Design (b) is on the other side of the fence with regards to the trade-off between minimal blockage along the polarization axis and an unambiguous calibration of its position. This grid design yields calibration points throughout the active area of the MCP and thereby limits interpolation of the position calibration to the spacing between strips; as a suggestion, to keep the open area reasonably large ($\approx 25\%$ blocked), a 5×5 mm^2 grid with holes every 2.5 mm should give a very robust calibration.

Neither of these designs is the final solution, but are instead meant to stimulate discussions and define the basic criteria. The TRINAT collaboration will need to consider possible constraints imposed for compatibility with future $a_{\beta\nu}$ experiments as well as the relative merits of the two basic concepts before finalizing any design of an online mask for the MCP.

Another improvement of the recoil detection that would complement a new $a_{\beta\nu}$ experiment is having a larger MCP. This would allow us acquire more of the angular distribution of the recoils, and in particular would help to increase statistics in an R_{slow} measurement. We are considering the wedge-and-strip readout to replace the resistive anode, because the wedge-and-strip readouts are known to have linear position calibrations over large active areas [108]. In addition, our electrostatic hoop system used to generate the uniform electric field will need to be amended to accommodate a larger MCP. It remains an open question as to whether or not we would

like to have a larger 2^{nd} chamber.

6.2 Directions for Further Development

In this section, we describe improvements to system that require extensive development which are likely required to go below the 0.3% level. These include new types of atom traps and new nuclear β detection systems.

6.2.1 Far-Off Resonance Traps

The TRINAT collaboration has been interested in utilizing the extremely high polarization capabilities of a new type of trap: circularly-polarized far off-resonance dipole force traps (CFORTs). These purely optical traps confine atoms within *only* one magnetic sublevel state [109, 110, 111]. By choosing the sublevel to be one of the fully stretched states, this type of trap allows one to simultaneously polarize and confine the sample of atoms. The basic idea behind a CFORT is depicted in Fig. 6.2 and as shown, the CFORT is simply a circularly polarized laser beam that is focused to a tight waist. The trapping forces arise from the spatially varying ac-Stark shift from the laser beam. An atom with a resonant transition above the laser frequency will feel a force towards the region of high intensity, and transitions below are repelled. By tuning the $\sigma^{\pm}$ laser frequency between the D_1 and D_2 transitions, the ac-Stark shift will create a potential well *only* for atoms in the $4S|2 \pm 2\rangle$ stretched state. This Stark potential is shown for light tuned $\approx 6\times$ closer to the D_1 line than the D_2 as a function of the radius from the beam centre (in units of the beam waist, w_o) in Fig. 6.2. The solid line corresponding to the $|2 \pm 2\rangle$ stretched state is the only one which feels a potential well, with all others (dashed) feeling a positive potential. With only atoms in the stretched state trapped, the cloud will have 100% atomic and nuclear polarization. This is true, at least, in the limit that we have shone in perfectly circularly polarized light; a small component of the wrong polarization will do two things: (1) it will pump atoms into lower sublevels through real absorption of the light, and (2) it will act like a magnetic field (the "analogous Zeeman effect" [112])

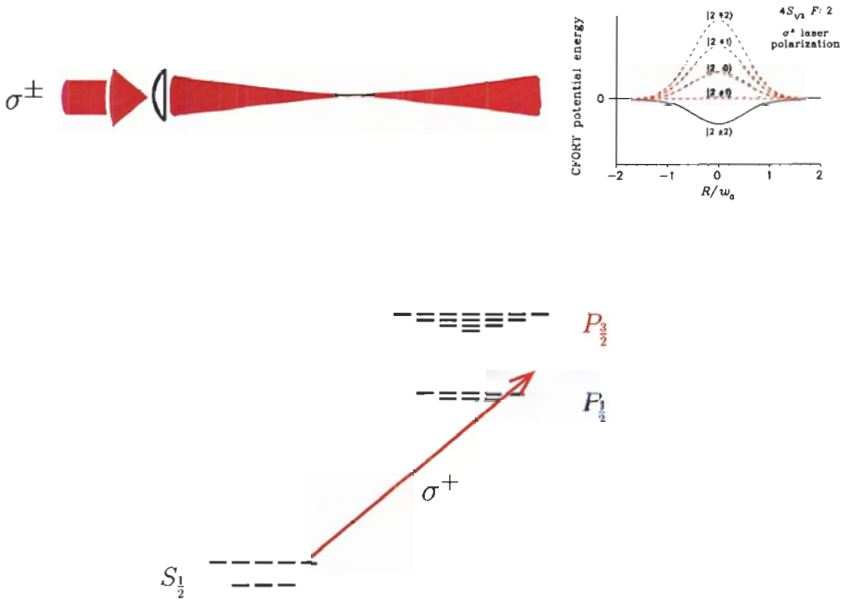

FIGURE 6.2: Schematic diagram of a circularly-polarized far off-resonance dipole force trap (CFORT). The graph indicates the trapping potential at the waist as a function of the radial position, and shows that the only negative potential is for the $|2 \pm 2\rangle$ fully stretched state.

and mix the stretched state with other magnetic sublevels, so that strictly speaking F is no longer a good quantum number. The first effect does not affect the polarization of the atoms because once in the wrong sublevel, it is no longer trapped and so this effect simply reduces the overall lifetime of the CFORT. The latter, however, will have a small effect on the polarization of the cloud because the atoms in the originally $F = 2, m_F = \pm 2$ state will remain trapped, but have small components of other levels which are not perfectly polarized. Explicit calculations of this effect will need to be done, but we expect that with the current quality of our circular polarization, that the CFORT will provide polarizations $\gtrsim 0.999$.

This is clearly a very well suited trap for polarized β decay experiments, however loading of such a trap is very difficult, particularly in potassium where the splitting between the $P_{1/2}$ and $P_{3/2}$ states is not very large; the dipole force in this alkali is not as far off-resonance as in, say, rubidium. Potassium therefore has inherently stronger heating from real absorption of photons, and so loading the CFORT and attaining

long lifetimes requires significant development. As a first step, TRINAT has recently demonstrated the ability to load atoms initially trapped in a MOT into a linearly-polarized FORT with 1% efficiency and lifetimes of 1 sec [113, 114]. We will continue development of this and then the circularly-polarized FORT using stable ^{39}K; if the loading efficiency and trap lifetimes are large enough for use with radioactives, then we would begin implementing the CFORT into our system for β decay experiments with ^{37}K.

6.2.2 β Detection

The dependence of B_ν on the β response function is relatively weak in the current experiment because the β-telescope simply tags events where the positron was emitted within a small solid angle centered around $+\hat{z}$; the physics is extracted by the position asymmetry of the recoils in the recoil detector. However, once we are able to control and minimize trap losses, a β singles measurement of A_β would certainly require better β detection than is presently obtained using the phoswich detectors. Telescopes similar to the DSSSD-scintillator detector used for the B_ν measurement would likely suffice, however the current constraints given the small port sizes make such detectors problematic.

It is suggested that TRINAT perform the B_ν experiment with the improvements listed in §6.1 before investing the time and effort needed to improve the β detection along the optical pumping axis. Once it is demonstrated that a β singles measurement of A_β is possible with reduced backgrounds, and once a serious attempt at a measurement of R_{slow} is performed, then we would know how well we would need to measure the βs and could design detectors and possibly a new 2$^{\text{nd}}$ chamber accordingly.

6.2.3 Shake-off Electron Detection

Inspired by the results of the Berkeley group [115], the TRINAT collaboration is investigating the use of a micro-channel plate in the chevron configuration as a detector of the shake-off electrons following β decay. The same electric field used to collect the Ar^+ ions accelerates low-energy electrons in the opposite direction which can be

detected with high efficiency. Since there are two (or more) shake-off electrons for each Ar^{+1} (or higher charge state) decay, and since the field accelerates all of the e^- onto the MCP electron detector, this technique provides a very high efficiency for recoil$-e^-$ coincidence detection.

Unfortunately, this technique is incompatible with the present $\beta-$Ar detection system, and so represents a path of research that is diverges greatly from the one presented in this thesis. However, a very promising aspect of this technique is the ability to perform a *clean* measurement of the β asymmetry. With a clean tag of decays from the laser-cooled atoms using the shake-off electron(s), we will be able to require a coincidence with the phoswich detectors and *greatly* reduce our backgrounds from untrapped atoms.

Once initial tests of the shake-off electron detection are performed* the collaboration will be able to compare the pros and cons of each detection system and decide which route to pursue.

6.3 Expected Sensitivities of Future Experiments

The previous sections have outlined how TRINAT can improve their search for right-handed currents using a laser-cooled, polarized ^{37}K source of β decay. In the short-term (§6.1), we can expect to reach the 0.5% level with minor modifications to the experiment presented in this thesis. §6.2 has indicated a couple of directions which will likely be necessary to go beyond towards our ultimate goal of 0.1% precision.

The sensitivity for various precisions of the experiment in the context of the manifest left-right symmetric model is summarized in Fig. 6.3. Shown are the 90% CL limits of the present work along with the limits one would get with an improved measurement of B_ν to 0.5% and 0.1%. With the 0.5% measurement of B_ν we expect to make after making the modest modifications outlined in §6.1, we will be sensitive to right-handed boson masses of 290 GeV. At this level, we would already be beyond the present world-average of neutron decay, and would even be complementary to the

*As of the writing of this thesis, the MCP electron detector was being installed, with an experiment planned for the end of November 2005.

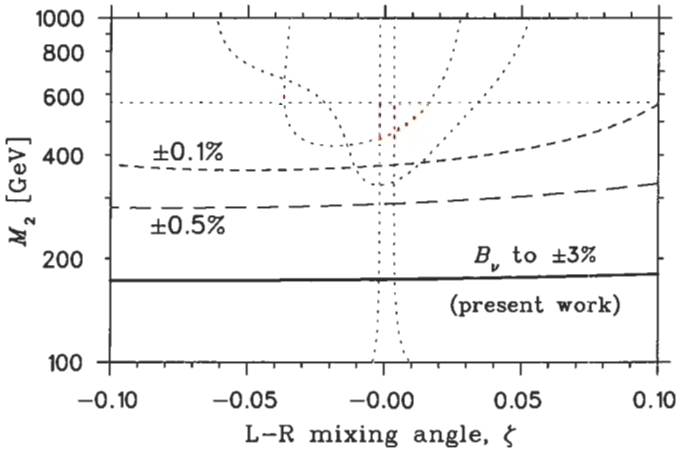

FIGURE 6.3: Expected sensitivities to right-handed current parameters M_2 and ζ in the minimal left-right symmetric model from the present and improved measurements of B_ν to ±0.5% and ±0.1%. Also plotted are the results from other model-independent experiments from Figs. 2.3 and 2.5 (dotted lines).

limits from the world-average of all nuclear β decay limits (save the $0^+ \rightarrow 0^+$ limits on ζ). To reach the limits imposed from μ decay and to significantly contribute to the world-average of nuclear β decay, we will need to re-evaluate our systematics after the next experiment and likely upgrade the system based on the new systematic evaluations.

Once we go beyond a 0.5% measurement, we will also need to consider theoretical uncertainties: recoil-order corrections, which are calculable from [24] given that this is an isobaric analogue decay (see §2.1.2); radiative corrections, which in principle are also calculable to the precision needed [19]; and uncertainties in $g_A M_{GT}/g_V M_F$, which are already small, but may require a new measurement [116].

If we are able to minimize losses to the walls or utilize the shake-off electron technique to perform a precise measurement of A_β, and assuming we are able to measure R_{slow} precisely, we can combine limits from these complementary correlations to our exclusion plot of future sensitivities. Fig. 6.4 is an exclusion plot similar to Fig. 6.3, except in this case we include β asymmetry and R_{slow} measurements to the same precision, *i.e.* all three to ±0.5% (long dashed line) and ±0.1% (short dashed line). As one can see, there is a significant increase in sensitivity and so it will

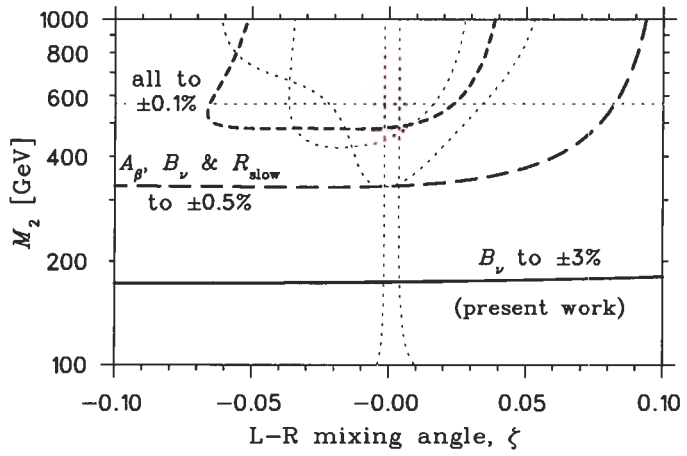

FIGURE 6.4: Expected limits to M_2 and ζ in the minimal left-right symmetric model from combined measurements of A_β, B_ν and R_{slow}. Shown, in addition to the result presented in this thesis, are the contour limits one would place if all three correlations could be measured to $\pm 0.5\%$ and to $\pm 0.1\%$ (which is the goal of TRINAT's polarized ^{37}K program).

be worth the effort to measure these other correlations. In addition to increased sensitivity, a precise measurement of A_β, B_ν and R_{slow} all in the same experiment will allow us to have cross-checks of systematics. For example, we could compare the result we get from A_β alone to that of B_ν; if they are significantly different, we could use the ratio of A_β/B_ν to test whether the discrepancy comes from our polarization measurement since in this ratio, the polarization cancels. Similarly, if A_β and B_ν both give consistent answers but differ from that of R_{slow}, it may be an indication that the value of $g_A M_{GT}/g_V M_F$ needs re-evaluation since R_{slow} is less sensitive to its value than the other correlations.

CHAPTER 7

Conclusions

This thesis has described what originally was expected to be a proof-of-principle experiment, but which resulted in the first correlation parameter measurement in β decay using a polarized, laser-cooled radioactive source. This experiment has required pioneering techniques in both atomic and nuclear physics. We are the first group to utilize optical pumping techniques to polarize a radioactive sample of laser-cooled atoms. We have developed photoionization techniques to both characterize the size and position of the cloud of atoms as well as to deduce the average polarization of the sample *in situ*. A detailed Monte Carlo simulation and analysis scheme has been developed to extract physics results from the observed asymmetries.

The neutrino asymmetry has been measured for the first time in a system other than the neutron*, and found to be $B_\nu = -0.755 \pm \underset{\text{(stat)}}{0.020} \pm \underset{\text{(syst)}}{0.013}$, in agreement with the Standard Model prediction of $-0.7692(15)$. In the context of the minimal left-right symmetric model, this limits the contribution of a possible right-handed boson to $M_2 > 180$ GeV/c^2 at the 90% CL. This measurement is not competitive with other searches for right-handed currents, however our dominant systematics have been identified and we have shown that they can be reduced.

We have also introduced the R_{slow} correlation and shown that it is a sensitive probe of right-handed current parameters which can be measured in parallel with B_ν. Being a $\beta-$Ar coincidence, it is not susceptible to backgrounds like a β asymmetry measurement and so we also expect to be able to make a precise measurement of R_{slow} the next time we run. The combined measurement of both B_ν and R_{slow}will be

*Except for the 15% measurement in ^{19}Ne.

a powerful probe of physics outside the Standard Model, and will complement other experiments which have limited the existence of right-handed currents in the weak interaction.

With the modest improvements to our system outlined in this thesis, we expect to to be able to measure B_ν to $\lesssim 0.5\%$ next time we run. The most important development projects are: improving the polarization and developing a more complete model of the optical pumping process; reducing the cloud movement during the OP/MOT cycle; and having an online MCP position calibration. These can all be investigated using stable potassium before we pursue another β decay measurement using ^{37}K.

Appendix A

Cloud Characteristics in Detail

Here we present the results of fitting the photoions to when the MOT was on, and also during the optical pumping part of the cycle. The MOT size and position immediately before and after the optical pumping time can be used to interpolate the cloud characteristics during the optical pumping process. For the cloud position, as discussed at the end of §4.6.3, we assume the sail velocity is constant, and so fit a straight line to the data.

The width of the MOT photoions defines the initial cloud size, and the width at the end of the optical pumping tells us how much the cloud expanded during the OP part of the cycle while the atoms are untrapped. In this case, we expect a quadratic dependence as was explained in §4.6.4.

In the figures that follow, the MOT photoion centroids and widths are depicted as diamonds and the interpolated cloud characteristics are depicted as blue lines with the $\pm 1\sigma$ uncertainties shown by dashed cyan lines. The black circles show the results of fitting Gaussians to the photoions during the optical pumping part of the cycle, and if the χ^2/ν is better than that interpolated by the MOT photoions, the red line shows the best direct fit to those points.

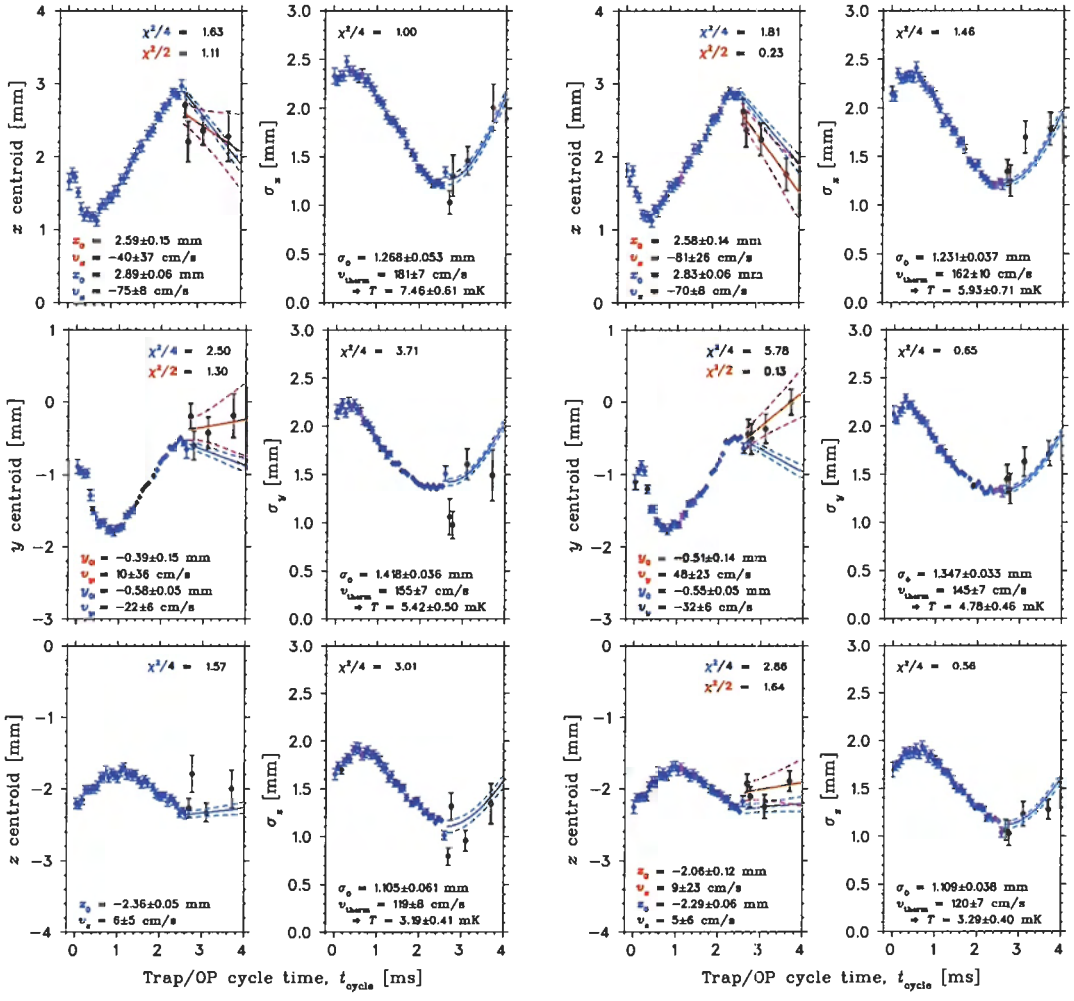

FIGURE A.1: Cloud/trap sizes and positions for the 1[a] data set with σ^+ (left) and σ^- (right) laser light polarization.

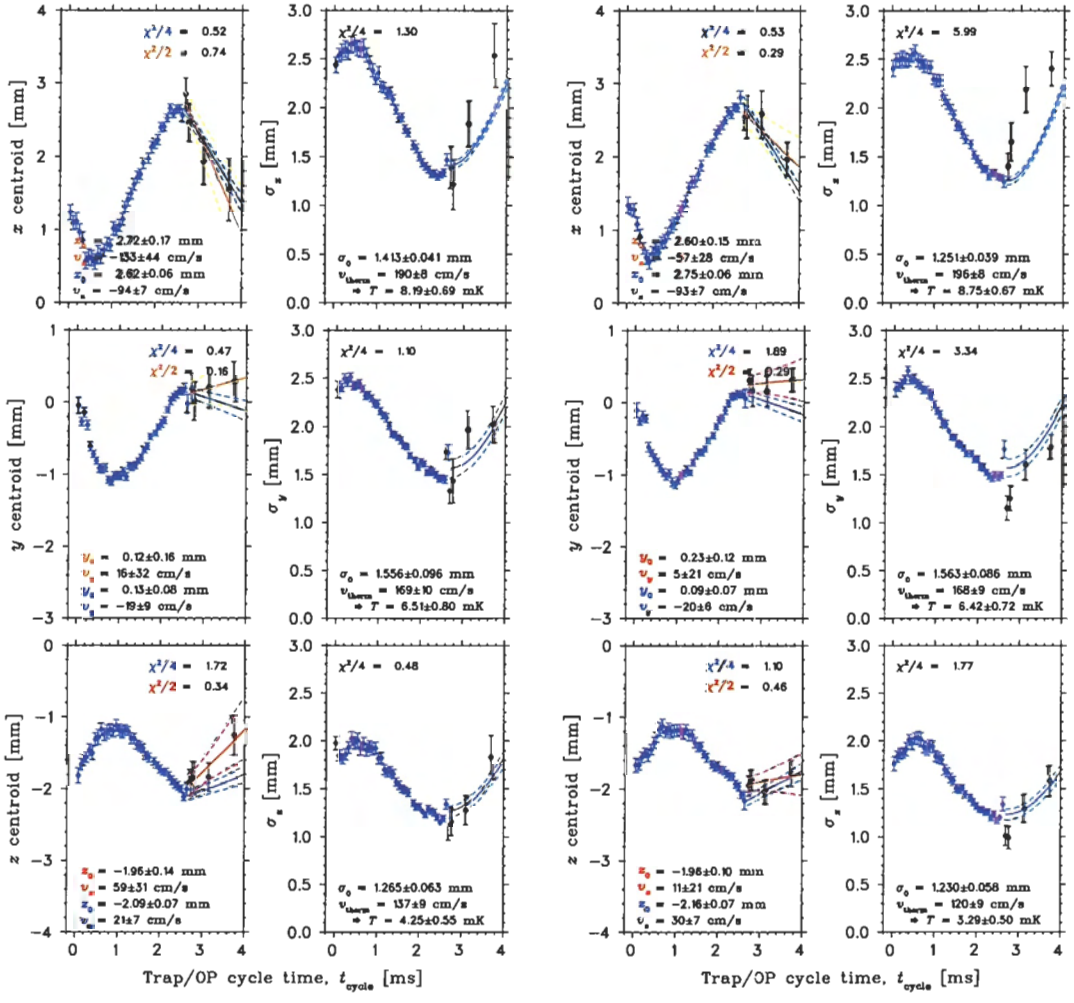

FIGURE A.2: Cloud/trap sizes and positions for the 1^b data set with σ^+ (left) and σ^- (right) laser light polarization.

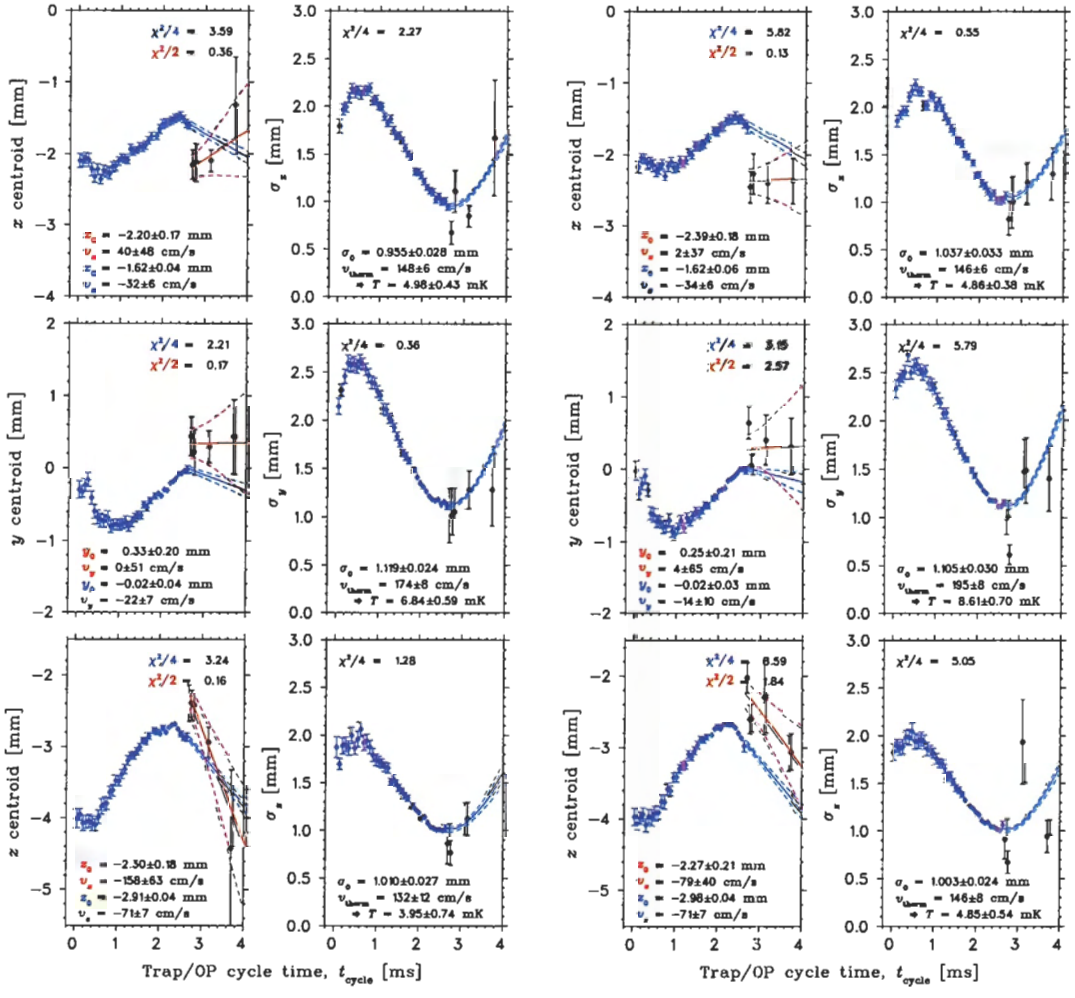

FIGURE A.3: Cloud/trap sizes and positions for the 2^- data set with σ^+ (left) and σ^- (right) laser light polarization and $B = -2$ G.

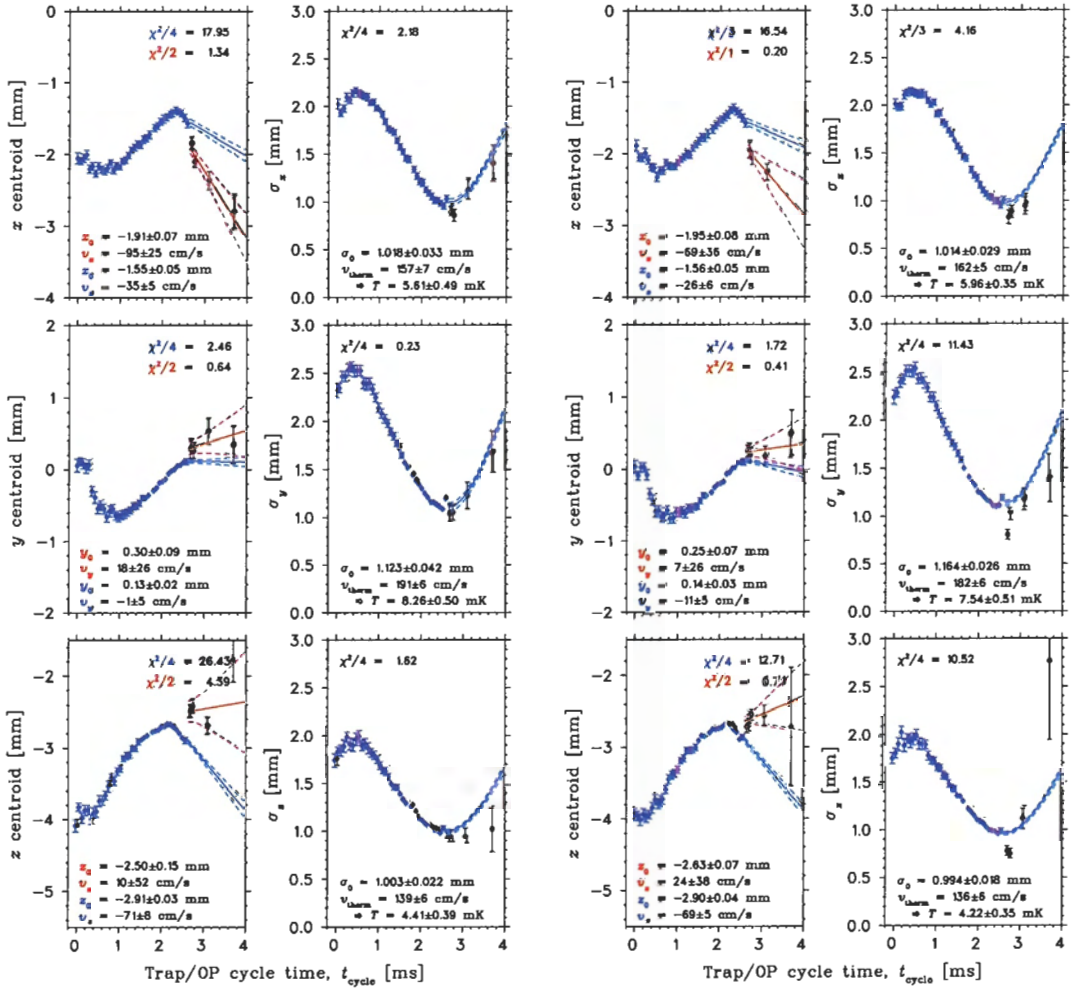

FIGURE A.4: Cloud/trap sizes and positions for the 3^+ data set with σ^+ (left) and σ^- (right) laser light polarization and $B = +2$ G.

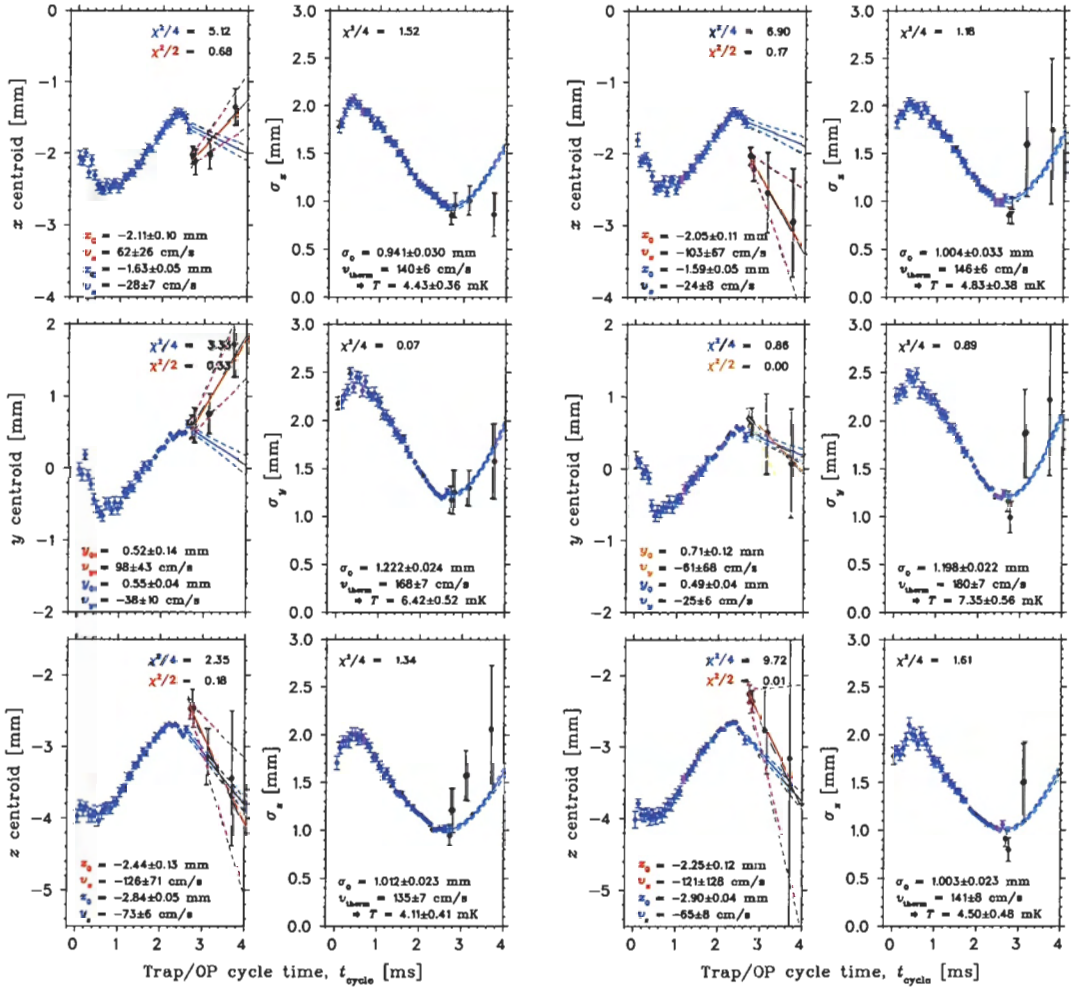

FIGURE A.5: Cloud/trap sizes and positions for the 3^- data set with σ^+ (left) and σ^- (right) laser light polarization and $B = -2$ G.

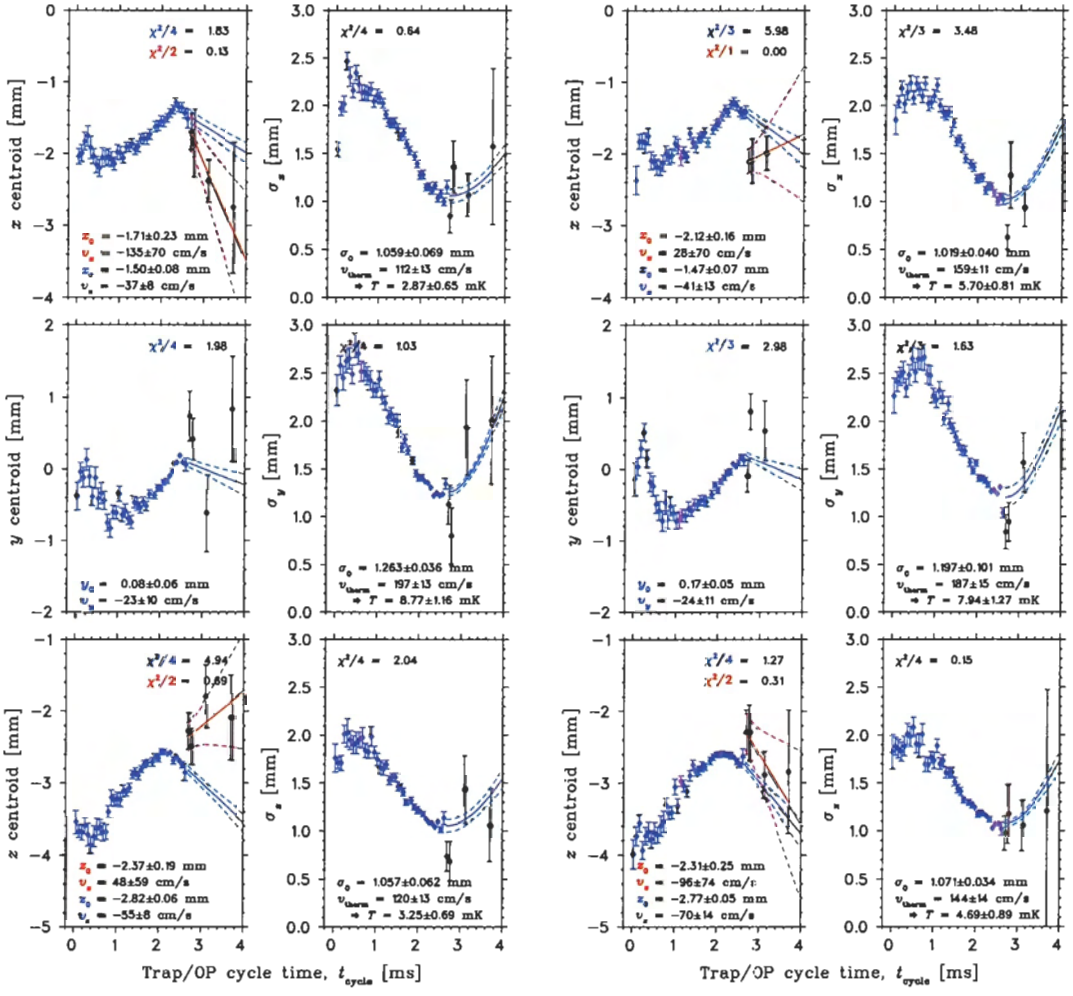

FIGURE A.6: Cloud/trap sizes and positions for the 4^+ data set with σ^+ (left) and σ^- (right) laser light polarization and $B = +2$ G.

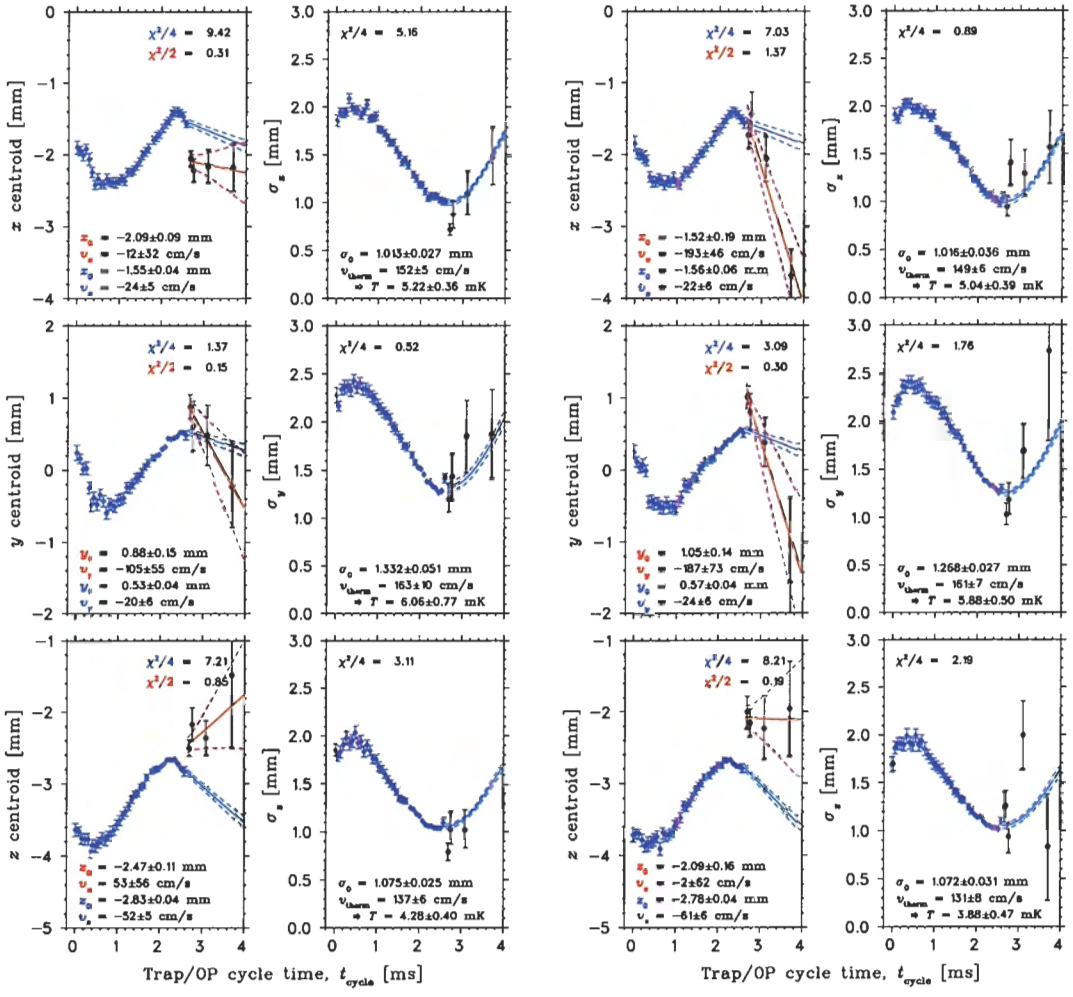

FIGURE A.7: Cloud/trap sizes and positions for the 4^- data set with σ^+ (left) and σ^- (right) laser light polarization and $B = -2$ G.

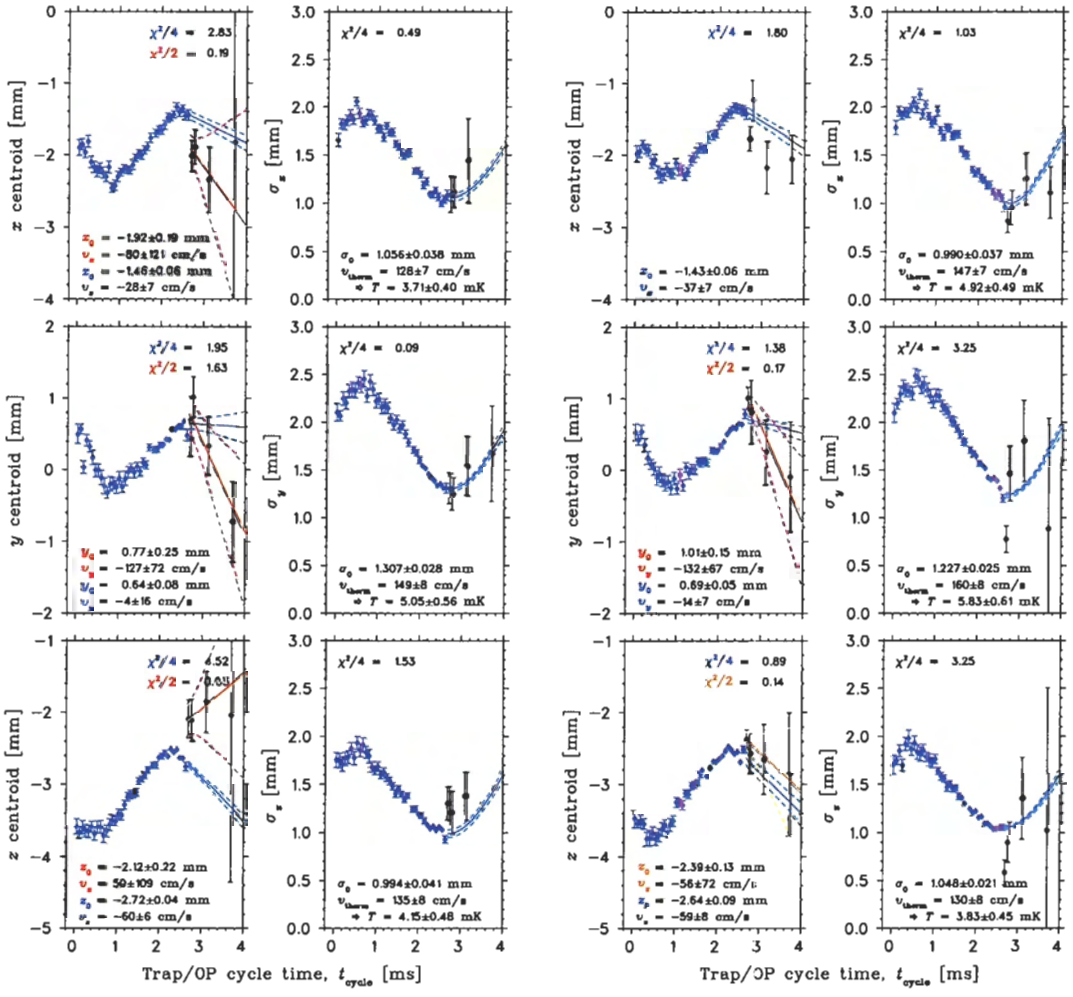

FIGURE A.8: Cloud/trap sizes and positions for the 5^- data set with σ^+ (left) and σ^- (right) laser light polarization and $B = -2$ G.

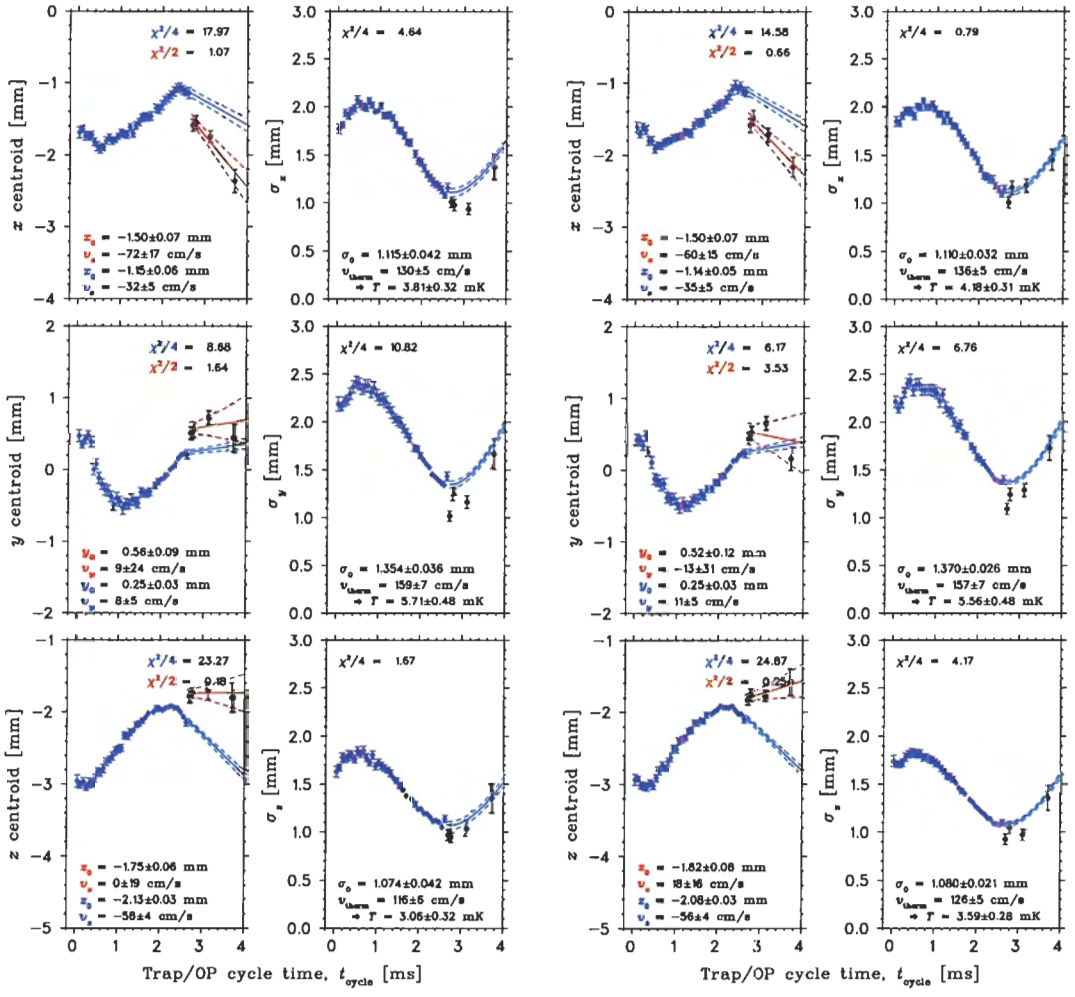

FIGURE A.9: Cloud/trap sizes and positions for the 6^+ data set with σ^+ (left) and σ^- (right) laser light polarization and $B = +2$ G.

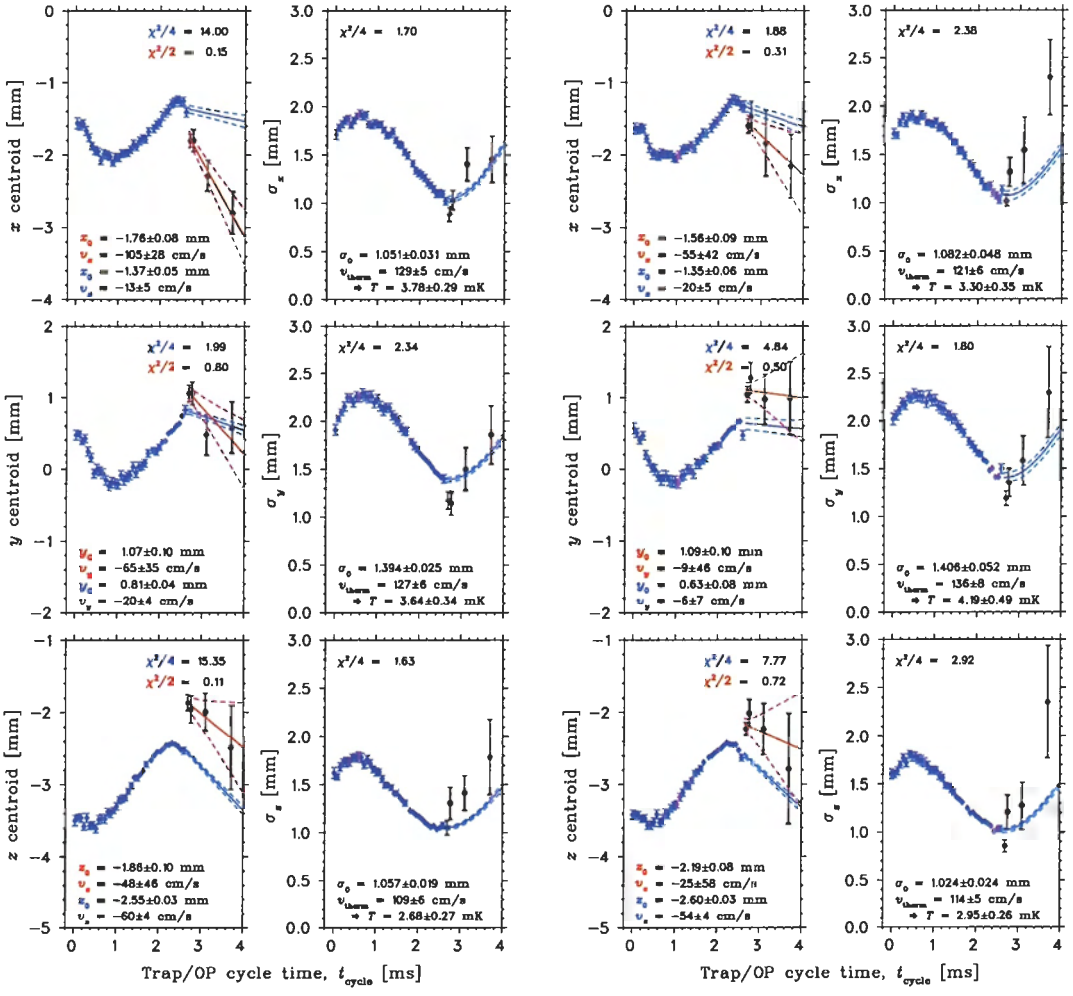

FIGURE A.10: Cloud/trap sizes and positions for the 6^- data set with σ^+ (left) and σ^- (right) laser light polarization and $B = -2$ G.

APPENDIX B

Details on Data Analysis

This thesis contains many fits to spectra, and it is important for one to understand how the quantities of interest were deduced. This appendix is meant to provide the reader with some details of the fit programs used, a discussion of their estimation of the statistical uncertainty, and to explain how, in general, non-random (or systematic) uncertainties are included and propagated.

B.1 Fitting Routines

We use two fitting routines throughout this thesis, both based on the maximum likelihood method for parameter estimation:

1. `physica` – a very powerful, graphical mathematical software package developed at TRIUMF [117]. Data input/output of vectors and matrices is straightforward, and many built-in functions provide the ability to do much of the data manipulation with great ease.

2. `fit.F` – a completely general Fortran fitting routine [118], where one can fit *any* function numerically through a user subroutine.

`Physica` was used for all analytic and any simple histogram fits because of its ease of use. By 'simple histograms', we mean MC simulations whose output is exactly the same as the data (e.g. the MCP positions, where both data and MC have 48×48 1 mm bins). In the case where non-analytic calculations were required (e.g. rate equations and 'complicated' MC simulations), the slightly less convenient `fit` was used. The

data and output of `fit` would then be processed through `physica` to view and plot the results. As discussed below, the same likelihood function is maximized by both programs, although the method to find that maximum is different: `physica` uses a gradient-search technique while `fit` uses the Marquardt algorithm [119]. Tests have been performed to prove that both return the same results, and this was found to be true to many significant digits.

B.1.1 Parameter Estimation

In what follows, let us assume that we have performed an experiment and have obtained a spectrum with observed values y_k, where $k = 1, 2, \ldots, N$ are the number of bins included in the fit. The model which we fit the data to will have predictions, $f_k(\boldsymbol{p})$, where $\boldsymbol{p} = (p_1, p_2, \ldots, p_n)$ are the n parameters being fitted. The data we observe represents a random sample from some parent probability distribution function. We consider below two examples of these distributions: Gaussian and Poissonianly-distributed data.

Gaussianly-distributed data

Let us assume that the probability to observe a count in bin k is distributed as a Gaussian whose mean is the model prediction, $f_k(\boldsymbol{p})$, and which has an unknown variance, σ_k^2:

$$P_k(\boldsymbol{p}) = \frac{1}{\sqrt{2\pi}\sigma_k} \exp\left(-\frac{(y_k - f_k(\boldsymbol{p}))^2}{2\sigma_k^2} \right) \tag{B.1}$$

In general (e.g. if y_k is the number of counts), one estimates the variance by the data which, if Gaussianly distributed, yields the well-known $\sigma_k = \sqrt{y_k}$. In fact, a better estimate is likely to come from the *model* prediction (properly normalized, of course), and one can take $\sigma_k = \sqrt{f_k}$.

The goal is to find the optimal values of the parameters, $\boldsymbol{p}^\circ$, which maximize the

joint probability function of all N bins being fit:

$$\begin{aligned} L(\boldsymbol{p}) &= P_1(\boldsymbol{p}) \times P_1(\boldsymbol{p}) \times \cdots \times P_N(\boldsymbol{p}) \\ &= \prod_{k=1}^{N} P_k(\boldsymbol{p}) \end{aligned} \tag{B.2}$$

This is the method of maximum likelihood, described in any number of texts on statistics [98, 120].

Taking the natural logarithm of the likelihood functions turns the troublesome product into a sum, but does nothing to change the maximum of the function. Similarly, if we then change the sign of the function, the maximum will become the minimum; many minimization techniques exist and so in practice one actually finds the maximum of the likelihood by *minimizing* the log-likelihood function, $\mathcal{L}$:

$$\mathcal{L}(\boldsymbol{p}) \equiv -\log L(\boldsymbol{p}) = \sum_{k=1}^{N} \log P_k(\boldsymbol{p}) \tag{B.3}$$

In the case of Gaussianly distributed values, Eq. (B.1), one finds equivalence with the χ^2 statistic:

$$\begin{aligned} \mathcal{L}(\boldsymbol{p}) &= \text{const} + \frac{1}{2} \sum_{k=1}^{N} \frac{\left[y_k - f_k(\boldsymbol{p})\right]^2}{\sigma_k^2} \\ &= \mathcal{L}_{\min} + \frac{1}{2}\chi^2 \end{aligned} \tag{B.4}$$

and we see that an increase $\chi^2 = \chi^2_{\min} + s^2$ corresponds to an increase in the log-likelihood $\mathcal{L} = \mathcal{L}_{\min} + s^2/2$. Here, $s = \Phi^{-1}(1 - \gamma/2)$ is the quantile of the standard Gaussian corresponding to a confidence level of $1 - \gamma$. The most commonly used central confidence intervals of 68.3%, 90% and 95% are given by $s = 1, 1.64$ and 1.96 respectively.

We are only interested in the minimum of the log-likelihood function and its behavior near that minimum, so let us now consider a Taylor expansion of $\mathcal{L}$ around the best fit values, $\boldsymbol{p}^\circ$:

$$\mathcal{L}(\boldsymbol{p}) = \mathcal{L}(\boldsymbol{p}^\circ) + \sum_{i=1}^{n} \frac{\partial \mathcal{L}}{\partial p_i}(p_i - p_i^\circ) + \frac{1}{2} \sum_{i=1}^{n} \sum_{j=1}^{n} \frac{\partial \mathcal{L}}{\partial p_i} \frac{\partial \mathcal{L}}{\partial p_j}(p_i - p_i^\circ)(p_j - p_j^\circ) + \ldots \tag{B.5}$$

where the partial derivatives are evaluated at the best fit values of the parameters. Substituting Eq. (B.4) into the expansion Eq. (B.5) inspires us to define a vector $\boldsymbol{b}$ and matrix $\boldsymbol{M}^{-1}$ as:

$$[\boldsymbol{b}]_i \equiv -\frac{\partial \mathcal{L}}{\partial p_i} = 2\sum_{k=1}^{N} \frac{\partial f_k}{\partial p_i} \frac{(y_k - f_k(\boldsymbol{p}))}{\sigma_k} \tag{B.6}$$

$$[\boldsymbol{M}^{-1}]_{ij} \equiv \frac{\partial^2 \mathcal{L}}{\partial p_i \partial p_j} = 2\sum_{k=1}^{N} \frac{\partial^2 f_k}{\partial p_i \partial p_j} \frac{1}{\sigma_k^2} \tag{B.7}$$

We will return to $\boldsymbol{M}^{-1}$ in §B.1.2 where we will see it is the inverse error matrix, hence the suggestive name. In (compact) matrix notation, we see that we are therefore interested in minimizing the function (T denotes the transpose):

$$\mathcal{L}(\boldsymbol{p}) \;=\; \mathcal{L}(\boldsymbol{p}^\circ) \;-\; \boldsymbol{b}\cdot(\boldsymbol{p}-\boldsymbol{p}^\circ) \;+\; \tfrac{1}{2}(\boldsymbol{p}-\boldsymbol{p}^\circ)^T \boldsymbol{M}^{-1}(\boldsymbol{p}-\boldsymbol{p}^\circ) \tag{B.8}$$

By linearizing this function (*i.e.* assuming $\frac{\partial^2(\ln P)}{\partial p_i \partial p_j} \to 0$) and imposing $\nabla\mathcal{L} = 0$, we reduce the problem to solving the matrix equation:

$$\boldsymbol{b} = \boldsymbol{M}^{-1}\,\nabla(\boldsymbol{p}-\boldsymbol{p}^\circ) \tag{B.9}$$

It is exactly this equation that both `physica` *and* `fit` solve to estimate their best fit parameters and matrix $\boldsymbol{M}^{-1}$. Therefore, as mentioned earlier, their results will be identical because any reasonably well-behaved fit will converge to the same minimum, regardless of the method used to get there.

Poissonianly-distributed data

In the case of low-statistics*, the probability of observing y_k events in a bin k where the true mean is f_k will be a Poisson distribution:

$$P_k(\boldsymbol{p}) = \big[f_k(\boldsymbol{p})\big]^{y_k} \frac{e^{-f_k(\boldsymbol{p})}}{y_k!} \tag{B.10}$$

The log-likelihood function will in this case be:

$$\mathcal{L} = \sum_{k=1}^{N} y_k \ln f_k(\boldsymbol{p}) - f_k(\boldsymbol{p}) \tag{B.11}$$

*When uncertainties do not need to be propagated! See discussion in §5.2.4.

In order to arrive at the same matrix equation to be minimized, Eq. (B.9), we should this time define:

$$[\boldsymbol{b}]_i \equiv -\frac{\partial \mathcal{L}}{\partial p_i} = -\sum_{k=1}^{N} \frac{\partial f_k}{\partial p_i}\left(\frac{y_k}{f_k} - 1\right) \tag{B.12}$$

$$[\boldsymbol{M}^{-1}]_{ij} \equiv \frac{\partial^2 \mathcal{L}}{\partial p_i \partial p_j} = -\sum_{k=1}^{N} \frac{\partial^2 f_k}{\partial p_i \partial p_j}\frac{y_k}{f_k^2} \tag{B.13}$$

For any and all histograms, Poisson statistics is assumed and the fit minimizes $\mathcal{L}$ based on Eq. (B.10). When we are fitting data that has been manipulated and uncertainties need to be propagated, we revert to using Gaussian statistics, *i.e.* the p.d.f. defined by Eq. B.1, since we have not derived an expression for $\mathcal{L}$ based on the difference of two Poisson variables. Until this is done and in order to be confident the bias introduced by this Gaussian approximation is small, one should rebin the data so that all bins have $\gtrsim 25$ counts*.

B.1.2 Statistical (Fit) Uncertainties

The statistical uncertainty of the fit parameters, $\boldsymbol{p}$, is determined by the shape of the likelihood function near the best fit values, $\boldsymbol{p}^\circ$. Generally, one estimates the uncertainties based on the change required to raise $\mathcal{L}$ from $\mathcal{L}_{\min}$ to $\mathcal{L}_{\min} + 1/2$ which, in the Gaussian limit, corresponds to an increase in χ^2 of one. This is then quoted as the 1σ, or 68.3% confidence level, uncertainty in the fit parameter. In general the s^{th} σ uncertainty is found where $\chi^2 = \chi^2_{\min} + s^2$, or equivalently where $\mathcal{L} = \mathcal{L}_{\min} + s^2/2$.

We take the form of our log-likelihood function to be a multi-variant Gaussian of the n fitting parameters:

$$\mathcal{L}(\boldsymbol{p}) = \frac{1}{(2\pi)^{n/2}}\frac{1}{|M|^{1/2}} \exp\left(-\frac{1}{2}(\boldsymbol{p}-\boldsymbol{p}^\circ)^T \boldsymbol{M}^{-1}(\boldsymbol{p}-\boldsymbol{p}^\circ)\right), \tag{B.14}$$

where $|M|$ represents the determinant of $\boldsymbol{M}$, and all other parameters retain the definitions of the previous section. Indeed, this is the same $\mathcal{L}(\boldsymbol{p})$ as Eq. (B.3); the

*Many people have many different thresholds, from 5 up to 500; just depends what one means by "a *small* bias."

difference is that here the sum over bins has already performed, and we are only considering the dependence of the log-likelihood as a function of the fit parameters, $\boldsymbol{p}$. At this time, we see that correlations between the fit parameters will be contained in the off-diagonals of the matrix, $\boldsymbol{M}$, which we now identify as the covariance, or error, matrix:

$$\boldsymbol{M} = \begin{pmatrix} \sigma_{p_1}^2 & \mathrm{cov}(p_1,p_2) & \dots & \mathrm{cov}(p_1,p_n) \\ \mathrm{cov}(p_1,p_2) & \sigma_{p_2}^2 & \dots & \mathrm{cov}(p_2,p_n) \\ \vdots & \vdots & \ddots & \vdots \\ \mathrm{cov}(p_1,p_n) & \mathrm{cov}(p_2,p_n) & \dots & \sigma_{p_n}^2 \end{pmatrix} \tag{B.15}$$

The diagonal elements of this matrix represent the total (statistical) variances of the fit parameters. As can be seen by Eqs. (B.7) and (B.13), the inverse error matrix is the one actually used in maximizing the likelihood; one calculates the error matrix by inverting the inverse error matrix using numerical techniques.

The covariance of two parameters, say $p_1 = x$ and $p_2 = y$, goes like $\mathrm{cov}(x,y) \rightarrow \frac{1}{N}\sum[(x_k - x_k^\circ)(y_k - y_k^\circ)]$ as the number of bins $N \rightarrow \infty$. In that limit, if the fit parameters were all independent, we would expect these product of deviations to average out and arrive at a net covariance of zero; in this case, the matrix would be diagonal and no correlations would exist between the fit parameters. In general, however, covariances exist and – especially if the correlations are high – one must be careful to include them when estimating and propagating uncertainties.

A two-parameter fit

In order to remove some of the abstraction of the previous section and to actually see how correlations may affect our uncertainty estimations, let us restrict ourselves for the moment to a simple two-parameter fit. With $n = 2$, the general multi-variant Gaussian p.d.f., Eq. (B.14), reduces to:

$$P(x,y) = \frac{1}{2\pi}\frac{1}{|M|^{1/2}} \exp\left[-\frac{1}{2}\begin{pmatrix} x-x^\circ & y-y^\circ \end{pmatrix}\begin{pmatrix} M_{xx}^{-1} & M_{xy}^{-1} \\ M_{xy}^{-1} & M_{yy}^{-1} \end{pmatrix}\begin{pmatrix} x-x^\circ \\ y-y^\circ \end{pmatrix}\right], \tag{B.16}$$

and the covariance matrix, Eq. B.15, similarly reduces to the 2×2 matrix:

$$M = \begin{pmatrix} \sigma_x^2 & \mathrm{cov}(x,y) \\ \mathrm{cov}(x,y) & \sigma_y^2 \end{pmatrix} = \begin{pmatrix} \sigma_x^2 & \rho\sigma_x\sigma_y \\ \rho\sigma_x\sigma_y & \sigma_y^2 \end{pmatrix}, \tag{B.17}$$

where we have let $\rho \equiv \mathrm{cov}(x,y)/\sigma_x\sigma_y$. In this simple case, analytic forms for the determinant and inverse of the error matrix are easily derived:

$$\det M = \sigma_x^2\sigma_y^2(1-\rho^2) \qquad \text{and} \qquad M^{-1} = \frac{1}{1-\rho^2}\begin{pmatrix} \frac{1}{\sigma_x^2} & \frac{-\rho}{\sigma_x\sigma_y} \\ \frac{-\rho}{\sigma_x\sigma_y} & \frac{1}{\sigma_y^2} \end{pmatrix}. \tag{B.18}$$

Substituting these expressions into Eq. (B.16) and performing the matrix multiplication yields:

$$P(x,y) = \frac{1}{2\pi\sigma_x\sigma_y\sqrt{1-\rho^2}} \exp\left[\frac{-1}{2(1-\rho^2)}\left(\frac{(x-x^\circ)^2}{\sigma_x^2} + \frac{(y-y^\circ)^2}{\sigma_y^2} - 2\frac{\rho}{\sigma_x\sigma_y}(x-x^\circ)(y-y^\circ)\right)\right]. \tag{B.19}$$

The *error ellipse* is defined as the contour in the $x-y$ plane which covers a 68.3% confidence level of the two fit parameters; as noted earlier, this is defined by the contour where $\mathcal{L} = \mathcal{L}_{\min} + \frac{1}{2}$. By definition, the best fit values give the maximum likelihood:

$$\mathcal{L}_{\min} \equiv -\log P(x^\circ, y^\circ) \tag{B.20}$$

With the likelihood function defined by the p.d.f., Eq. (B.19), we find:

$$\mathcal{L} = \mathcal{L}_{\min} + \frac{1}{2}\left[\frac{1}{1-\rho^2}\left(\frac{(x-x^\circ)^2}{\sigma_x^2} + \frac{(y-y^\circ)^2}{\sigma_y^2} - 2\rho\frac{(x-x^\circ)}{\sigma_x}\frac{(y-y^\circ)}{\sigma_y}\right)\right] \tag{B.21}$$

The $s\sigma^{\text{th}}$ error ellipse is therefore the contour which satisfies:

$$\frac{1}{1-\rho^2}\left[\left(\frac{x-x^\circ}{\sigma_x}\right)^2 + \left(\frac{y-y^\circ}{\sigma_y}\right)^2 - 2\frac{\rho}{\sigma_x\sigma_y}(x-x^\circ)(y-y^\circ)\right] = s^2 \tag{B.22}$$

The 1σ ellipses are plotted for different values (and signs) of the correlation coefficient, ρ, in Fig. B.1. In the absence of correlations, the ellipse is a circle (black curve) and the

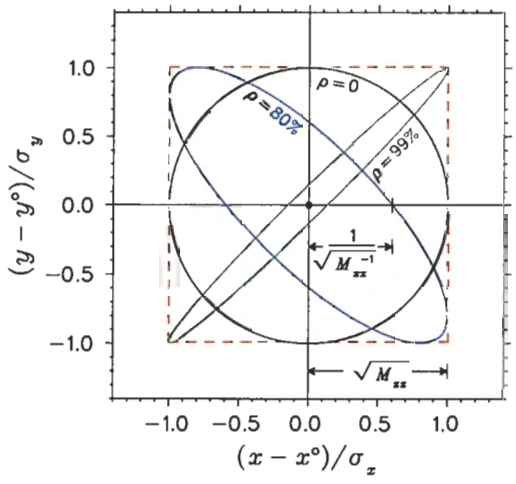

FIGURE B.1: Error ellipses for (un)correlated fit parameters. Plotted is the contour where $\mathcal{L} = \mathcal{L}_{\min} + \frac{1}{2}$ for values of $\rho = 0, -0.8$ and 0.99. The dashed box spanning $x^\circ \pm \sigma_x$ and $y^\circ \pm \sigma_y$ is the maxima for all contours, regardless of the value of the correlation coefficient.

maximum deviations all lie on-axis. As the definition implies, a *positive* correlation indicates that a change in x such that $x \gtrless x^\circ$ implies a corresponding change in y such that $y \gtrless y^\circ$, as shown by the $\rho = 99\%$ case (green curve). The semi-major axis of positively correlated parameters will be $+45^\circ$ from the $\hat{x}$ axis. Parameters that are anti-correlated (e.g. $\rho = -80\%$; blue curve) are rotated -45° so that that $y \lessgtr y^\circ$ for $x \gtrless x^\circ$.

The dashed box contains all the possible values of x and y, independent of whether correlations exist or not. As the figure indicates, these values are the square root of the diagonal elements of the error matrix. The intercepts, on the other hand, are determined by the inverse error matrix as shown in $\hat{x}$ for the $\rho = -80\%$ case; they represent the amount one parameter needs to vary to increase the log-likelihood by $1/2$ when correlations are neglected and the other parameter remains at its optimal value (the "uncorrelated" uncertainty).

The quoted (statistical) uncertainty

If one is fitting the parameter of interest directly, say y, then one quotes the total standard deviation as the uncertainty, and this will include any correlations with x.

If, however, the measurement is of a function of the fit parameters, $f = f(x, y)$, then the best fit value* is $f(x^\circ, y^\circ)$, and its uncertainty will be given by†:

$$\sigma_f^2 = \left(\frac{\partial f}{\partial x}\sigma_x\right)^2 + \left(\frac{\partial f}{\partial y}\sigma_y\right)^2 + 2\rho\sigma_x\sigma_y\left(\frac{\partial f}{\partial x}\right)\left(\frac{\partial f}{\partial y}\right) \tag{B.23}$$

As can be seen by, e.g. Eqs. (B.12) and (B.13), these partial derivatives are necessarily calculated as part of the fitting routine, so one can fall back on numerical estimates of them when they cannot be calculated analytically.

When fitting n parameters, there are $n(n-1)/2$ correlations to contend with, and these are best dealt with in matrix notation (which, incidentally, is also convenient when programming a fitting routine). For a function f of the fit parameters, $p_1, p_2, \ldots, p_n$, we evaluate it at the minimum of the log-likelihood to find the best value: $f(\boldsymbol{p}^\circ)$. The uncertainty associated with this evaluation of f is found by propagating the variances of the fit parameters, *including* their correlations. In matrix notation, the general formula is simply given by:

$$\sigma_f^2 = \boldsymbol{\mathcal{D}}^T \boldsymbol{M} \boldsymbol{\mathcal{D}}, \tag{B.24}$$

where the transpose of the directional derivative is a row vector defined as:

$$\boldsymbol{\mathcal{D}}^T \equiv \left(\frac{\partial f}{\partial p_1}, \frac{\partial f}{\partial p_2}, \cdots, \frac{\partial f}{\partial p_n}\right). \tag{B.25}$$

Perhaps more familiar as the law of propagation of uncertainty is the above in summation form:

$$\sigma_f^2 = \sum_{i=1}^{n}\left(\sigma_i\frac{\partial f}{\partial p_i}\right)^2 + 2\sum_{j>i}^{n}\mathrm{cov}(p_i, p_j)\left(\frac{\partial f}{\partial p_i}\right)\left(\frac{\partial f}{\partial p_j}\right).$$

This is just the generalization of Eq. (B.23) to n fit parameters.

B.1.3 Comparison of the fitting routine to a χ^2 map

An alternative to performing a maximum likelihood fit to the data is to define a grid of two parameters (say p_i and p_j) and to then map out the χ^2, point-by-point. In

*This and the rest of this section are only true for symmetric uncertainties, which random fluctuations generally are in the limit of reasonable (Gaussian) statistics. The case of asymmetric uncertainties will be discussed in §B.2.2.

this case, the data is never actually *fit*; the χ^2 is simply *calculated.* Once the grid is completed, contours of constant χ^2 can be interpolated and plotted (e.g. in `physica`), giving error "ellipses" (more properly 'error contours') which truly represent a χ^2 increase of one. In particular, no assumptions regarding the shape of the χ^2 around the minimum have been required, whereas the fitting routines assume it is quadratic. Initially, the error ellipses from the χ^2 map were compared to the fit results as a test of the fitting routine and propagation of uncertainties (and it served as an excellent debugging tool).

Once proven that the fitting routine found the same minimum and yielded error ellipses consistent with the χ^2 map, these comparisons were performed to investigate non-linear effects in the polarization deduced from the photoion data (*cf.* §4.7.1). Let us consider two parameter fits to the vanishing of the fluorescence in order to deduce the polarization, P. The results of a fit to σ^+ data with $B_\perp$ and I free to vary is shown in Fig. B.2(a). The solid lines are the calculated 1- and 2σ error ellipses from the fitting program, `fit`. From the χ^2 map, we get the corresponding contours of $\chi^2_{\min}+1$ and $\chi^2_{\min}+2$ (dashed lines). The fit and χ^2 error ellipses all overlap well for the most part, though some non-linearities are apparent at strong intensities. The χ^2 map also gives contours of constant polarization: shown are the best fit value, P° (dash-dotted line), $P^\circ \pm \sigma_P$ **and** $P^\circ \pm 2\sigma_P$ (dotted lines) where σ_P was calculated using Eq. (B.24) and the fit results. If the polarization was perfectly linear in these parameters, we would get a straight line, which appears to be approximately true. If our 1σ estimates were perfect, the dotted lines of $P^\circ \pm \sigma_P$ **and** $\pm 2\sigma_P$ would touch the extremes of the corresponding error ellipses ($P^\circ + n\sigma_P$ is to the left of the best estimate, *i.e.* to lower $B_\perp$). The deviations are quite small for the 1σ ellipse, indicating the fit returned a good estimate of the parameters' uncertainties and correlations. The difference at 2σ is becoming significant for $P^\circ + \sigma_P$.

The same comparison was performed on σ^- data with S_3 and I free to vary, with the results in Fig. B.2(b). The 1σ error ellipses still overlap well, but the 2σ contour shows greater distortions, and looks more pear-shaped than elliptical. Note also that the contours of constant P show larger non-linearities. Even in this distorted case, the 1σ error ellipses line up rather well with the contours of $P^\circ \pm \sigma_P$. The 2σ ellipses

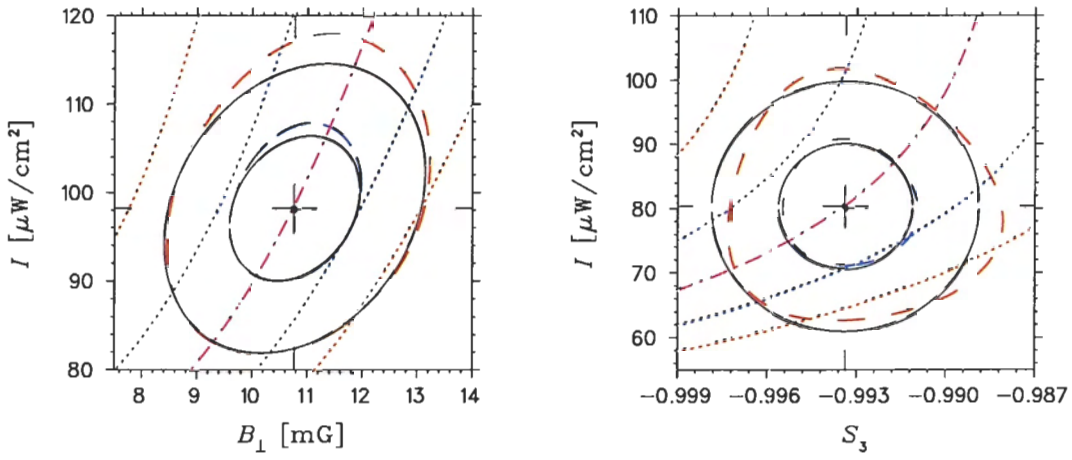

(a) σ^+ polarization; $B_\perp$ vs. I.

(b) σ^- polarization; S_3 vs. I.

FIGURE B.2: χ^2 map and comparison to the error ellipse from a two-parameter fit. Shown are the results of fitting the vanishing of the fluorescence of the 2^- group of data sets to a rate equation model (see text for details).

are off by much more than in Fig. B.2(a), indicating a greater non-linearity in the dependence of P on the Stoke's parameter, S_3.

B.2 Random versus Systematic Uncertainties

It is very important as a physicist and scientist in general to assign an honest, quantitative measure of the uncertainty in any estimate of a parameter deduced using scientific means. Implicit in that statement is that we also *express* this uncertainty in a way that others can understand. In order to make that possible, one needs to precisely define what is meant by 'uncertainty,' and so the International Organization for Standardization (ISO) has outlined the policy by which uncertainties should be expressed [121]. This standard has been adopted by many labs around the world, particularly the National Institute of Standards and Technology (NIST) which kindly offers a report publicly available on the internet summarizing the ISO proposal [122].

The uncertainty of a measurement is grouped into two categories according to how it was evaluated:

A. statistical methods,

B. other means.

The NIST Technical Note emphasizes the distinction between these classifications and the commonly referred phrases "random" and "systematic" uncertainties. Type A uncertainties are *any* uncertainty ('systematic' or otherwise) which is evaluated using statistical techniques (*i.e.* a fit result). As a concrete example, we deduced our best estimate of the polarization based on a fit to a rate equation model. The fit result gives a statistical uncertainty associated with each data set's photoion spectrum. In addition, Type B uncertainties were estimated 'by other means'. Now, in terms of P, this agrees with the common notions of statistical versus systematic. However, when we propagate the uncertainty of our deduced polarization into our B_ν measurement, *both* become a systematic uncertainty; one was estimated by statistical means and the other is not, but both are potential sources of systematic error in the deduced value of B_ν.

When combining Type A uncertainties, the overall uncertainty is reduced because the more measurements we make, the smaller the random fluctuations. Type B uncertainties on the other hand are not random and so do not improve with increased number of measurements. In the case that these systematics are common between measurements, we can reduce the statistical fluctuations in the estimate of these Type B uncertainty by averaging them.

Both Type A and B uncertainties are expressed as a standard deviation, σ, which is the positive square root of the variance of some probability distribution, 'normally' assumed to be Gaussian. The difference between Type A and B uncertainties is *not* in the assumption of the parent p.d.f. but, as mentioned above, only in the manner by which the variances were estimated.

B.2.1 Evaluating Type A Uncertainties

Estimation of the Type A standard uncertainty of a measurement is based on a statistical treatment of the data. §B.1 describes in detail the method used throughout this thesis for fitting data to a model using the method of maximum likelihood.

B.2.2 Evaluating Type B Uncertainties

Estimation of Type B uncertainties differs from Type A in that repeated measurements will not decrease the uncertainty because it is not random. As the NIST report states (§4.1) "A Type B evaluation of standard uncertainty is usually based on scientific judgment using all the relevant information available." A number of methods and examples are outlined, however the one used in this thesis is based on the assumption that the probability distribution is Gaussian. In this case, we vary parameters around their best fit by $\pm 1\sigma$, and see what effect they have on our fit result. The difference from the best estimate is taken to be the 1σ Type B uncertainty.

In what follows, we adopt the propagation of asymmetric uncertainties as outlined in Ref. [103]. We begin by assuming that a measurement of some observable, f, has been made as a function of one parameter, p, the best estimate of which is p°. Normally, one would take the best estimate of the observable to be $f(p^\circ)$ (*cf.* end of §B.1.2), however this is only true if the uncertainties are symmetric about p°. Below we consider the possibility of asymmetric uncertainties by first assuming f can be Taylor expanded around p° with the series truncated at 2^{nd} order:

$$f(p) \;=\; f(p^\circ) \;+\; \frac{\partial f}{\partial p}(p-p^\circ) \;+\; \frac{1}{2}\frac{\partial^2 f}{\partial p^2}(p-p^\circ)^2 \tag{B.26}$$

The linear case (*i.e.* symmetric uncertainties) is a special case of the above when $\partial^2 f/\partial p^2 \to 0$. In the general case, the expectation value of f is *not* $f(p^\circ)$ because the asymmetric uncertainties bias the most likely value of f towards whichever uncertainty is larger. Specifically, the expectation value of f as given by Eq. (B.26) is:

$$\begin{aligned} E[f] &= \frac{\int f(p)dp}{\int dp} \\ &= f(p^\circ) + \frac{1}{2}\frac{\partial^2 f}{\partial p^2}\sigma_p^2 \end{aligned} \tag{B.27}$$

where we have used

$$\sigma_p \equiv \frac{\int (p-p^\circ)^2 dp}{\int dp} \tag{B.28}$$

and the term involving $\partial f/\partial p$ drops out because we are integrating from $p^\circ - \sigma_p$ to $p^\circ + \sigma_p$, and $(p - p^\circ)$ is symmetric about p°. Thus we see that the best estimate of f is the evaluation at p° as in §B.1.2, but there may be a second-order shift if the uncertainties are asymmetric.

The variance of f about its expectation value similarly depends on potential higher-order corrections. The result is:

$$\begin{aligned}\mathrm{Var}(f - E[f]) \equiv \sigma_f^2 &= \langle f^2 \rangle - (E[f])^2 \\ &= \left(\frac{\partial f}{\partial p}\right)^2 \sigma_p^2 + \left(\frac{\partial f}{\partial p}\right)\left(\frac{\partial^2 f}{\partial p^2}\right)\sigma_p^3 \mathcal{S} + \frac{1}{4}\left(\frac{\partial^2 f}{\partial p^2}\right)\sigma_p^4 [\mathcal{K} - 1] \qquad \text{(B.29)}\end{aligned}$$

where the skewness and kurtosis are defined as

$$\mathcal{S} \equiv \frac{\int (p - p^\circ)^3 dp}{\sigma_p^3 \int dp} \qquad \text{and} \qquad \mathcal{K} \equiv \frac{\int (p - p^\circ)^4 dp}{\sigma_p^4 \int dp} \qquad \text{(B.30)}$$

For the Gaussian distributions assumed throughout this thesis, the skewness is zero and $\mathcal{K} = 3$. Again, in the case of symmetric uncertainties, the variance of f reduces to the usual propagation of uncertainties: $\sigma_f = |\partial f/\partial p|\sigma_p$.

To simplify notation somewhat, let us define

$$\delta \equiv \frac{1}{2}\frac{\partial^2 f}{\partial p^2}\sigma_p^2 \qquad \text{and} \qquad \bar{\Delta} \equiv \frac{\partial f}{\partial p}\sigma_p \qquad \text{(B.31)}$$

so that the expectation value and variance are simply:

$$E[f] = f(p^\circ) + \delta \qquad \text{(B.32)}$$

$$\text{and} \qquad \sigma_f^2 = \bar{\Delta}^2 + 2\delta^2. \qquad \text{(B.33)}$$

We obtain estimates of δ and $\bar{\Delta}$ by evaluating f at various values of p near p°, and then fitting the results to Eq. (B.26). Once these two parameters are estimated, we can calculate the expectation value and standard deviation by the equations given above. A minimum of three points is required, with which we can uniquely solve for δ and $\bar{\Delta}$. If we check the dependence of f at p° and $p^\circ \pm \sigma_p$, and find differences in f of:

$$\Delta_+ \equiv f(p^\circ + \sigma_p) - f(p^\circ) \qquad \text{(B.34)}$$

$$\text{and} \qquad \Delta_- \equiv f(p^\circ) - f(p^\circ - \sigma_p), \qquad \text{(B.35)}$$

then δ is their half-difference and $\bar{\Delta}$ their half-sum:

$$\delta = \tfrac{1}{2}(\Delta_+ - \Delta_-) \qquad \text{and} \qquad \bar{\Delta} = \tfrac{1}{2}(\Delta_+ + \Delta_-) \tag{B.36}$$

As mentioned earlier, the best estimate of f can potentially be biased towards higher or lower values if the dependence is highly non-linear. In these cases, we have two choices:

1. we can keep f at it's best fit value and quote asymmetric 1σ uncertainties:

$$f = f(p^\circ)^{+\Delta_+}_{-\Delta_-}, \tag{B.37}$$

   or,

2. we can assume it is nearly Gaussian (linear) and, as described above, take the best estimate to be shifted by δ

$$f = f(p^\circ) + \delta \tag{B.38}$$

   and assign an uncertainty of

$$\sigma_f = \sqrt{\bar{\Delta}^2 + 2\delta^2}. \tag{B.39}$$

In general, the asymmetric uncertainties are quoted when deduced, but when adding $i = 1, n$ systematic effects together, approach (2) above is used, with the various δ_i shifts added together to give the expectation value of f:

$$E[f] = f(p^\circ) + \sum_{i=1}^{n} \delta_i \tag{B.40}$$

and the final uncertainty is the sum in quadrature of the various σs:

$$\sigma_f^2 = \sum_{i=1}^{n} \bar{\Delta}_i^2 + 2\delta_i^2. \tag{B.41}$$

The Central Limit Theorem guarantees that the combination of a large number of variances will approach Gaussian, and so this approach is valid.

B.2.3 The Combined Standard Uncertainty

Whenever possible, a result is quoted with the Type A uncertainty separate from the Type B so that one can easily see their relative contributions. The combined standard uncertainty, which represents the total estimated standard deviation of a result, is the combination of all Type A and Type B standard deviations. Statistically speaking, as long as the variances of the distributions have been estimated well and they are approximately Gaussian, one does not need to differentiate between the two; in other words, it doesn't matter *how* the variances of the distributions were deduced, when they are combined one simply uses the usual propagation of uncertainty, Eq. B.24.

APPENDIX C

Perpendicular $\boldsymbol{B}$-fields and Optical Pumping

If we do not take $\boldsymbol{B}$ to be aligned with $\hat{z}$, the situation becomes more complicated, even for the static fields we have been considering. This may occur, for example, when another interaction is most easily described by defining a quantization axis that is not necessarily aligned with $\hat{B}$. Such is the case in our optical pumping process: we take the propagation direction of the laser beam to define the quantization axis in order to keep that description relatively simple. In order to be able to use the usual rate equations to describe the optical pumping process (discussed in §3.3.2), we include the magnetic field effects on the eigenvectors of the Hamiltonian, which as we will see amounts to a mixing of (I, J) basis states, mostly between adjacent M_F levels within the same hyperfine manifold. Then we can proceed with the rate equations neglecting any B-field effects* in our model of the optical pumping process, as long as we substitute the calculated eigenvectors of the total Hamiltonian for the zero-field approximation $|F\ M_F\rangle$ when calculating observables, such as the nuclear polarization and alignment.

Whatever the direction of the magnetic field, $\boldsymbol{\mu}$ will precess around that axis; if $\boldsymbol{B}$ is misaligned with $\hat{z}$, then this plane of precession is tilted slightly with respect to the x-y plane, by $\theta_{\hat{z}\hat{B}} = \tan^{-1}(B_\perp/B_\circ)$ as depicted in Fig. C.1. Again thinking of a

*Aside from the fact that since the atom is precessing around a slightly tilted axis, the apparent polarization will change.

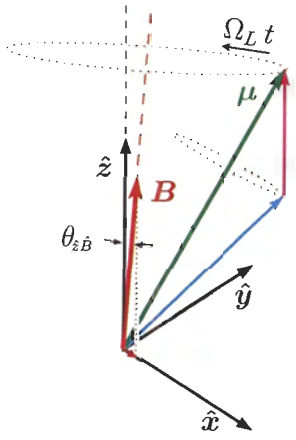

FIGURE C.1: Vector model of spin precession in a field with a small perpendicular component. The plane of precession in this case will be slightly tilted with respect to the quantization axis.

classical dipole, the rate change of $\boldsymbol{\mu}$ due to this field is:

$$\frac{d}{dt}\boldsymbol{\mu} = \boldsymbol{\mu} \times \boldsymbol{B}_{\text{ext}}, \tag{C.1}$$

where, if we let $\hat{i}$ represent some arbitrary direction in the $\hat{x}$-$\hat{y}$ plane, we can define a general static field by:

$$\boldsymbol{B}_{\text{ext}} = B_{\circ}\hat{z} + B_{\perp}\hat{i}. \tag{C.2}$$

Unlike the simpler case described earlier, F_x and F_y are now coupled to the field, which is problematic because they are not eigenfunctions of the Hamiltonian of the system. If we limit ourselves to cases where one component of the field is much larger than the other, we can consider the parallel and perpendicular effects independently. The results of the §3.2.3 account for the parallel component, and now we add in a $B_{\perp}$ component which can be treated as a perturbation, in which case $\theta_{\hat{z}\hat{B}} \ll 1$. This corresponds to treating the problem classically and neglecting coherences between the two components, which makes the solution much simpler*.

*A complete description can only be realized through the density matrix formalism using the optical Bloch equations.

To understand the effect of $\boldsymbol{\mu}$ precessing in a field with a small $\hat{x}$ component, let us work in the rotating frame of the magnetic dipole. In that reference frame, the perpendicular field appears to acquire a time-dependence and vary sinusoidally at the Larmor rate:

$$\boldsymbol{B}'_{\perp}(t) = \big(\cos\Omega_L t\,\hat{x}' + \sin\Omega_L t\,\hat{y}'\big)B_{\perp}. \tag{C.3}$$

where we have aligned $\hat{x}'$ with $\boldsymbol{B}_{\perp}$ at $t = 0$ and neglected the small tilt of the plane of precession. By analogy with electromagnetic waves, we expect the perpendicular modes to be two-fold degenerate, and described best in the circular basis defined by the $\hat{\epsilon}_{\pm} = \hat{x}' \pm i\,\hat{y}'$ axes:

$$\boldsymbol{B}'_{\perp}(t) = \frac{1}{2}B_{\perp}\big(\hat{\epsilon}_{+}e^{-i\Omega_L t} + \hat{\epsilon}_{-}e^{i\Omega_L t}\big). \tag{C.4}$$

This says that the field in the x'-y' plane may be made up of a superposition of two axes rotating at the Larmor frequency; one motion is in the positive (counter-clockwise) direction and the other is in the negative (clockwise) direction. To agree with Eq. (C.3), we take the real part of $\boldsymbol{B}'_{\perp}(t)$ above. Letting $\phi_{\circ}$ represent the initial phase between $\boldsymbol{B}_{\perp}$ and the component of $\boldsymbol{\mu}$ perpendicular to $\hat{z}$, Eq. (3.9) becomes:

$$\mathcal{H}_{\boldsymbol{B}}(t) = g_F\mu_B\Big[B_{\circ}F_z + B_{\perp}\Re e\big(F_{+}e^{-i(\Omega_L t+\phi_{\circ})} + F_{-}e^{i(\Omega_L t-\phi_{\circ})}\big)\Big], \tag{C.5}$$

and we see that the perpendicular field couples states whose angular momenta differ by $\pm\hbar$. Furthermore, we note that the precession may be positive or negative, depending on the value of g_F for a given hyperfine level. The effect of the perpendicular field depends on time: it is a maximum when $\boldsymbol{\mu}$ is aligned with the perpendicular component of B (along $\hat{x}$), and it is zero when it is aligned with $\hat{y}$. This variation is sinusoidal as μ precesses around the magnetic field, as one would expect. Expressing this in terms of I and J, the equation used to calculate the $\mathcal{H}_{\boldsymbol{B}}$ matrix is:

$$\begin{aligned}\mathcal{H}_{\boldsymbol{B}}(t) = {}& \mu_B B_{\circ}\big(g_J J_z + g'_I I_z\big) \\ & + \mu_B B_{\perp}\Re e\Big[(g_J J_{+} + g'_I I_{+})e^{-i(\phi_{\circ}+\Omega_L t)} \\ & \qquad + \ (g_J J_{-} + g'_I I_{-})e^{-i(\phi_{\circ}-\Omega_L t)}\Big]\end{aligned} \tag{C.6}$$

A perpendicular field is found to have a negligible effect on the the expansion coefficients affected by a parallel field (see end of previous section) and does not cause any (appreciable) additional energy shifts. What it *does* do is mix all of the other M_I, M_J states and so affects all of the other expansion coefficients, a_k, such that almost none of them remain zero. This makes sense considering it creates non-zero expectation values between levels of different M_Q and simply reflects the fact that in the limits we are working in, parallel and perpendicular field effects are decoupled.

Finally, referring to the example used when describing parallel fields in §3.2.3 (see page 45), the once short and succinct $|Q=2\ M_Q=1\rangle$ state now has every a_k non-zero. The two dominant ones remain $\tilde{a}_4$ and $\tilde{a}_7$, with negligible ($\lesssim 1\%$) differences from the parallel field values. Other components, however, can become as large as 4.5%:

$$\tilde{a}_1=0.00002,\ \tilde{a}_2=0.0011,\ \tilde{a}_3=0.036,\ \tilde{a}_5=0.0007,\ \tilde{a}_6=0.036,\ \text{and}\ \tilde{a}_8=-0.042.$$

These values are quoted for the $S_{1/2}$ state, but because the perturbation is relative to the 2 G parallel field, the effects are essentially independent of the hyperfine coupling, and so very similar values are found for the $P_{1/2}$ state as well.

Clearly, this mixing can have an appreciable effect on the expectation values of M_I and M_I^2 (*i.e.* the nuclear polarization and alignment), even for small perpendicular fields.

APPENDIX D

Expressions for the Angular Distribution Parameters

The expressions for the angular distribution parameters in Eq. (2.6) are reproduced from [18] and presented below. The upper sign is for β^- decay and the lower – relevant for this thesis – is for positron decay. The relativistic factor is $\Gamma = \sqrt{1-\alpha^2 Z^2}$ and $\delta_{I'I}$ is the usual Kronecker delta function. The spin functions $\lambda_{I'I}$ and $\Lambda_{I'I}$ used in some of the expression below are given by:

$$\lambda_{I'I} = \begin{cases} 1, & I \to I' = I - 1 \\ \dfrac{1}{I+1}, & I \to I' = I \\ -\dfrac{I}{I+1}, & I \to I' = I + 1 \end{cases} \tag{D.1}$$

$$\Lambda_{I'I} = \begin{cases} 1, & I \to I' = I - 1 \\ -\dfrac{2I-1}{I+1}, & I \to I' = I, \\ \dfrac{I(2I-1)}{(I+1)(2I+3)}, & I \to I' = I + 1 \end{cases} \tag{D.2}$$

The parameter, ξ, which multiplies the whole decay rate, is given by:

$$\begin{aligned} \xi = |M_F|^2 \Big(|C_V|^2 + |C'_V|^2 + |C_S|^2 + |C'_S|^2 \Big) \\ + |M_{GT}|^2 \Big(|C_A|^2 + |C'_A|^2 + |C_T|^2 + |C'_T|^2 \Big) \end{aligned} \tag{D.3}$$

The expressions for the angular distribution parameters are:

$$a\,\xi = |M_F|^2\left[|C_V|^2 + |C'_V|^2 - |C_S|^2 - |C'_S|^2 \mp \frac{2\alpha Z m_e}{p_e}\Im m\Big(C_S C_V^* + C'_S C'^*_V\Big)\right]$$
$$+ \tfrac{1}{3}|M_{GT}|^2\left[|C_T|^2 + |C'_T|^2 - |C_A|^2 - |C'_A|^2 \pm \frac{2\alpha Z m_e}{p_e}\Im m\Big(C_T C_A^* + C'_T C'^*_A\Big)\right] \quad \text{(D.4)}$$

$$b_{\text{Fierz}}\,\xi = \pm 2\Gamma\Re e\left[|M_F|^2\Big(C_S C_V^* + C'_S C'^*_V\Big) + |M_{GT}|^2\Big(C_T C_A^* + C'_T C'^*_A\Big)\right] \quad \text{(D.5)}$$

$$c_{\text{align}}\,\xi = |M_{GT}|^2\Lambda_{I'I}\left[|C_T|^2 + |C'_T|^2 - |C_A|^2 - |C'_A|^2 \pm \frac{2\alpha Z m_e}{p_e}\Im m\Big(C_T C_A^* + C'_T C'^*_A\Big)\right] \quad \text{(D.6)}$$

$$A\,\xi = |M_{GT}|^2\lambda_{I'I}\left[\pm 2\Re e\Big(C_T C'^*_T - C_A C'^*_A\Big) + \frac{2\alpha Z m_e}{p_e}\Im m\Big(C_T C'^*_A + C'_T C_A^*\Big)\right]$$
$$+ \delta_{I'I} M_F M_{GT}\sqrt{\frac{I}{I+1}}\left[2\Re e\Big(C_S C'^*_T + C'_S C_T^* - C_V C'^*_A - C'_V C_A^*\Big) \pm \frac{2\alpha Z m_e}{p_e}\Im m\Big(C_S C'^*_A + C'_S C_A^* - C_V C'^*_T - C'_V C_T^*\Big)\right] \quad \text{(D.7)}$$

$$B\,\xi = 2\Re e\Bigg\{|M_{GT}|^2\lambda_{I'I}\Big[\frac{\Gamma m_e}{E_e}\big(C_T C'^*_A + C'_T C_A^*\big) \pm \big(C_T C'^*_T + C_A C'^*_A\big)\Big]$$
$$- \delta_{I'I} M_F M_{GT}\sqrt{\frac{I}{I+1}}\left[\Big(C_S C'^*_T + C'_S C_T^* + C_V C'^*_A + C'_V C_A^*\Big) \pm \frac{\Gamma m_e}{E_e}\Big(C_S C'^*_A + C'_S C_A^* + C_V C'^*_T + C'_V C_T^*\Big)\right]\Bigg\} \quad \text{(D.8)}$$

$$D\,\xi = \delta_{I'I} M_F M_{GT}\sqrt{\frac{I}{I+1}}\left[2\Im m\Big(C_S C_T^* + C'_S C'^*_T - C_V C_A^* - C'_V C'^*_A\Big) \mp \frac{2\alpha Z m_e}{p_e}\Re e\Big(C_S C_A^* + C'_S C'^*_A - C_V C_T^* - C'_V C'^*_T\Big)\right] \quad \text{(D.9)}$$

APPENDIX E

Electronics Diagrams of the DAQ System

As discussed in this thesis, the nuclear detection system consists of four detectors: a β telescope, two phoswich β detectors and a recoil MCP detector. Below we provide a brief overview of these systems as well as the logic of the system as a whole.

The Maximum Integrated Data Acquisition System (MIDAS) [123] is used to acquire and write the data to the disk of the host Pentium III 500 MHz Linux PC. The on-line data analysis was done using a TRIUMF standard program, NOVA [124], with a special subroutine added to incorporate the position decoding of the DSSSD [10]. Off-line, we opted to write our own Fortran codes to analyze the data for maximum flexibility, though NOVA was still used to write out all triggered events.

A separate computer controls the laser system, including the trapping and optical pumping cycling. Aside from the information provided to the nuclear DAQ system discussed below, details of this atomic aspect of the experiment is deferred to the one who set it up [125].

E.1 The β Telescope

A schematic diagram of the electronics used in relation to the β telescope is shown in Fig. E.1.

The DSSSD provides us with 24 $\hat{x}$ + 24 $\hat{y}$ = 48 energy signals and 6 groups of $\hat{y}$ timing signals (consisting of 4 strips each). Each of the 24 y-strip's timing signals

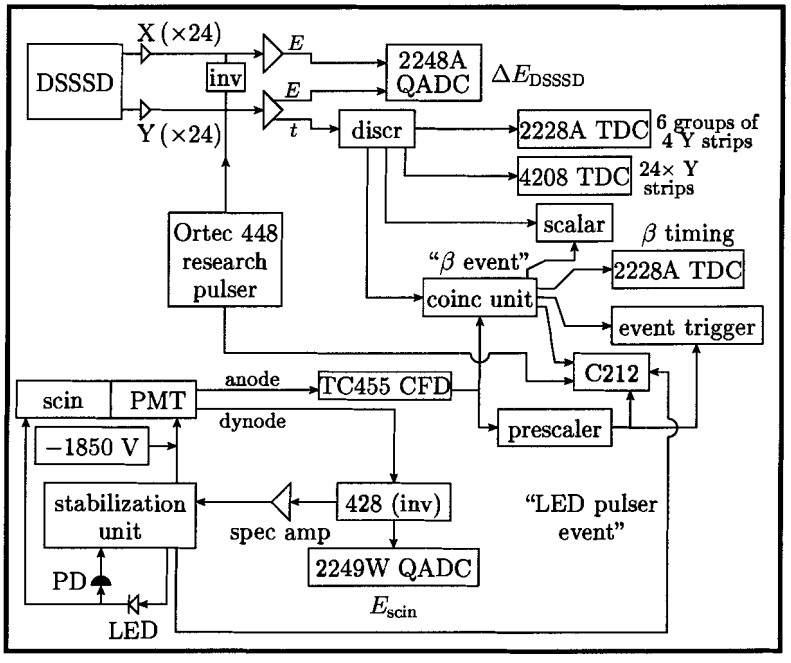

FIGURE E.1: Schematic electronics diagram for the β telescope.

have discriminators set to $\lesssim 15$ keV; if any of the strips pass this hardware threshold, the timing signal is used to generate a (wide) DSSSD event trigger. The gain of all 48 strips is monitored using the Ortec 448 research pulser.

The BC408 scintillator energy reading is taken from the dynode output of the PMT after it is inverted by a LeCroy 428F linear fan-in/fan-out. The high voltage applied to the PMT is adjusted by a stabilization unit [126] based on the LED signals observed; the intensity of the LED is (independently) maintained constant using a temperature-stabilized photodiode. The Tennelec 455 constant fraction discriminator uses the anode signal to generate the scintillator's (fast) timing signal.

A "β event" is determined by a hardware coincidence condition between the DSSSD and scintillator timing. If satisfied, a signal is sent to a LeCroy 429A fan in/out which acts as our event trigger. To retain information on the scintillator singles, we prescale the anode timing and input this into the event trigger as well; this gives us 1 in 100 of the singles events without overwhelming our DAQ with background events. The C212 coincidence register (see below) labels both types of events, as well as pulser

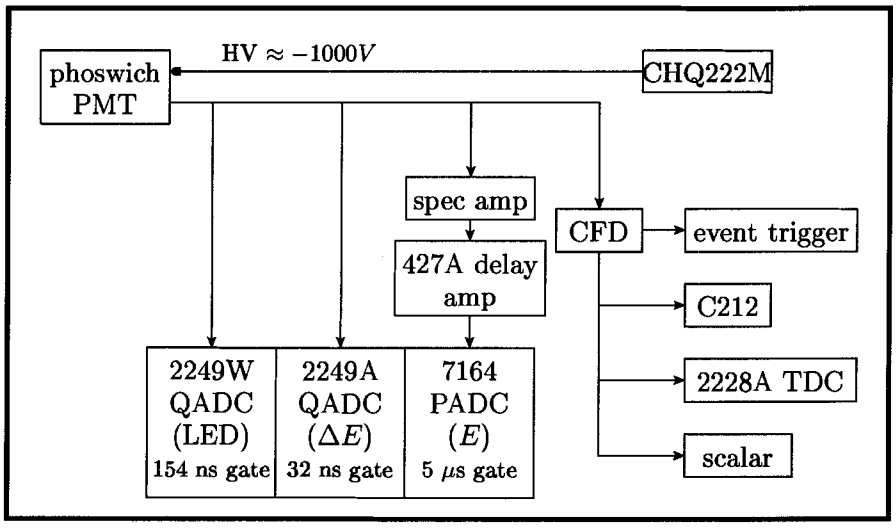

FIGURE E.2: Schematic electronics diagram for (one of) the phoswich detectors.

events from either the LED or research pulser.

E.2 The Phoswich Detectors

A schematic diagram of the electronics for one of the phoswich detectors is shown in Fig. E.2. Both phoswiches have identical electronics.

A CHQ222M DAC, controlled by the frontend code of the DAQ, provides the high-voltage for the PMTs of the phoswich detectors. The LED used as part of the gain stabilization of the β telescope's scintillator is also input into the phoswich detectors in order to monitor their gains. For these events, the signal is read out by a charge-sensitive ADC with a 150 ns wide gate. β events will generate a signal with a fast component from the thin scintillator (ΔE) and a slow component from the CaF_2(Eu) (E). Their signals are separately read out in charge- and peak-sensing ADCs with gate widths of 32 ns and 5 μs respectively. The fast ΔE signal is used to provide the timing of the event, to provide the event trigger, and to label the event in the C212 as a phoswich event.

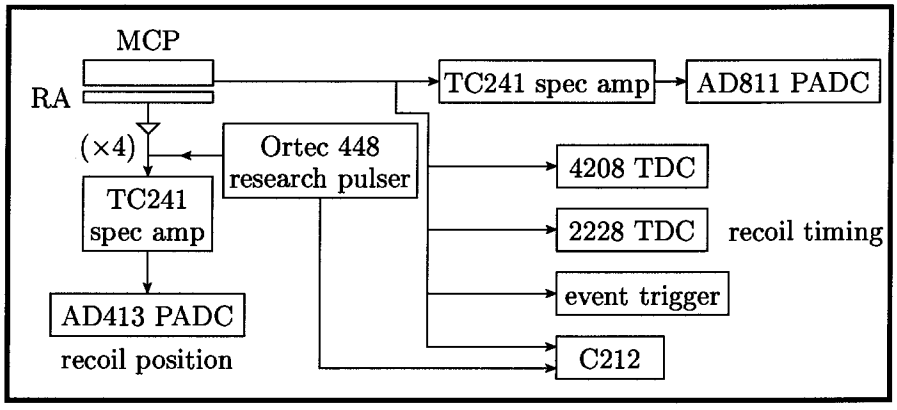

FIGURE E.3: Schematic electronics diagram for the recoil MCP detector.

E.3 The MCP

A schematic diagram of the electronics used in relation to the MCP recoil detector is shown in Fig. E.3.

The recoil detection system is essentially unchanged from previous experiments. The four resistive anode signals are pre-amplified and then amplified before being read out by a peak-sensing ADC. These signals are used to deduce the position of the hit in the MCP. The same research pulser used with the DSSSD monitors the gains of the resistive anodes. The timing from the last plate of the MCP is used to define the recoil TOF by stopping the 2228 multi-hit TDC. In addition, we use this signal to generate a recoil event trigger and to label it as such in the C212.

E.4 Event Types

The gates for the ADCs and the starts for the TDCs are all derived from the LeCroy 429A unit labeled 'event trigger'. The inputs to this unit, i.e. the various event types, are:

1. A prescaled scintillator singles event,

2. A β event from the hardware DSSSD-scintillator coincidence,

3. A recoil-triggered event from the MCP,
4. a β event from the phoswich A detector,
5. a β event from the phoswich B detector,
6. DSSSD/MCP pulser events from the Ortec 448, and
7. Scintillator pulser (LED) events from the stabilization unit.

A C212 coincidence unit allows us to record which of these generated the event trigger. It is a 16 bit register which is strobed with every event trigger and so records the status of a number of aspects of our system with each event:

1. if the event was generated by the LED pulser in the scintillators,
2. whether the D_1 optical pumping laser was on or off,
3. whether the push beam was on and transferring atoms from the collection trap to the detection chamber,
4. if there are atoms in the trap or if they're being loaded,
5. if the event was generated by a prescaled scintillator event,
6. if the MCP started the event trigger,
7. if the research pulser of the DSSSD/MCP triggered the event,
8. whether the optical pumping light polarization was σ^+ or σ^-,
9. if phoswich A generated the event,
10. if phoswich B generated the event,
11. if the photoionization laser was pulsed,
12. a flag to warn us if the MCP or one of the electrostatic hoops tripped,

The C212 information provides our basic conditions when analyzing the data. For example, if we are interested monitoring the gains of the detectors, we would require that either the LED or research pulser generated the event; if we're looking at the β decay events, we would instead veto these pulser events.

In addition to the C212 label for $\sigma^{\pm}$ polarization of the D_1 light, we read out the DAC from the PC controlling the atomic part of the system into an ADC; the value of the ADC (high vs. low) provided an extra check of the polarization state, and allowed us more than two states (as a diagnostic, we sometimes used linear polarization of the optical pumping light, which would have required another signal to the C212 to be able to flag this polarization state).

Bibliography

[1] C. L. Cowan and F. Reines. *The neutrino.* Nature, **178**, (1956) 446.

[2] E. Fermi. *Versuch einer theorie der βstrahlen I.* Zeitschrift für Physik, **88**, (1934) 161–171.

[3] S. Eidelman, et al. (the Particle Data Group). *Review of Particle Physics.* Physics Letters B, **592**, (2004) 1+.

[4] T. D. Lee and C. N. Yang. *Question of parity conservation in weak interactions.* Physical Review, **104**, (1956) 254–258.

[5] C. S. Wu et al. *Experimental test of parity conservation in beta decay.* Physical Review, **105**, (1958) 1413.

[6] L. M. Chirovsky et al. *Directional distributions of beta-rays emitted from polarized ^{60}Co nuclei.* Physics Letters, **94B**, (1980) 127.

[7] R. L. Garwin, L. M. Lederman, and M. Weinrich. *Observations of the failure of conservation of parity and charge conjugation in meson decays: the magnetic moment of the free muon.* Physical Review, **105**, (1957) 1415.

[8] J. I. Friedman and V. L. Telegdi. *Nuclear emulsion evidence for parity nonconservation in the decay chain $\pi^+ \rightarrow \mu^+ \rightarrow e^+$.* Physical Review, **106**, (1957) 1290.

[9] A. Gorelov et al. *Scalar interaction limits from the $\beta - \nu$ correlation of trapped radioactive atoms.* Physical Review Letters, **94**, (2005) 142501.

[10] D. Melconian. A positron detector for precision beta decay experiments from a magneto-optical trap. Master's thesis, Simon Fraser University, 2000.

[11] A. Gorelov. *Positron-Neutrino Correlation Measurements in the Beta-Decay of Magneto-Optically Trapped ^{38m}K Atoms.* PhD thesis, Simon Fraser University. In preparation.

[12] M. Trinczek. *Limits on Heavy Neutrino Mixing from the Beta Decay of ^{38m}K Confined in a Magneto-Optical Trap.* PhD thesis, Simon Fraser University, 2001.

[13] M. Trinczek et al. *Novel search for heavy ν mixing from the β^+ decay of ^{38m}K confined in an atom trap.* Physical Review Letters, **90**, (2003) 012501.

[14] J. D. Jackson, S. B. Treiman, and H. W. Wyld. *Possible tests of time reversal invariance in beta decay.* Physical Review, **106**, (1957) 517–521.

[15] R. P. Feynman and M. Gell-Mann. *Theory of the Fermi interaction.* Physical Review, **109**, (1958) 193.

[16] M. L. Goldberger and S. B. Treiman. *Decay of the pi meson.* Physical Review, **110**, (1958) 1178.

[17] Y. Nambu. *Axial vector current conservation in weak interactions.* Physical Review Letters, **4**, (1960) 380.

[18] J. D. Jackson, S. B. Treiman, and H. W. Wyld. *Coulomb corrections in allowed beta transitions.* Nuclear Physics, **A4**, (1957) 206–212.

[19] F. Glück. Private communication. For ^{38m}K, Ferenc collaborated with us to include radiative corrections in our scalar search; he has said he would be interested to do the same for polarized decays once we reached relevant sensitivities.

[20] E. Hagberg et al. *Measurement of the l-forbidden Gamow-Teller branch of ^{37}K.* Physical Review C, **56**, (1997) 135–141.

[21] G. C. Ball. Tests of the standard model from nuclear beta-decay studies at ISAC. In A. Astbury et al., editors, *Proceedings of the 15th Lake Louise Winter Institue.* World Scientific, 2000.

[22] I. S. Towner. Private communication.

[23] S. Raman et al. *Mixed Fermi and Gamow-Teller β-transitions and isoscalar magnetic moments.* Atomic Data and Nuclear Data Tables, **21**, (1978) 567.

[24] B. R. Holstein. *Recoil effects in allowed beta decay: The elementary particle approach.* Reviews of Modern Physics, **46**, (1974) 789–814.

[25] C. von Platen et al. Zeitschrift für Physik, **244**, (1971) 44.

[26] J. A. Behr et al. *Magneto-optic trapping of β-decaying ^{38m}K, ^{37}K from an on-line isotope separator.* Physical Review Letters, **79**, (1997) 375–378.

[27] M. M. Robertson, J. E. Mack, and V. W. Cohen. *Nuclear spin and magnetic moment of Ar^{37}.* Physical Review, **140**, (1965) B820.

[28] M. L. Pitt. Bulletin of the American Physical Society, **33**, (1988) 1564.

[29] M. L. Pitt. *Test of the Linearity of Quantum Mechanics Using ^{37}Ar Polarized by Spin-Exchange Optical Pumping.* PhD thesis, Princeton University, 1992. ; and private communication.

[30] N. J. Stone. *Table of nuclear magnetic dipole and electric quadrupole moments.* Atomic Data and Nuclear Data Tables, **90**, (2005) 75–176.

[31] P. M. Endt. *Energy levels of $A = 21 - 44$ nuclei (VII).* Nuclear Physics, **A521**, (1990) 1.

[32] P. Raghavan. *Table of nuclear moments.* Atomic Data and Nuclear Data Tables, **42**, (1989) 189.

[33] A. Klein et al. *Moments and mean square charge radii of short-lived argon isotopes.* Nuclear Physics, **A607**, (1996) 1–22.

[34] B. R. Holstein and S. B. Treiman. *Tests for second-class currents in nuclear β decay.* Physical Review C, **3**, (1971) 1921.

[35] J. C. Pati and A. Salam. *Lepton number as the fourth "color".* Physical Review D, **10**, (1974) 275.

[36] R. N. Mohapatra and J. C. Pati. *Left-right gauge symmetry and an "isoconjugate" model of CP violation.* Physical Review D, **11**, (1975) 566.

[37] R. N. Mohapatra and G. Senjanovic. *Exact left-right symmetry and spontaneous violation of parity.* Physical Review D, **12**, (1975) 1502.

[38] P. Herczeg. *Beta decay beyond the standard model.* Progress in Particle and Nuclear Physics, **46**, (2001) 413.

[39] M. A. B Bég et al. *Manifest left-right symmetry and its experimental consequences.* Physical Review Letters, **38**, (1977) 1252. Erratum, Phys. Rev. Lett. **39** (1977) 54.

[40] B. R. Holstein and S. B. Treiman. *Tests of spontaneous left-right symmetry breaking.* Physical Review D, **16**, (1977) 2369.

[41] P. Herczeg. *On muon decay in left-right symmetric electroweak models.* Physical Review D, **34**, (1986) 3449–3456.

[42] O. Naviliat-Cuncic et al. *Left-right symmetry breaking sensitivity of β-asymmetry measurements.* Journal of Physics G, **17**, (1991) 919.

[43] N. D. Scielzo et al. *Measurement of the $\beta-\nu$ correlation using magneto-optically trapped ^{21}Na.* Physical Review Letters, **93**, (2004) 102501.

[44] M. Hausmann et al. *Beta-asymmetry studies on polarized ^{82}Rb atoms in a top trap.* Nuclear Physics, **A746**, (2004) 669c.

[45] S. G. Crane et al. *Parity violation observed in the beta decay of magnetically trapped ^{82}Rb atoms.* Physical Review Letters, **86**, (2001) 2967.

[46] D. Acosta, et al. (The CDF Collaboration). *Search for a W' boson decaying to a top and bottom quark pair in 1.8 TeV $p\bar{p}$ collisions.* Physical Review Letters, **90**, (2003) 081802.

[47] S. Abachi, et al. (The D0 Collaboration). *Search for right-handed W bosons and heavy W' in $p\bar{p}$ collisions at $\sqrt{s} = 1.8$ TeV.* Physica Review Letters, **76**, (1996) 3271.

[48] H. Abramowicz et al. *Limit on right-handed weak coupling parameters from inelastic neutrino interactions.* Zeitschrift für Physik C, **12**, (1982) 225.

[49] S. R. Mishra et al. *Search for right-handed coupling in $\nu-N$ scattering.* Physical Review Letters, **68**, (1992) 3499–3502.

[50] C. Bouchiat and L. Michel. *Theory of μ-meson decay with the hypothesis of nonconservation of parity.* Physical Review, **106**, (1957) 170.

[51] J. R. Musser et al. *Measurement of the Michel parameter ρ in muon decay.* Physical Review Letters, **94**, (2005) 101805.

[52] A. Gaponenko et al. *Measurement of the muon decay parameter δ.* Physical Review D, **71**, (2005) 071101R.

[53] The numerical limits are courtesy of A. Gaponenko, private communication.

[54] J. C. Hardy and I. S. Towner. *Superallowed $0^+ \rightarrow 0^+$ nuclear β decays: A critical survey with tests of the conserved vector current hypothesis and the standard model.* Physical Review C, **71**, (2005) 055501.

[55] A. Sher et al. *High statistics measurement of the $K^+ \rightarrow \pi^0 e^+ \nu (K^+_{e3})$ branching ratio.* Physical Review Letters, **91**, (2003) 261802.

[56] T. Alexopoulos et al. *A determination of the Cabibbo-Kobayashi-Maskawa parameter $|V_{us}|$ using K_l decays.* Physical Review Letters, **93**, (2004) 181802.

[57] N. Severigns et al. *Limits on right-handed charged weak currents from a polarization-asymmetry correlation experiment with ^{107}In.* Physical Review Letters, **70**, (1993) 4047. Erratum: Phys. Rev. Lett. **73** (1994) 661.

[58] E. Thomas et al. *Positron polarization in the decay of polarized ^{12}N: a precision test of the Standard Model.* Nuclear Physics, **A694**, (2001) 559.

[59] L. Dick et al. *A novel efficient method for measuring the polarisation of positrons.* Physics Letters, **3**, (1963) 326–329.

[60] G. Gerber et al. *Precision measurement of positron polarization in ^{68}Ga decay based on the use of a new positron polarimeter.* Physical Review D, **15**, (1977) 1189–.

[61] P. Quin and T. Girard. *Sensitivity of the polarized nucleus-beta polarization correlation to right-handed currents in the weak interaction.* Physics Letters B, **29**, (1989) 29–32.

[62] J. Deutsch. Symmetry-tests in semileptonic weak interactions: a search for new physics. In P. Langacker, editor, *Precision tests of the Standard Electroweak Model.* World Scientific Advanced Series on directions in high energy physics, 1993.

[63] A. S. Carnoy et al. *Limits on nonstandard weak currents from the polarization of ^{14}O and ^{10}C decay positrons.* Physical Review C, **43**, (1991) 2825–2834.

[64] V. A. Wichers et al. *Bounds on right-handed currents from nuclear beta decay.* Physical Review Letters, **58**, (1987) 1821.

[65] H. Abele. *The Standard Model and the neutron β-decay.* Nuclear Instruments and Methods in Physics Research, **A440**, (2000) 499–510.

[66] A. Serebrov et al. *Measurement of the neutron lifetime using a gravitational trap and a low-temperature Fomblin coating.* Physics Letters B, **605**, (2005) 72.

[67] F. P. Calaprice et al. *Experimental study of weak magnetism and second-class interaction effects in the β decay of polarized ^{19}Ne.* Physical Review Letters, **35**, (1975) 1566.

[68] P. Langacker and S. U. Sankar. *Bounds on the mass of w_r and the $w_l - w_r$ mixing angle ζ in general $su(2)_l \times su(2)_r \times u(1)$ models.* Physical Review D, **40**, (1989) 1569–1585.

[69] R. Barbieri and R. N. Mohapatra. *Limits on right-handed interactions from SN 1987A observations.* Physical Review D, **39**, (1989) 1229.

[70] E. L. Raab et al. *Trapping of neutral sodium atoms with radiation pressure.* Physical Review Letters, **59**, (1987) 2631–2634.

[71] G. D. Sprouse and L. A. Orozco. *Laser trapping of radioactive atoms.* Annual Reviews of Nuclear and Particle Science, **47**, (1997) 429–461.

[72] H. J. Metcalf and P. van der Straten. *Laser cooling and trapping.* Springer, 1999.

[73] D. Melconian, 1997–2005. `alksplit.F` is a general fortran code that solves eigenvalue problems by numerically diagonalizing a given matrix.

[74] A. Corney. *Atomic and Laser Spectroscopy.* Oxford University Press, 1977.

[75] E. Arimondo, M. Inguscio, and P. Violino. *Experimental determinations of the hyperfine structure in the alkali atoms.* Reviews of Modern Physics, **49**, (1977) 31–75.

[76] J. Emsley. *The Elements.* Oxford University Press, 1995.

[77] H. Metcalf and P. van der Straten. *Cooling and trapping of neutral atoms.* Physics Reports, **244**, (1994) 203–286.

[78] E. Arimondo, W.D. Phillips, and F. Strumia, editors. *Laser Manipulation of Atoms and Ions.* Amsterdam: North Holland, 1992.

[79] D. R. Swenson and L. W. Anderson. *Relaxation rates for optically pumped Na vapor on silicone surfaces.* Nuclear Instruments and Methods in Physics Research, **B29**, (1988) 627–642.

[80] R. Gückert et al. *Magneto-optical trapping of radioactive ^{82}Rb atoms.* Physical Review (rapid communications), **A58**, (1998) R1637–R1640.

[81] D. Melconian et al. *Release of ^{37}K from catcher foils.* Nuclear Instruments and Methods in Physics Research, **A538**, (2005) 93–99.

[82] T. Swanson et al. *Efficient transfer in a double magneto-optic trap system.* Journal of the Optical Society of America, **B15**, (1998) 2641–2645.

[83] A. Kastler. *Quelques suggestions concernant la production optique et la détection optique d'une inégalité de population des niveaux de quantification spatiale des atomes. application a l'éxperience de Stern et Gerlach et a la résonance magnétique.* J. Physique Rad., **11**, (1950) 255–265.

[84] S. Gu et al. *Coherent population trapping states with cold atoms in a magnetic field.* Optics Communications, **220**, (2003) 365–370.

[85] C. Cohen-Tannoudji, J. Dupont-Roc, and G. Grynberg. *Atom-photon interactions.* John Wiley & Sons, Inc., 1992. Exercise 18 is on pages 601–604.

[86] E. de Clerq et al. *Laser diode optically pumped caesium beam.* Journal de Physique, **45**, (1984) 239.

[87] Y. Natcha et al. *Coherence-induced population redistribution in optical pumping.* Physical Review A, **52**, (1995) 3126.

[88] A. R. Edmonds. *Angular momentum in quantum mechanics.* Princeton University Press, 1974.

[89] CERN Software Group. The Wigner $3j$ and $6j$ symbols are part of `mathlib`.

[90] Galileo. *Galileo Micro-Channel Plate data sheets.* The recoil detector is largely the work of A. Gorelov.

[91] M. Lampton and C. W. Carlson. *Low-distortion resistive anodes for two-dimensional position-sensitive MCP systems.* Review of Scientific Instruments, **50**, (1979) 1093.

[92] J. A. Behr. Private communication.

[93] CERN. *GEANT Detector Description and Simulation Tool*, October 1994 edition, 1993.

[94] D. Melconian, 1997–present. this Monte Carlo package is available at `http://trshare.triumf.ca/~melcon/smc`.

[95] D. H. Wilkinson. *Evaluation of beta-decay II. Finite mass and size effects.* Nuclear Instruments and Methods in Physics Research, **A290**, (1990) 509–515.

[96] I. S. Towner and J. C. Hardy. *Superallowed* $0^+ \rightarrow 0^+$ *nuclear* β*-decays.* Nuclear Instruments and Methods in Physics Research, **A335**, (1993) 182–200.

[97] J. von Neumann. *Various techniques used in connection with random digits.* U.S. National Bureau of Standards – Applied Mathematics Series, **12**, (1951) 36–38.

[98] P. R. Bevington. *Data Reduction and Error Analysis for the Physical Sciences.* McGraw-Hill, 1969.

[99] WestGrid is funded in part by the Canada Foundation for Innovation, Alberta Innovation and Science, BC Advanced Education, and the participating research institutions. Further information can be found at `http://www.westgrid.ca`.

[100] P. M. Endt. *Supplement to energy levels of $A = 21 - 44$ nuclei (VII).* Nuclear Physics, **A633**, (1998) 1–220. ^{37}K on page 180; ^{38,38m}K on page 187.

[101] C. Kittel and H. Kroemer. *Thermal Physics*, chapter 14, page 393. W.H.Freeman and Company, 2nd edition, 1980.

[102] J. D. Jackson. *Classical Electrodynamics.* John Wiley & Sons, 2nd edition, 1975. (page 277).

[103] G. D'Agostini and M. Raso. *Uncertainties due to imperfect knowledge of systematic effects: general considerations and approximate formulae.* CERN-EP/2000-026, (2000). Available at hep-ex/0002056, and submitted to Am. J. Phys.

[104] A. Gorelov, 2000. Private communication.

[105] J. A. Behr. Private communication, based on Holstein's paper [127].

[106] L. J. Lising et al. *New limit on the D coefficient in polarized neutron decay.* Physical Review C, **62**, (2000) 055501.

[107] A. L. Hallin et al. *Test of time-reversal symmetry in the β decay of ^{19}Ne.* Physical Review Letters, **52**, (1984) 337–340.

[108] C. Martin et al. *Wedge-and-strip anodes for centroid-finding position-sensitive photon and particle detectors.* Review of Scientific Instruments, **52**, (1981) 1067–1074.

[109] K. L. Corwin et al. *Spin-polarized atoms in a circularly polarized optical dipole trap.* Physical Review Letters, **83**, (1999) 1311.

[110] S. Dürr, K. W. Miller, and C. E. Wieman. *Improved loading of an optical dipole trap by suppression of radiative escape.* Physical Review A, **63**, (2001) 011401.

[111] K. W. Miller, S. Dürr, and C. E. Wieman. *rf-induced Sisyphus cooling in an optical dipole trap.* Physical Review A, **66**, (2002) 023406.

[112] D. Cho. *Analogous Zeeman effect from the tensor polarizability in alkali atoms.* Journal of the Korean Physical Society, **30**, (1997) 373–376.

[113] E. Prime et al. To be submitted to the Canadian Journal of Physics.

[114] E. Prime. Loading of a far off resonance dipole force trap for stable ^{39}K. Master's thesis, University of British Columbia, 2005.

[115] N. D. Scielzo et al. *Detecting shake-off electron-ion coincidences to measure beta-decay correlations in laser trapped Na-21.* Nuclear Physics, **A746**, (2004) 677c.

[116] G. C. Ball. Private communication. The 8π collaboration at TRIUMF is able to improve both the lifetime and branching ratio, and is willing to pursue this measurement if we require an improved ft value.

[117] J. L. Chuma. `physica`, 2004. See `http://www.triumf.ca/~chuma/physica`.

[118] D. Melconian, 2004. `fit.F` is a general minimization routine based on the Marquardt algorithm [119].

[119] D. W. Marquardt. *An algorithm for least squares estimation of nonlinear parameters.* J. Soc. Industr. Appl. Math., **11**, (1963) 431–441.

[120] L. Lyons. *Statistics for nuclear and particle physics.* Cambridge University Press, 1989. See Eq. (3.40).

[121] ISO Technical Advisory Group 4 and Working Group 3. Guide to the expression of uncertainty in measurement, 1993.

[122] B. N. Taylor and C. E. Kuyatt. Guidelines for evaluating and expressing the uncertainty of NIST measurement results, 1994. This report can be obtained at `http://www.physics.nist.gov/Pubs/guidelines/contents.html`.

[123] S. Ritt and P.-A. Amaudruz. The Maximum Integrated Data Acquisition System, 1993–2000. This software was developed as a joint venture between PSI and TRIUMF. More information can be found at `http://midas.triumf.ca`.

[124] P. W. Green. *NOVA.* TRIUMF / The University of Edmonton, v2.0 edition, 1995.

[125] J. A. Behr. Senior research scientist, TRIUMF (`behr@triumf.ca`).

[126] Y. Holler, J. Koch, and A. Naini. *A stabilized NE213 scintillator for neutron time-of-flight spectroscopy.* Nuclear Instruments and Methods in Physics Research, **204**, (1983) 485–490.

[127] B. R. Holstein. *Tests for T invariance in allowed nuclear beta decay.* Physical Review C, **5**, (1972) 1529.